

BepiColombo Laser Altimeter (BELA) Performance Evaluation: From Laboratory Tests to Simulations of Flight Observations

Inauguraldissertation
der Philosophisch-naturwissenschaftlichen Fakultät
der Universität Bern

vorgelegt von

Alireza HosseiniArani

von Iran

Leiter der Arbeit:

Prof. Dr. Nicolas Thomas

Dr. Stefano Bertone

Dr. Daniel Arnold

Physikalisches Institut der Universität Bern

**BepiColombo Laser Altimeter (BELA)
Performance Evaluation:
From Laboratory Tests to Simulations of Flight
Observations**

Inauguraldissertation
der Philosophisch-naturwissenschaftlichen Fakultät
der Universität Bern

vorgelegt von

Alireza HosseiniArani

von Iran

Leiter der Arbeit:

Prof. Dr. Nicolas Thomas

Dr. Stefano Bertone

Dr. Daniel Arnold

Physikalisches Institut der Universität Bern

Von der Philosophisch-naturwissenschaftlichen Fakultät angenommen.

Bern, 31. January 2020

Der Dekan:

Prof. Dr. Zoltan Balogh

Copyright licence: CC BY-NC
<https://creativecommons.org/licenses/by-nc/4.0/>

Abstract

The BepiColombo Laser Altimeter [BELA, [Thomas et al., 2007](#)] is one of the main instruments on board Mercury Planetary Orbiter (MPO), one of the two spacecrafts of the European Space Agency's (ESA) BepiColombo mission [Benkhoff et al. \[2010\]](#). It will arrive at Mercury by 2025 and start its measurements of Mercury's surface.

The main goal of this study is to analyse the laboratory test results in the framework of a comprehensive in-orbit performance model for BELA. We determine the quality of observations and the recovery of surface features.

To determine the in-flight performance, we first use the laser altimetry performance model described in [Gardner \[1992\]](#) as our basis and we implement the end-to-end test results on BELA in the laser altimetry test laboratory of the University of Bern to our modeling of the instrumental noise. We then model the probability of false detection for each observation and based on that, we produce a coverage map over different surface terrains.

At each observation time we use the dynamical model to determine the position of MPO around Mercury and to determine the bouncing time and coordinates of the laser beam on the planet surface. Then, using a synthetic topography model, we determine the surface properties (e.g. local slope, roughness, ...) at that point and calculate the properties of the return signal. Finally, using the instrument noise model, we determine the time of flight, pulse width and pulse energy measurement errors.

This results in a performance map over the surface of Mercury and we study the attainable topography and the expected accuracy of the measurements of surface properties, *e.g.* local slopes, roughness and albedo, in different conditions and over different terrains.

The second goal of this PhD thesis is to estimate the impact of BELA on the improvement of the orbit of spacecraft and planet geophysical parameters. To achieve this goal, we first perform a Doppler-only orbit determination. We simulate one year of 2-way X-band and K-band Doppler radio-science tracking data, including station and planetary eclipses. These are in turn used to reconstruct MPO orbit and evaluate its accuracy within a closed-loop simulation. In addition to this, we set-up pseudo-measurements at the crossover points of BELA ground-tracks, based on the nominal orbit and evaluate their potential contribution to the recovery of MPO orbit and of Mercury geophysical parameters.

Finally, we recommend technical settings to improve the pulse detection and the quality of observations. We also suggest potential calibrations and several approaches for the recovery of surface properties, which would enhance the scientific outcome of BELA and, in general, of the BepiColombo mission.

CONTENTS

| | |
|---|----|
| 1. <i>Introduction</i> | 1 |
| 1.1 Planet Mercury | 1 |
| 1.2 Missions to planet Mercury | 2 |
| 1.3 Mercury Planetary Orbiter | 4 |
| 1.4 Mercury radio science experiment | 8 |
| 1.5 BELA | 8 |
| 1.6 Pulse detection algorithm | 11 |
| 1.7 Previous studies and goals | 14 |
| 2. <i>Laboratory-based performance tests on BELA range finder module</i> | 17 |
| 2.1 Test set up and assumptions | 17 |
| 2.2 Time of flight measurement error | 20 |
| 2.2.1 Time of flight deviation as a function of spacecraft altitude | 20 |
| 2.2.2 Systematic bias on time of flight | 20 |
| 2.3 Pulse width measurement error | 23 |
| 2.4 Pulse energy measurement error | 26 |
| 3. <i>Probability of false detection</i> | 31 |
| 3.1 PFD determination in a simulation environment | 31 |
| 3.2 Special performance tests before and after BELA hardware modification | 31 |
| 3.2.1 Test execution summary | 31 |
| 3.2.2 Science data analysis | 31 |
| 3.3 PFD calculation using spacecraft noise environment | 34 |
| 3.3.1 PFD tests in different altitudes and return pulse widths | 34 |
| 3.3.2 The impact of Instrument gain settings | 34 |
| 3.4 The impact of solar noise on PFD | 35 |
| 4. <i>In-flight performance evaluation: modelling</i> | 39 |
| 4.0.1 TOF measurement noise model | 40 |
| 4.0.2 Pulse width measurement noise model | 42 |
| 4.0.3 Pulse energy measurement noise model | 43 |
| 4.1 Dynamical model of Bepicolombo spacecraft | 43 |
| 4.1.1 Spacecraft orbit | 43 |
| 4.1.2 Pointing uncertainty | 44 |
| 4.2 Mercury terrain model | 45 |
| 4.2.1 Surface elevation model | 46 |

| | | |
|-------|--|-----|
| 4.2.2 | Terrain types | 46 |
| 4.2.3 | Local slope model | 46 |
| 4.2.4 | Surface roughness model | 48 |
| 4.2.5 | Surface reflectance model | 48 |
| 4.3 | BELA instrument noise model | 48 |
| 4.3.1 | Instrument degradation model | 51 |
| 4.3.2 | the impact of solar noise on the measurements | 52 |
| 5. | <i>In-flight performance evaluation: results</i> | 53 |
| 5.1 | BELA in-orbit measurement error | 53 |
| 5.1.1 | Time of flight measurement errors | 53 |
| 5.1.2 | Pulse width and pulse energy measurement errors | 53 |
| 5.2 | Expected instrument coverage | 57 |
| 5.2.1 | The impact of degradation on the coverage | 59 |
| 5.2.2 | The impact of local albedo on the coverage | 59 |
| 5.3 | Expected performance in measuring surface features | 64 |
| 5.3.1 | Topography measurement accuracy | 64 |
| 5.3.2 | Performance in measuring the surface slope | 67 |
| 5.3.3 | Performance in measuring the surface roughness | 71 |
| 5.3.4 | Albedo measurement performance | 75 |
| 5.3.5 | The impact of instrument degradation | 76 |
| 5.3.6 | Performance sensitivity to Mercury average slope angle | 77 |
| 5.4 | Height difference performance on crossover points | 78 |
| 6. | <i>Precise orbit determination using Doppler and laser altimetry data</i> | 81 |
| 6.1 | Theory of orbit determination for deep space missions | 81 |
| 6.1.1 | Least-squares adjustment | 81 |
| 6.1.2 | Dynamics of orbit determination | 82 |
| 6.1.3 | Variational equations | 84 |
| 6.1.4 | Orbit determination using multi-arc approach | 85 |
| 6.2 | Doppler-only orbit determination for MPO: modelling | 85 |
| 6.2.1 | Dynamical model | 86 |
| 6.2.2 | Observation model | 88 |
| 6.2.3 | Modelling the non-gravitational forces and accelerometer model | 89 |
| 6.2.4 | Parameter estimation model | 94 |
| 6.3 | Doppler-only orbit determination: results | 95 |
| 6.3.1 | Doppler-only orbit determination: zero test results | 95 |
| 6.3.2 | The impact of solar plasma noise | 96 |
| 6.3.3 | Orbit recovery tests for 100 days | 98 |
| 6.4 | Improvement of orbit and geophysical parameters using laser altimetry data | 101 |
| 6.4.1 | Modelling | 101 |
| 6.4.2 | Detection of the crossover points | 101 |
| 6.4.3 | Results | 102 |

| | |
|--|-----|
| 7. <i>Conclusion and perspective</i> | 111 |
| 7.1 Objectives and approach | 111 |
| 7.2 Summary of the results | 112 |
| 7.3 Recommendations for the improvement of BELA performance | 115 |
| 7.3.1 Gain settings | 116 |
| 7.3.2 DTM recovery | 116 |
| 7.4 Future studies and possible experiments | 117 |
| 7.4.1 Investigating the potential sources for the systematic biases | 117 |
| 7.4.2 Calibration of systematic biases for all types of return signal | 117 |
| 7.4.3 Optimisation of the pulse families | 117 |
| 7.4.4 Pointing calibration study using crossover points | 118 |
| 7.4.5 Improving the orbit and planet geophysical parameters using laser al- timetry crossovers | 118 |
| 7.4.6 Studying the impact of off-nadir maneuvers for orbit and geodesy im- provement | 118 |
| 7.4.7 Further developing the simulation environment | 119 |
| 7.4.8 In-orbit performance evaluation of Ganymede Laser Altimeter (GALA) for the JUICE Mission | 119 |
| <i>Appendices</i> | 121 |
| A. <i>MPO Relative Orbit Error Modelling Using the Bernese GNSS software: A technical report on BELA</i> | 123 |
| A.1 Scope of the report | 123 |
| A.2 Introduction | 123 |
| A.3 Assumptions | 123 |
| A.4 Modelling the orbit | 124 |
| A.5 Approach | 124 |
| A.6 Results | 127 |
| B. <i>Submitted paper on Planetary and space science journal</i> | 129 |

1. INTRODUCTION

1.1 Planet Mercury

Mercury is the least known planet in the inner solar system and it is the closest to the Sun. The planet has been known since Man was interested in observing the night sky. Compared to planets such as Mars, Jupiter and Saturn, Mercury has received much less attention. Mercury has a diameter and a gravity approximately three times lower than that of the Earth. The temperature at its surface can vary from 430°C (dayside) to −180°C (night side). Of the planets, Mercury has the most eccentric orbit with the largest inclination from the ecliptic plane. The rotational axis of the planet is perpendicular to the orbital plane, and as a consequence, there are no seasons on Mercury. The orbital properties of Mercury are listed in table 1.1.

Mercury consists of approximately 70% metallic and 30% silicate material. Mercury's density is 5.427g/cm^3 which is the highest value among the terrestrial planets. The formation process leading to Mercury's high density is not yet fully known. This value is only slightly less than Earth's density of 5.515g/cm^3 . If the effect of gravitational compression were to be factored out, the materials of which Mercury is made would be denser than those of Earth, with an uncompressed density of 5.3g/cm^3 versus Earth's 4.4g/cm^3 .

The pock-marked surface of Mercury is highly reminiscent of the Earth's Moon. Mercury was heavily bombarded by comets and asteroids during and shortly following its formation 4.6 billion years ago, as well as during a possibly separate subsequent episode that ended 3.8 billion years ago [Fassett, 2013]. During this period of intense crater formation, Mercury received impacts over its entire surface, facilitated by the lack of any atmosphere to slow impactors down.

Craters on Mercury range in diameter from small bowl-shaped cavities to multi-ringed impact basins hundreds of kilometers across. They appear in all states of degradation, from relatively fresh rayed craters to highly degraded crater remnants. With further degradation, the craters lose their crisp morphology and rays and features on the continuous ejecta become more blurred until only the raised rim near the crater remains recognizable. Because craters become progressively degraded with time, the degree of degradation gives a rough indication

Tab. 1.1: Mercury properties

| Parameter | Value | Unit |
|----------------------|----------|-------------------------|
| Mass | 0.33E24 | <i>kg</i> |
| Diameter | 4879 | <i>km</i> |
| Density | 5427 | <i>kg/m³</i> |
| Surface gravity | 3.7 | <i>m/s²</i> |
| Escape Velocity | 4.3 | <i>km/s</i> |
| Rotation Period | 1407.6 | <i>hours</i> |
| Length of Day | 4222.6 | <i>hours</i> |
| Distance from Sun | 0.387098 | <i>AU</i> |
| Perihelion | 0.307499 | <i>AU</i> |
| Aphelion | 0.466697 | <i>AU</i> |
| Orbital Period | 88 | <i>days</i> |
| Orbital Velocity | 47.4 | <i>km/s</i> |
| Orbital Inclination | 7 | <i>degrees</i> |
| Orbital Eccentricity | 0.205 | - |
| Obliquity to Orbit | 0.034 | <i>degrees</i> |

of the crater's relative age [Spudis, 2001].

Although Mercurian and lunar craters are superficially similar, they show subtle differences, especially in deposit extent. The continuous ejecta and fields of secondary craters on Mercury are far less extensive (by a factor of about 0.65) for a given rim diameter than those of comparable lunar craters. This difference results from the 2.5 times higher gravitational field on Mercury compared with the Moon [Kabin et al., 2000].

The largest known crater is Caloris Basin, with a diameter of 1,550 km. The impact that created the Caloris Basin was so powerful that it caused lava eruptions and left a concentric ring over 2 km high surrounding the impact crater.

1.2 Missions to planet Mercury

Mariner 10 was the first spacecraft to visit Mercury. It was a flyby mission that happened in 1974 and 1975 studying Mercury's geology, chemical composition and magnetic field. Mariner 10 data revealed a surprising magnetic field and a metallic core comprising about 80 percent of Mercury's mass. MESSENGER [Solomon et al., 2007] was a NASA spacecraft that orbited the planet Mercury between 2011 and 2015. Many of the results and observations by Mariner 10 have been superseded by MESSENGER spacecraft. The mission name is a acronym for "MErcury

Surface, Space ENvironment, GEochemistry, and Ranging".

MESSENGER's initial orbit was highly eccentric with a periherm of around 200 km to 500 km and apoherm of 15200 km with a 12 h orbital period. During the extended mission, the spacecraft apoherm was lowered, while the periherm of the orbit was kept almost the same. The highly elliptical orbit of MESSENGER, didn't allow for almost no observation of the planet southern hemisphere (Figure 1.1).

MESSENGER was built to explore the whole planet from core to exosphere and featured a wide range of instruments.

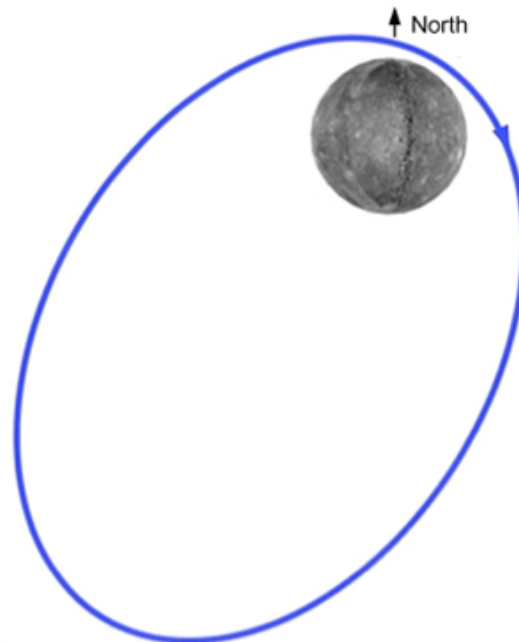


Fig. 1.1: Orbit of MESSENGER spacecraft around Mercury

One of the instruments onboard MESSENGER, was the Mercury Laser Altimeter (MLA). MLA measured the round trip time-of-flight of transmitted laser pulses reflected from the surface of the planet that, in combination with the spacecraft orbit position, gives a measurement of surface topography referenced to Mercury's center of mass.

The BepiColombo mission to Mercury [Benkhoff et al., 2010] is composed of two separate orbiters that will work in different orbits to explore the planet and its environment: the Mercury

Planetary Orbiter (MPO) led by the European Space Agency (ESA), and the Mercury Magnetospheric Orbiter (MMO) led by the Japanese Aerospace Exploration Agency (JAXA). The MPO has the primary goals to image and map Mercury throughout its orbit, while the MMO will study Mercury's magnetic environment. BepiColombo were launched in October 2018, and will arrive at Mercury in December 2025.

MPO and MMO will journey to Mercury together with the Mercury Transfer Module (MTM). When approaching Mercury, the MTM will separate and the two spacecraft, still together, will be captured into a polar orbit around the planet. Their altitude will be adjusted using MPO's thrusters until the MMO's orbit has been reached. Then MPO will separate and descend to its orbit.

The orbit of MMO will be highly eccentric with a perihelion altitude of 400 km and an aphelion altitude of 11824 km. It carries instruments to study the planet's magnetosphere and exosphere and the solar wind.

1.3 Mercury Planetary Orbiter

The Mercury Planetary Orbiter (MPO) is a three-axis stabilised spacecraft with a perihelion altitude of 480 km and an aphelion altitude of 1508 km. The orbit is polar with its perihelion over the equator to ensure a global coverage of the planet and has a period of 2.3 h (Figure 1.2). At the start of mission the argument of the perihelion is around 16 degree, the altitude of spacecraft over the North Pole is around 800 km and over the south pole is around 1050 km. But the orbital elements drift over time and the argument of perihelion goes to around -40 degree at the end of extended 2-year mission [Jehn, 2015][Luedicke, 2014] (figure 1.4). Unlike MESSENGER, MPO's orbit is designed such that the spacecraft instruments will observe both the northern and southern hemisphere of Mercury.

Also the orbit becomes more elliptical, so that after two years of mission (one year of nominal and one year of extended mission), the perihelion is expected to lower to 260 km and the aphelion is also expected to increase to around 1720 km (figure 4.4). It has to be mentioned that considering the uncertainties of the gravity field determined by the analysis of the NASA MESSENGER radio science data (*e.g.*, Genova et al. [2019]), the orbit of the spacecraft after two year might be different from the predicted orbit and in the worst case scenario, the orbit can get as low as 125 km after two years in Mercury orbit [Luedicke, 2014].

The instruments of MPO aim at investigating the interior, surface, exosphere, and magnetosphere, as well as test the theory of General relativity. The remote sensing instruments are

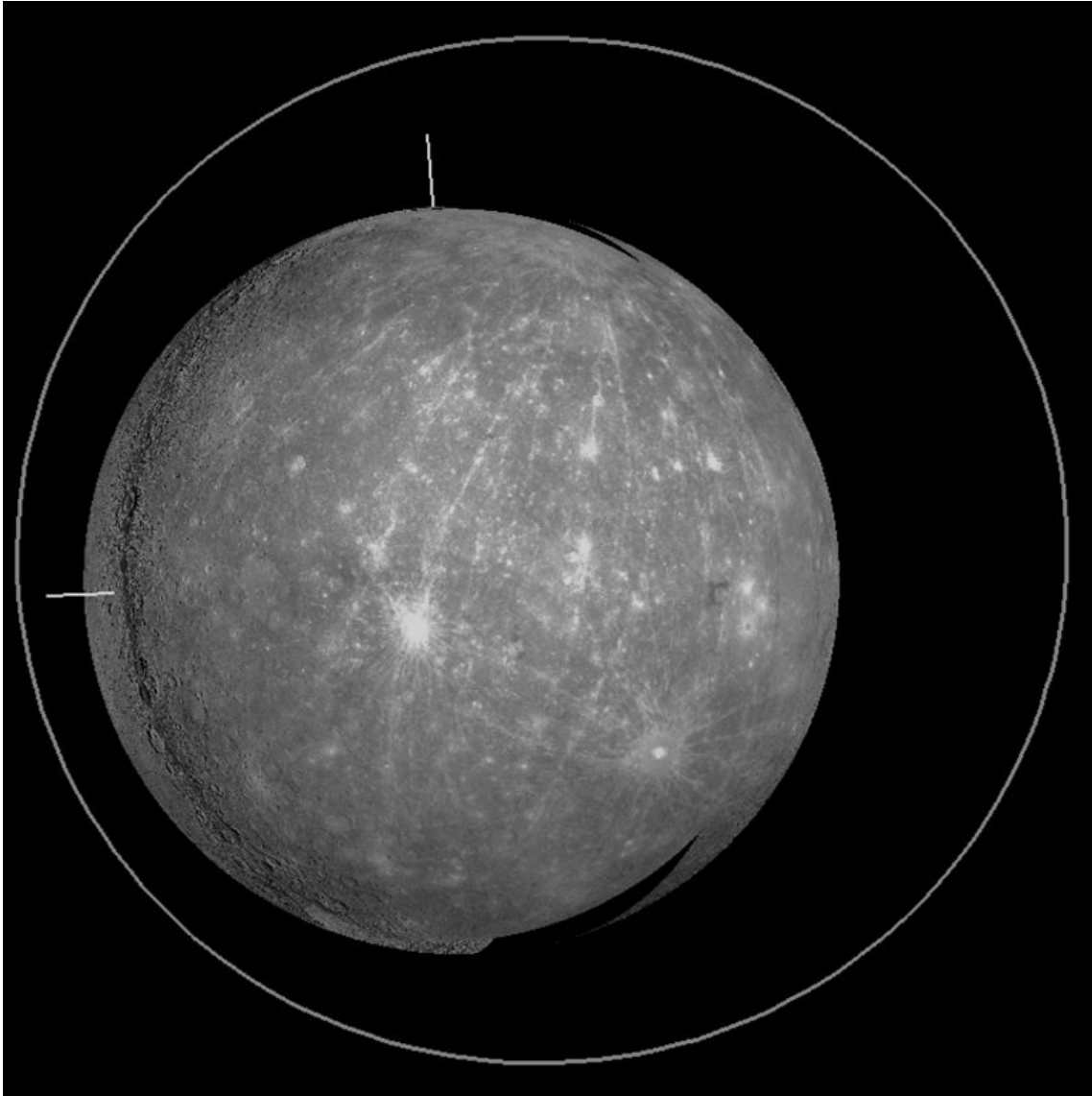


Fig. 1.2: Orbit of MPO and MMO

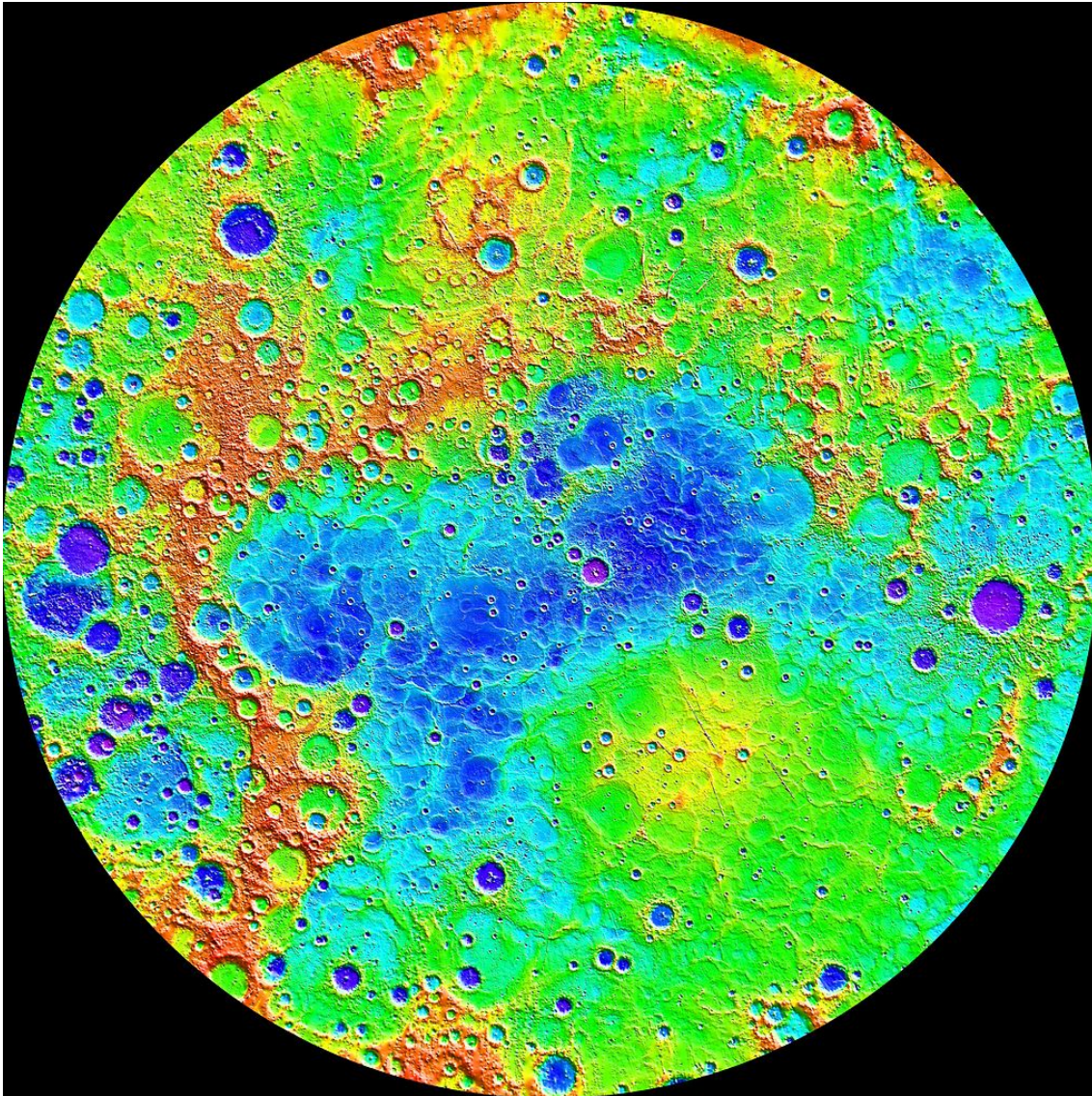


Fig. 1.3: Topographic map of Mercury's northern hemisphere by the MLA instrument on MESSENGER spacecraft. lowest (purple) to highest (red, 10 km); Credits: NASA/Johns Hopkins University Applied Physics Laboratory/Carnegie Institution of Washington.

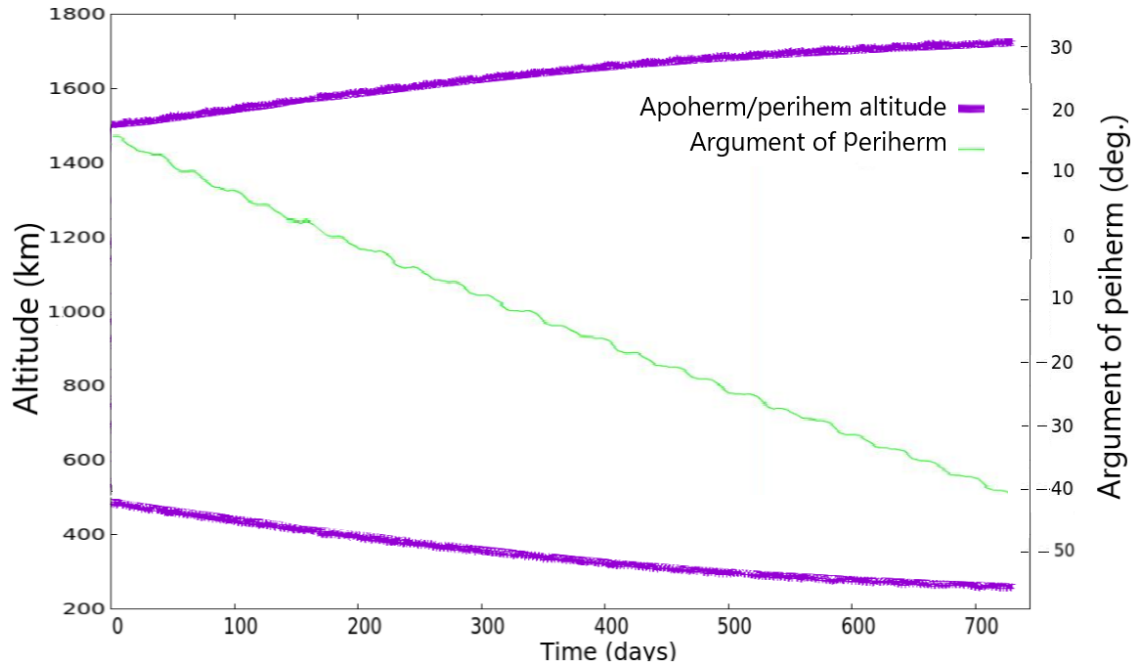


Fig. 1.4: Purple: Periherm and Apoherm altitudes during the nominal and extended mission; Green: Argument of perihelion of MPO during the nominal and extended mission

designed to point in the nadir direction. All surfaces and payloads are designed for the high thermal load from both the Sun and Mercury. A radiator that always faces away from the Sun allows thermal radiation towards deep space. MPO accommodates 11 science instruments in total:

- BELA: BepiColombo laser altimeter
- ISA: Italian spring accelerometer
- MPO-MAG: Mercury Planetary Orbiter Magnetometer
- MERTIS: MErcury Radiometer and Thermal Infrared Spectrometer
- MGNS: Mercury Gamma-ray and Neutron Spectrometer
- MIXS: Mercury Imaging X-ray Spectrometer (-C: collimator; -T: telescope)
- MORE: Mercury Orbiter Radio-science Experiment
- PHEBUS: Probing of Hermean Exosphere by Ultraviolet Spectroscopy
- SERENA: Search for Exospheric Refilling and Emitted Natural Abundance (ELENA: Emitted Low-Energy Neutral Atoms;

- MIPA: Miniature Ion Precipitation Analyser; PICAM: Planetary Ion Camera; STROFIO: Start from a Rotating Field Mass Spectrometer)
- SIMBIO-SYS: Spectrometer and Imagers for MPO BepiColombo Integrated Observatory System
- SIXS: Solar Intensity X-ray and particle Spectrometer

The MPO design is optimised to meet the needs of the payload in orbit around Mercury. The payload components are mounted on the nadir side of the spacecraft, with certain instruments or sensors located directly at the main radiator, to achieve low detector temperatures. The MERTIS and PHEBUS instruments are located at the radiator. The SIMBIO-SYS sensors and the BELA optical head are located on a optical bench with the star trackers and gyroscopes, to provide the required pointing performance. The ISA instrument is located close to the centre of mass. The MERMAG sensor is mounted on a 3.2-metre deployable boom, providing it with a suitably low magnetic background.

1.4 *Mercury radio science experiment*

This study will concentrate on the BELA instrument, but to find the impact of the instrument orbit improvement, we include the data from radioscience experiment, MORE.

The MORE instrument addresses BepiColombo's scientific goals in geodesy, geophysics and fundamental physics. It will help to precisely determine the orbit of spacecraft, gravity field of Mercury and the physical state of the core of the planet. It will provide crucial experimental constraints to models of the planet's internal structure and test theories of gravity with unprecedented accuracy. These scientific goals will be achieved by means of several data types, generated by MORE at the ground station, other on-board instruments (BELA, ISA, and SIMBIO-SYS) and the on-board attitude determination and control system.

1.5 *BELA*

Laser altimetry is a powerful remote sensing technique used in both Earth and planetary science. The basic concept is rather simple: we measure the time-of-flight (TOF) of a pulse of light from an orbiter equipped with a laser to a reflecting surface and back. The range z from the laser to the illuminated spot on the surface is related to the laser pulse time-of-flight ΔT by

$$z = c \frac{\Delta T}{2}, \quad (1.1)$$

with c the speed of light. This means that a 1 ns delay corresponds to around 15 cm in range.

The main objectives of BELA are to measure the figure parameters of Mercury, to establish accurate reference surfaces, topographic variations relative to the reference figures, surface roughness, local slopes and albedo variations, also in permanently shaded craters near the poles.

The instrument was built in collaboration of several institutions and industries in different countries. The main contributors were the Physikalisches Institut in Bern, the German Aerospace Center in Berlin and the Instituto de Astrofísica de Andalucía in Spain as well as the Max-Planck-Institute for Solar System Research in Germany. The system development was mainly split into two parts: the receiver section (Physikalisches Institut) and the transmitter section (German Aerospace Center). The final integration and verification of the instrument was performed at the University of Bern.

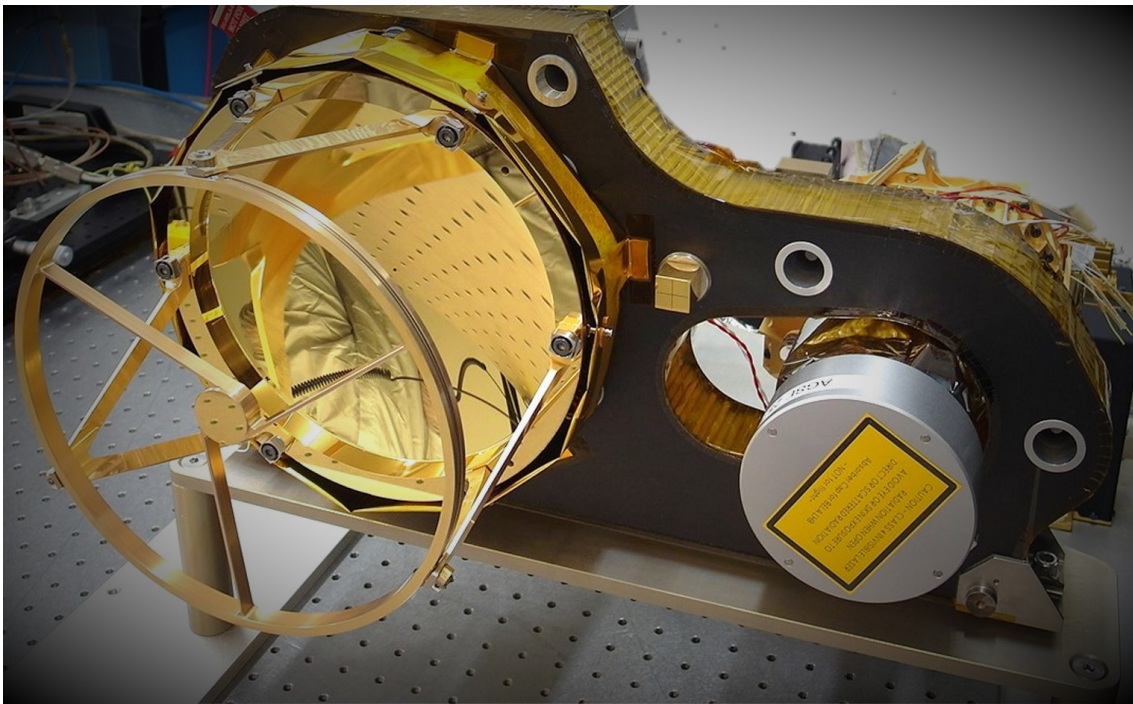


Fig. 1.5: BELA

BELA uses the "direct-detection" approach to laser altimetry. High power pulses (~ 50 mJ) at 1064 nm are emitted from a Q-switched laser at 10 Hz. The emission time of each pulse is measured by a photodiode. The beam is reflected from the surface and received around 5 ms later at a 20 cm diameter telescope. The image is refocused onto a silicon avalanche photodiode (APD) through a narrow bandpass interference filter. Since the receiver field of

view is larger than the laser beam divergence angle, the total energy of the return pulse energy is given by

$$E_R = E_T \cdot \rho \cdot T_r \cdot r_R^2 / z^2 \quad (1.2)$$

Where: E_R is the received energy, E_T is the transmitted energy, ρ is the bidirectional reflectance, T_r is the transmission of Receiver optical subsystem (ROSS) and r_R is the telescope radius. In figure 1.6 the amplitude of the return pulse is plotted in voltage against the altitude of the spacecraft. In the case of a nadir looking laser altimeter, the bidirectional reflectance at zero phase-angle is [Gunderson et al., 2006]:

$$\rho(\theta_t, \theta_R, 0) = \alpha_N / \pi \quad (1.3)$$

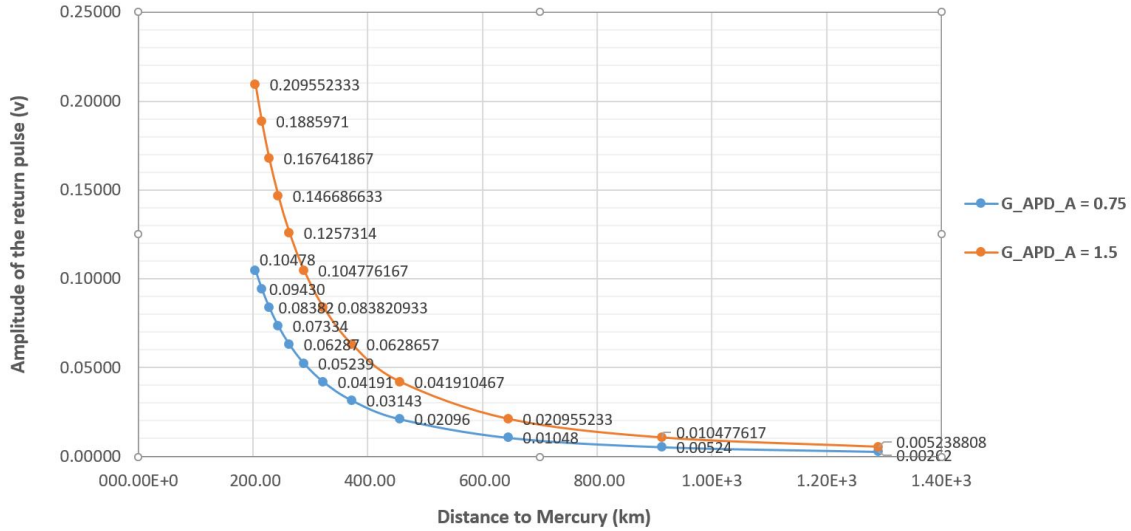


Fig. 1.6: Amplitude of the return pulse (v) as a function of distance to Mercury (gain Code 7, FWHM = 10ns, average surface reflectance)

Where α_N is the normal albedo. The received signal is then sampled and fed to a digital pulse discrimination electronics. This system determines the time of flight (and therefore range), the integrated pulse intensity, and its width. The data are passed to a digital processing unit which controls the operation and services the spacecraft interface [Thomas et al., 2007].

BELA will provide 2 ns time resolution which is commensurate with the expected knowledge of the spacecraft position. The experiment will provide return pulse intensity and width information allowing for an assessment of surface albedo and roughness at 20 m scales including in unilluminated polar craters. The instrument properties [Steinbrügge et al., 2018] are sum-

Tab. 1.2: Instrument parameters in the beginning of life used for the modelling

| Parameter | Symbol | Value | Unit |
|--|-------------|-----------|------------------|
| Laser pulse energy | E_t | 50 | mJ |
| Laser pulse width (1- σ , Gaussian) | σ_0 | 2.2 | ns |
| Shot frequency | f | 10 | Hz |
| Wavelength | λ_T | 1064 | nm |
| 1/ e^2 beam divergence (half cone) | Θ_T | 25 | μrad |
| Telescope radius | r_R | 0.1 | m |
| Field of view of the receiver telescope | Θ_R | 450 | rad |
| Transmission of receiver optics | T_r | 76.7 % | |
| High voltage | HV | 340 – 370 | |
| Analog (TIA) bandwidth | B0 | 25 | MHz |
| Sample resolution | adc | 12.5 | ns |
| Noise floor | n_f | 3.24 | $PA/\sqrt{(Hz)}$ |
| APD dark current (bulk) | I_{db} | 100 | pA |
| APD dark current (surface) | I_{ds} | 100 | nA |

marized in Table 1.2 in order to get a complete overview about the assumptions made for the modeling.

We define two kinds of gain for BELA: The *Avalanche Photodiode Assembly (APD-A)* gain, which is a function of high voltage (HV) and determines the AEU input voltage amplification and the *instrument gain code*, defining the voltage gain factor of the *Analogue Electronics Unit (AEU)*. The instrument gain code has an integer value between 0 to 15, corresponding to the lowest and highest amplification, while the APD-A gain is between 0.75 MV/W (Mega-Volts / Watt) to 1.5 MV/W depending on the HV set point.

An APD-A gain of 0.75 MV/W corresponds to high voltage (HV) set point of 370 V, while an APD-A gain of 1.5 MV/W corresponds to the HV set point of 340 V. The recommended HV set point was reduced from 370 V to 340 V to avoid any danger arising from possibly exceeding the APD breakdown voltage. We need to stress that 340 V produces a responsively (gain) that is considerably lower than can be achieved in optimum condition.

1.6 Pulse detection algorithm

Like the other classic laser altimeters, BELA sends a laser pulse to the surface. The beam produces a spot of 20-50 m on the surface. The laser beam is reflected from the surface and around 5 ms later it is received with the telescope. The received signal may have a much

higher amplitude by the noise floor (e.g. when the altitude is low and the surface is smooth) or it may be close to or even below the noise level (e.g. when the altitude is high and the surface is rough or steep). In both cases the instrument tries to find the returned signal in the noise using the pulse detection algorithm. According to the requirement, the instrument should be able to detect the pulses up to the altitude of 1050 km.

For the instrument to meet the requirement there has been a hardware modification on BELA during which, a Pi filter was installed to reduce APD noise and The nominal harness B11H8 was replaced with the modified B11H8 FS2, which hosts a ferrite core in the backshell P450 to filter the common mode noise.

We determine the performance of pulse detection algorithm by determining the probability of false detection (PFD). The PFD of the instrument depends on the altitude of the spacecraft, return pulse width, instrument gain settings and also on the performance of pulse detection algorithm.

BELA uses digital pulse sampling. For this purpose, the Rangefinder Electronics Module (RFM) digitizes the analog signal coming from the APD using analog to digital converters (ADCs). The two ADCs are implemented with 12 bits resolution in order to be able to detect low signal variations. This is a novel characteristic of BELA. Other planetary laser altimeters (e.g. MLA) have used analogue detection techniques.

The built in ADCs together have an equivalent sampling frequency of 80 MHz, which corresponds to one sample in 12.5 ns. In order to be able to resolve very short pulses, the analog signal first undergoes a low pass filtering (20 MHz cut-off frequency) which results in pulse broadening of the short pulses. A typical 20 ns Gaussian pulse after being digitized is show in figure 1.7.

The RFM knows roughly when to expect the return pulse to come back from the target. It opens a window (the range window) and collects data from the APD. These data are digitized and analysed using a specific (proprietary) algorithm to determine the time delay between emission and reception with respect to the oscillator.

A usual round trip time is about 2.6 ms to 10 ms, depending on the spacecraft height. The RFM would not be able to analyze the coarse samples ($2.6 \text{ ms} / 12.5 \text{ ns} = 208000$ samples) of the whole round trip time within 100 ms. Hence a shorter window needs to be used. This window length is 200 μ seconds (about 16000 samples) and the opening of the range window is estimated by a range tracking algorithm. The algorithm makes use of the ranging from the

previous returns as well as from predicted altitude information delivered by the spacecraft [Beck, 2011].

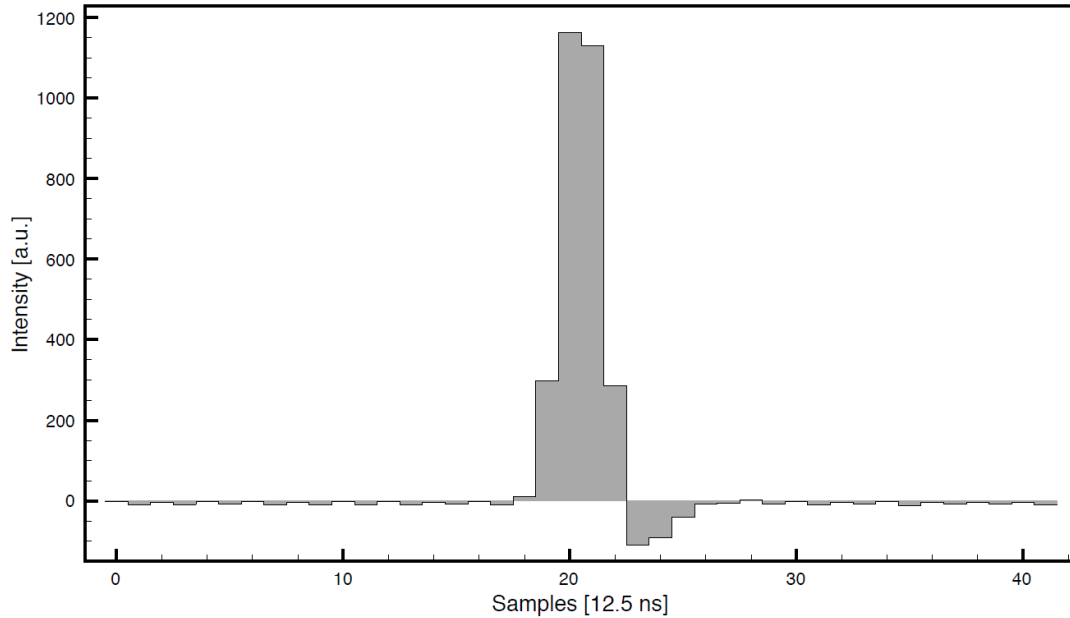


Fig. 1.7: Typical ADC response of a 20 ns FWHM Gaussian pulse

A time of flight measurement resolution of 12.5 ns corresponds to a height resolution of 1.9 meters. This resolution is called here "coarse" measurement resolution.

The RFM however is designed to have a time of flight resolution which is better than the coarse resolution. This is done using a set of reference (or basis) functions which are predefined and stored in the built in field programmable gate array. The digitized signal from the ADCs is compared with the basis functions to obtain the detailed pulse parameter. It is basically performing a pulse fitting on the signal which leads to a so-called "sub-sampling" resolution.

In order to have an efficient pulse fitting, at a 10 Hz repetition rate, the arbitrary fitting functions are represented as bi-quadratic polynomials in pulse width and sub-sampling offset [Beck, 2011]. The RFM performs the pulse fitting in-flight and produces parameters which are sent back to Earth. Using these parameters and the basis functions, the time-of-flight at sub-sampling resolution as well as pulse parameters (pulse width and pulse energy) can be recalculated on ground.

The major advantage of this implementation compared to analog signal detection lies in the possibility of defining the basis functions in-flight. These functions can be programmed according to the actual pulse shapes which are expected to be obtained from the hermean surface.

1.7 Previous studies and goals

[Gunderson et al. \[2006\]](#) presents an analytical model of the BELA system performance. The model draws on a diverse set of instrument and environmental parameters to predict signal-to-noise ratios, false detection probabilities and range measurement uncertainties. The model shows that the baseline instrument is capable of meeting the performance requirements of $\text{PFD} < 0.1$ and range error < 10 m out to altitudes of 1050 km. [Gunderson and Thomas \[2010\]](#) extended the above model contain the time-varying orbital conditions and instrument degradation over the mission life time. Also measurement accuracy predictions has been broadened to include albedo and return pulse width in addition to range accuracy.

[Steinbrügge et al. \[2018\]](#) presents a semi-analytical instrument performance model, in which signal-to-noise ratio, single shot probability of false detection, range errors and the accuracy of pulse width reconstruction are estimated. It also performs numerical simulations of the instrument performance expected in orbit about Mercury and studies the measurement accuracy of topography, slopes and surface roughness.

In this study, we focus on a comprehensive performance analysis for BELA by including all of the above factors synthesised in to one single numerical model. Moreover, we base our analysis on a more accurate instrument noise model based on the noise information gathered from the laboratory tests on BELA. Our modelling contains instrument degradation, the planet surface model and an in-flight model of the laser altimetry. We use this model to have an extensive and accurate performance evaluation of BELA on its orbit around the planet Mercury.

In section [2](#), we discuss the laboratory-based performance tests that has been done at the University of Bern and the analysis of the test results. In section [3](#) we present the probability of false detection model that is used in this study. In section [4](#), we present extensive modeling of BELA in-orbit around Mercury. Section [5](#) presents results about the different measurements noise components and the working limits of the instrument.

In section [6](#), we present results on orbit determination using Doppler tracking only and the preliminary results on the impact of BELA crossovers on precise orbit determination (POD) and on the recovery of Mercury geophysical parameters. We summarize the conclusions in section [7](#).

The thesis will be followed by two appendixes: first, in appendix 1, a technical report about

"MPO relative orbit error modelling" that was prepared for DLR and second, in appendix 2, the submitted paper to Planetary and Space Science journal with the title of "Comprehensive in-orbit performance evaluation of BepiColombo laser altimeter (BELA)".

2. LABORATORY-BASED PERFORMANCE TESTS ON BELA RANGE FINDER MODULE

We discuss here the performance tests which have been made at the University of Bern with the qualification model of the BELA RFM. With these low level tests, the BELA laboratory-based performance in terms of measurement accuracy can be estimated. The RFM has been electrically stimulated by simulated laser pulses in order to verify the performance of the subsystem.

These tests have been performed by a previous PhD student, Thomas Beck, and we here analyzed the test results to find a noise model for the three main measurements (TOF, Pulse width and pulse energy) of the instrument. By analysing these results we try to identify systematic biases on all three measurements. The details of the tests has been written in Beck's PhD thesis. Here we only give a summary of the test settings and then move to the data analysis.

2.1 *Test set up and assumptions*

Several tests were performed with the RFM using electrically generated pulses. These pulses were sent to the RFM in order to verify the ranging performance. They have been programmed and generated by an arbitrary waveform generator (AWG) with a timing resolution of 0.4 ns. The assumptions made on the planets properties are limited to the target surface reflectance of Mercury (geometric albedo).

The setup for the RFM subsystem tests involves several different auxiliary electronics components which were designed and programmed at the University of Bern. The test procedure starts with a control file which is sent to the RFM from the control computer. The control file contains information/commands for the RFM such as the range window start time (calculated by the range tracking algorithm), the high voltage set point for the APD and other commands. Details can be found in the RFM interface control document [[Schulze-Walewski, 2011](#)].

The control file is executed by the RFM when the trigger signal arrives from the FPGA board. The same trigger signal releases the AWG sequence which has been programmed and stored before. The AWG releases, usually 1 ms after the trigger signal (programmed), the transmitter pulse which is then sampled by the RFM. After the Tx sampling, the RFM reads the house-keeping (HK) data which includes, among other things, APD temperature, high voltage settings

and clock cycles since the last PPS as explained before. The range finder module waits a pre-defined time (commanded by the control file) before start sampling the Rx pulse. This time corresponds to the time of flight minus (usually) half of the range window. Within the range window the AWG releases the receiver pulse which is then detected by the RFM. Afterwards the range finder performs the pulse processing (pulse fitting, coarse time of flight calculation) before sending the data back to the control computer.

This has been performed using ideal, Gaussian, pulse shapes and noise modulated pulse shapes including Mercury background for comparison. In total $2 \times 288 \times 1000 = 576000$ pulses have been produced to obtain statistically relevant results. For each scenario (ideal and real pulse shapes), 288 different height, pulse width and gain setting variations have been simulated.

The Mercury background radiation contributes to the noise behavior of the system. The spectral noise density of the APD is a function of the illumination power. Therefore the unwanted radiation had to be taken into account. For the tests, three different optical backgrounds input were chosen. The case where BELA is ranging at the dark side of Mercury (Point A in figure 2.1), the perihelion case (Point B in figure 2.1) and the aphelion case (Point C in figure 2.1).

The different sequences are simulated with and without noise modulation. The simplification that is made here is that the Mercury expected background noise was chosen such that for heights greater or equal to 1000 km perihelion's expected background offset (= 2.5nW) and for the others aphelion expected background (= 1.1 nW) was added. In this way a lot of orbital cases for the BELA operation are covered.

The different model sequences are a variation of three different parameters listed in table 2.1. Different spacecraft heights, different pulse widths as well as amplifications have been chosen to account for. The pulse shapes that are used in this experiment are Gaussian, which is not always true in reality. Therefore, we need to consider this simplification when we use the results of this performance tests.

The results are subdivided in three sub sections, each showing the measurement accuracy of the three different parameters (time of flight, pulse width and pulse energy). The results show the difference between ideal pulse shapes and noise modulated pulse shapes for low and high gain settings as well. The low gain setting resulted in RFM input voltage of roughly 0.1 V and corresponds to gain code 0 while high gain setting resulted in roughly 1 V and corresponds to gain code 15.

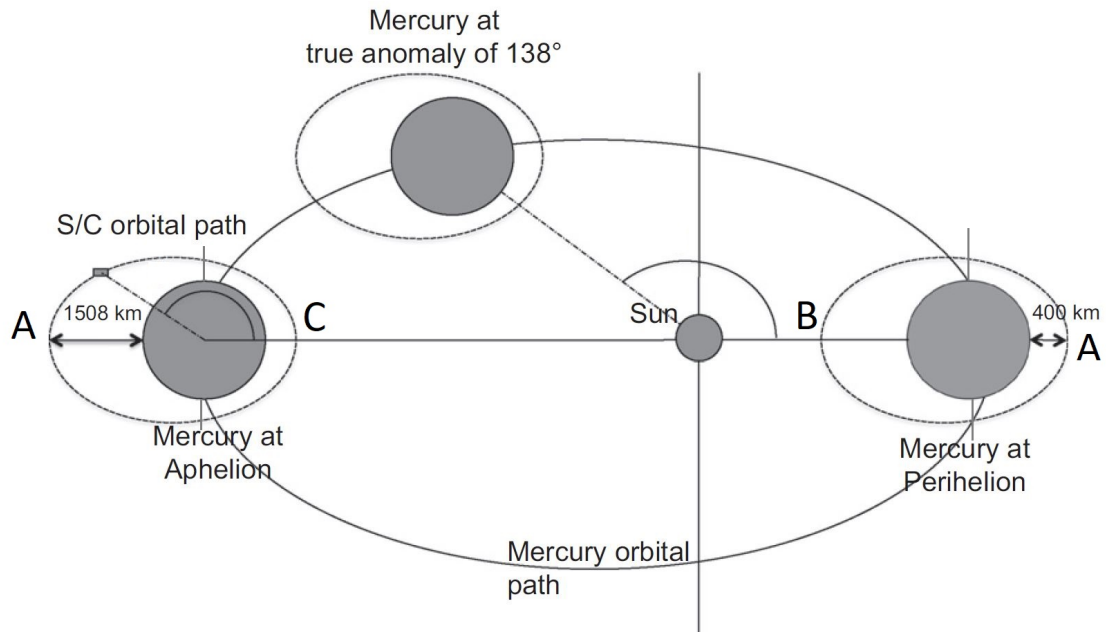


Fig. 2.1: Orbit of the BepiColombo spacecraft for three different positions of Mercury. The planet is positioned at Mercury true anomaly of 0, 138 and 180 degrees [Beck, 2011]

Tab. 2.1: Parameter that have been varied for the performance estimation

| Variable | Range |
|---------------------|------------------|
| Spacecraft height | 400 km - 1500 km |
| Pulse width FWHM | 5 ns - 100 ns |
| Pulse amplification | 0 dB - 21 dB |

It has to be mentioned that all the errors that are given in this study are derived from the analysis of the test results in the laboratory and therefore, they do not include the error component due to orbital error or pointing uncertainties. The in-flight performance of the instrument that includes all the errors will be presented in chapter 5.

2.2 Time of flight measurement error

2.2.1 Time of flight deviation as a function of spacecraft altitude

The time of flight accuracy is shown here as function of the spacecraft height (time of flight) as well as function of pulse width. The deviation from the commanded time of flight is shown in figures 2.2 to 2.3, for low and high gain settings. The resulting height deviation is given, in addition, on the second y-axis.

These figures show that the time of flight deviation depends on the height for the noise modulated pulses because the signal to noise ratio (SNR) is decreasing with height. In addition, the height deviation depends on the pulse widths.

Figure 2.2 and 2.3 show that the TOF measurement accuracy for spacecraft heights up to 800 km above Mercury is very high. The standard deviation of error on range measurement is about 25 cm. This error also depends on the measured pulse width and it has smaller values in smaller pulse widths. For spacecraft heights above 1000 km the measurement accuracy decreases mainly for larger measured pulse widths.

2.2.2 Systematic bias on time of flight

By fitting a linear function to the noise modulated data of the above plots, one can clearly see a systematic component on the range measurement that depends on the altitude, pulse width and gain settings. Figures 2.2 and 2.3 show a fitted line on the noise modulated data for different altitudes and for two different gain settings. Figure 2.4 shows the random noise after removing the systematic bias. The TOF measurement error decreases by 60 % and down to 1 ns (equal to 15 cm in range measurement) for low altitudes after removing the systematic bias.

The TOF measurement error in different condition are shown in table 2.4. Also the suggested equations for systematic bias is presented in table 2.2. It has to be mentioned that the TOF error here is assumed as "real TOF - measured TOF". It means that the actual systematic bias is a negative error on TOF and the suggested value has to be deducted from the measured TOF.

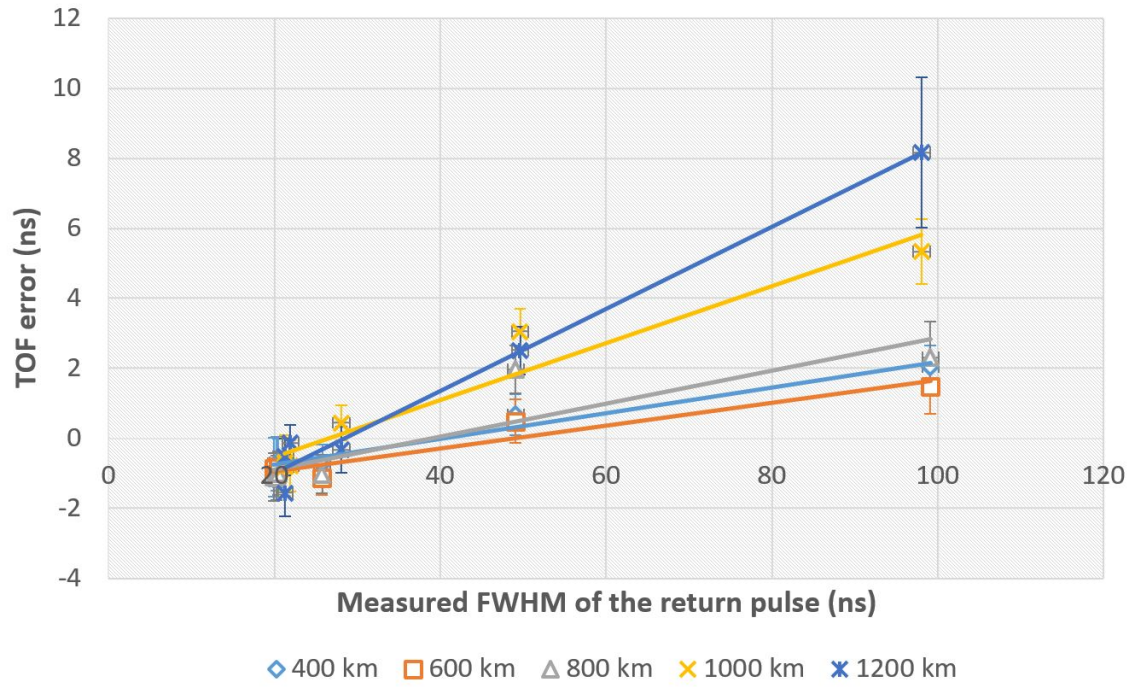


Fig. 2.2: Time of flight measurement error (Low gain)

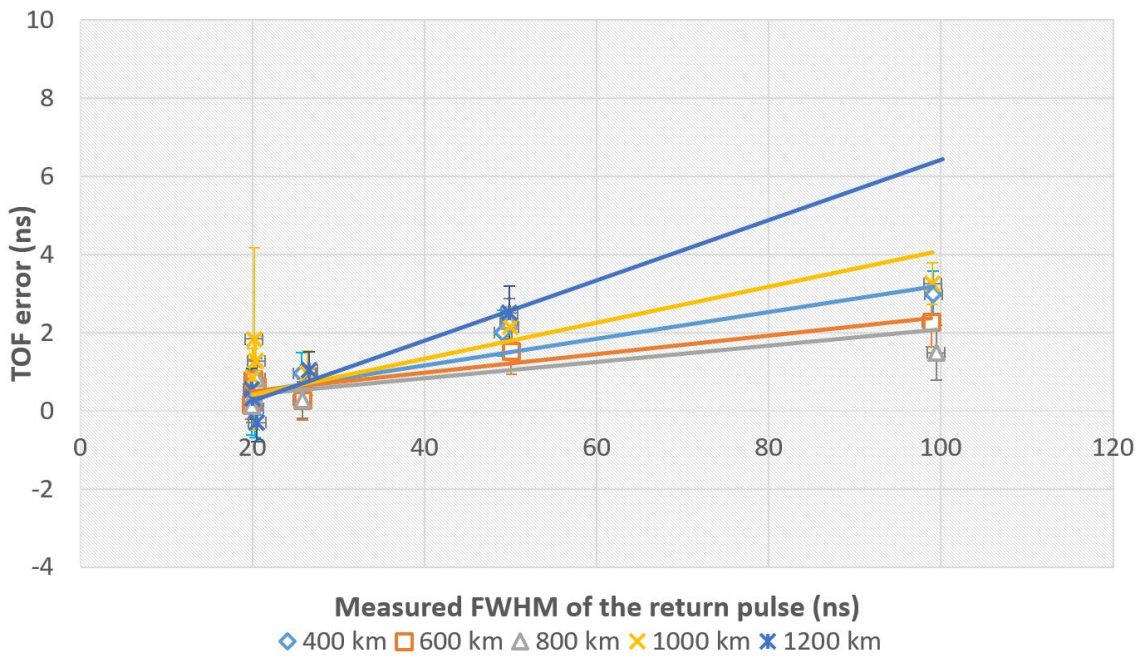


Fig. 2.3: Time of flight measurement error (High gain)

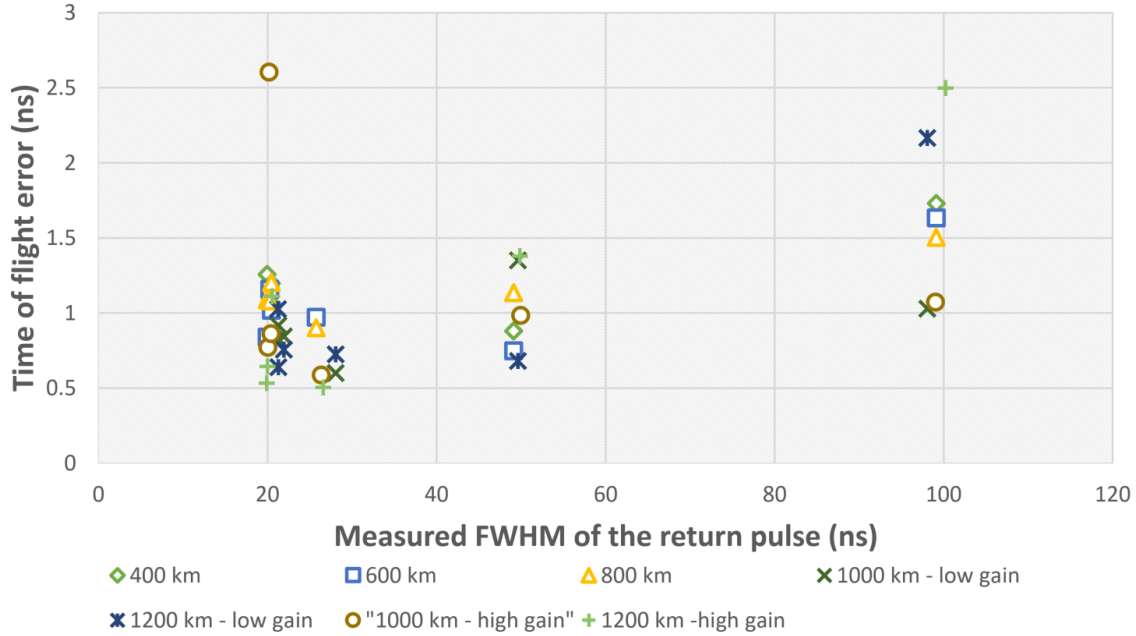


Fig. 2.4: Random error on time of flight measurements after removing the systematic bias

Tab. 2.2: Suggested equation for systematic offset on TOF measurement

| Altitude | Gain setting | Fit equation |
|------------|--------------|--|
| 400-800 km | Low | $TOF_{offset} = 3.6 \cdot 10^7 \cdot FWHM - 1.48$ |
| | High | $TOF_{offset} = 2.2 \cdot 10^7 \cdot FWHM$ |
| 1000 km | Low | $TOF_{offset} = 8.12 \cdot 10^7 \cdot FWHM - 2.16$ |
| | High | $TOF_{offset} = 4.6 \cdot 10^7 \cdot FWHM - 0.5$ |
| 1200 km | Low | $TOF_{offset} = 1.17 \cdot 10^8 \cdot FWHM - 3.34$ |
| | High | $TOF_{offset} = 7.75 \cdot 10^7 \cdot FWHM - 1.27$ |

2.3 Pulse width measurement error

Measured pulse width is plotted as function of the expected (commanded) pulse width for different altitudes of the spacecraft in figure 2.5. Because of the broadening caused by the effect of low-pass filtering on the return signal, the width of the measured pulse width is always higher than 20 ns.

To study the pulse width measurement error in different conditions we plot this error against the measured pulse width in low and high gain settings (figures 2.6 and 2.7). Similar to the range measurement error there is a systematic bias in this measurement. The offsets shows a linear dependency to the FWHM of the return pulse and the gradient of this fit is higher in higher gains. The suggested difference equations to correct those systematic offsets are shown in table 2.3. We need to stress that one can suggest other possible fit equations, but since the linear function is the simplest and it fits the results very well, we don't use more complicated equations.

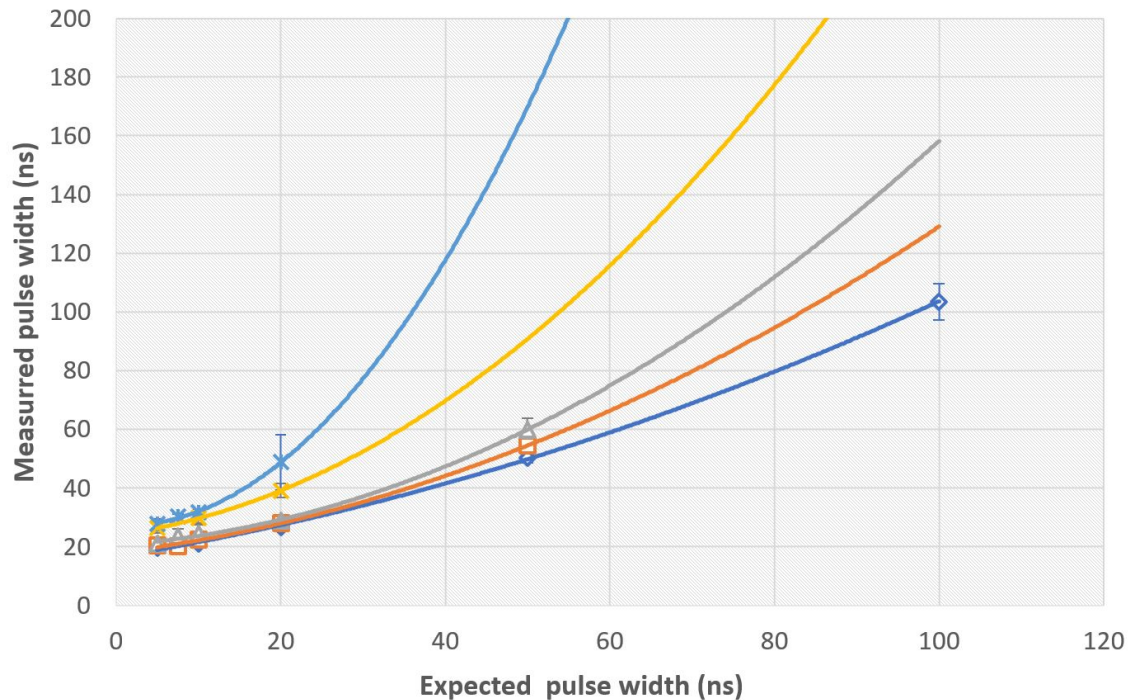


Fig. 2.5: Measured pulse width against expected (commanded) pulse width

Figure 2.8 compares the pulse width measurement errors as function of altitude before and after the removal of the systematic bias. Figure 2.9 shows the random error after removing the

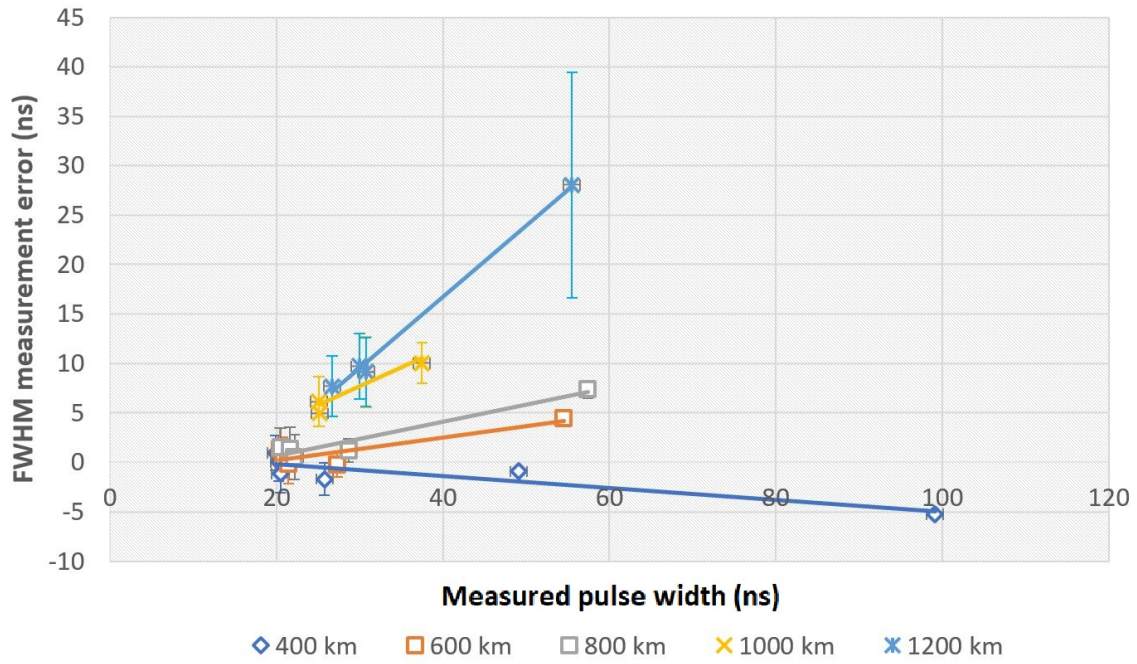


Fig. 2.6: systematic bias on pulse width measurement (high gain setting)

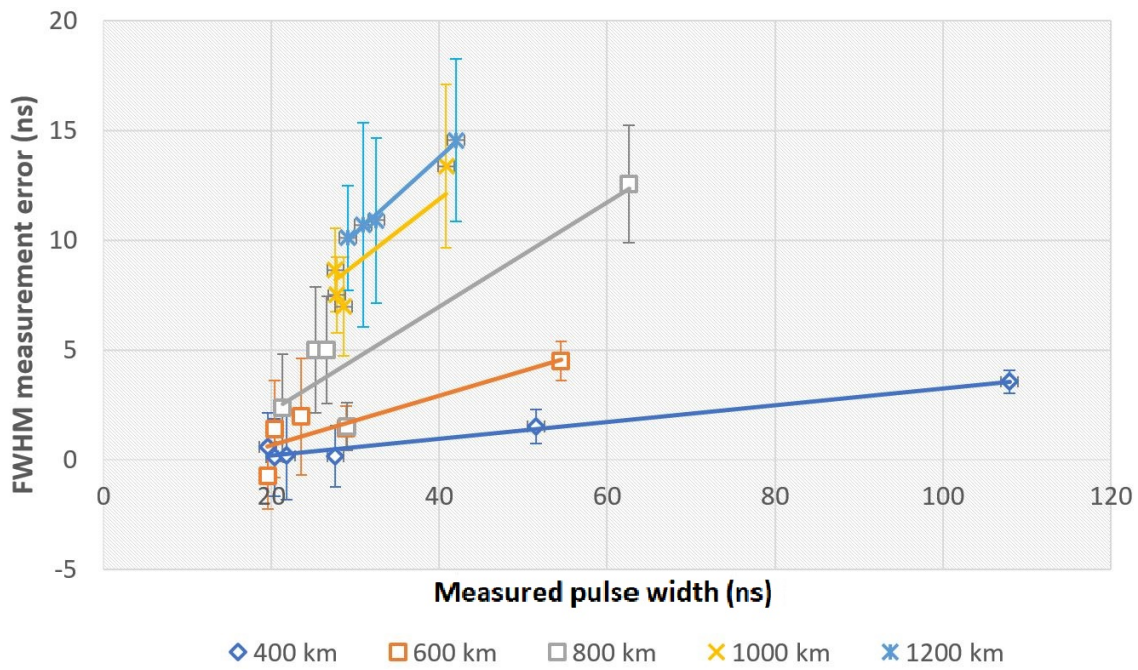


Fig. 2.7: systematic bias on pulse width measurement (low gain setting)

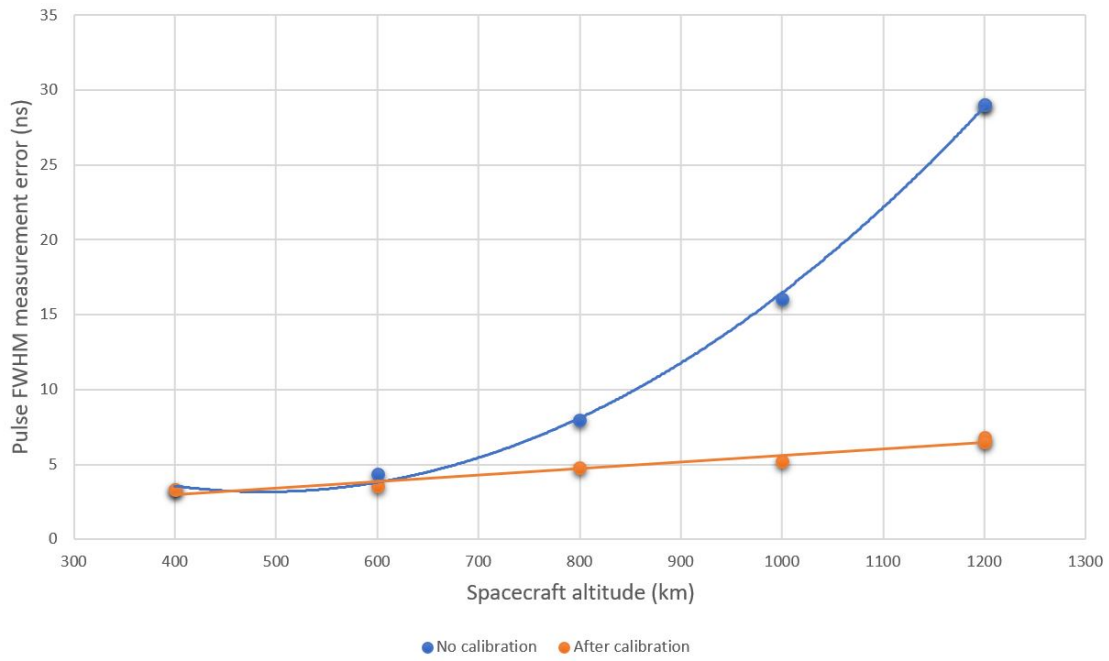


Fig. 2.8: Random error on pulse width measurement as a function of altitude before and after removal of the systemic offset

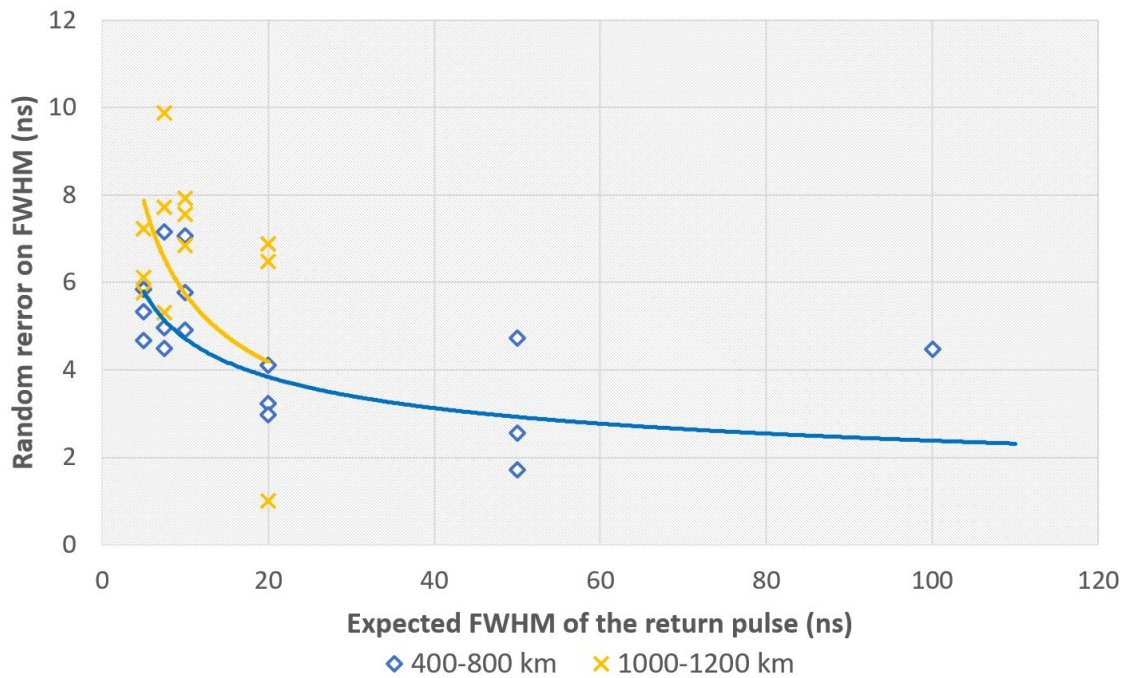


Fig. 2.9: Random error on pulse width measurement as a function of FWHM of the return pulse after removal of the systemic offset

systematic bias from the measurements. This curve is showing the error in different return pulse widths. It can be seen that in lower pulse widths (coming from low slope), the pulse width measurement error is almost three times higher than the error on broaden pulses (coming from steep slopes).

There are two main issues resulting from the tests. On the one hand it can be seen that the measurement accuracy decreases with the spacecraft height beginning from about 800 km. This happens due to the lower SNR at higher altitude. On the other hand, from figure 2.9, it is obvious that pulse widths below 20 ns FWHM are detected with large errors, because of the effect of low-pass filtering.

Tab. 2.3: Suggested equations for systematic offset on pulse width measurement. This offset has to be deducted from the measured FWHM. The filter broadening has to be considered separately to calculate the real received pulse width

| Altitude | Gain setting | Offset equation |
|----------|--------------|---|
| 400 km | Low | $FWHM_{offset} = 4.3 \cdot 10^7 \cdot FWHM$ |
| | High | $FWHM_{offset} = 3.4 \cdot 10^9 \cdot FWHM$ |
| 600 km | Low | $FWHM_{offset} = 5.4 \cdot 10^7 \cdot FWHM$ |
| | High | $FWHM_{offset} = 2.9 \cdot 10^8 \cdot FWHM$ |
| 800 km | Low | $FWHM_{offset} = 9.6 \cdot 10^7 \cdot FWHM$ |
| | High | $FWHM_{offset} = 1.7 \cdot 10^8 \cdot FWHM$ |
| 1000 km | Low | $FWHM_{offset} = 2.5 \cdot 10^8 \cdot FWHM$ |
| | High | $FWHM_{offset} = 6.7 \cdot 10^7 \cdot FWHM$ |
| 1200 km | Low | $FWHM_{offset} = 4.1 \cdot 10^8 \cdot FWHM$ |
| | High | $FWHM_{offset} = 2.9 \cdot 10^7 \cdot FWHM$ |

2.4 Pulse energy measurement error

Like the range and pulse width measurements, there also appears to be a systematic bias on the pulse energy measurements. The linear fit on the plot shows that the measured values are always around 50 % lower than the real energies. To find the measurement systematic bias we plot the pulse energy measurement error as a function of measured pulse energy (Figure 2.10).

We need to mention that the energy measurement test results for altitudes higher than 800 km are very bad. We have plotted some of them in figure 2.10, but we do not consider them for finding the fit to the data. The measurement data analysis shows that by removing the offset that from the measurement, the error on the pulse energy measurement will improve from 20% to 35%. Here we describe the errors as the percentage of the measured pulse energy.

Tab. 2.4: Instrument laboratory-based performance before and after removal of systemic offset

| Measurement | Altitude | Error STD | |
|----------------|-----------|----------------------|--------------------|
| | | With systematic bias | No systematic bias |
| Time of flight | < 1000 km | 1.64 ns | 1.00 ns |
| | ≥ 1000 km | 3.35 ns | 1.28 ns |
| | total | 2.63 ns | 1.13 ns |
| Pulse width | <1000 km | 5.6 ns | 4.2 ns |
| | ≥ 1000 km | 23.4 ns | 6.2 ns |
| | total | 15.4 ns | 5.3 ns |
| Pulse energy | < 1000 km | 35 % | 18 % |
| | ≥ 1000 km | 40 % | 26 % |
| | total | 40 % | 20 % |

It also has to be mentioned that the pulse energy range that led to the presented errors are between 1 Vns to 12 Vns. Outside this range the accuracy of the pulse energy estimation drops since the RFM has not been programmed for that.

Figures 2.11 and 2.12 show the remaining random error on pulse energy after removing the systemic offset. Since this pulse energy measurement error has a linear dependency with the pulse energy itself, we present the pulse energy errors in table 2.4 in the form of percentage from the expected pulse energy. The final error after removal of the systematic bias is about 18 % for altitudes lower than 1000 km and 26% for higher altitudes. The accuracy of the pulse energy measurement will determine the accuracy of the local albedo measurements that will be discussed in chapter 5

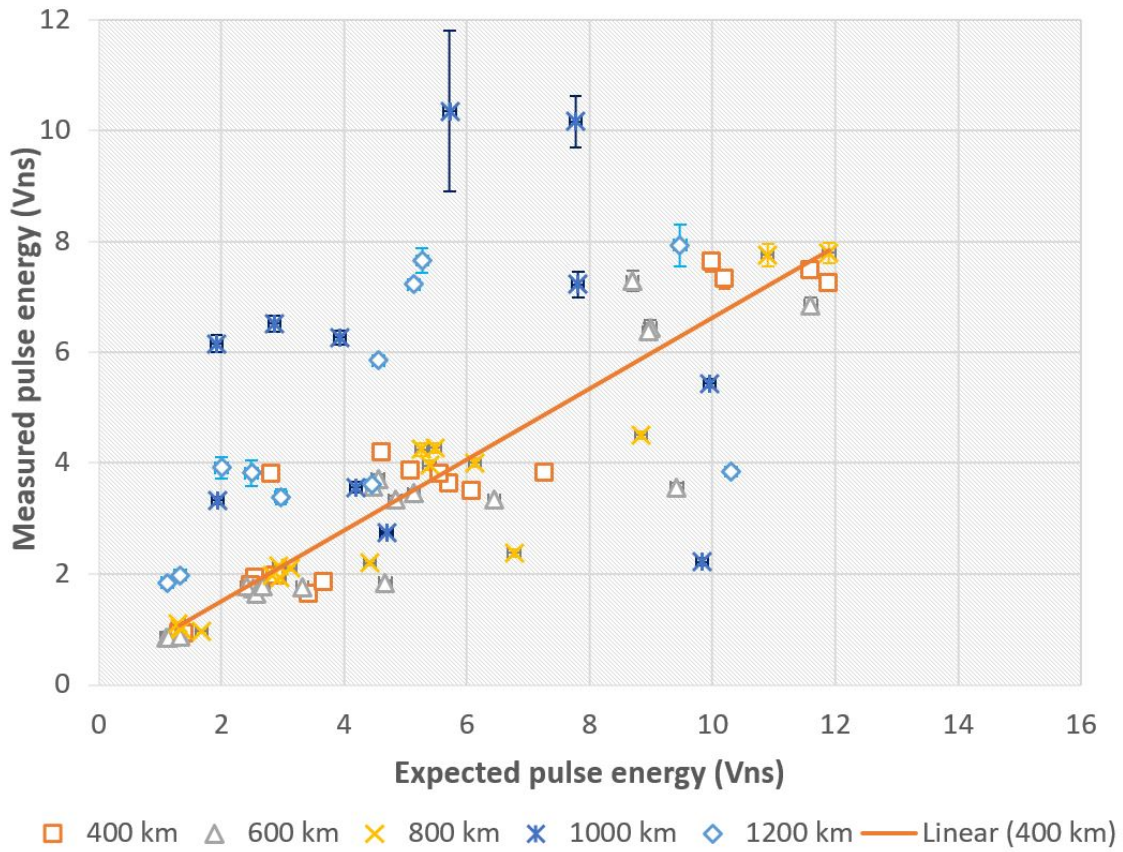


Fig. 2.10: Measured pulse energy as a function of expected pulse energy for different spacecraft altitudes.

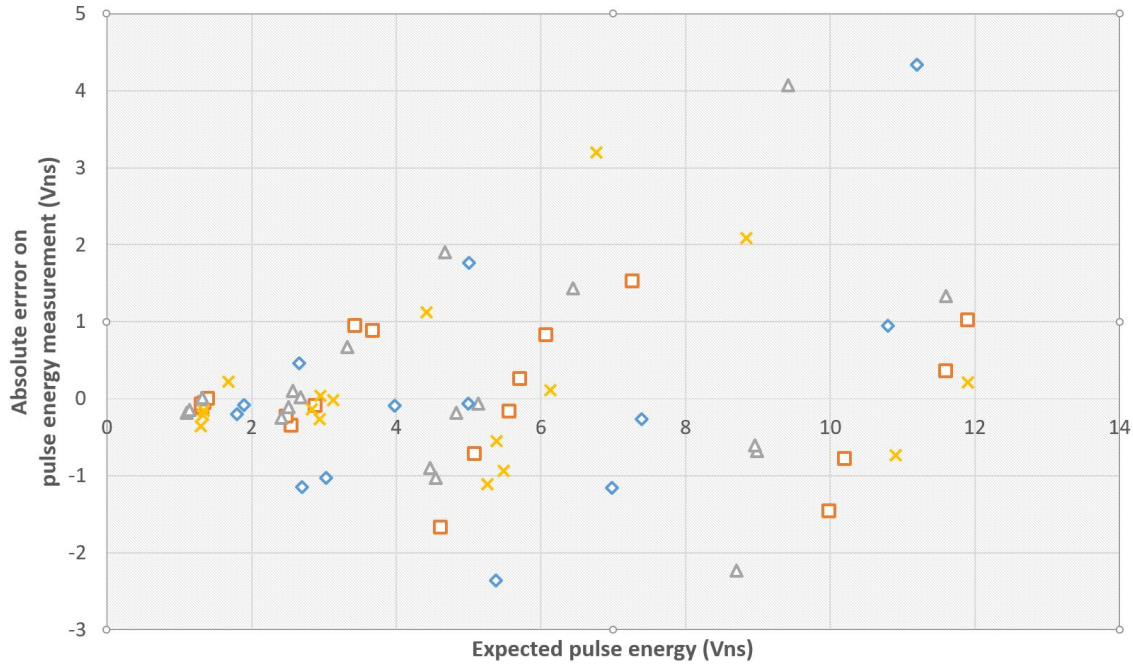


Fig. 2.11: Absolute pulse energy measurement error after removal of the systemic offset

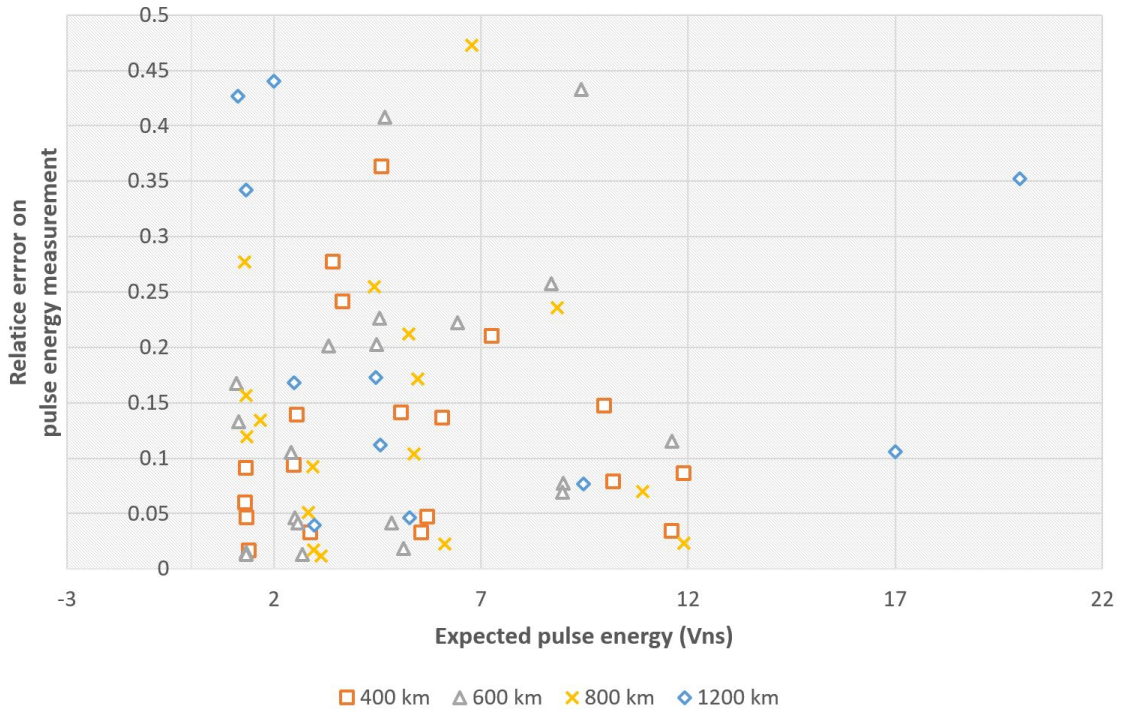


Fig. 2.12: Relative pulse energy measurement error after removal of the systemic offset

3. PROBABILITY OF FALSE DETECTION

3.1 PFD determination in a simulation environment

We determine the single shot PFD in a simulation environment software developed at the University of Bern. We use the simulation environment to simulate the RFM algorithm and to see if the pulse can be detected or not. To have a value for the PFD, we repeat the process several times for different pulse width and pulse energies. Then we check the number of times the algorithm has been able to find the pulse inside the noise environment and from this we calculate the PFD.

3.2 Special performance tests before and after BELA hardware modification

3.2.1 Test execution summary

Special Performance Test (SPT) was performed in August 2017. The SPT was executed in combination with required hardware modification on BELA FM to reduce APD noise.

The SPT was executed twice, once before and once after hardware modification. These tests were required in order to verify that BELA is not exceeding SpaceWire limits after the hardware modification. It was tested and confirmed that the hardware modification doesn't have a negative impact on the communication noise with and from spacecraft. As a result of the required hardware modifications the noise was reduced significantly and the instrument performance is now decisively better than before.

3.2.2 Science data analysis

The recorded noise samples for both before and after hardware modification is fed to the simulation environment and the PFD is calculated accordingly. An overview of determined PFDs before and after hardware modification at Gain Code 0 and at a typical return pulse width can be found in table [3.1](#).

Tab. 3.1: PFD before and after BELA's hardware modification at gain code 7 and at 35 ns pulse width

| | | FWHM = 35 ns | | |
|---------------|------------------|-------------------|---|--|
| Distance (km) | Pulse Energy (J) | PFD | | |
| | | Old configuration | Modified hardware + pi filters (No ferrite) | Modified hardware + pi filters + ferrite |
| 300 | 7.93333E-16 | 0 % | 0 % | 0 % |
| 400 | 4.4625E-16 | 10 % | 0 % | 0 % |
| 500 | 2.856E-16 | 50 % | 0 % | 0 % |
| 600 | 1.98333E-16 | 65 % | 0 % | 0 % |
| 700 | 1.45714E-16 | 99 % | 0 % | 0 % |
| 800 | 1.11563E-16 | 100 % | 0 % | 0 % |
| 900 | 8.81481E-17 | 100 % | 0 % | 0 % |
| 1000 | 7.14E-17 | 100 % | 0 % | 0 % |
| 1100 | 5.90083E-17 | 100 % | 0 % | 0 % |
| 1200 | 4.95833E-17 | 100 % | 4% | 0 % |
| 1300 | 4.22485E-17 | 100 % | 24% | 0 % |
| 1400 | 3.64286E-17 | 100 % | 44% | 20 % |
| 1500 | 3.17333E-17 | 100 % | 76% | 36 % |
| 1600 | 2.78906E-17 | 100 % | 90 % | 72 % |
| 1700 | 2.47059E-17 | 100 % | 96 % | 80 % |

3.2. SPECIAL PERFORMANCE TESTS BEFORE AND AFTER BELA HARDWARE MODIFICATION 33

Tab. 3.2: Probability of false detection in different altitudes and return pulse widths. provided for gain code 7 and APD-A gain = 0.75 MV/W

| Return Pulse energy (Joules) | Altitude (km) | FWHM of the return signal | | | | | | | | | | | |
|------------------------------|---------------|---------------------------|-------|-------|-------|-------|-------|-------|-------|-------|-------|--------|-------|
| | | 10 ns | 25 ns | 30 ns | 35 ns | 40 ns | 50 ns | 60 ns | 70 ns | 80 ns | 90 ns | 100 ns | |
| 7.93E-16 | 300 | 0 % | 0 % | 0 % | 0 % | 0 % | 0 % | 0 % | 0 % | 0 % | 0 % | 0 % | 0 % |
| 4.46E-16 | 400 | 0 % | 0 % | 0 % | 0 % | 0 % | 0 % | 0 % | 0 % | 0 % | 0 % | 0 % | 0 % |
| 2.86E-16 | 500 | 0 % | 0 % | 0 % | 0 % | 0 % | 0 % | 0 % | 0 % | 0 % | 0 % | 0 % | 0 % |
| 1.98E-16 | 600 | 0 % | 0 % | 0 % | 0 % | 0 % | 0 % | 0 % | 0 % | 0 % | 0 % | 0 % | 0 % |
| 1.46E-16 | 700 | 0 % | 0 % | 0 % | 0 % | 0 % | 0 % | 0 % | 0 % | 0 % | 0 % | 0 % | 0 % |
| 1.12E-16 | 800 | 0 % | 0 % | 0 % | 0 % | 0 % | 0 % | 0 % | 0 % | 0 % | 2 % | 2 % | 4 % |
| 8.81E-17 | 900 | 0 % | 0 % | 0 % | 0 % | 0 % | 0 % | 0 % | 4 % | 10 % | 10 % | 32 % | 34 % |
| 7.14E-17 | 1000 | 0 % | 0 % | 0 % | 2 % | 2 % | 8 % | 34 % | 34 % | 44 % | 66 % | 66 % | 66 % |
| 5.90E-17 | 1100 | 6 % | 2 % | 8 % | 14 % | 34 % | 64 % | 52 % | 64 % | 82 % | 90 % | 92 % | 92 % |
| 4.96E-17 | 1200 | 22 % | 12 % | 28 % | 30 % | 60 % | 76 % | 84 % | 84 % | 92 % | 90 % | 96 % | 96 % |
| 4.22E-17 | 1300 | 56 % | 36 % | 46 % | 70 % | 70 % | 88 % | 90 % | 100 % | 96 % | 96 % | 98 % | 98 % |
| 3.64E-17 | 1400 | 62 % | 58 % | 78 % | 82 % | 84 % | 92 % | 92 % | 100 % | 100 % | 98 % | 98 % | 98 % |
| 3.17E-17 | 1500 | 80 % | 76 % | 86 % | 96 % | 92 % | 96 % | 96 % | 100 % | 100 % | 100 % | 100 % | 100 % |
| 2.79E-17 | 1600 | 92 % | 94 % | 84 % | 96 % | 96 % | 96 % | 100 % | 100 % | 100 % | 100 % | 100 % | 100 % |
| 2.47E-17 | 1700 | 98 % | 94 % | 96 % | 98 % | 98 % | 96 % | 100 % | 100 % | 100 % | 100 % | 100 % | 100 % |

Tab. 3.3: Probability of false detection in different altitudes and return pulse widths. provided for gain code 7 and APD-A gain = 1.5 MV/W

| Return Pulse Energy (Joules) | Altitude (km) | FWHM of the return signal | | | | | | | | | | | |
|------------------------------|---------------|---------------------------|-------|-------|-------|-------|-------|-------|-------|-------|-------|--------|------|
| | | 10 ns | 25 ns | 30 ns | 35 ns | 40 ns | 50 ns | 60 ns | 70 ns | 80 ns | 90 ns | 100 ns | |
| 7.93E-16 | 300 | 0 % | 0 % | 0 % | 0 % | 0 % | 0 % | 0 % | 0 % | 0 % | 0 % | 0 % | 0 % |
| 4.46E-16 | 400 | 0 % | 0 % | 0 % | 0 % | 0 % | 0 % | 0 % | 0 % | 0 % | 0 % | 0 % | 0 % |
| 2.86E-16 | 500 | 0 % | 0 % | 0 % | 0 % | 0 % | 0 % | 0 % | 0 % | 0 % | 0 % | 0 % | 0 % |
| 1.98E-16 | 600 | 0 % | 0 % | 0 % | 0 % | 0 % | 0 % | 0 % | 0 % | 0 % | 0 % | 0 % | 0 % |
| 1.46E-16 | 700 | 0 % | 0 % | 0 % | 0 % | 0 % | 0 % | 0 % | 0 % | 0 % | 0 % | 0 % | 0 % |
| 1.12E-16 | 800 | 0 % | 0 % | 0 % | 0 % | 0 % | 0 % | 0 % | 0 % | 0 % | 0 % | 0 % | 0 % |
| 8.81E-17 | 900 | 0 % | 0 % | 0 % | 0 % | 0 % | 0 % | 0 % | 0 % | 0 % | 0 % | 0 % | 0 % |
| 7.14E-17 | 1000 | 0 % | 0 % | 0 % | 0 % | 0 % | 0 % | 0 % | 0 % | 0 % | 0 % | 0 % | 0 % |
| 5.90E-17 | 1100 | 0 % | 0 % | 0 % | 0 % | 0 % | 0 % | 0 % | 0 % | 0 % | 0 % | 0 % | 0 % |
| 4.96E-17 | 1200 | 0 % | 0 % | 0 % | 0 % | 0 % | 0 % | 0 % | 0 % | 2 % | 6 % | 16 % | 16 % |
| 4.22E-17 | 1300 | 0 % | 0 % | 0 % | 0 % | 0 % | 0 % | 6 % | 8 % | 18 % | 24 % | 52 % | 52 % |
| 3.64E-17 | 1400 | 0 % | 0 % | 0 % | 2 % | 4 % | 2 % | 20 % | 24 % | 66 % | 72 % | 76 % | 76 % |
| 3.17E-17 | 1500 | 4 % | 2 % | 2 % | 6 % | 10 % | 20 % | 46 % | 56 % | 66 % | 78 % | 86 % | 86 % |
| 2.79E-17 | 1600 | 6 % | 8 % | 10 % | 24 % | 38 % | 56 % | 72 % | 74 % | 88 % | 86 % | 94 % | 94 % |
| 2.47E-17 | 1700 | 30 % | 22 % | 26 % | 40 % | 54 % | 66 % | 74 % | 36 % | 92 % | 96 % | 98 % | 98 % |

3.3 PFD calculation using spacecraft noise environment

3.3.1 PFD tests in different altitudes and return pulse widths

The noise samples that were used for above tests were measured in the laser altimetry test laboratory of the University of Bern but they do not represent the electromagnetic noise environment of the spacecraft. To provide the most realistic PFD calculation, we use the noise samples that were measured onboard MPO during the final tests of the instrument before flight. Tables 3.2 and 3.3 show the PFD in different altitudes and pulse widths. It can be seen that the PFD increases with the pulse width. In other words, the maximum working altitude decreases when we have more broaden pulses arriving at the telescope.

3.3.2 The impact of Instrument gain settings

Table 3.4 provides the results of the PFD tests that were conducted on BELA using the same noise samples as in section 3.3.1, but in different gain settings. Therefore one can use it to compare the impact of different gains on the PFD results. BELA can have 16 different gain codes (from 0 to 15). The gain code and the gain of the APD can change the PFD [Thomas et al., 2019]. We tested the PFD in six different gain settings for the instrument: three gain codes (0, 7 and 15) and two APD-A gains (0.75 and 1.5 MV/W).

Tab. 3.4: PFD in different spacecraft altitudes and in different gain settings for a return pulse width of 10 ns

| FWHM = 35 ns | | | | | | | |
|---------------|------------------|------------------|-------------------|------------------|-------------------|------------------|-------------------|
| Distance (km) | Pulse Energy (J) | PFD | | | | | |
| | | Gain code 0 | | Gain code 7 | | Gain code 15 | |
| | | APD-A gain = 1.5 | APD-A gain = 0.75 | APD-A gain = 1.5 | APD-A gain = 0.75 | APD-A gain = 1.5 | APD-A gain = 0.75 |
| 300 | 7.93333E-16 | 0 % | 0 % | 0 % | 0 % | 0 % | 0 % |
| 400 | 4.4625E-16 | 0 % | 0 % | 0 % | 0 % | 0 % | 0 % |
| 500 | 2.856E-16 | 0 % | 0 % | 0 % | 0 % | 0 % | 0 % |
| 600 | 1.98333E-16 | 0 % | 0 % | 0 % | 0 % | 0 % | 0 % |
| 700 | 1.45714E-16 | 0 % | 0 % | 0 % | 0 % | 0 % | 0 % |
| 800 | 1.11563E-16 | 0 % | 0 % | 0 % | 0 % | 0 % | 0 % |
| 900 | 8.81481E-17 | 0 % | 0 % | 0 % | 0 % | 0 % | 0 % |
| 1000 | 7.14E-17 | 0 % | 20 % | 0 % | 2 % | 0 % | 2 % |
| 1100 | 5.90083E-17 | 0 % | 44 % | 0 % | 14 % | 0 % | 16 % |
| 1200 | 4.95833E-17 | 0 % | 70 % | 0 % | 28 % | 0 % | 48 % |
| 1300 | 4.22485E-17 | 2 % | 80 % | 0 % | 70 % | 0 % | 66 % |
| 1400 | 3.64286E-17 | 4 % | 86 % | 2 % | 82 % | 0 % | 86 % |
| 1500 | 3.17333E-17 | 32 % | 94 % | 10 % | 96 % | 0 % | 96 % |
| 1600 | 2.78906E-17 | 40 % | 94 % | 24 % | 96 % | 20 % | 96 % |
| 1700 | 2.47059E-17 | 82 % | 100 % | 40 % | 98 % | 42 % | 100 % |

As shown in table 3.4, using instrument gain code 7 BELA will have a better performance with respect to gain code 0, but the difference between gain codes 7 and 15 is negligible in most of the cases. It is important to mention that all the tables in this section are provided assuming a constant surface reflectance of 19% and no degradation on instrument characteristics.

3.4 The impact of solar noise on PFD

In general the noise consists of four components. Solar noise, shot noise, dark current and the electronic noise floor (see Steinbrügge et al. [2018] for further details). The first contribution, the solar noise, is the sunlight reflected from the surface of the planet within the field of view of the receiver. The second contribution is the shot noise. This is the additional noise caused by the statistical nature of the multiplication process that the APD experiences when it is illuminated. This contribution is called shot noise and depends on the incident optical power.

To add the impact of solar noise on top of the calculated PFD, we use the relation between PFD to Signal-to-Noise. This relation has been found empirically by testing the actually implemented algorithm for a statistical set of laser pulses under different SNR conditions by Steinbrügge et al. [2018].

$$\text{PFD} = \frac{\text{erfc}(0.69 \cdot \text{SNR} - 1.64)}{1.98} \quad (3.1)$$

Signal-to noise ration can also be calculated by the following equation:

$$\text{SNR} = \frac{R_0^2 M^2 P_{peak}^2 R_i^2}{\left(2q * (I_{ds} + (I_s + I_{db} + I_{sn}) M^{(2+x)}) + n_f^2\right) * B_0 R^2} \quad (3.2)$$

Where I_s is the solar noise, I_{SN} is the shot noise, I_{ds} is APD dark current (surface), I_{db} is APD dark current (bulk), M is the nominal gain, x the excess noise factor and n_f the noise floor. The assumed values are given in table 1.2. The solar noise can be calculated using the following equation:

$$I_s = q \epsilon_t \epsilon_o \epsilon_{qe} \rho_0 \cos(i) A_{F \circ V} \Omega_R \frac{F \lambda}{hc} \sigma_{rf} \quad [\text{A}] \quad (3.3)$$

Where:

$$A_{FOV} = \pi H^2 \tan^2(\theta_{FOV}) \quad [\text{m}^2] \quad (3.4)$$

To find the impact of solar noise on PFD we first find the SNR based on the PFD that is predicted without solar noise. Then we find the change in SNR after adding the solar noise and finally, we go back from SNR to PFD and find the corrected PFD using the new value for SNR.

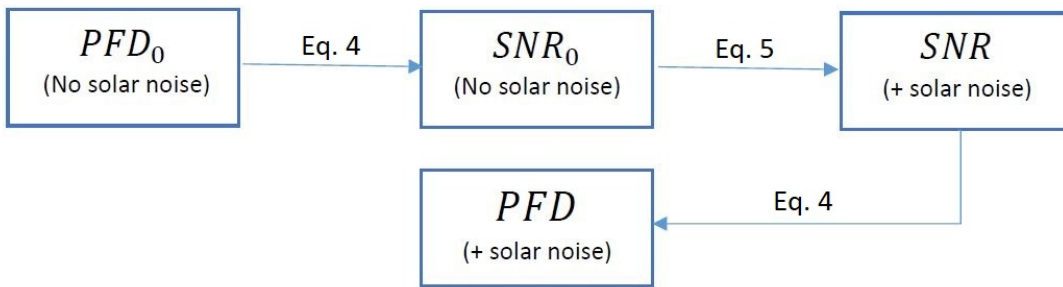


Fig. 3.1: Process of calculating the impact of solar noise on PFD using SNR to PFD relation

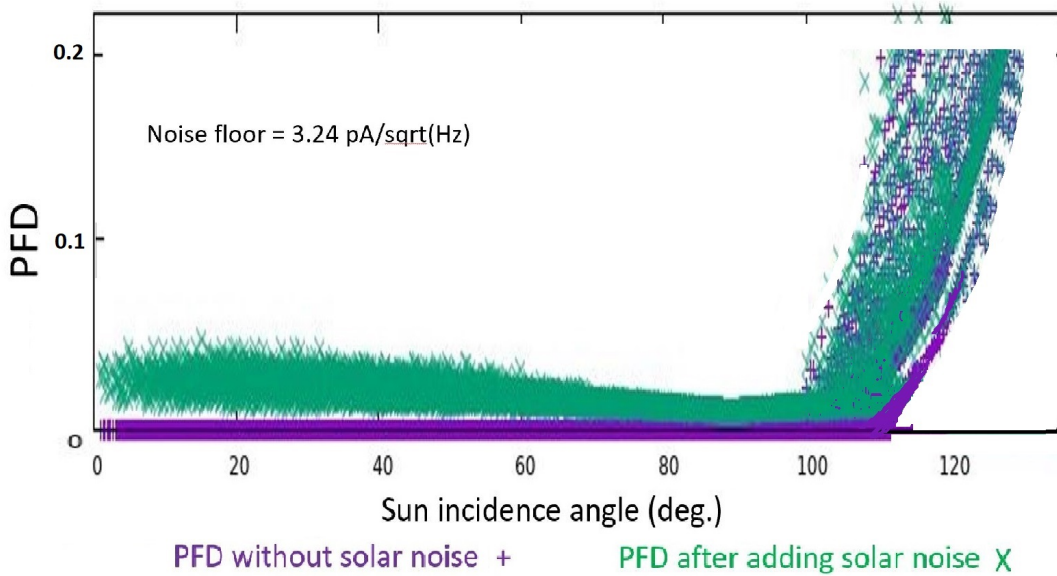


Fig. 3.2: PFD as a function of Sun incidence angle

Assuming the noise floor to be $3.2 \text{ pA}/\sqrt{\text{Hz}}$, adding the impact of solar noise on PFD, brings the PFD from zero up to around 5% (in worst case) when sun is shining directly from behind (figure 3.2). The average value of PFD at zero incidence angle would be 2.5 %. Considering that the effect of solar noise can increase the PFD from zero to a maximum percentage of 5 % and considering that we assume the signal to be detectable when the PFD is below 10%, we conclude that the solar noise has a negligible impact on the coverage of BELA and therefore it will not be considered on in-orbit simulations of BELA in sections 3 and 4.

4. IN-FLIGHT PERFORMANCE EVALUATION: MODELLING

Our modeling consists of several different components, as detailed in figure 4.1. In particular, we model the error budget for the three main measurements by BELA: Time of flight (TOF), pulse width and pulse energy measurements, including the noise directly from the instrument, the noise caused by uncertainties in the dynamics of the system and the noise affecting measurements due to the properties of the surface. Therefore, our setup consists of a model for the planet surface properties (eg. local height, slope, roughness), in a dynamical model for the rotation of the planet and one for the orbit and attitude of the spacecraft carrying the instrument.

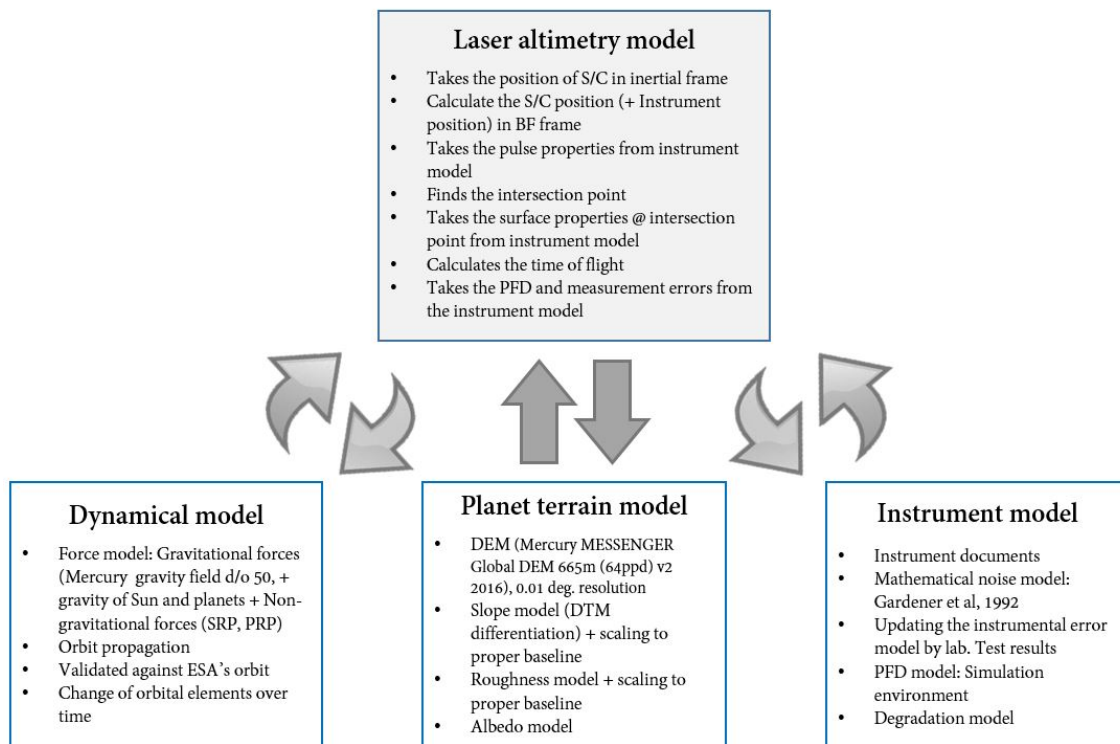


Fig. 4.1: Modelling of the in-flight laser altimetry

We use such model to predict the accuracy of the instrument in measuring the surface properties. We also study the working limit of the instrument by modeling the PFD for each observation.

We determine a set of observation epochs for BELA, based on a repetition rate of 10 Hz for the whole nominal mission. At these epochs, we use the dynamical model to determine the position of MPO around Mercury and the rotational state of the planet itself. Then using the spacecraft attitude and knowing the position of the instrument inside the spacecraft frame, we calculate the onward laser leg, the incidence time and position on the planet surface. Then from the planet terrain model, we determine the surface properties at the laser spot (see section 4.2) and we calculate the properties of the return signal. Then, we calculate the laser return leg and finally, using the instrument model and considering the noise from different sources, we determine the TOF, pulse width and pulse energy measurement errors [Hosseiniarani et al., 2018].

4.0.1 TOF measurement noise model

The time of flight (TOF) measurement, like any other observation is not ideal. Several sources of error are presented in Gardner [1992]. The TOF measurement error is a combination of:

- Error caused by surface slope:

$$\sigma(\Delta T)_{slope} = \frac{2\sqrt{2}}{C} \left[\frac{F}{N} + \frac{1}{K_s} \right]^{\frac{1}{2}} z \tan \theta_t \tan S \quad (4.1)$$

- Error caused by surface roughness:

$$\sigma(\Delta T)_{Roughness} = \frac{2}{C} \left[\frac{F}{N} + \frac{1}{K_s} \right]^{\frac{1}{2}} Std(\Delta\zeta) \quad (4.2)$$

- Error caused by pointing uncertainties:

$$\sigma(\Delta T)_{PointingError} = \frac{2\sqrt{2}}{C} z \tan S Std(\Delta\Phi) \quad (4.3)$$

- Instrumental error

where

- F: Excess noise factor of the detector
 N: Mean number of total detected photons
 K_s : Ratio of receiver area to speckle correction area
 θ_t : Laser beam divergence HW @ $e^{-1/2}$ (rad)
 C: Speed of light (m/s)
 z: Altimeter altitude (m)
 S: Surface slope (rad)
 $\Delta\Phi$ pointing uncertainty

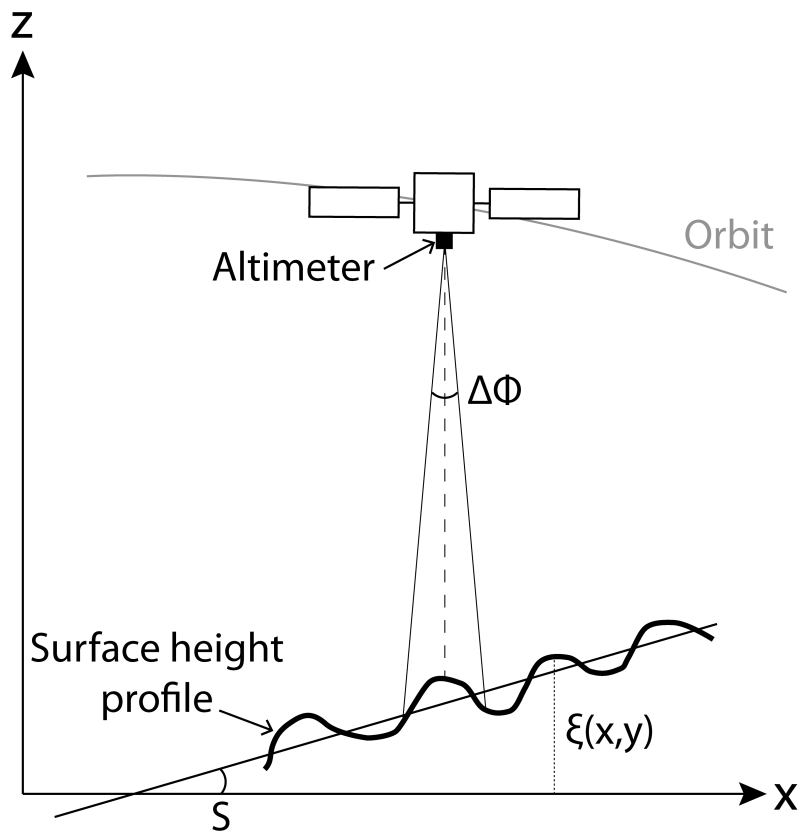


Fig. 4.2: geometry of a beautiful laser altimeter and ground target

The total TOF measurement error can be formulated as the quadratic sum of the above values. The last component of the TOF measurement is the instrumental error which just depends on the instrument properties and pulse detection algorithm. This error is called "system error" in the work of Gardner, but here, for avoiding a confusion between this and the systematic bias in different measurements, we call this component "instrumental error".

BELA uses a digital pulse sampling and performs a pulse fitting on the signal using a specific pulse detection algorithm. This technique is different from older laser altimetry techniques which try to detect the analog signal among the noise and is more advantageous since it leads to a better TOF resolution. As a result of using this algorithm, the nature of BELA instrumental errors are different from the instrumental errors in [Gardner et al, 1992]. Therefore, we do not use the proposed equation in [Gardner et al, 1992] for instrumental errors and instead we measure this error by analysing the test results on BELA at the laser altimetry test laboratory of the University of Bern. The summary of the results are provided in section 4.3 and the detail of this study is presented in section 2.

4.0.2 Pulse width measurement noise model

According to Gardner [1992], the return pulse from the planet surface, experiences a broadening because of the surface slope, the surface roughness and the beam curvature, resulting in a global error σ_t , so that

$$\sigma_t = \sqrt{\sigma_0^2 + \sigma_{bc}^2 + \sigma_r^2 + \sigma_s^2} \quad (4.4)$$

with

$$\sigma_{bc} = \frac{2z}{c} \tan^2 \theta_t \quad : \text{beam curvature} \quad (4.5)$$

$$\sigma_r = \frac{2}{c} Std(\Delta\zeta) \quad : \text{roughness effect} \quad (4.6)$$

$$\sigma_s = \frac{\sqrt{2}z}{c} \tan \theta_t \tan S \quad : \text{slope effect} \quad (4.7)$$

Where $Std(\Delta\zeta)$ is the definition of roughness in our work. Due to the limited bandwidth of the receiver system, the analog signal experiences an additional broadening [Gunderson and Thomas, 2010], which can be expressed by

$$\sigma_p = \left(2\sqrt{2\pi}B_0\right)^{-1} \quad (4.8)$$

leading to a total temporal width of the Gauss function of

$$\sigma = \sqrt{\sigma_t^2 + \sigma_p^2} \quad (4.9)$$

The full width half maximum (FWHM) of the pulse can be calculated as

$$FWHM = 2\sqrt{2 \ln 2} \sigma \quad (4.10)$$

Fig. 5.5 provides the FWHM of the return pulse width in different altitudes and over different terrain types. According to the model described in Gardner [1992], the error on pulse width measurement has the same component as the TOF error with the difference that the pointing error doesn't have any impact on the results. The components of pulse width error can be calculated using

$$Std(\sigma)_{roughness} = \frac{2}{c} \left[\frac{F}{2N} \right]^{\frac{1}{2}} Std(\Delta\zeta) \quad (4.11)$$

and

$$Std(\sigma)_{slope} = \frac{2}{c} \left[\frac{F}{N} \right]^{\frac{1}{2}} z \tan \theta_t \tan S \quad (4.12)$$

The third component of the pulse width measurement is the instrumental error in the pulse width measurements. For the same reason as TOF error, we do not use the proposed equation in [Gardner et al, 1992] for instrumental errors and instead calculate this error by analysing the tests results on BELA at the laser altimetry test laboratory of the University of Bern that is explained in section 2.

4.0.3 Pulse energy measurement noise model

The pulse energy measurement is not sensitive to the local slope and roughness and it is independent of the pointing uncertainties. So for determining the performance in pulse width measurement, we only consider the instrumental errors from the laboratory based tests on BELA RFM.

In order to compute the value of Eqs. (4.1) to (4.3) and also (4.11) to (4.12) for realistic operative configurations of BELA, we developed a detailed modeling for both ESA BepiColombo orbit and attitude and for Mercury surface properties.

4.1 Dynamical model of Bepicolombo spacecraft

4.1.1 Spacecraft orbit

For modelling the orbit of MPO around Mercury, we use an extensive force model, including Mercury gravity field GGMEs_100V07 (up to degree and order 50), solid tides, solar and planetary -including albedo and IR- radiation pressure, third body perturbations and relativistic effects including the Schwarzschild term, Lense-Thirring and De Sitter. To consider the effect of non-gravitational forces on the spacecraft, we use a 33-plates macromodel of MPO, including

both visible and IR optical properties.

With these assumptions, the MPO orbit has been propagated and verified against orbits provided by ESA [Jehn, 2015]. This modelling is done using the planetary extension of the Bernese GNSS Software [Dach et al., 2015] that has been developed at the Astronomical Institute of the University of Bern (AIUB).

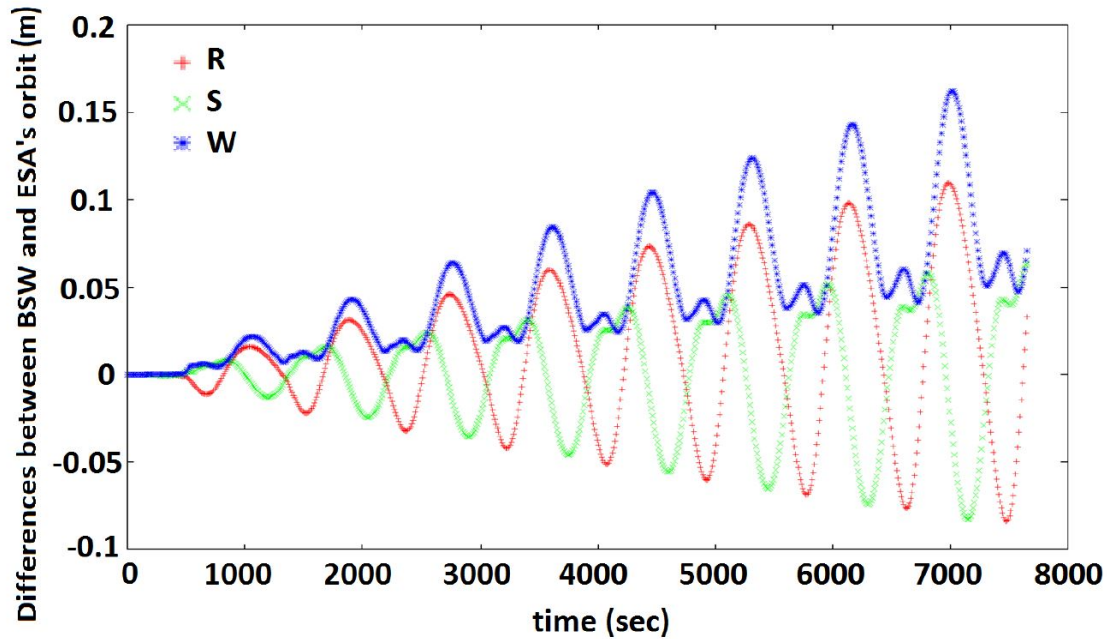


Fig. 4.3: Orbit differences between BSW propagation and ESA SPK orbit, not exceeding 15 cm over 1 day

4.1.2 Pointing uncertainty

The Attitude and Orbit Control Subsystem (AOCS) contribution to attitude estimation varies between 1.06 to 2.09 arc seconds, depending on the AOCS configuration (e.g. number of Gyro and star trackers involved)[Casasco, 2017]. Nevertheless, the biggest contribution to BELA's attitude estimation is caused by thermo-elastic effects which correspond to deformations of the spacecraft optical bench and distortions between the star trackers' lines-of-sight and the BELA line-of-sight.

BELA's pointing performance can be compatible with the 20 arc seconds scientific requirements only if the static and slowly-varying thermo-elastic distortions can be cross-calibrated against camera data and the orbital position of the spacecraft is known with high accuracy by

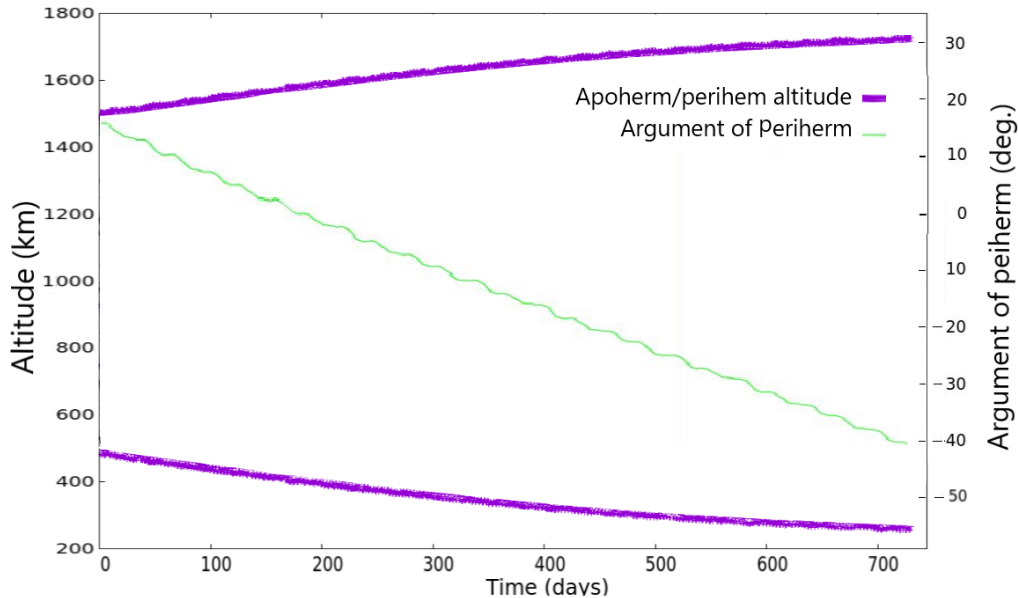


Fig. 4.4: Purple: Periherm and Apoherm altitudes during the nominal and extended mission; Green: Argument of periherm of MPO during the nominal and extended mission [Jehn, 2015].

means of the radio science experiment [Marabucci, 2012].

Several approaches for in-flight calibration of BELA's line of sight are suggested. Among them, in-flight cross-calibration with high spatial resolution images taken by BepiColombo on-board camera provides the best cross-calibration accuracy and allows compliance with the requirement. According to Casasco [2017], such an in-flight calibration can reduce the pointing uncertainty to an average value of 15 arc seconds (2σ).

Hence, we assume this value as our first estimate of the pointing error. Moreover, we take into account the possibility of further calibrations of BELA based on, *e.g.*, data analysis at crossover points. For this reason, we compare the measurement errors resulting from three possible pointing error values: the nominal 15 arc second error; 7.5 arc seconds (calibration of 50% of pointing error); 3 arc seconds (a best case scenario with an 80% decrease in pointing error).

4.2 Mercury terrain model

For determining the in-flight performance of BELA, we need to have a realistic model of the surface of Mercury. We use the Messenger MLA and camera derived digital elevation model (DEM) from Becker et al. [2016] (figure 4.5), local slopes and roughness and a reflectance model.

4.2.1 Surface elevation model

We linearly interpolate the DEM from [Becker et al. \[2016\]](#) which has a resolution of 665.24 meters/pixel.

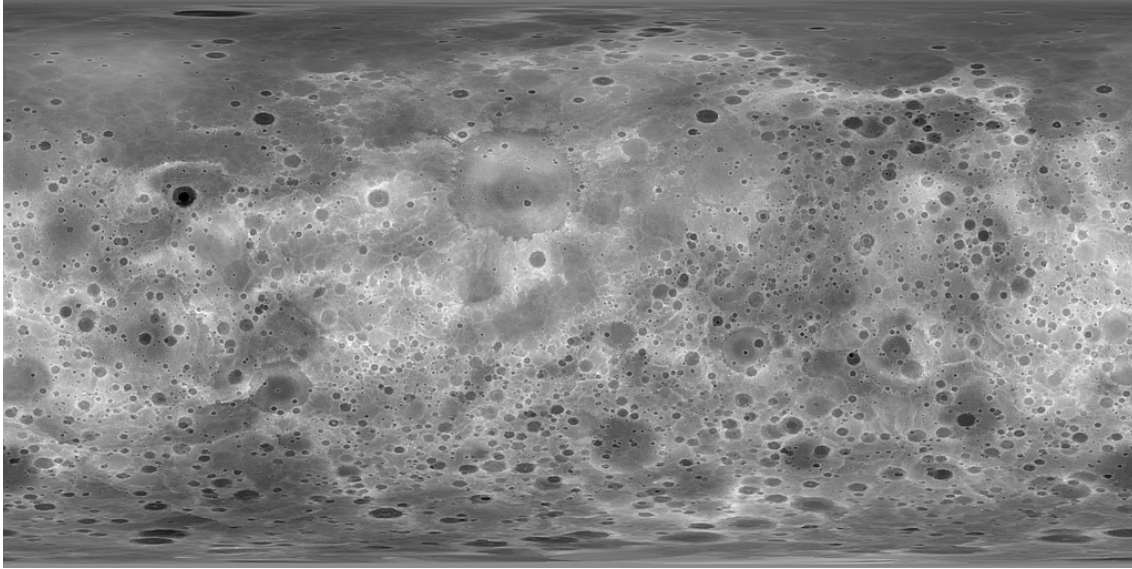


Fig. 4.5: Mercury digital elevation model [[Becker et al., 2016](#)]

4.2.2 Terrain types

We consider two types of terrains in our simulation of the Mercury's surface, according to Figure 1 of [Denevi et al. \[2013\]](#): a) smooth plains and b) rough (cratered) terrains. On the surface of Mercury, topographic depressions turn out to be rather smooth, whereas most of the highlands are heavily cratered [[Yang et al., 2016](#)].

4.2.3 Local slope model

Slope and roughness have different definitions in different studies. According to the model presented in Gardner (1992), we differentiate the vertical linear variation of surface height, which we assume as slope, from the quasi-random height variation, the RMS of which is assumed as roughness in our model (Figure 4.2).

The distribution of slopes is only known for baselines larger than the average laser altimetry footprint (the size of footprint increases with the altitude). To model the expected average

slopes within the laser altimetry footprint, we fit the distribution of average slope angles given in Pommerol et al. [2012] using an exponential law $y = Ax^b$. We get $A = 1.182$ and $b = -0.416$ for the smooth plains and $A = 2.533$ and $b = -0.311$ for the rough terrains (see Fig. 4.6). Based on this fit, we extrapolate the expected slopes down to the laser altimetry footprint sizes.

We model the local slopes by differentiating the DEM, then rescale them so that the average slope at each baseline is consistent with the extrapolated values from Pommerol et al. [2012]. This extrapolation predicts an average slope of around 7 degrees over a 20 meter baseline. We need to stress that the slope angles over meter sized baselines is not known for Mercury and this average is coming from the best model to our knowledge. In reality there might be a break point for slope extrapolation that causes a different fit for smaller baselines and as a result, the slopes might be smaller than this prediction. Since there is no information available on this we continue with our extrapolation results, but later we perform a sensitivity study to find the impact of smaller slopes on instrument measurement errors.

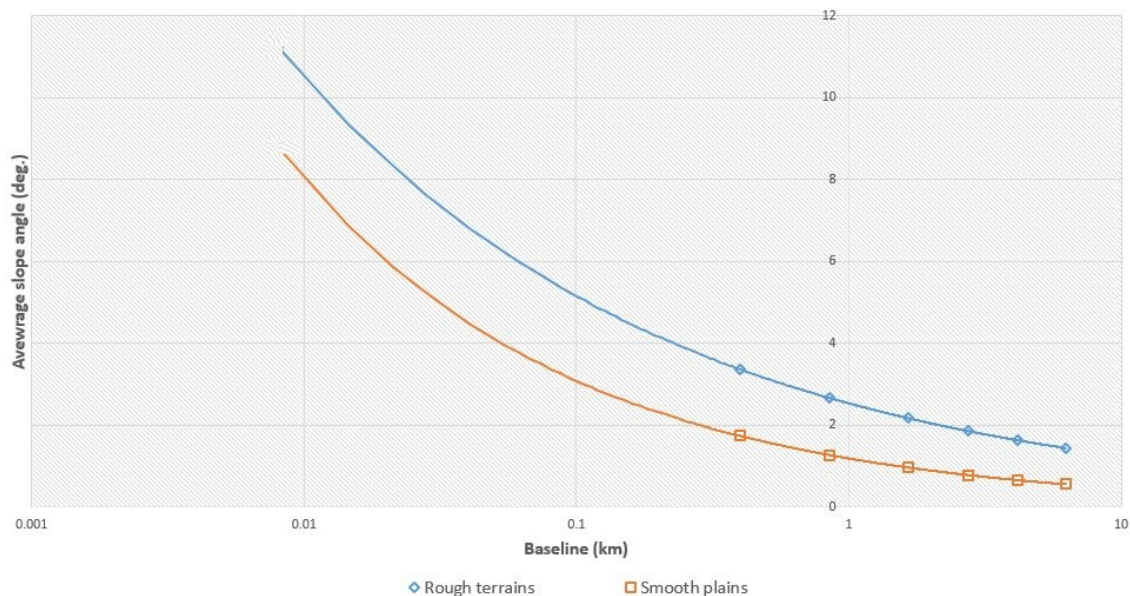


Fig. 4.6: Extrapolation of average slope to smaller baselines

4.2.4 Surface roughness model

Similar to the slope angles, the mean roughness of mercury's surface is only known in kilometer-scale baselines. Therefore, we fit a power law such as

$$y = Ax^b \quad (4.13)$$

to values from [Susorney et al. \[2017\]](#) to extrapolate the average roughness at the laser altimetry footprint size for different terrain types (Figure 4.7). We get $A = 57.91$ and $b = 0.8769$ for smooth plains and $A = 69.49$ and $b = 0.8769$ for rough terrains.

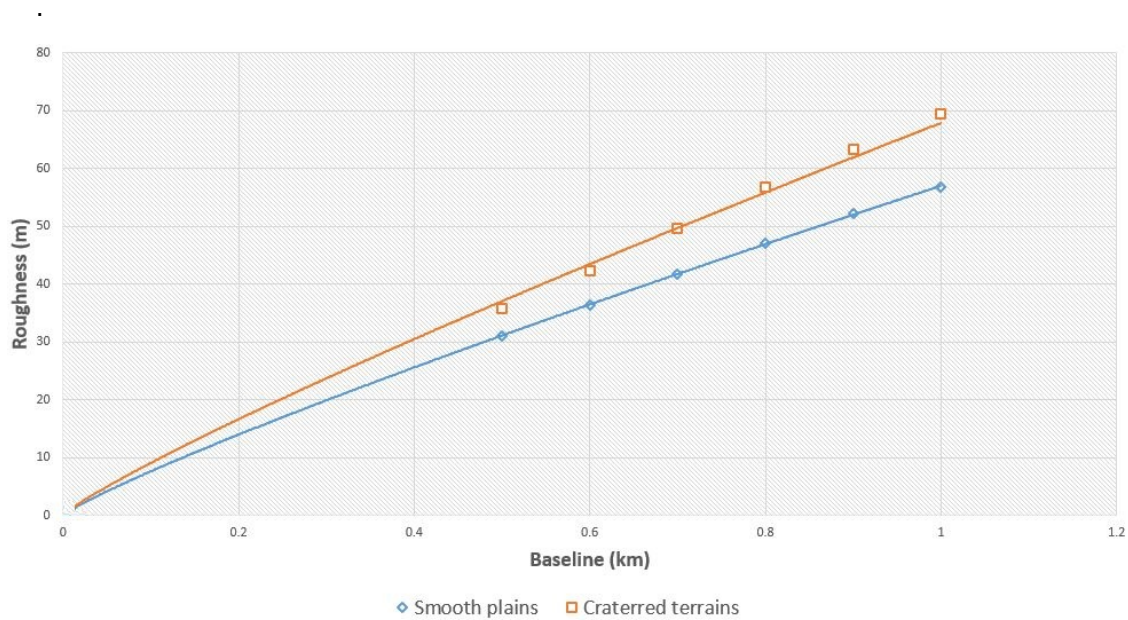


Fig. 4.7: Extrapolation of roughness to smaller baselines

4.2.5 Surface reflectance model

Maps are available from MLA data or from MESSENGER MDIS camera data [\[Denevi, 2016\]](#), but due to the insufficient accuracy at the laser altimetry wavelength, we rather base our analysis on the distribution of reflectance provided in [Gouman \[2015\]](#), which is an asymmetrical Gaussian with average value 0.19.

4.3 BELA instrument noise model

The modelling of the BELA instrument in our simulation is based on the experimental results obtained in the laser altimetry test laboratory of the University of Bern. We send several thousand Gaussian pulses to the Range finder module (RFM) standalone and test the instrumental

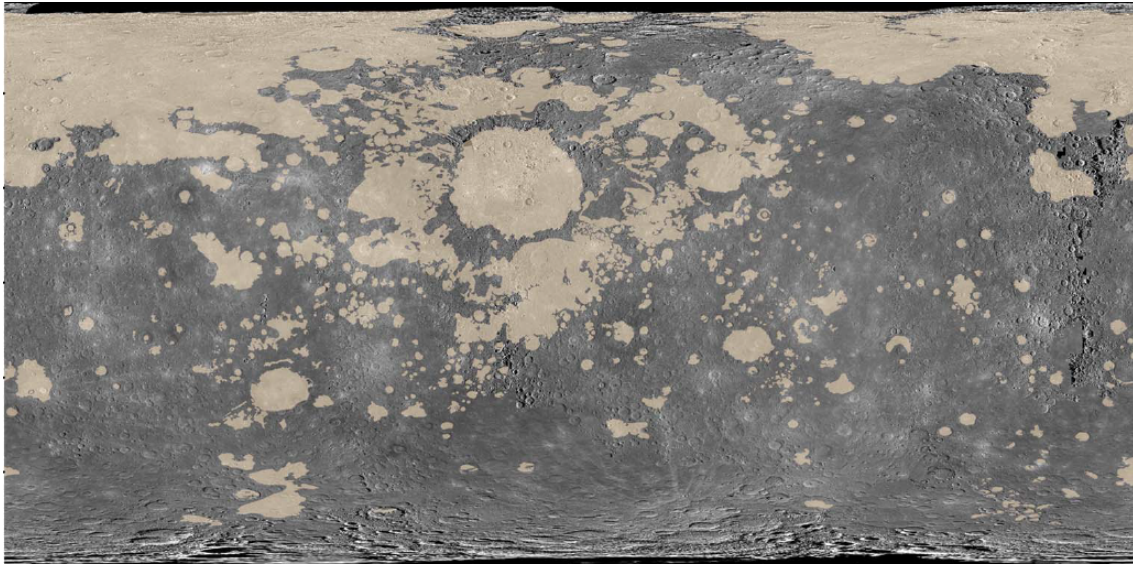


Fig. 4.8: Mercury surface terrains. khaki: Smooth plains; gray: rough terrains [Denevi et al., 2013]

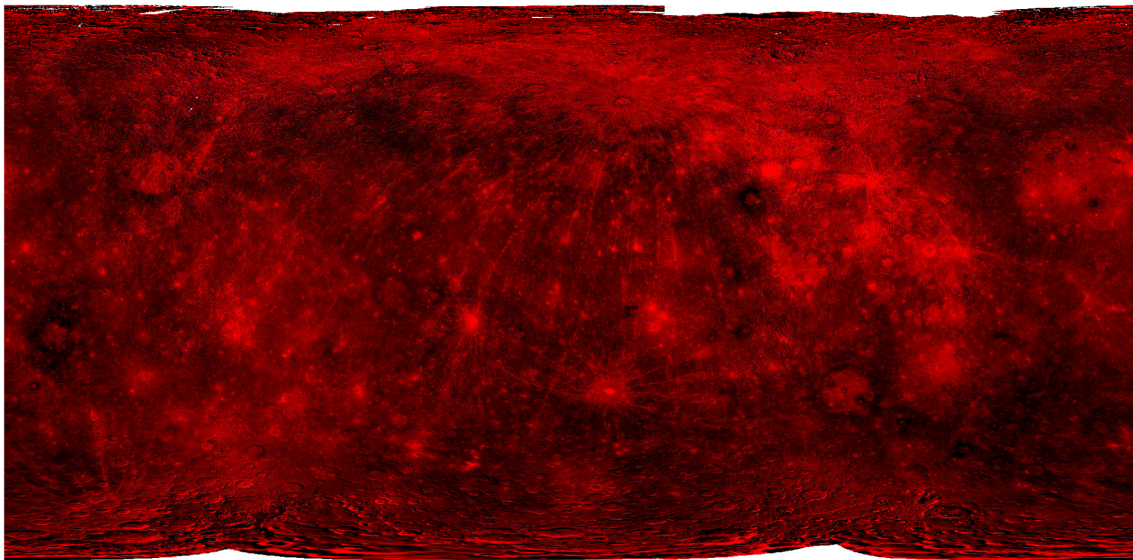


Fig. 4.9: Mercury reflectance map based on Messenger MDIS data [Denevi, 2016]

performance on determining the range, pulse width and pulse energy.

The details of this study are shown in section 2. To summarise, a systematic offset on TOF, pulse width and pulse energy measurement noises seems to be present depending on the gain settings. Figures 2.2 and 2.3 (appendix) show a TOF deviation between the high gain and low

gain sequences leading to an offset of about 10 cm to 40 cm.

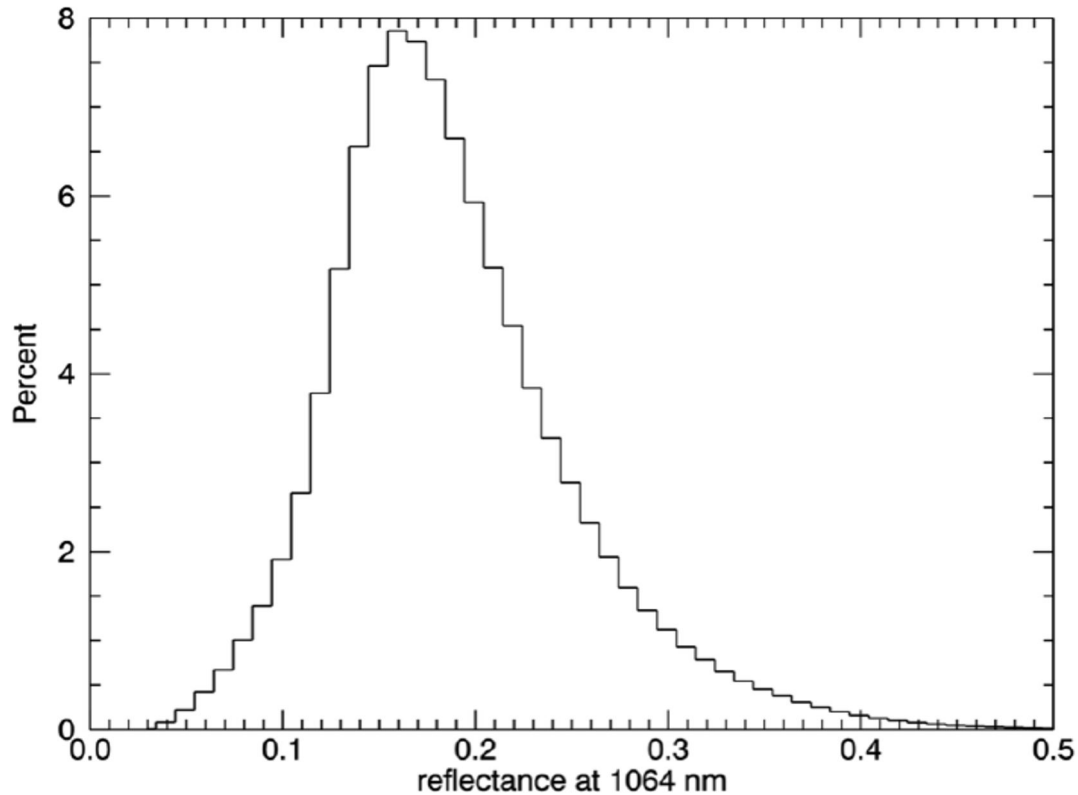


Fig. 4.10: Reflectance histogram [Gouman, 2015]

The pulse width error contains both random errors and biases terms due to laser divergence and receiver impulse response. These terms can be subtracted from the pulse width measurement. Knowing the specifications of the instrument, it is possible to calibrate the systematic part of this error [Gardner, 1992]. To be conservative in our analysis, we determine the performance in pulse width measurement in both cases (with or without calibration).

We also see a scale error when we measure the pulse energy, *i.e.* a systematic bias in the measured pulse energy that is proportional to the amount of expected pulse energy. To improve the instrumental accuracy, such an offset should be removed. Table 2.4 provides the instrumental noise on different measurement before and after removal of the systematic measurement errors.

We obtained these results in a controlled experimental setup, by sending a Gaussian signal

to the RFM standalone. This is a favorable situation w.r.t. actual operations, when non-Gaussian pulses will be measured from the ground. Therefore, we consider both cases (whether the offsets can be removed or not) and compare the results.

4.3.1 Instrument degradation model

According to different studies by [Gunderson and Thomas \[2010\]](#), [Kallenbach et al. \[2013\]](#), [Heesel \[2014\]](#) and [Metz \[2014\]](#), there will be three major instrument degradation affecting the instrument: The degradation of the laser power, the degradation of the physical transmission of ROSS and the degradation of the APD bulk dark current.

BELA delivers at least 300 million laser pulses with 50 mJ. In the study by [Kallenbach et al. \[2013\]](#), a BELA laser life model, containing flight representative optics, passed the required 300 Mshots of operation at 10 Hz repetition rate. This life model shows a initial power degradation of around 10% after about four million shots that is presumed to be caused by a phenomenon known as "infant mortality" (See figure 7 of [Kallenbach et al. \[2013\]](#) and is probably the influence of early mortality of the diode laser bars. When present, this typically occurs during the first 10 to 20 Mshots of operation. This reduction in laser power could be compensated for by increasing the pump time.

A degradation of 8.3% has been measured after 200 kRad of gamma irradiation and a total degradation of 11.3% has been measured following an additional 200 kRad of proton irradiation (See Fig. 9 of [Kallenbach et al. \[2013\]](#)). This degradation too could be compensated by increasing the pump time from (typically) 125 μ sec to 200 μ sec. However, the BELA laser should only experiences up to 20 krad of irradiation during the full mission duration of BepiColombo at its well-shielded location [[Kallenbach et al., 2013](#)].

Considering all these laser degradation effects together, we study three possible scenarios for laser power degradation: no degradation of the pulse energy during the nominal life time (through compensation); a 10% degradation (either from the "infant mortality" phenomenon or from the bad shielding against radiation); a 20% degradation due to uncompensated effects of both infant mortality and radiation in space (worst case scenario).

The degradation also effects the performance of BELA receiver. The ROSS transmission was measured to be 76.7 % during the tests at the University of Bern. But according to the BELA reports by [Heesel \[2014\]](#) and [Metz \[2014\]](#), this value at the end of the nominal life is expected to be 67.3%. Since the degradation of ROSS transmission is due to the radiations and it starts from the launch date, we use the value for EOL for the whole simulation of two years of mission.

Tab. 4.1: Degraded values of instrument parameters over its mission lifetime (Begin Of Life: BOL; End Of Life: EOL; Receiver Optical Sub-System: ROSS).

| Time degradation level | BOL | EOL | | |
|------------------------|----------------|-------|--------|--------|
| | No degradation | Low | Medium | High |
| ROSS transmission | 76.7% | 67.3% | 67.3% | 67.3% |
| Laser pulse energy | 50 mj | 50 mj | 45 mj | 40 mj |
| APD bulk dark current | 50 pA | 50 pA | 75 pA | 100 pA |

The last parameter that we expect to degrade is the APD bulk dark current. The value of this parameter at the BOL is 50 pA, but according to [Gunderson and Thomas \[2010\]](#), we expect an increase up to 100 pA.

Four degradation scenarios will be considered in the simulations. First, the beginning of life condition with no degradation at all. Second, a low degradation where we only assume the degradation of ROSS transmission. In this scenario, it is assumed that the laser power can be compensated and there will be no decrease in the power. Considering that there is a redundant laser, this will be the most likely scenario for the time the spacecraft arrives Mercury.

Third, we assume a medium level of degradation, where we also assume a 10 % deprecation of laser power and a 25% increase in APD bulk dark current (I_{db}) in additional to the ROSS transmission degradation. Finally the final scenario contains a high level of degradation where all the impacts has considered at it's maximum level (20 % deprecation of laser power and a 50% increase in APD bulk dark current, I_{db}). This will be the least likely scenario.

4.3.2 *the impact of solar noise on the measurements*

[Gunderson et al. \[2006\]](#) and [Gunderson and Thomas \[2010\]](#) have studied the impact of solar noise on the range error and they find that range errors arising from SNR effects in the receiver chain will be dominated by other range error components. The latest study shows that both the range error and pulse width error at low altitudes in the presence of the solar background are insensitive to the solar background, even at aphelion, where the solar backscatter is strong. Therefore we ignore this impact in our study.

5. IN-FLIGHT PERFORMANCE EVALUATION: RESULTS

5.1 BELA in-orbit measurement error

5.1.1 Time of flight measurement errors

Table 5.1 and figures 5.1 and 5.2 show the main components of the simulated TOF measurement errors computed as described in section 4.1 for several assumptions about the pointing uncertainty and calibration. It can be clearly seen that the error caused by pointing uncertainty is the dominating part of range measurement error. The results of TOF measurements in different condition are summarized in table 5.2. A major improvement can be done on TOF measurement by the calibration of pointing uncertainties. But there is no huge improvement done on by removing the systematic bias of the instrumental noise.

5.1.2 Pulse width and pulse energy measurement errors

Table 5.3 and figures 5.4 and 5.3 show the pulse width and pulse energy measurement errors due to different error sources. If no systematic bias removal is performed, the dominating part is the instrumental error. So the key parameter in determining the pulse width is the systematic bias on instrumental error and whether it can be removed or not. Table 5.4 show the total accuracy with and without the systematic biases.

Tab. 5.1: Components of TOF (range) measurement error

| Component of error | Condition | RMS error |
|--------------------------------|-----------------------------------|------------------|
| Caused by the surface slope | | 1.33 ns (0.20 m) |
| Caused by the roughness | | 1.6 ns (0.24 m) |
| Instrumental errors | Before removal of systematic bias | 2.2 ns (0.33 m) |
| | After removal of systematic bias | 1 ns (0.15 m) |
| Caused by pointing uncertainty | 15 arc sec. | 29.4 ns (4.41 m) |
| | 7.5 arc sec. | 18.3 ns (2.75 m) |
| | 3 arc sec. | 9.2 ns (1.38 m) |

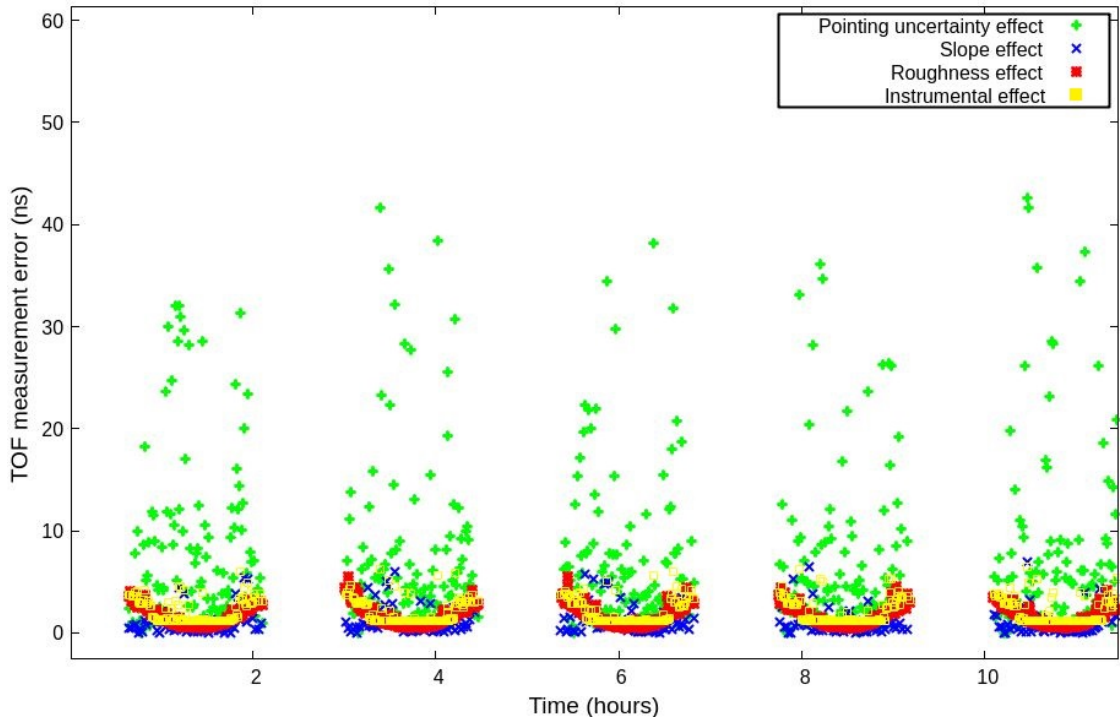


Fig. 5.1: Time of flight measurement error (pointing uncertainty is 3 arc sec.). Gap in data is due to the high PFD

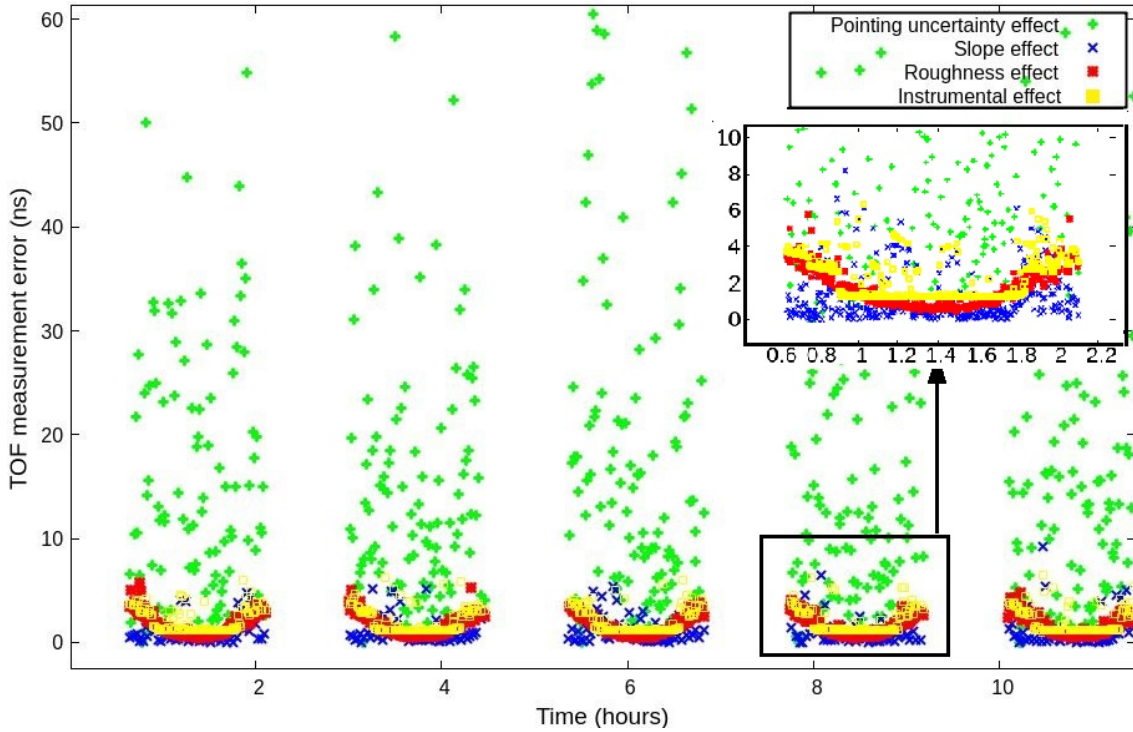


Fig. 5.2: Time of flight measurement error (pointing uncertainty is 15 arc sec.). Gap in data is due to the high PFD

Tab. 5.2: BELA TOF measurement total error

| Measurement condition | total TOF RMS error |
|---|---------------------|
| Pointing uncertainty = 15 arc seconds Before removal of systematic bias | 29.5 ns |
| Pointing uncertainty = 7.5 arc seconds Before removal of systematic bias | 18.4 ns |
| Pointing uncertainty = 3 arc seconds Before removal of systematic bias | 10.2 ns |
| Pointing uncertainty = 3 arc sec. + Removal of systematic bias | 9.4 ns |

Tab. 5.3: Components of pulse width (FWHM) measurement error

| Component of error | Condition | RMS error |
|--------------------------|-----------------------------------|-----------|
| Due to the surface slope | - | 2.45 ns |
| Due to roughness | - | 3.0 ns |
| Instrumental error | Before removal of systematic bias | 11.5 ns |
| | After removal of systematic error | 3.0 ns |

Tab. 5.4: BELA pulse energy and pulse width measurement errors

| Measurement | Measurement condition | RMS error |
|--------------------|------------------------------------|-----------|
| Pulse width (FWHM) | Before removal of systematic error | 11.9 ns |
| | After removal of systematic error | 4.9 ns |
| Pulse energy | Before removal of systematic error | 35 % |
| | After removal of systematic error | 20 % |

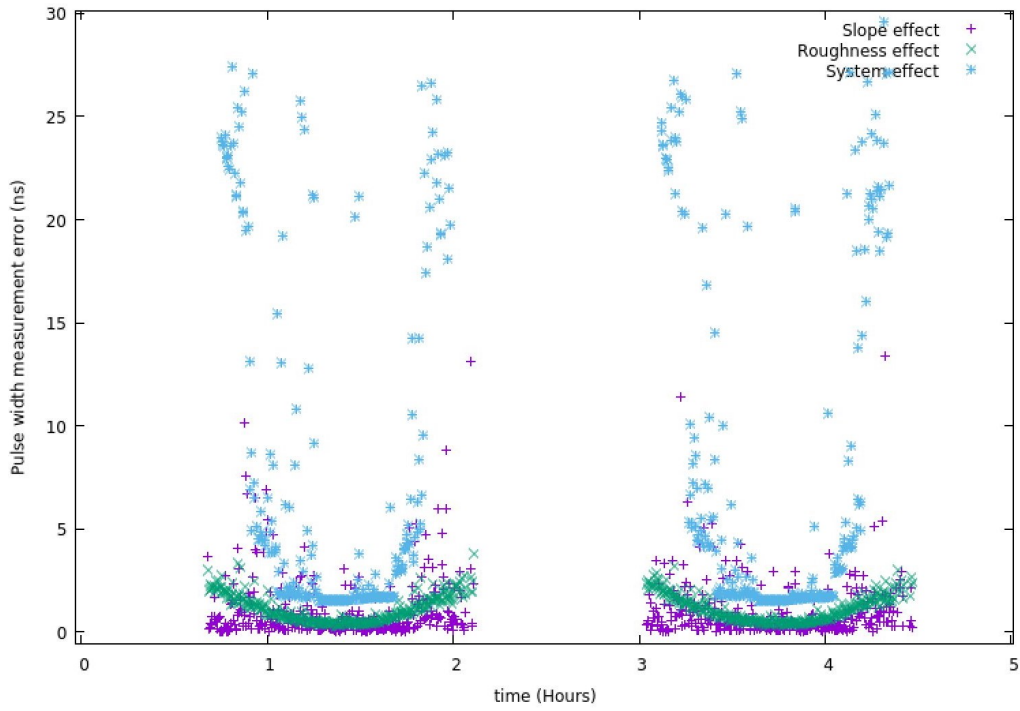


Fig. 5.3: Pulse width measurement error (Before removal of systematic error). Gap in data is caused by the high PFD

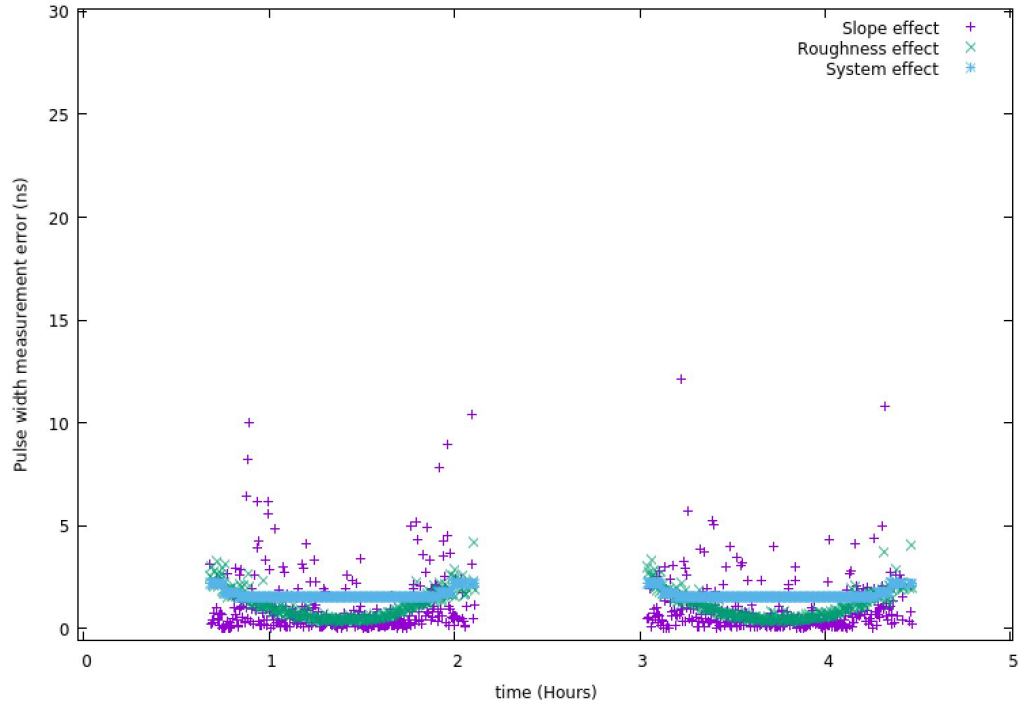


Fig. 5.4: Pulse width measurement error (After removal of systematic error). Gap in data is caused by the high PFD

Tab. 5.5: Predicted instrument working limit with high APD-A gain based on different degradation levels (BOL: Beginning of life, EOL: end Of Life).; Green: Meet/better than the requirement; yellow: Sometimes not meet the requirement; Red: Not meet the requirement

| Region | BOL | EOL | | |
|---------------------|----------------|-----------------|--------------------|------------------|
| | No degradation | Low degradation | Medium degradation | High degradation |
| Over smooth plains | 1260 km | 1180 km | 1125 km | 1060 km |
| Over rough terrains | 1200 km | 1145 km | 1090 km | 1040 km |
| Over crater walls | 700-1050 km | 670-1000 km | 640-950 km | 615-890 km |

Tab. 5.6: Predicted instrument working limit with low APD-A gain based on different degradation levels (BOL: Begin Of Life; EOL: End of life)

| Region | BOL | EOL | | |
|---------------------|----------------|-----------------|--------------------|------------------|
| | No degradation | Low degradation | Medium degradation | High degradation |
| Over smooth plains | 1100 km | 1050 km | 985 km | 925 km |
| Over rough terrains | 980 km | 940 km | 900 km | 850 km |
| Over crater walls | 575-900 km | 550-850 km | 530-810 km | 500-760 km |

5.2 Expected instrument coverage

We determine the coverage of the instrument by checking the PFD for each measurement. We simulate the pulse detection algorithm and the process performed by BELA to detect the pulse. This simulation environment can predict the PFD of a specific return pulse in a specific noise environment (See section 3). On top of the calculated PFD, we add the impact of degradation on the receiver optical subsystem transmission and the laser power, which finally leads to a decrease in return pulse amplitude and signal to noise ratio.

Surface slope and roughness both cause a broadening on the return pulse width. In smooth plains the broadening of the return pulse has the smallest value, while crater walls cause the largest broadening because of the highest slope angles. As spacecraft is not in circular orbit, the broadening varies with altitude because of the footprint size.

Figure 5.5 shows the return pulse width against spacecraft altitude for different types of terrains, while figure 5.6 shows the detectable pulses (PFD lower than 10 %) at different altitudes and return pulse widths. These plots are generated assuming the instrument gain code to be 7 and APD-A gain to be 1.5 MV/W (see section 1.5) and also assuming a low instrument degradation.

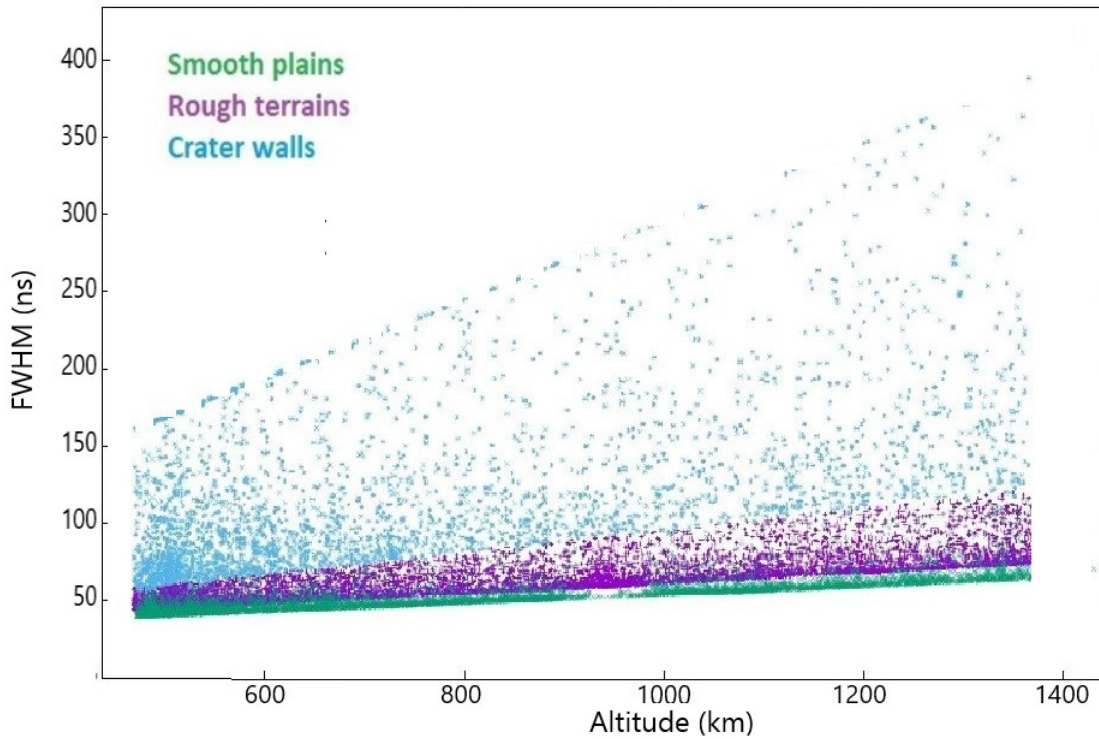


Fig. 5.5: The FWHM of the return pulse as a function of altitude for different terrain types; Green: over a smooth plain; Purple: over a rough terrain; Blue: over a crater wall

One can conclude that with high APD-A gain, the smooth plains can be covered up to an altitude of 1180 km, rough terrains can be covered up to an altitude of 1145 km. Some shallow crater walls can be covered up to 1000 km but steep crater walls provide a reassurable return pulse if the spacecraft altitude is less than 670 km. The instrument can meet its ranging requirement for smooth plains and rough terrains even with the highest degradation.

On the other hand, with lower APD-A gain of 0.75 MV/W and with low degradation, the smooth plains can be covered up to 1050 km and the requirement can be met, but over the other terrains or with higher degradation the maximum working limit of the instrument would be below the requirement. Figures 5.7 to 5.14 show the average PFD over the entire surface of the planet for beginning of the mission and end of the extended mission for both APD-A gains of 1.5 MV/W and 0.75 MV/W . One can see that as a result of the MPO orbit evolution (see section 1.3 and figure 1.4) at the end of 2-year mission, the altitude of spacecraft over the North Pole is higher and therefore the average PFD has higher values in the northern hemisphere. The same applies to the southern hemisphere where due to the lower altitude of spacecraft at the

end of mission, the average PFD is also lower.

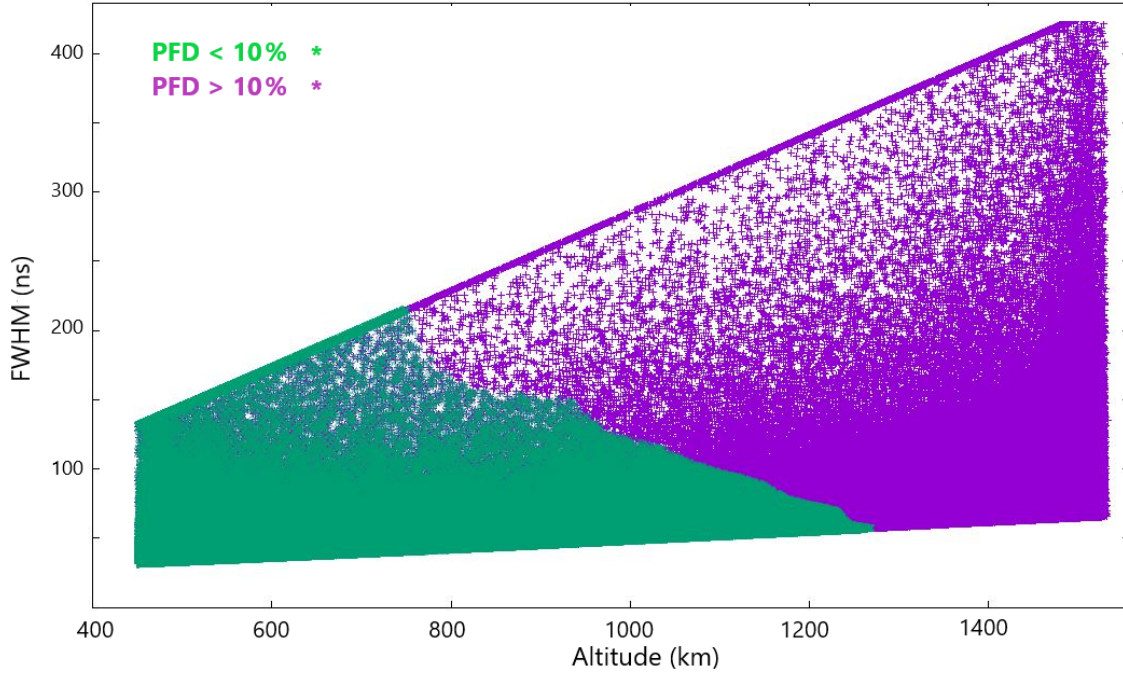


Fig. 5.6: The range of altitude and return pulse width that make the pulse detectable ($PFD < 0.1$)

5.2.1 The impact of degradation on the coverage

Tables 5.5 and 5.6 provide the working limit of the instrument over different terrain types and in different degradation levels for high and low APD-A gains. Because of the wide range of slope angles on the crater walls, the working limit of the instrument over this type of terrain is shown in a range. The first value on this range corresponds to the steep (>30 deg) and the second value corresponds to the shallow (<15 deg) crater walls. One can notice that the impact of degradation decreases the working limit of the instrument by 50 km (for low degradation) to 150 km (for high degradation).

5.2.2 The impact of local albedo on the coverage

The above PFD and coverage is assuming a constant value of 0.19 for the surface albedo all over the planet's surface. Moreover, the local reflectance can vary between 4 % to around 50 % [Gouman, 2015]. This means that when the PFD is zero, there is still a chance of having a false detection caused by the low reflectivity of the surface at the laser spot. The return pulse energy as a function of spacecraft altitude and local reflectance is given by equation 1.2. In this

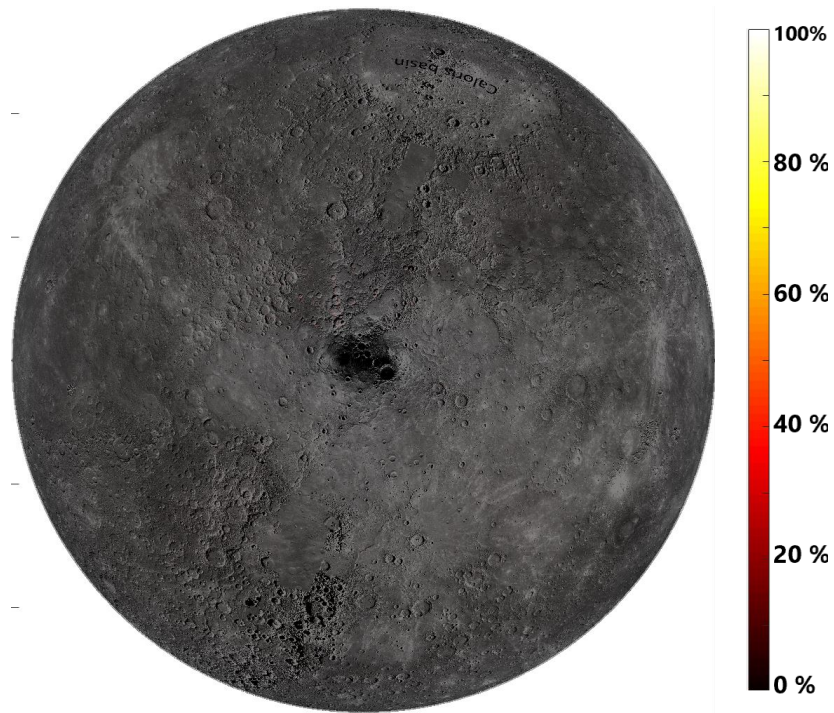


Fig. 5.7: Average probability of false detection at the beginning of mission over Mercury's northern hemisphere (APD-A gain = 1.5 MV/W, Low degradation)

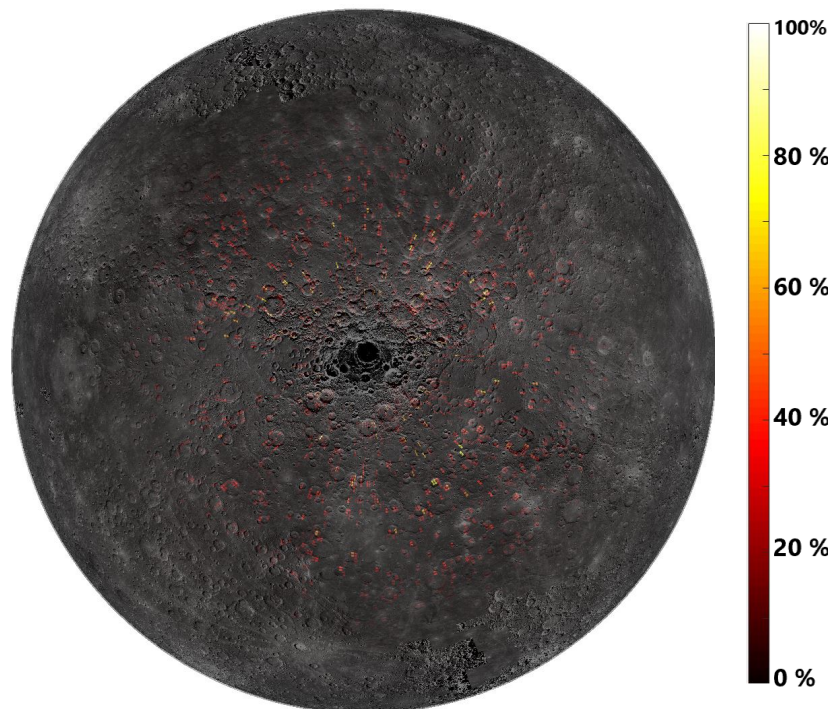


Fig. 5.8: Average probability of false detection at the beginning of mission over Mercury's southern hemisphere (APD-A gain = 1.5 MV/W, Low degradation)

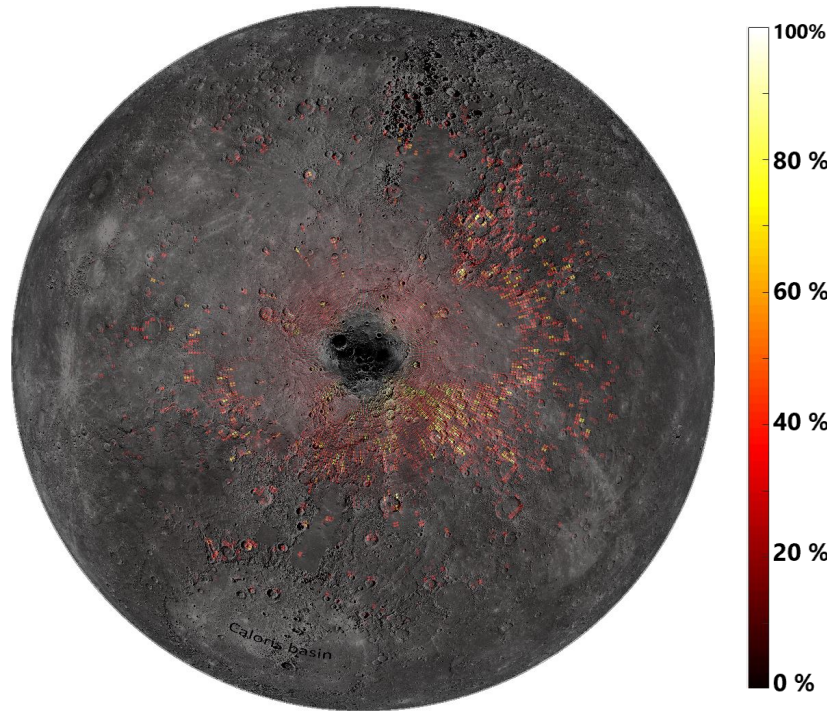


Fig. 5.9: Average probability of false detection at the end of extended mission over Mercury's northern hemisphere (APD-A gain = 1.5 MV/W, Low degradation)

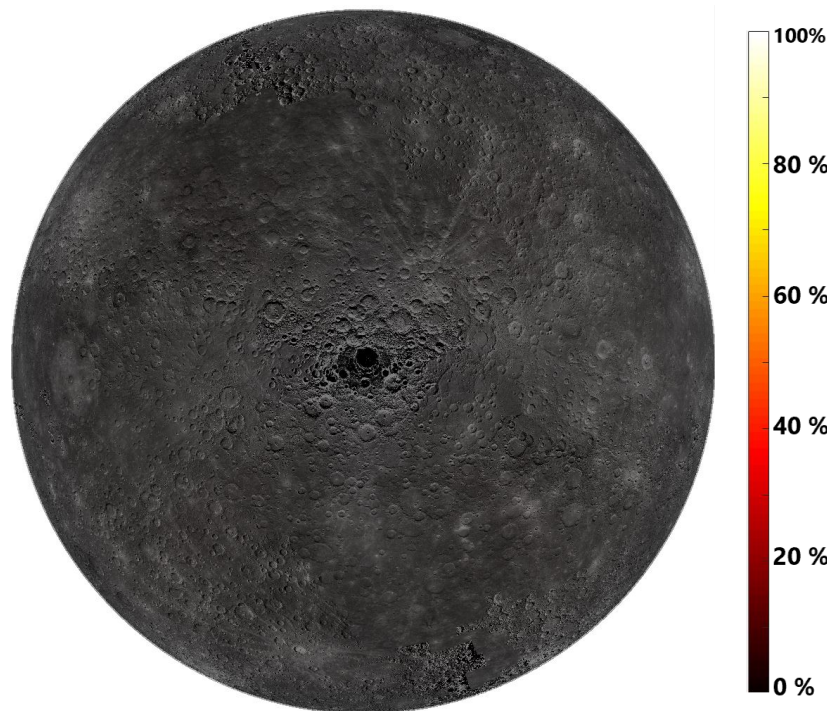


Fig. 5.10: Average probability of false detection at the end of extended mission over Mercury's southern hemisphere (APD-A gain = 1.5 MV/W, Low degradation)

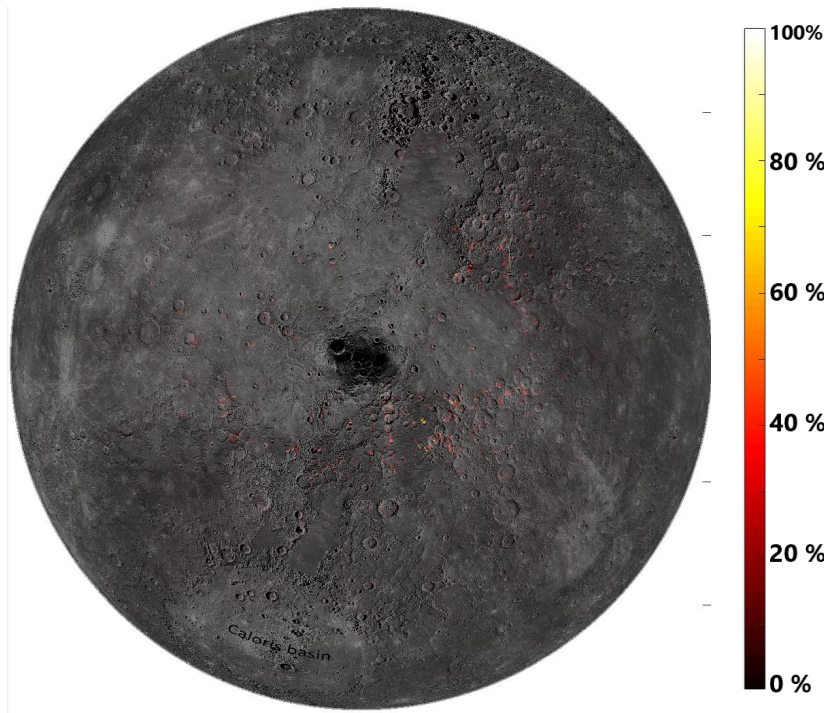


Fig. 5.11: Average probability of false detection at the beginning of mission over Mercury's northern hemisphere (APD-A gain = 0.75 MV/W, Low degradation)

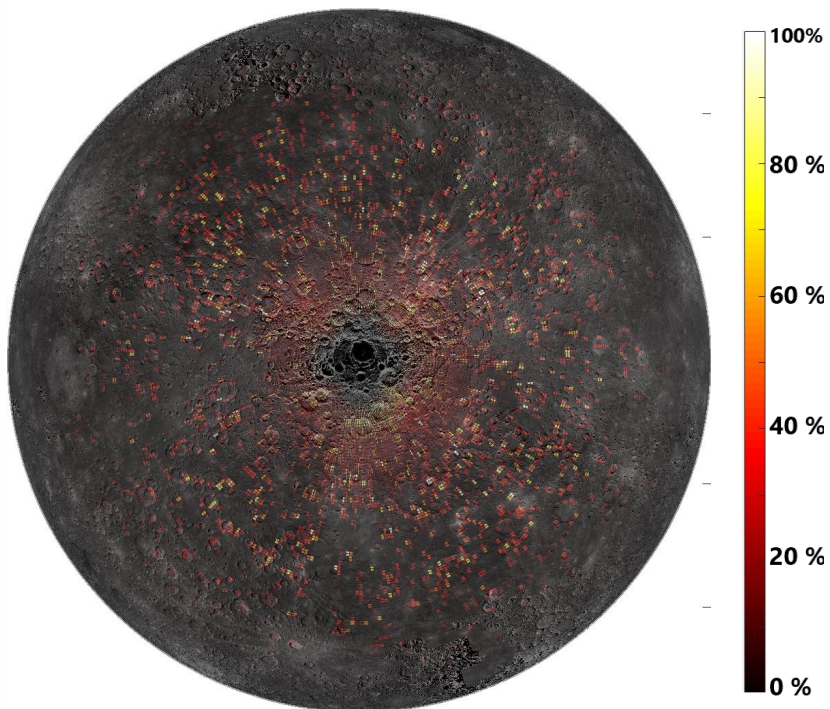


Fig. 5.12: Average probability of false detection at the beginning of mission over Mercury's southern hemisphere (APD-A gain = 0.75 MV/W, Low degradation)

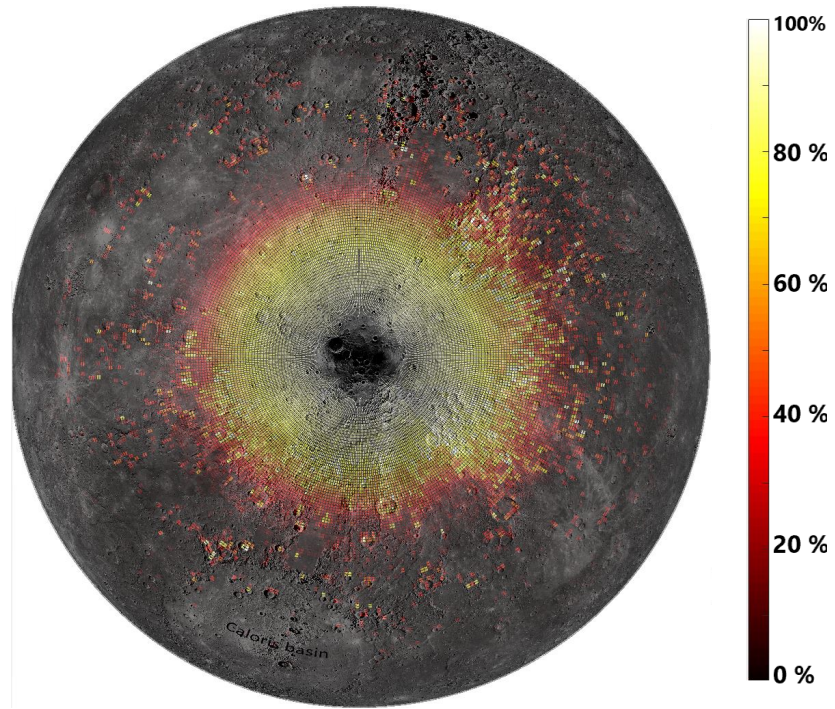


Fig. 5.13: Average probability of false detection at the end of extended mission over Mercury's northern hemisphere (APD-A gain = 0.75 MV/W, Low degradation)

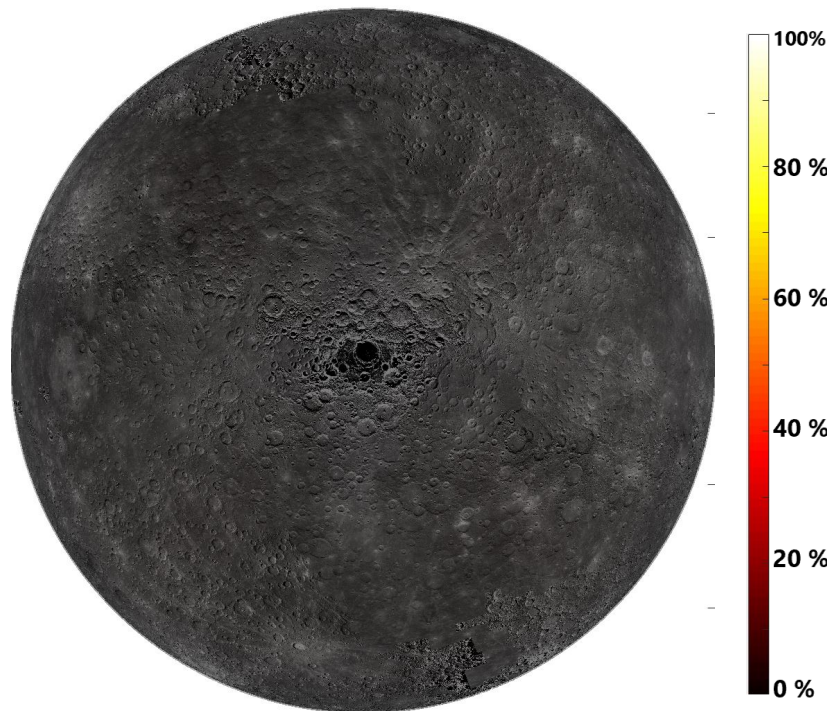


Fig. 5.14: Average probability of false detection at the end of extended mission over Mercury's southern hemisphere (APD-A gain = 0.75 MV/W, Low degradation)

equation, E_T , T_r and r_R are instrumental parameters and we assume them as fixed values. As the minimum detectable pulse energy E_{Rmin} is a constant value, one can write that ρ/z_{wl}^2 is constant for the minimum detectable pulse energies. z_{wl} is the maximum working limit of the instrument. This altitude corresponds to the critical (minimum detectable) pulse energy, where the PFD of the return signal reaches 10%.

We take into account that the local albedo, ρ , can differ from $\rho_0 = 19\%$. The real working limit of the instrument can be written as

$$z_{wl_{real}} = z_{wl_0} \cdot \sqrt{\rho/\rho_0} = z_{wl_0} \cdot \sqrt{\rho/0.19} \quad (5.1)$$

Where z_{wl_0} is the working limit of spacecraft when the albedo is assumed to be 19 % and ρ is the real local albedo. In figure 5.15 the real working limit of the spacecraft is plotted against the local albedo for different terrains. Over an area with the lowest reflectivity, the instrument would not be able to work higher than 550 km even over a smooth plain. On the other hand, with highest local reflectivity, the real working limit of the instrument could reach 2000 km for smooth plains and a return pulse from the steepest crater wall could be detected up to an altitude of 1200 km. These considerations should be applied to the expected coverage, as soon as there is an accurate reflectance map available for the planet.

5.3 Expected performance in measuring surface features

5.3.1 Topography measurement accuracy

The horizontal resolution of the topography measurement depends on the proximity of laser spots on the planet surface at the end of mission. The laser spot size changes with the spacecraft altitude. It has a size of 24 m to 66 m depending on the spacecraft altitude. The consecutive spot to spot distance is 245 m at 480 km and it decreases to 174 m at the altitude of 1050 km. The laser spots in two adjacent orbits are separated by 25 km at the equator, crossing at the poles. But the distance between tracks decrease at the end of the mission lifetime. At the EOL, the accumulated measurements are expected to be 6 km apart at the equator as a results of multiple passes and orbital phasing.

The accuracy of the elevation recovery at the laser spot is equal to the total range error (Table 5.7). As described in section 5.1, the key parameter here is the pointing uncertainty. The vertical accuracy with 15 arc sec pointing uncertainty is expected to be around 4.4 meters ($1 - \sigma$). If we assume the pointing uncertainties to be half this value (7.5 arc sec) the vertical accuracy will improve to 2.8 meters and if we assume the pointing error to be 3 arc sec, the total local height accuracy of DTM will be around 1.5 meters.

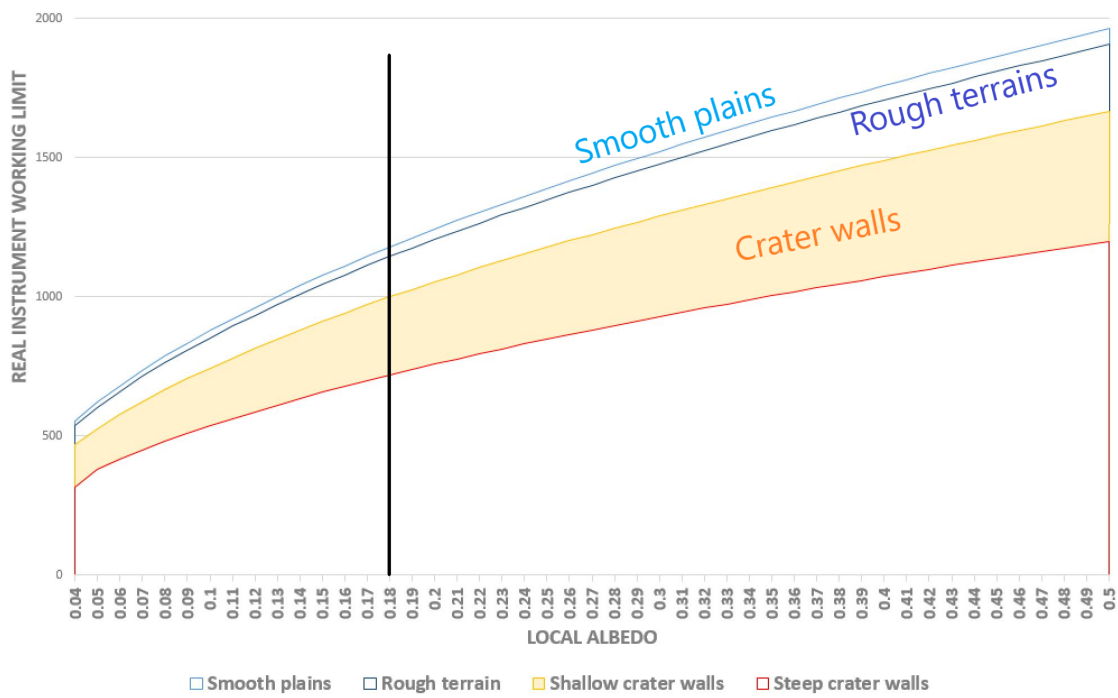


Fig. 5.15: Real instrument working limit as a function of local reflectance of the surface for different terrains, the vertical bar shows the average albedo

Tab. 5.7: Instrument performance in local height measurement

| Measurement | Pointing uncertainty | systematic removal | RMS error |
|-------------|----------------------|--------------------|-----------|
| Height | 15 arc seconds | No | 4.4 m |
| | 7.5 arc seconds | No | 2.8 m |
| | 3 arc seconds | No | 1.5 m |
| | 3 arc seconds | Yes | 1.4 m |

Tab. 5.8: Regional performance in local height measurement

| Measurement | Condition | RMS error | | |
|-------------|-----------------|---------------|----------------|--------------|
| | | smooth plains | rough terrains | crater walls |
| Height | 15 arc seconds | 1.55 m | 2.15 m | 8.70 m |
| | 7.5 arc seconds | 1.05 m | 1.40 m | 5.40 m |
| | 3 arc seconds | 0.65 m | 0.8 m | 2.70 m |

The accuracy of the elevation recovery will be different at different latitudes and also over different terrain types (Table 5.8). The most accurate range measurements would be collected over smooth plains, with a RMS of 0.65 to 1.50 meters (depending on the pointing uncertainty). Over the rough terrains, we expect an accuracy of 0.80 to 2.15 meters, while over crater walls we expect larger RMS of 2.70 to 8.70 meters, depending on the pointing uncertainty.

The accuracy of the orbit using radio science data is predicted by Marabucci [2012] and is shown in table 5.9. According to this study the radial component is negligible with respect to the radial error on altimetry given in Table 5.7.

Figures 5.16 and 5.17 show the instrument performance map in local height measurements over the entire surface of the planet and figure 5.18 shows the same performance over a smaller

Tab. 5.9: Position formal uncertainties after Doppler orbit reconstruction using multi-arc approach [Marabucci, 2012]

| Formal uncertainties | R (m) | T (m) | H (m) |
|----------------------|--------|--------|--------|
| | 0.0476 | 13.377 | 16.772 |

area around the North Pole. It can be seen that over the smooth plains, the instrument has the best accuracy. The accuracy gets worse over cratered areas and the worst accuracy happens over crater walls.

5.3.2 Performance in measuring the surface slope

There are two ways for determining the surface slope from laser altimetry data. The first method is to calculate the slope by dividing the height difference of two consecutive shot by distance between the spots (double shot slope measurement). The second method is to determine the slope inside the laser slope by using the width of the return pulse (single shot slope measurement).

According to [Gardner \[1992\]](#) the accuracy of double shot slope measurements can be calculated from the following equations.

$$Var(\tan S) = \frac{2F}{N(\Delta x)^2} [Var(\Delta\xi) + z^2(\tan S)^2(\tan \theta_t)^2 + Var(\Delta\phi)] \quad (5.2)$$

And the accuracy of single shot slope measurement can be calculated from:

$$Var(\tan S) = \frac{F}{2N} [(\tan S)^2 + (\tan \theta_t)^2 + \frac{Var(\Delta\xi)}{z^2(\tan \theta_t)^2}] \quad (5.3)$$

To predict the error with the "single shot" method, one can use the suggested equation in [Gardner \[1992\]](#). But instead we calculate directly the slope error from the broadening of the return pulse using the equations 4.4 to 4.10. Using this approach has two advantageous: First, the impact of low-pass filtering, which causes larger errors on slope measurement on smaller slopes, is not taken into account in Gardner's equation. Second, we can distinguish between negative errors and positive errors on the slope measurement, which are different over smaller slope angles. Since the absolute slope angle cannot be smaller than zero, the negative error on slope measurement cannot be bigger than the slope angle itself.

Table 5.10 provides the accuracy of these measurements with different methods and with different assumptions. Figure 5.19 shows the single shot measurement errors (positive and negative) in different surface slopes. These errors are calculated from the direct measurement of pulse broadening. In smaller slope angles, the negative error goes to zero, while the positive side of error reaches higher values with RMS of 7.7 degrees. With the increase of slope angle, the RMS of this error decreases to a minimum value of 1.8 degrees.

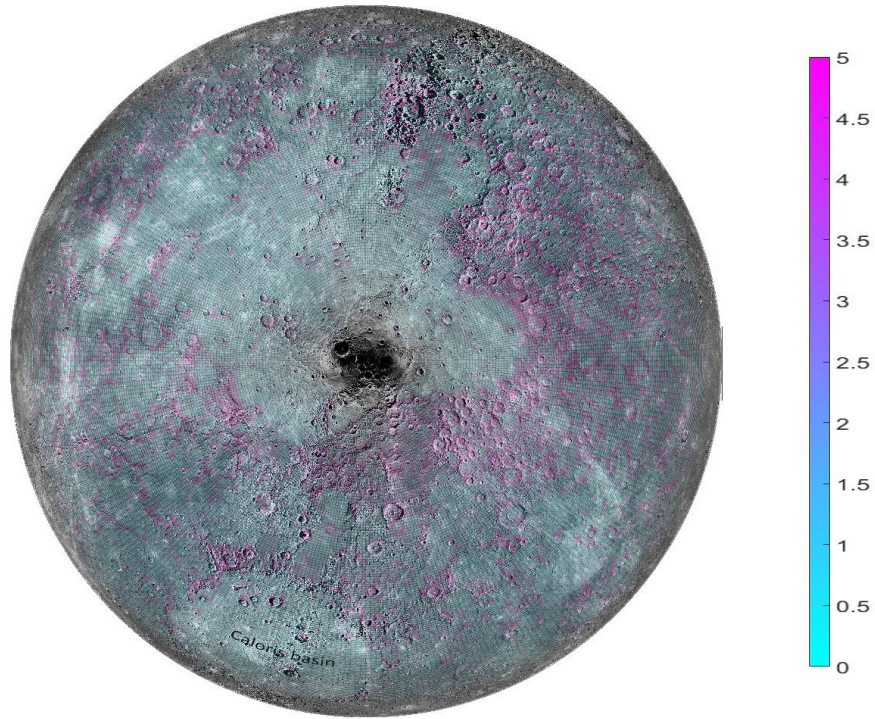


Fig. 5.16: Local height measurement error over Mercury's northern hemisphere (m)

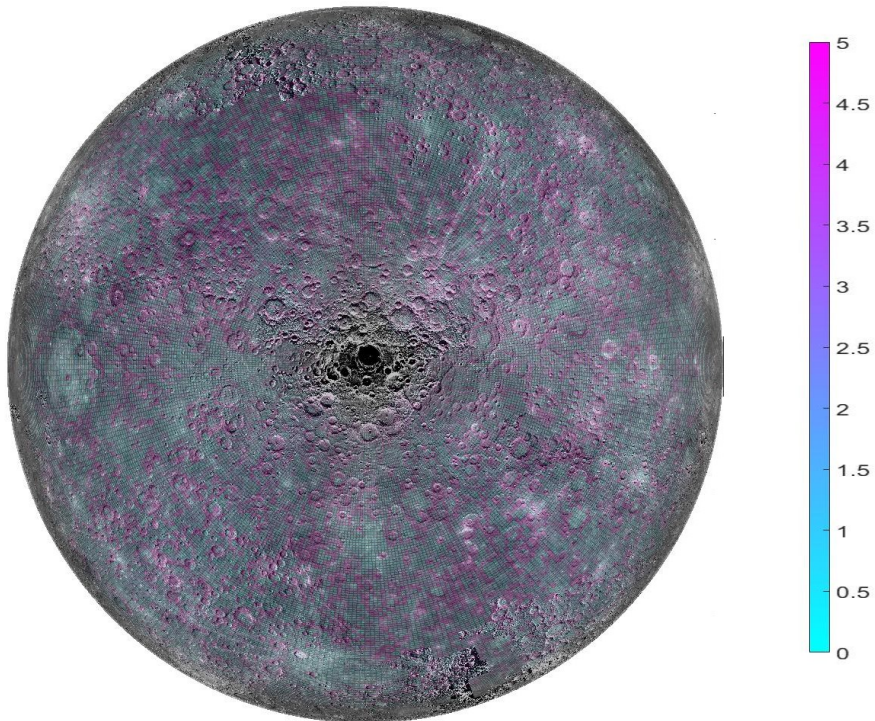


Fig. 5.17: Local height measurement error over Mercury's southern hemisphere (m)

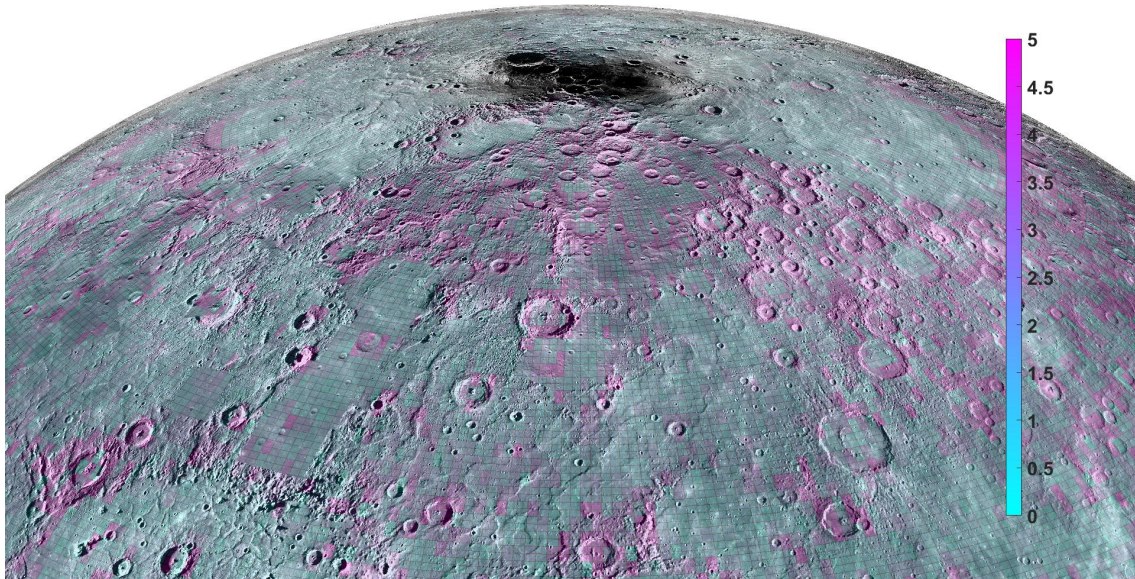


Fig. 5.18: Local height measurement error over the North Pole (m)

Figure 5.20 provides the same errors with an assumption that a priori knowledge of roughness is available. By comparison to figure 5.19, it can be seen that the slope measurement error is always lower if a priori knowledge of roughness is available. As can be seen in figure 5.20, the positive measurement error in small slope angles has a RMS of 3 degrees, while the negative error is close to zero. In larger slope angles the negative error goes up but it cannot be larger than the slope angles itself.

Figure 5.21 compares the average value of positive and negative errors calculated from the broadening of the return pulse in figure 5.20 with the same error calculated using the suggested equation in Gardner [1992]. In the small slope angles, the Gardner's equation predicts smaller errors, but over the higher slope angles, both approaches predict the same error RMS. The accuracy of double shot slope measurement is always better than one degree, while the single shot method leads to average accuracies between 1.2 to 3.8 degrees.

Figures 5.19 and 5.20 are plotted for the altimetry observations with low PFD. Considering all the observations, including the ones with high PFD, we see another increase in RMS error at larger slope angles (see the red dots in figure 5.21).

The other conclusion that can be drawn is that with single shot method and no a priori knowledge of roughness, the slopes smaller than 5-6 degrees are hard to detect. The reason is

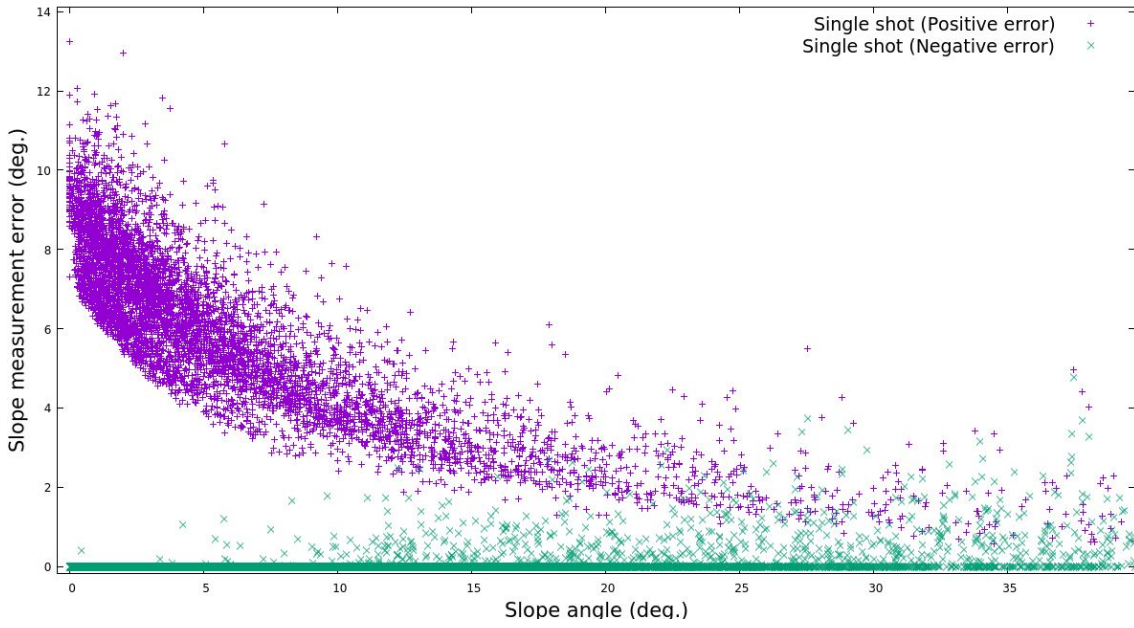


Fig. 5.19: Single shot slope measurement error in different slope angles (Assumption: no knowledge of local roughness is available)

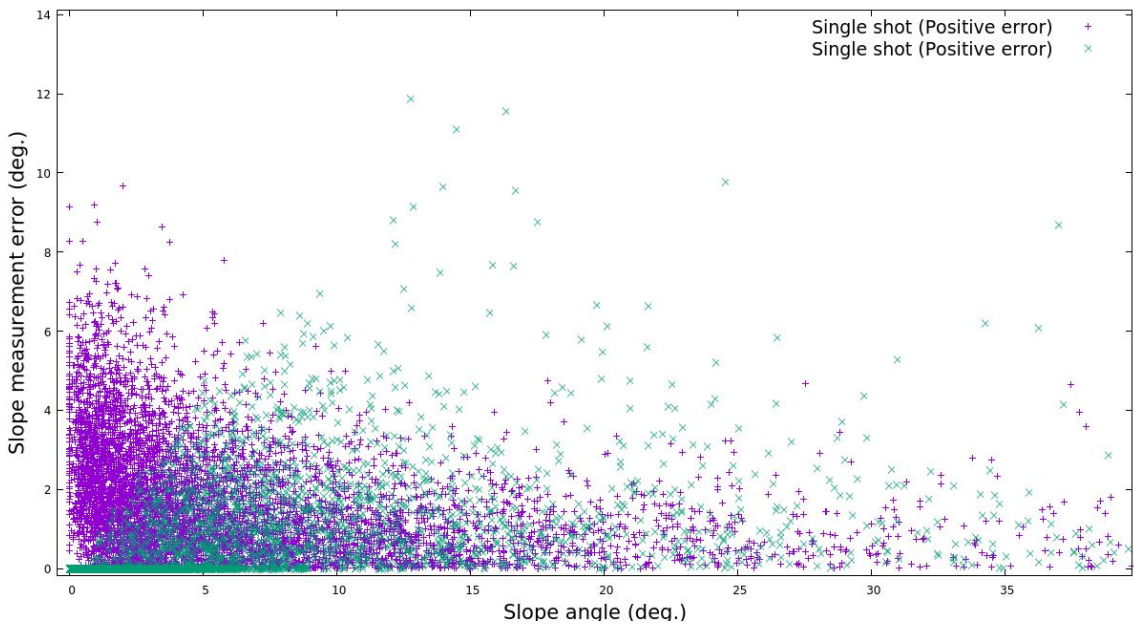


Fig. 5.20: Single shot slope measurement error in different slope angles (Assumption: a priori knowledge on local roughness is available)

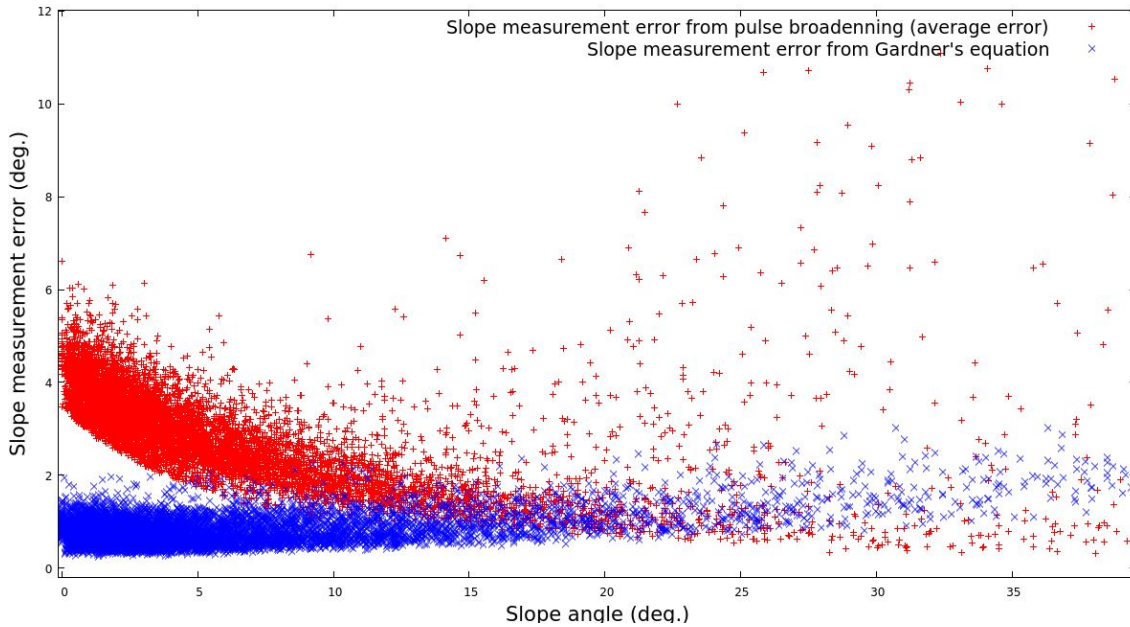


Fig. 5.21: Slope measurement average error compared to the measurement error from suggested equation in Gardner [1992]

that the amplitude of error at slope angles smaller than 5-6 degrees are as big as the slope itself.

5.3.3 Performance in measuring the surface roughness

The surface slope and roughness both cause a broadening in the return signal and there is no straight forward way to differentiate between them. One approach is to use the double shot method for measuring the surface slope and then use the pulse broadening to determine the roughness assuming that the slope inside the laser spot is constant. The other possible approach would be to have a priori knowledge on either slope or roughness and use the pulse

Tab. 5.10: Instrument performance in measurement of surface slope and roughness

| Measurement | Condition | STD error |
|---------------------|---------------------------------|-----------|
| Slope (single shot) | No knowledge of roughness | 3.1 deg |
| | a priori knowledge of roughness | 2.0 deg |
| Slope (double shot) | 15 arc seconds pointing error | 0.16 deg |
| | 3 arc seconds pointing error | 0.11 deg |
| Roughness | No priori knowledge of slope | 1.7 m |
| | Local slope as a priori | 0.45 m |

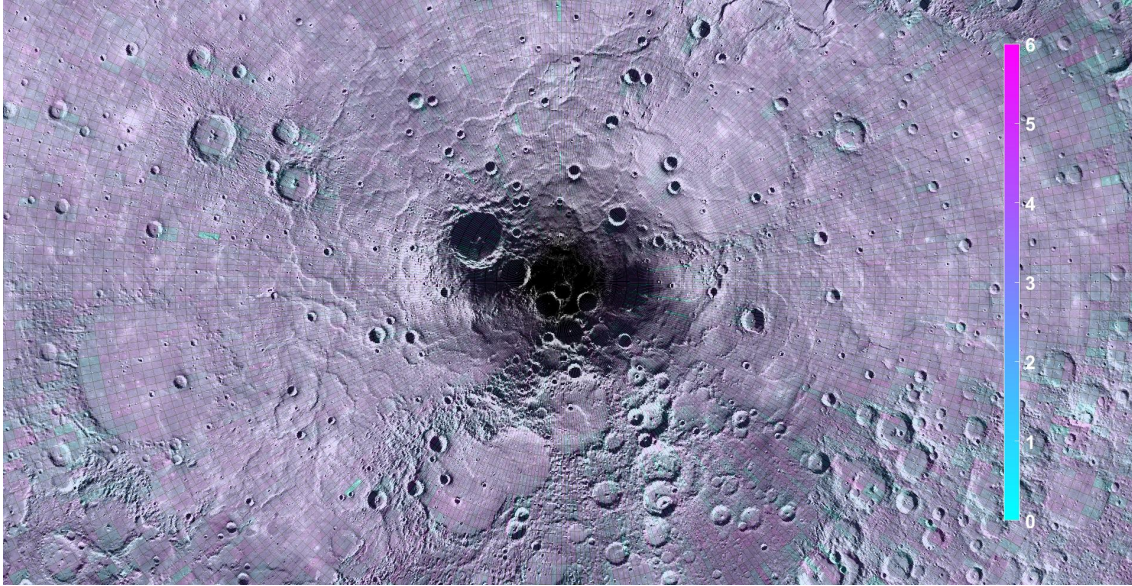


Fig. 5.22: Single shot slope measurement error over the North Pole of the planet (deg)

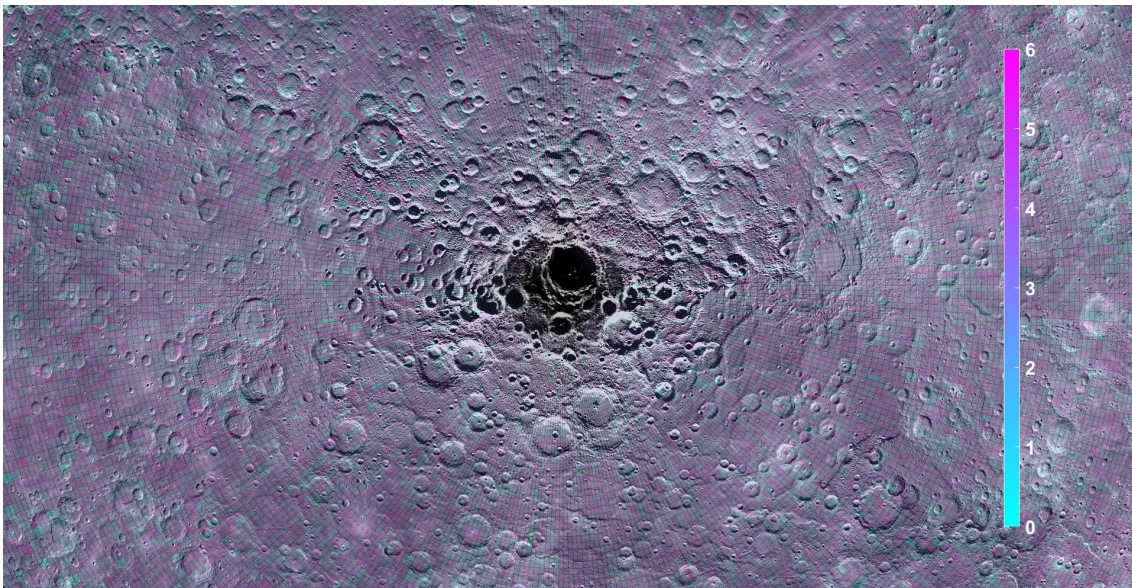


Fig. 5.23: Single shot slope measurement error over the South pole of the planet (deg)

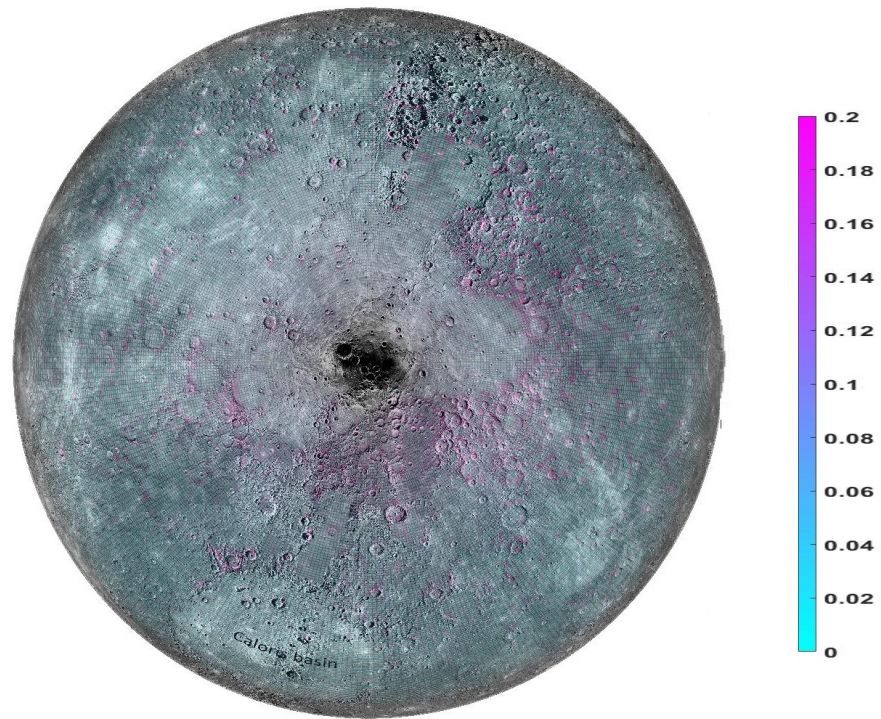


Fig. 5.24: Double shot slope measurement error over Mercury's northern hemisphere (deg)

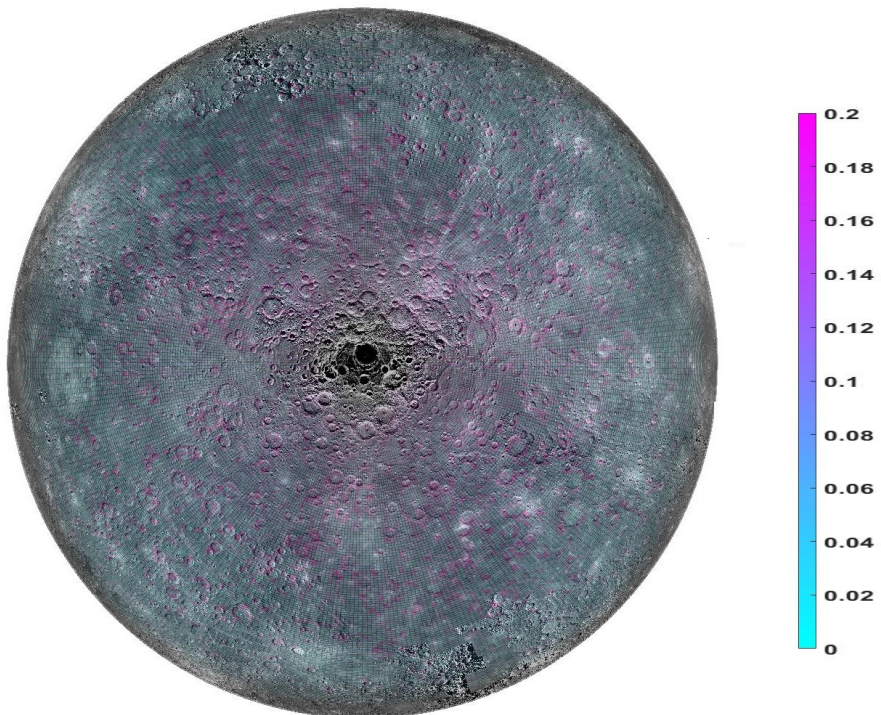


Fig. 5.25: Double shot slope measurement error over Mercury's southern hemisphere (deg)

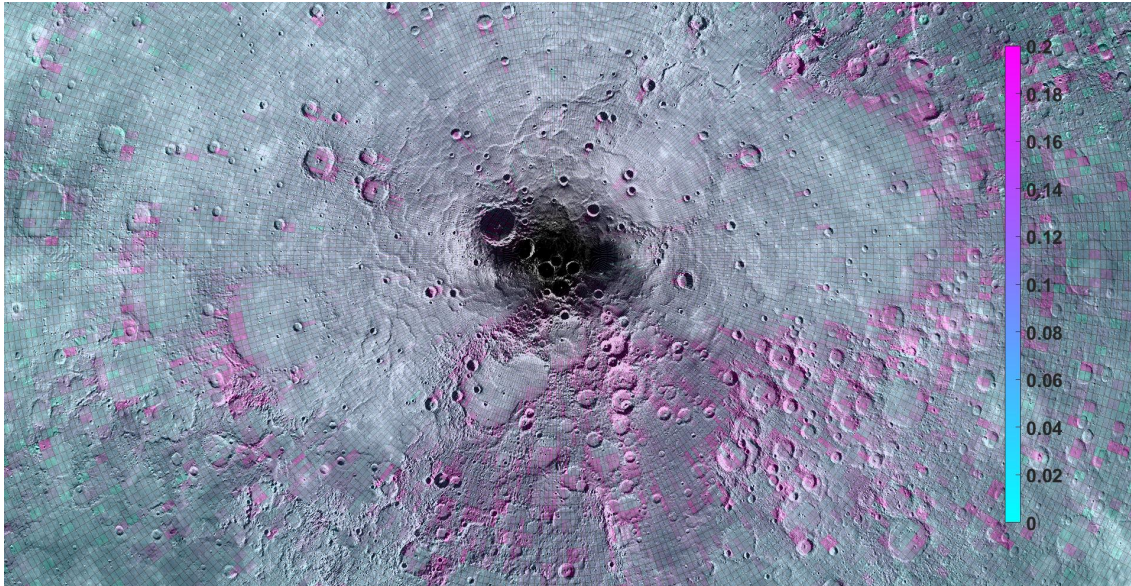


Fig. 5.26: Double shot slope measurement error over the North Pole (deg)

broadening to calculate the other variable.

Table 5.10 provides the accuracy of the roughness measurements for both the conditions that a priori information on slope is available or that it is not. This means that depends on how accurate we can predict the slope angles, the roughness measurement will have a RMS error of 0.45 up to 1.7 m. Figure 5.27 also shows the same accuracy over surfaces with different slope angles.

Figures 5.23 to 5.26 and tables 5.11 and 5.12 provide more information on the distribution of slope and roughness measurement errors over different regions and terrains of the planet. For instance one can clearly see that the single shot slope measurement accuracy is better over crater walls and worse over smooth plains, while the double shot slope measurement has better accuracy over plains and flat surfaces. Knowing this, we recommend to use a combination of both approaches to determine the slope angles over the surface of the planet.

Also, all the different slope measurement approaches have better accuracy in the equatorial regions when compared to north and South poles. For example, the double shot slope measurement has a very good accuracy of 0.08 deg over the equatorial region. At the beginning of life the accuracy of slope measurement is better over the North Pole due to lower altitude of the spacecraft, while at the end of life, the accuracy over the South pole is better.

Tab. 5.11: Regional performance in slope and roughness measurement

| Measurement | RMS error | | |
|--|---------------|----------------|--------------|
| | smooth plains | rough terrains | crater walls |
| Slope (single shot-No roughness knowledge) | 3.2 deg | 3.6 deg | 1.6 deg |
| Slope (single shot-Roughness as a priori) | 2.0 deg | 2.2 deg | 1.4 deg |
| Slope (double shot-15" pointing error) | 0.12 deg | 0.14 deg | 0.24 deg |
| Slope (double shot- 3" pointing error) | 0.10 deg | 0.11 deg | 0.12 deg |
| Roughness (No knowledge of slope) | 0.42 m | 0.52 m | 3.5 m |
| Roughness (Slope as a priori info) | 0.32 m | 0.32 m | 0.8 m |

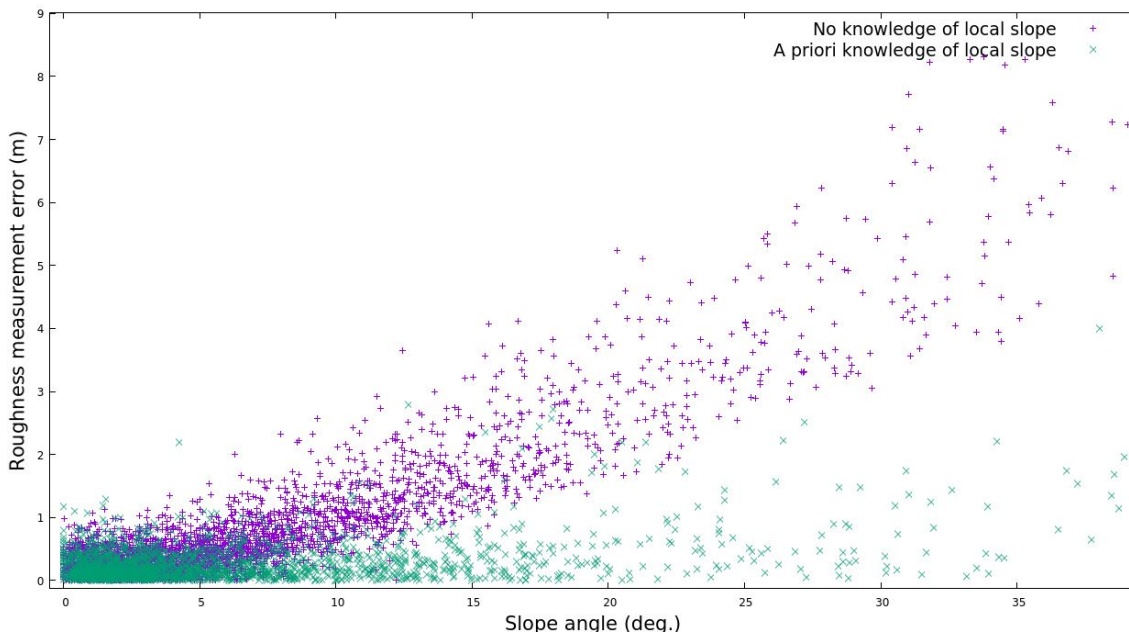


Fig. 5.27: Roughness measurement error in different slope angles

5.3.4 Albedo measurement performance

The local albedo can be directly calculated from the received pulse energy. A bias observed on the measured pulse energy (details in section 2), can cause a systematic error on the albedo measurement. Table 5.13 provides the errors of the albedo measurement ($\delta\alpha$) before and after removal of systematic bias.

Tab. 5.12: Regional performance in slope and roughness measurement (BOL condition)

| Measurement | RMS error | | |
|--|-------------------|------------|------------|
| | Equatorial region | North pole | South pole |
| Slope (single shot-No roughness knowledge) | 3.1 deg | 3.2 deg | 3.9 deg |
| Slope (double shot-15" pointing error) | 0.08 deg | 0.18 deg | 0.22 deg |
| Slope (double shot- 3" pointing error) | 0.04 deg | 0.14 deg | 0.15 deg |
| Roughness (No knowledge of slope) | 1.8 m | 085 m | 1.45 m |
| Roughness (Slope as a priori info) | 0.45 m | 0.4 m | 0.5 m |

Tab. 5.13: Instrument performance in measurement of absolute albedo ($\alpha_{real} = \alpha_{measured} \pm \delta\alpha$)

| Measurement | Condition | RMS error |
|-----------------------------------|-----------------------------------|-----------|
| Surface albedo ($\delta\alpha$) | Before removal of systematic bias | 7 % |
| | After removal of systematic bias | 4 % |

5.3.5 The impact of instrument degradation

The effect of degradation on the instrument working limit is presented in section 4.3. Here we want to investigate the impact of degradation on the instrument measurement accuracy. Table 5.14 provides this effect in four situations: BOL situation with no degradation and EOL situation with three different levels of degradation. As it can be seen from this table, there is a very small impact (3% inferior in worst case scenario) on the measurement accuracy due to the degradation effects. Considering table 5.14 and table 5.5, one can conclude that the degradation effects will cause an earlier rise in the probability of false detection of the pulse and a lower working limit for the instrument, but if the pulse is detected, there is no major impact on the measurement accuracy as a result of the degradation.

Tab. 5.14: Predicted performance degradation of BELA instrument over its mission lifetime

| Measurement | Accuracy degradation | | |
|-------------------|----------------------|--------------------|------------------|
| | Low degradation | Medium degradation | High degradation |
| Local elevation | 0.8 % | 1.6 % | 2.4 % |
| Surface slope | 0.6 % | 1.2 % | 1.8 % |
| Surface roughness | 1 % | 2 % | 3 % |
| Local albedo | 0.1 % | 0.1 % | 0.2 % |

5.3.6 Performance sensitivity to Mercury average slope angle

In section 4.2 we mentioned that because of the absence of knowledge about the slopes at meter size baselines, we extrapolated the average slope angles at longer baselines to shorter baselines using a power function and we scale our slope model based on the predicted average slopes.

In reality, the power function might change in smaller slopes and as a result the average slope angles might be smaller than the predicted values. This will impact the results of the elevation recovery, slope and roughness measurement. Since we do not have any information on this, we continued to use one power function for the performance model. But, here we want to do a sensitivity study to find the impact of smaller slope values on our measurement accuracies.

Let us assume a break point at 100 meters for the slope extrapolation and then assume that average slope angle stays constant for baselines lower than this. This assumption is qualitatively similar to the slope-baseline function over the surface of Moon [Pommerol et al., 2012]. Using this assumption, the average slope angles will be around 3 degrees, instead of around 7 degrees in the main model. We repeat the performance analysis using this slope model to find the sensitivity of instrument to average slope angles. The results of this study can be found in table 5.15.

As expected, all the modelled measurement expected accuracies have smaller values with respect to the previous slope model, but the single shot slope measurement has a slightly higher error. The reason is that this measurement is less accurate at smaller slope angles. The biggest change here is in the elevation recovery, where we get around 33% smaller errors.

Tab. 5.15: Instrument performance when assuming a break point for surface slope extrapolation

| Measurement | Condition | STD error |
|---------------------|---------------------------------|-----------|
| Elevation recovery | Pointing error = 15" | 3.1 m |
| | Pointing error = 3" | 0.9 m |
| Slope (single shot) | No knowledge of roughness | 3.5 deg |
| | a priori knowledge of roughness | 2.2 deg |
| Slope (double shot) | 15 arc seconds pointing error | 0.14 deg |
| | 3 arc seconds pointing error | 0.11 deg |
| Roughness | No priori knowledge of slope | 1.05 m |
| | Local slope as a priori | 0.35 m |

Tab. 5.16: Instrument performance in ΔH measurement over crossover points

| Condition | Pointing uncertainty | Systematics removal | RMS error |
|-----------------------|----------------------|---------------------|-----------|
| Temporal proximity | 1.5" (Only jitter) | No | 1.22 m |
| | 1.5" (Only jitter) | Yes | 1.07 m |
| No temporal proximity | 15" | No | 6.2 m |
| | 7.5" | No | 4.0 m |
| | 3" | No | 2.1 m |
| | 3" | Yes | 2.0 m |

5.4 Height difference performance on crossover points

Crossovers points are locations where two altimetry ground tracks intersect (figure 6.13). It can be imagined as a differential measurement between two observations at the same location but at different times. Any difference in the height measurements δh at a crossover intersection is either caused by errors in the orbit or pointing reconstruction, interpolation errors of the surface topography between BELA footprints and/or any residual geophysical signal (*e.g.*, due to mismodelings of the planetary rotation).

According to Steinbrügge et al. [2018], the pointing error is one of the main sources of uncertainty in the crossover analysis. However, when the two intersecting tracks are close in time, only the error caused by the spacecraft pointing jitter [Casasco, 2017] should be accounted for.

Most of the pointing error is caused by deformation of the spacecraft optical bench, which is a very slow process. Since crossovers are a differential measurement, we assume this "quasi-

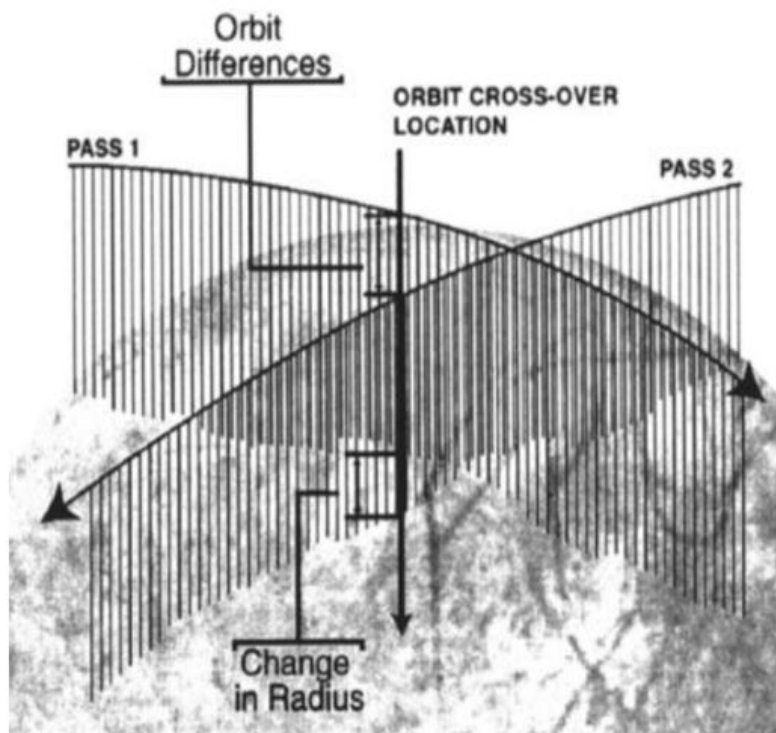


Fig. 5.28: Crossover point and discrepancies dR (Rowlands, 1999)

constant" component to be negligible over short timescales.

These considerations lead to an improved error budget for BELA crossover analysis (see Table 5.16), likely increasing its impact on both orbit determination and on the expected accuracy of its recovery of geophysical parameters (*e.g.*, tidal deformations) with respect to previous estimates [Marabucci, 2012, Steinbrügge et al., 2018].

6. PRECISE ORBIT DETERMINATION USING DOPPLER AND LASER ALTIMETRY DATA

This chapter addresses the work that is done on precise orbit determination (POD) of MPO using radio science data using Bernese software [Dach et al., 2015] and the study of orbit improvement using Bernese and We present our extensive modelling on orbit determination using Doppler tracking and on altimetry crossover measurements. Then we present the results on Doppler-only orbit determination and on the impact of BELA crossover measurements on orbit improvement separately.

6.1 Theory of orbit determination for deep space missions

Orbit determination is the process for obtaining knowledge about the motion of objects such as moons, planets, and spacecraft relative to the center of mass of the central planet for a specific coordinate system. Precise orbit determination of deep space missions is not only needed for the navigation of the spacecraft, but it can help us to determine the geolocation of other measurements and the geophysical parameters of the planet, e.g. gravity field, amplitude of libration. These parameters can then be used to give us an insight about the planet interior structure.

Generally speaking, it can be said that at least six independent measurements are required to determine uniquely an orbit without a priori knowledge. For the spacecraft orbit determination problem, the minimal set of parameters are the position and velocity vectors at a given epoch. This minimal set can be expanded to not just determine the spacecraft's orbit, but also to include dynamic and measurement model parameters (such as tracking equipment biases and environmental forces affecting spacecraft motion), which may be needed to improve the prediction accuracy.

6.1.1 Least-squares adjustment

To drive the orbit of spacecraft from Doppler observation, we use Least-squares adjustment. Here we present a summary of this method and for further detail we refer to Jäggi [2007]. Also for more information on other parameter estimation algorithms in the context of orbit determination we refer to [Tapley et al., 2004].

Let us assume that each observation may be expressed as a function of the parameters of a given mathematical model. We write the system of observation equations as

$$\mathbf{L}' + \boldsymbol{\epsilon} = \mathbf{F}(\mathbf{X}) \quad (6.1)$$

where F is the model function. If F is a non-linear function of the parameters, it can be linearized as

$$\mathbf{L}' + \boldsymbol{\epsilon} = \mathbf{F}(\mathbf{X}_0) + \mathbf{A}\mathbf{x} \quad (6.2)$$

where L' is the the column array of actual observations, ϵ observation corrections, $\bar{\mathbf{L}} = \mathbf{L}' + \boldsymbol{\epsilon}$ is the adjusted observations, $\mathbf{X} = \mathbf{X}_0 + \mathbf{x}$ is the adjusted model parameters, X_0 is the approximate (or a priori) model parameters and x is the model parameter corrections with respect to X_0 (solution vector). The first Jacobi matrix, A , is defined by

$$\mathbf{A} \doteq \left. \frac{\partial \mathbf{F}(\mathbf{X})}{\partial \mathbf{X}} \right|_{\mathbf{X}=\mathbf{X}_0} \quad (6.3)$$

Rearranging equation 6.2 yields

$$\boldsymbol{\epsilon} = \mathbf{A}\mathbf{x} - (\mathbf{L}' - \mathbf{F}(\mathbf{X}_0)) = \mathbf{A}\mathbf{x} - \mathbf{l} \quad (6.4)$$

where the term $\mathbf{l} \doteq \mathbf{L}' - \mathbf{F}(\mathbf{X}_0)$ is referred to as “observed-minus-computed” (O-C). In least-squares adjustment method, the solution of the equation 6.4 is obtained by minimizing the quadratic form $\boldsymbol{\epsilon}^T P \boldsymbol{\epsilon}$. This variation problem can be solved by Lagrange multipliers. According to [Jäggi, 2007] this yield to the normal equation system

$$(\mathbf{A}^T \mathbf{P} \mathbf{A}) \mathbf{x} - \mathbf{A}^T \mathbf{P} \mathbf{l} = \mathbf{N} \mathbf{x} - \mathbf{b} = \mathbf{0} \quad (6.5)$$

where $\mathbf{N} \doteq \mathbf{A}^T \mathbf{P} \mathbf{A}$ is the normal equation matrix and $\mathbf{b} \doteq \mathbf{A}^T \mathbf{P} \mathbf{l}$ is the right-hand side of the normal equation system. \mathbf{N} is by definition a quadratic and symmetric matrix. If it is regular, the solution vector can be written as

$$\mathbf{x} = (\mathbf{A}^T \mathbf{P} \mathbf{A})^{-1} \mathbf{A}^T \mathbf{P} \mathbf{l} = \mathbf{N}^{-1} \mathbf{b} \quad (6.6)$$

where \mathbf{N}^{-1} is the inverse normal equation matrix.

6.1.2 Dynamics of orbit determination

Different gravitational and non-gravitational forces act on a spacecraft. The equation of motion of a spacecraft orbiting a planet including all perturbations can be written as

$$\ddot{\mathbf{r}} = -GM \frac{\mathbf{r}}{r^3} + \mathbf{f}_1(t, \mathbf{r}, \dot{\mathbf{r}}, Q_1, \dots, Q_d) \doteq \mathbf{f} \quad (6.7)$$

with the initial conditions

$$\mathbf{r}(t_0) = \mathbf{r}(a, e, i, \Omega, \omega, u_0; t_0) \quad (6.8)$$

and

$$\dot{\mathbf{r}}(t_0) = \dot{\mathbf{r}}(a, e, i, \Omega, \omega, u_0; t_0) \quad (6.9)$$

where GM is the gravity constant times the mass of the Earth, r is the planetocentric position of the spacecraft, expressed in the inertial frame, f_1 is the perturbing acceleration acting on the spacecraft, expressed in the inertial frame, and \mathbf{f} is the total acceleration.

The acceleration f_1 consists of all gravitational and non-gravitational accelerations taken into account to model the orbit perturbations. The gravitational and non-gravitational perturbations acting on the spacecraft, may depend on the time t , the position r , and the velocity \dot{r} of the spacecraft, as well as on additional force model parameters Q_1, \dots, Q_d to be adjusted.

Often, the perturbation model consists of a known part with accelerations given by analytical models, and of a part which includes force model parameters to be adjusted. Following the naming convention in Bertiger et al. [1994], we address the equation of motion 6.7 as deterministic if f_1 only consists of (deterministic) accelerations given by analytical models. This implies that initial conditions, e.g., given by six Keplerian elements $a, e, i, \Omega, \omega, u_0$ at time t_0 , and scaling factors Q_1, \dots, Q_d of analytically known accelerations (dynamical parameters) may be addressed as deterministic orbit parameters.

The actual orbit $\mathbf{r}(t)$ is expressed as a truncated Taylor series with respect to the unknown orbit parameters P_i about the a priori orbit, which we assume to be always available and is represented by the (a priori) parameter values $P_{0,i}$:

$$\mathbf{r}(t) = \mathbf{r}_0(t) + \sum_{i=1}^n \frac{\partial \mathbf{r}_0}{\partial P_i}(t) \cdot (P_i - P_{0,i}) \quad (6.10)$$

where n denotes the total number $6 + d$ of orbit parameters and $\frac{\partial \mathbf{r}_0}{\partial P_i}(t)$ describes the orbital change due to a change in the parameter P_i [Jäggi, 2007].

Equation 6.10 allows us to improve the a priori orbit provided that the orbit parameter corrections $p_i = P_i - P_{0,i}$ and the partial derivatives of the a priori orbit with respect to the orbit parameters are known. Equation 6.10 should be addressed as the “linearized” solution of

the original (non-linear) orbit determination problem. Alternatively, it is also possible to again use the dynamic models together with the improved dynamical parameters to propagate the improved initial state vector by numerical integration. Usually the latter method is used in this work. If $P_i, i = 1, \dots, n$ are deterministic orbit parameters, we also speak of dynamic orbit determination. If additional pseudo-stochastic parameters occur in the equation of motion (6.7), we speak of a special kind of reduced-dynamic orbit determination [Jäggi, 2007].

6.1.3 Variational equations

Because initial conditions and force model parameters are estimated as part of the orbit determination process, knowledge of the partial derivatives of the a priori orbit with respect to the estimated parameters as a function of time is required for modeling the observations [Jäggi, 2007].

Let us assume that P_i is one of the parameters defining the initial conditions or the dynamics in the equation of motion (6.7), and that the partial derivative of the a priori orbit $r_0(t)$ with respect to this parameter is designated by the function

$$z_{P_i}(t) \doteq \frac{\partial r_0}{\partial P_i}(t) \quad (6.11)$$

The initial value problem associated with above equation is obtained from the dynamic force models by taking the partial derivative of the equation of motion (6.7). The result is subsequently referred to as the variational equation of parameter P_i , which can be written as

$$\ddot{z}_{P_i} = \mathbf{A}_0 \cdot z_{P_i} + \mathbf{A}_1 \cdot \dot{z}_{P_i} + \frac{\partial f_1}{\partial P_i} \quad (6.12)$$

with the 3×3 (Jacobian) matrices defined by

$$A_{0[i;k]} \doteq \frac{\partial f_i}{\partial r_{0,k}} \quad \text{and} \quad A_{1[i;k]} \doteq \frac{\partial f_i}{\partial \dot{r}_{0,k}}$$

where f_i denotes the component i of the total acceleration f and $r_{0,k}$ denotes the component k of the planetocentric position from 6.7 [Jäggi, 2007].

The variational equation (6.12) is a linear, homogeneous differential equation system of second order in time with initial values $z_{P_i}(t_0) \neq \mathbf{0}$ and $\dot{z}_{P_i}(t_0) \neq \mathbf{0}$. For $P_i \in \{Q_1, \dots, Q_d\}$, equation 6.12 is inhomogeneous, but has zero initial values since the initial spacecraft state does not depend on the force model parameters. It is important to mention that the homogeneous part of equation 6.12 is the same for dynamical parameters and for parameters defining the initial conditions, which allows for the implementation of an efficient integration process

[Beutler, 2005].

The solutions of the variational equations related to the orbit parameters $P_i, i = 1, \dots, n$ are needed to set up the first Jacobi matrix (??), which allows us to eventually solve for the improvements of the orbit parameters in a standard least-squares adjustment process together with all other relevant parameters, and to finally improve the orbit using equation 6.10. Although each variational equation 6.12. represents a different initial value problem, it is not necessary to solve differential equation systems as their solutions can be represented by definite integrals [Beutler, 2005].

6.1.4 Orbit determination using multi-arc approach

If the dynamics of the spacecraft is complicated and when there is a large number of solved-for parameters, the above solution may not be sufficient. In these cases, the trajectory could be divided into shorter arcs. It allows obtaining convergence and considerably improves the estimation of the global parameters.

In this strategy, each arc has its own initial conditions and is independent from the others. The solved-for parameters are divided into two groups: the local parameters that are defined for each arc (i.e. initial state vector), and global parameters (e.g. the gravity field coefficients).

In this way, the total number of parameters increases, since each arc has its individual set of local parameters. The total number of solved-for parameters are higher in this strategy, but we can absorb the errors caused by the lack of knowledge and unmodelled dynamics. The arc length must be chosen wisely: if they are too long, the errors accumulate. if they are too short, the solution becomes unstable.

6.2 Doppler-only orbit determination for MPO: modelling

Navigation of deep space probes is most commonly operated using the spacecraft Doppler tracking technique. Orbital parameters are determined from a series of repeated measurements of the frequency shift of a microwave carrier over a given integration time. Just a small number of software packages are nowadays used to process Doppler observations. The Astronomical Institute of the University of Bern (AIUB) has developed the Doppler data processing capabilities within the Bernese GNSS Software. This software has been extensively used for Precise Orbit Determination of Earth orbiting spacecrafts using GPS data collected by on-board receivers and for subsequent determination of the Earth gravity field [Bertone et al., 2015].

6.2.1 Dynamical model

We use a full force model containing all the gravitational and non-gravitational forces to propagate the orbit of spacecraft. The gravitational forces that are used in this model are the Mercury gravity field GGME5_100V07 (up to d/o 50), the gravity of Sun and planets. We also apply the relativistic corrections including the Schwarzschild term, Lense-Thirring and De sitter.

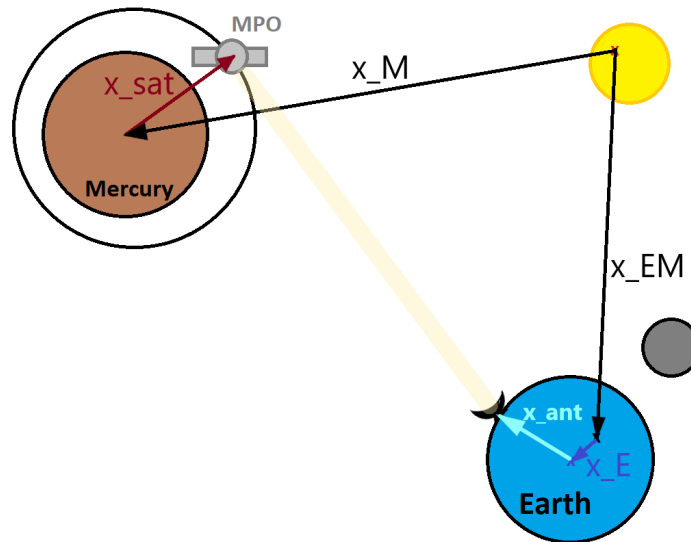


Fig. 6.1: Geometry of tracking of the spacecraft around Mercury from the Earth: x_{sat} is the Mercury-centric position of the MPO, x_M and x_{EM} are the Solar system barycentric positions of Mercury and Earth-Moon barycenter (EMB), x_E is the position of the Earth barycentre with respect to the EMB and x_{ant} is the position of the ground antenna

A sketch of the dynamics used to compute the observables is showed in figure 6.1. To compute the range distance from the ground station on the Earth to the spacecraft around Mercury, and the corresponding range-rate, we need the following state vectors, each one evolving according to a specific dynamical model:

- The position of the spacecraft in Mercury centric frame.
- The Solar System barycentric (SSB) position of Mercury.
- The Solar System barycentric (SSB) position of Earth-Moon system.
- The position of the Earth barycenter with respect to the Earth-Moon barycenter.

- The geocentric position of the ground antenna.

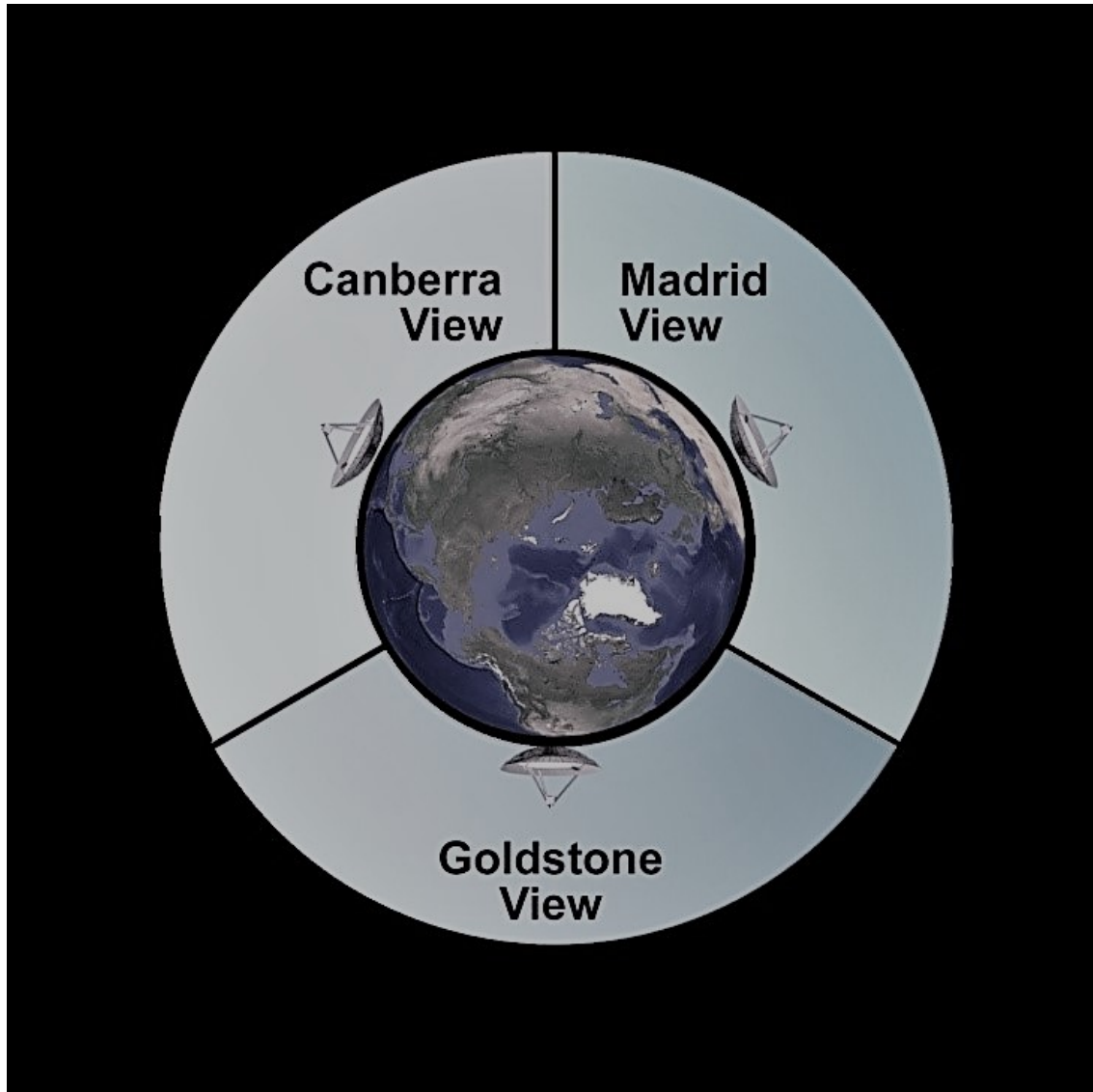


Fig. 6.2: Deep space network

The communication with interplanetary missions is supported by a worldwide network of Antennas that is called Deep Space Network (DSN). The DSN relies on three observation points at three different locations around the globe: California (USA), Canberra (Australia) and Madrid (Spain). Each observation point is about one third the length of the Earth's surface from the other two. This is to ensure that communication with any spacecraft is always possible by at least one of the three centers, whose antennas are about 120 degrees from each other.

Because of the geometry of the system shown in figure 6.1 the communication between the antenna on the Earth's surface and the antenna on the spacecraft is not always possible. The tracking period will usually have 15-16 hours of observation that will be followed by a dark period. For the visibility condition, the spacecraft should be visible from Earth, the available ground station should be visible from the spacecraft and the spacecraft should be above the horizon of the ground station. We consider all these factors in our modelling of the system.

6.2.2 Observation model

Doppler tracking observations conceptually seek to measure the relative velocity of the Earth and a spacecraft by comparing the frequency of the radio signal received from the spacecraft with the frequency of a ground-based reference signal. When the signal transmitted by the spacecraft is derived from an onboard oscillator, the measurement is said to be "one-way." If the spacecraft transponds a signal transmitted from the ground and the ground-based reference for the Doppler is the same one that drives the transmitter, the observation is "two-way" [Asmar et al., 2005].

Our simulations of Doppler tracking measurements include 2-way X-band and K-band Doppler measurements, station and planetary eclipses and the relativistic corrections.

According to [less and Boscagli \[2001\]](#), a nominal white noise can be associated with the tracking measurements error. Assuming accuracy performances of the transponder in Ka band, the following Gaussian errors have to be added to simulated range and range-rate [[Cicalò et al., 2016](#)].

$$\sigma_r = 15cm @300 s$$

$$\sigma_{rr} = 1.5 \times 10^{-4} cm/s^{-1} @1000 s \text{ integration time}$$

$$\sigma_r/\sigma_{rr} \sim 1 \times 10^5 s$$

where σ_r is sigma of range error and σ_{rr} is sigma of range-rate error. From a comparison of the accuracies for the range and the range-rate it turns out that $\sigma_r/\sigma_{rr} \sim 1 \times 10^5 s$, which implies that the range-rate measurements are more accurate than the range when we are observing phenomena with a period shorter than $1 \times 10^5 s$. Since the spacecraft orbital period, and then the periods related to the gravity field perturbations, are less than $10^4 s$, the POD is performed mainly with the range-rate tracking data (Milani et al. 2002).

We assume a white noise on Doppler observations. Based on the characteristics determined by the MORE team, we assume the sigma of the noise to be 4 mHz on X-band and 1.5 mHz on Ka band. When the Sun-Earth-spacecraft angle has smaller values and the spacecraft is behind the Sun, the telemetry link has to pass through the plasma of the Sun and this cause an extra noise on the measurements. Figure 6.3 shows the power spectral density of one-way plasma phase scintillation versus the Sun-Earth-spacecraft angle. If differential X-Ka downlinks are available, the downlink plasma contribution can be estimated and removed. We expect to be able to calibrate the plasma noise, but we perform orbit determination tests in both scenarios that the plasma noise is calibrated or not.

We model three ground stations around the globe that can be used for receiving signals from the spacecraft. We study the impact of having different number of ground stations on the accuracy of the orbit recovery. The daily tracking period from each station is approximately 8 hours, but loss of the radio link caused by occultation has also been accounted for.

6.2.3 *Modelling the non-gravitational forces and accelerometer model*

We model the solar radiation pressure (SRP) and planetary radiation pressure (PRP) due to reflected and emitted radiation. To consider the effect of non-gravitational forces on the spacecraft, we use a 33-plates macromodel of MPO, including both visible and IR optical properties. The details of the calculation of non-gravitational forces in Bernese software is given in Girardin [2016].

The proximity of Mercury to the Sun has caused difficulty in modelling the non-gravitational forces such as SRP and PRP. A simple, cannonball model for the strongest effect (direct solar radiation pressure) can only provide order-of-magnitude estimates of the force. More elaborate models, that would take into account the shape of spacecraft, will also have at least 10% error on the estimation of the non-gravitational forces at each epoch [Santoli et al., 2018].

The pointing accuracy that is needed for instruments onboard MPO, is reached thanks to the onboard reaction wheels. Therefore there will be unavoidable manoeuvres for desaturation of the reaction wheels, which are necessary to remove the accumulated angular momentum. These desaturation maneuvers are foreseen approximately every 12 hours, during these maneuvers, the unbalanced thrusters will produce a large along-track ΔV . The knowledge of the ΔV associated to desaturation maneuvers is possible to a level of 2 - 5% (1.2 - 3 mm/s).

The desaturation maneuvers consist of 60 impulse at every 9 s (total: 540 s). Following

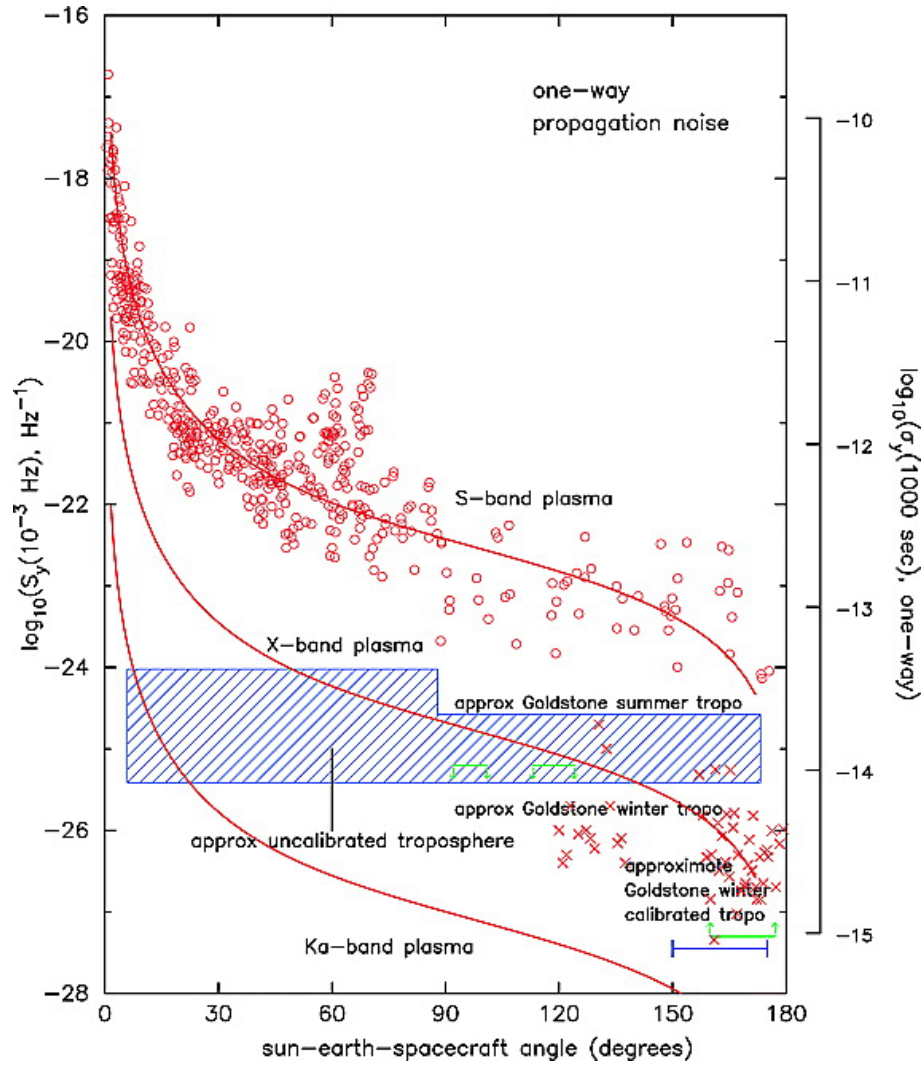


Fig. 6.3: Power spectral density of one-way plasma phase scintillation at $f = 0.001$ Hz versus Sun-Earth-spacecraft angle [Asmar et al., 2005]

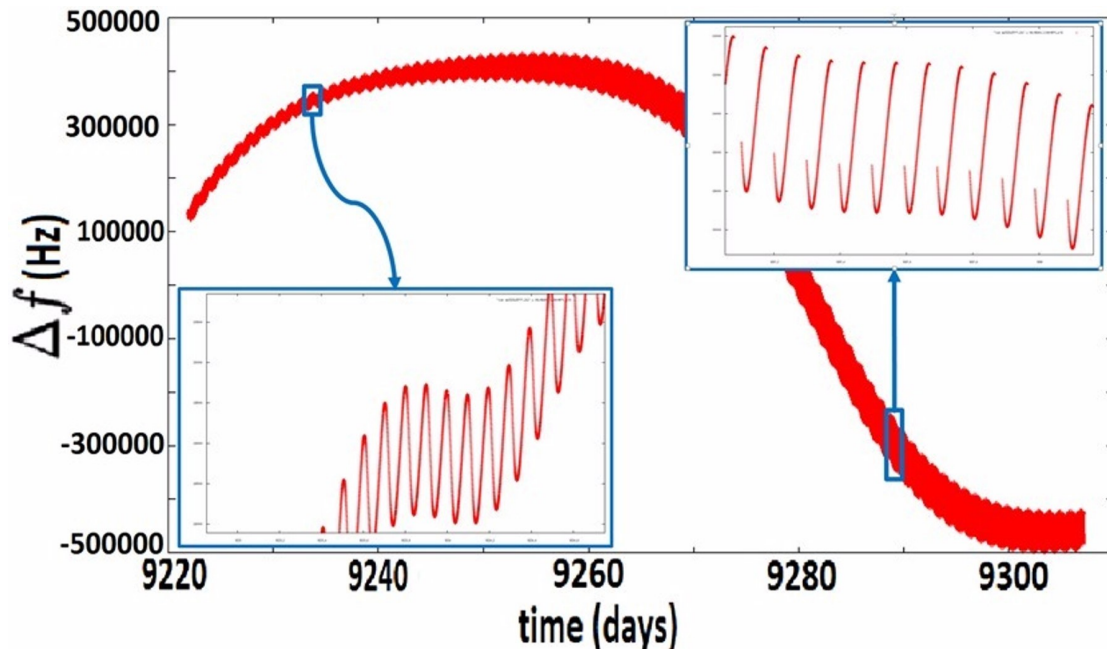


Fig. 6.4: Modelling of Doppler observation using three ground stations for three month of mission. The loss of data in the end of this period is caused by occultation of spacecraft behind Mercury. At the beginning of this period the spacecraft orbital plane is perpendicular to the Earth-Mercury line of sight and therefore, there is no loss of signal caused by occultation.

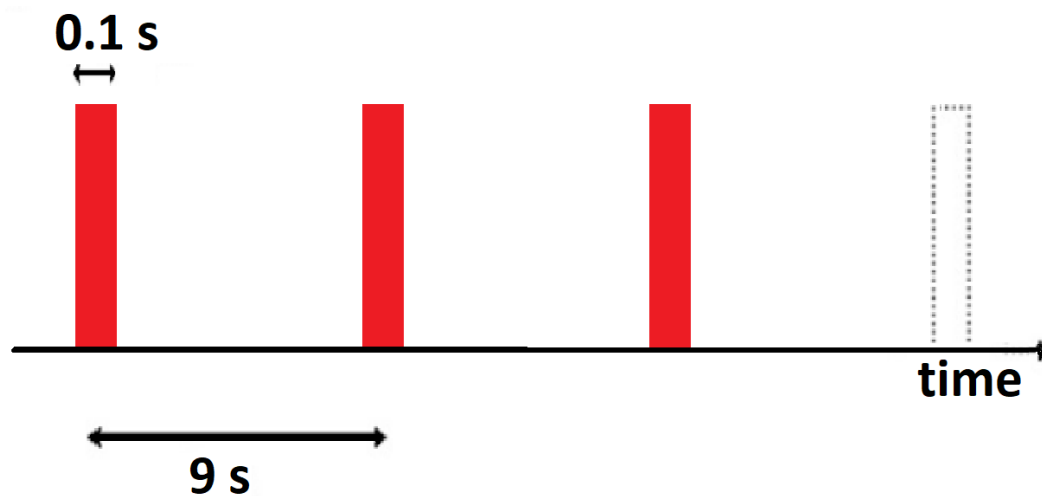


Fig. 6.5: Profile of the MPO thruster firing during the desaturation maneuvers

the first assessment of the MORE team using the instrument characteristic, the desaturation maneuvers will have estimated uncertainties equal to:

- knowledge of ΔV in radial direction: $0.85 \times 10^{-3} m/s$;
- knowledge of ΔV in along track direction: $0.15 \times 10^{-3} m/s$;
- knowledge of ΔV in cross track direction $2.10 \times 10^{-3} m/s$;

For the simulation, instead of each ΔV , we use an equivalent and constant acceleration for each period of 9 sec computed from:

$$a_r = \frac{\Delta V_r}{\Delta t} \quad (6.13)$$

$$a_s = \frac{\Delta V_s}{\Delta t} \quad (6.14)$$

$$a_w = \frac{\Delta V_w}{\Delta t} \quad (6.15)$$

where ΔV_r , ΔV_s and ΔV_w are components of the impulses in radial, cross-track and along-track and a_r , a_s and a_w are components of the equivalent acceleration respectively. The assumption here is that the RSW coordinate system doesn't change during the Δt period of 9 seconds.

To overcome the difficulties in determining the non-gravitational forces, a three-axis high sensitivity accelerometer (ISA - Italian Spring Accelerometer) is placed on-board MPO to give accurate information on the non-gravitational accelerations. ISA detects the displacements of a proof-mass as a result of perturbing accelerations and uses them to estimate the non-gravitational accelerations.

The ISA error model is presented in [Cicalò et al. \[2016\]](#). In short, the model consists of the following terms:

- Spacecraft orbital period term or resonant term:
- Mercury orbital period term or main thermal term.
- Other systematic components

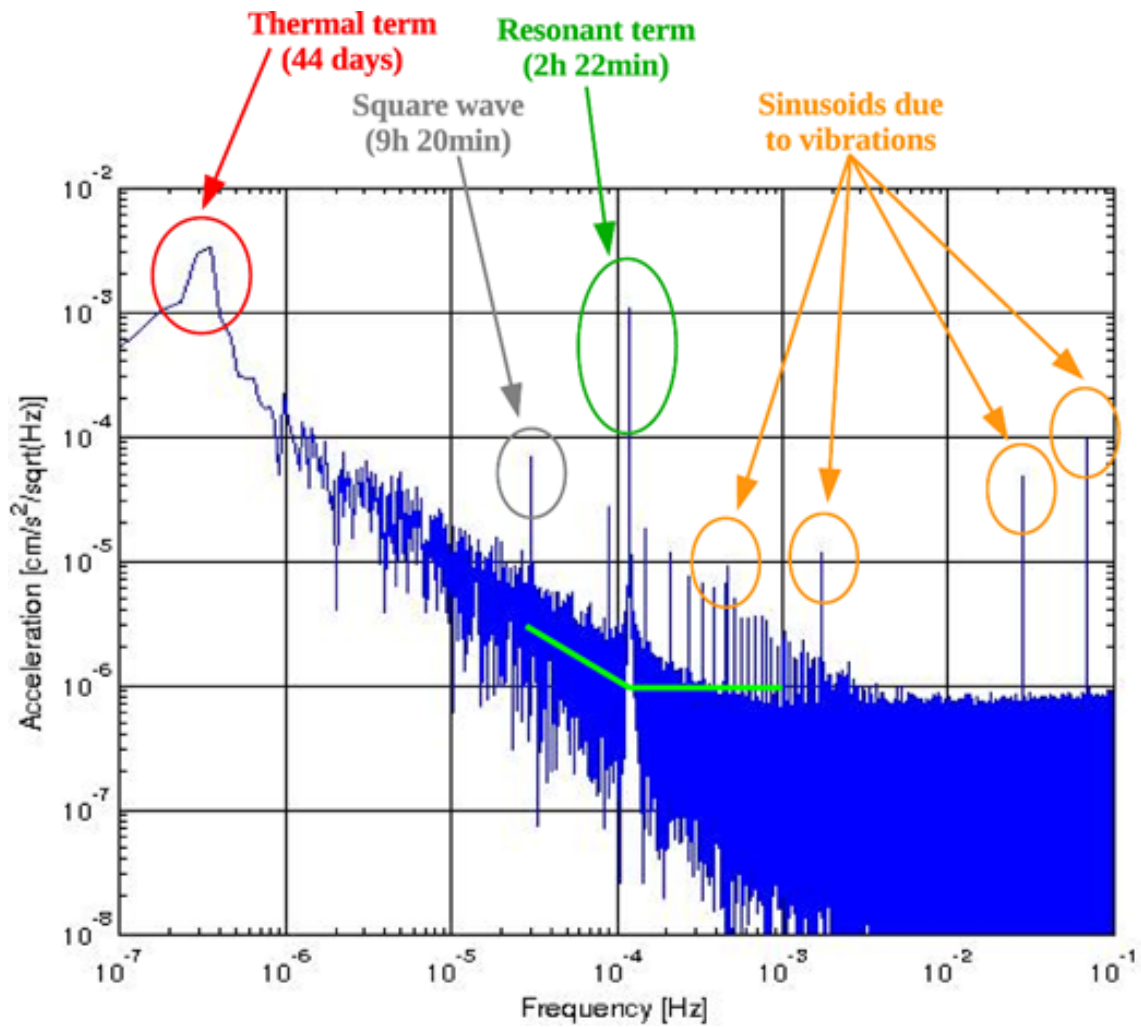


Fig. 6.6: Spectrum of the ISA error model integrated over 88 d; Thick green line shows the expected behaviour from requirements for a comparison [Cicalò et al., 2016]

- Random component: it consists of a random background at $10^{-6} \text{ cm/s}^2/\sqrt{\text{Hz}}$

The measurement bandwidth of ISA is between 3×10^{-5} Hz and 10^{-1} Hz. The amplitude ascribed to the resonant term component is a critical parameter. According to [Cicalò et al. \[2016\]](#), considering a calibration, a residual amplitude after calibration of $1 \times 10^{-7} \text{ cm/s}^2$ can be assumed. Also Mercury orbital period term or main thermal term has an amplitude of $4.2 \times 10^{-6} \text{ cm/s}^2$. This term of the accelerometer noise is described by a sinusoidal function with the period of Mercury orbital period around the Sun.

The modelling of the accelerometer noise has a huge impact on the results of the POD. On the other hand, there are a lot of uncertainties in the model. For instance, good thermal control and calibration effects might bring the noise below to lower values, while assuming an calibrated accelerometer can cause problems for the POD . To have a fair estimate of the accelerometer noise in our modeling we use the value of $1 \times 10^{-6} \text{ cm/s}^2$ from [lafolla et al. \[2011\]](#).

6.2.4 Parameter estimation model

We perform several orbit reconstruction tests using daily arcs with noise modulated Doppler data. We take the initial condition of each arc from the simulation, add some random offset to it and use them as a priori values for the estimation. The sigma of the initial offset in each direction is chosen as:

$$\sigma(\Delta X)_0 = 10 \text{ m} \quad (6.16)$$

$$\sigma(\Delta V)_0 = 0.01 \text{ m/s} \quad (6.17)$$

We use a realistic dynamical model to produce synthetic Doppler observations. We perform several orbit reconstruction tests using daily arcs with noise modulated Doppler data. We use a realistic observation model, taking into account the availability of ground antenna, visibility conditions and occlusion of spacecraft behind Mercury. Then we solve for the initial state vector of each arc separately and find the RMS of error of the orbit determination by comparing the reconstructed orbit with the real one. The goal of these tests is to find the best possible orbit determination accuracy that can be achieved using only Doppler data and the impact of different settings on the results.

We assume two series of maneuvers, each consist of 60 constant accelerations every 9 s (total: 540 s) to be performed per day. These maneuvers are modelled in the simulation to-

gether with the accelerometer model.

In orbit reconstruction process, the models for the non-conservative forces (i.e. solar radiation pressure) were replaced by the noisy simulated accelerometer measurements. To simulate the accelerometer measurements at each observation time, we first calculate the non-gravitational acceleration that acts on the spacecraft, then we read the accelerometer noise that comes from the conversion of noise to time domain. Finally, we add the noise to the total non-gravitational accelerations and create the accelerometer measurement.

For the first step of orbit recovery, we do not solve for the gravity field and therefore use the same gravitational force model with errors on the initial state vector as the “a priori” knowledge of the orbit. At the moment the scale and bias parameters of the accelerometer is assumed to be known in the orbit determination. Later, this has to be updated and these parameters have to be considered as solved-for parameters. Finally, a dynamic orbit recovery based on the Doppler and simulated accelerometer data is carried out.

6.3 Doppler-only orbit determination: results

6.3.1 Doppler-only orbit determination: zero test results

To make sure about the convergence of the code we start with a zero test. In this test we do not apply any desaturation maneuver or accelerometer noise model and we use the exact same force model for the simulation and reconstruction. We perform the test on a time period with no occultation. We add noise to the Doppler observation and an error on the initial state vector and we would like to see if the code can converge to the real orbit or not. The position residuals and Doppler residuals resulting from this test are shown in figures 6.7 and 6.9 for one arc (24 hours).

An improvement in the residuals can be seen up to the third iteration, but after the third iteration the level of error stays the same. A periodic term with the period of MPO orbital period around Mercury can be seen in the position residuals, which is caused by the error in the estimation of initial state vector. Since we use the same force model in both simulation and estimation, this periodic term is the only term of error that can be seen in the position residuals. Also while the norm of the position residuals reaches to values around 0.5 meter in the third iteration, the radial direction of the position residual has an error around 1-2 cm. We do not have a reference to compare our zero test position residuals with, but since the RMS of Doppler residuals are in the third iteration reaches the the order of Doppler noise, we can validates the orbit determination process.

In the next step, we repeat the test on a time period where we have gaps in the Doppler data as a result of spacecraft occultation behind Mercury. The result is plotted in figure 6.10, where it can be seen that the position residuals are in the order of 2 meters.

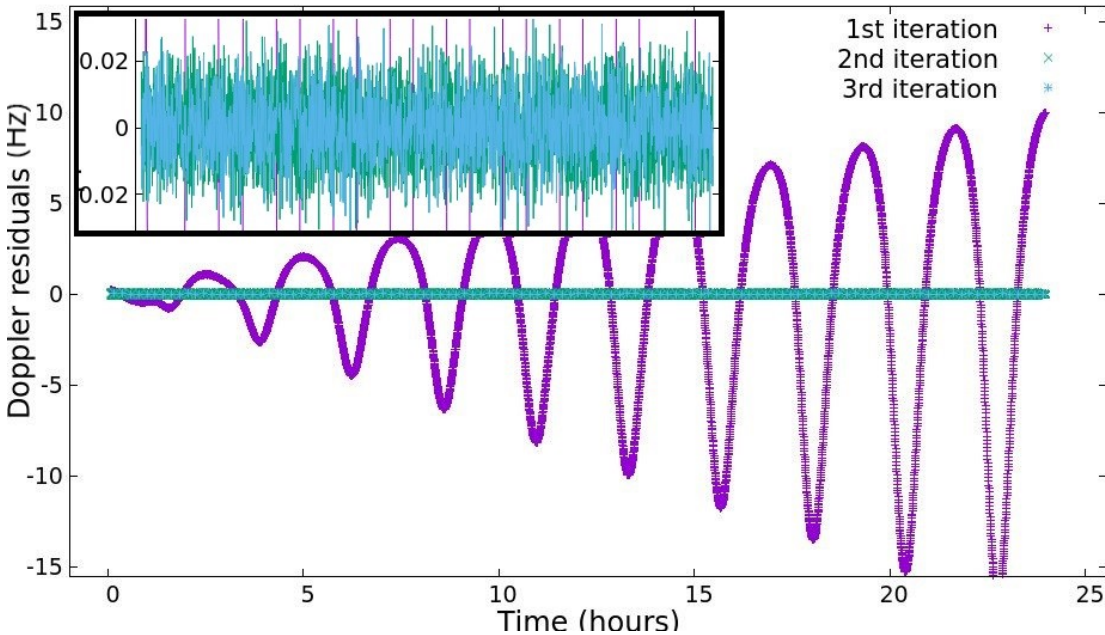


Fig. 6.7: Doppler residuals in different iterations resulted from a zero test for one daily arc

6.3.2 The impact of solar plasma noise

In section 6.2.2 the impact of solar plasma on making additional noise on Doppler data is discussed. To calculate this effect, we assume that the given Doppler noise is for the situation the spacecraft is relatively far from the Sun (around 30 degrees). Then we find the SUN-Earth-Spacecraft at each observation time and using the Allan deviation from figure 6.3, we calculate the increase in Doppler noise.

We need to stress that effect of Solar plasma noise will be calibrated up to some point using the X-band and K-band Doppler data together [IMPERI, 2015-2016]. Here we perform an orbit recovery test to see the impact of including this extra noise source and assuming the worst case scenario that no calibrations applies to the noise.

Figure 6.11 compares the norm of the position residuals resulting from above mentioned tests. In the case of having a varying noise, the residuals do not have good values during the days that the spacecraft is passing behind the Sun and the Sun-Earth-Mercury angle has small

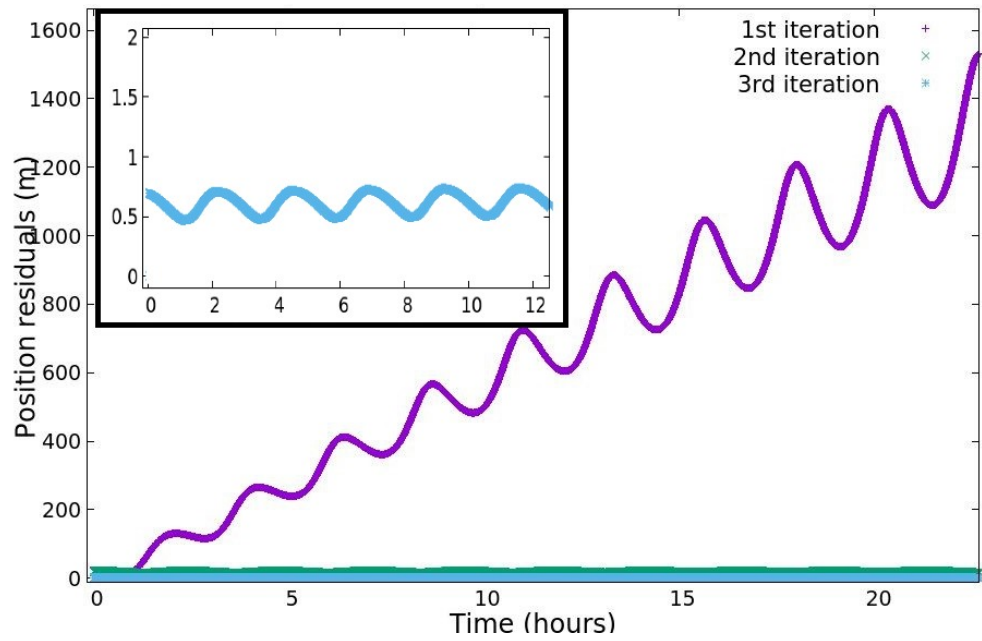


Fig. 6.8: Norm of position residuals in different iterations resulted from a zero test for one daily arc

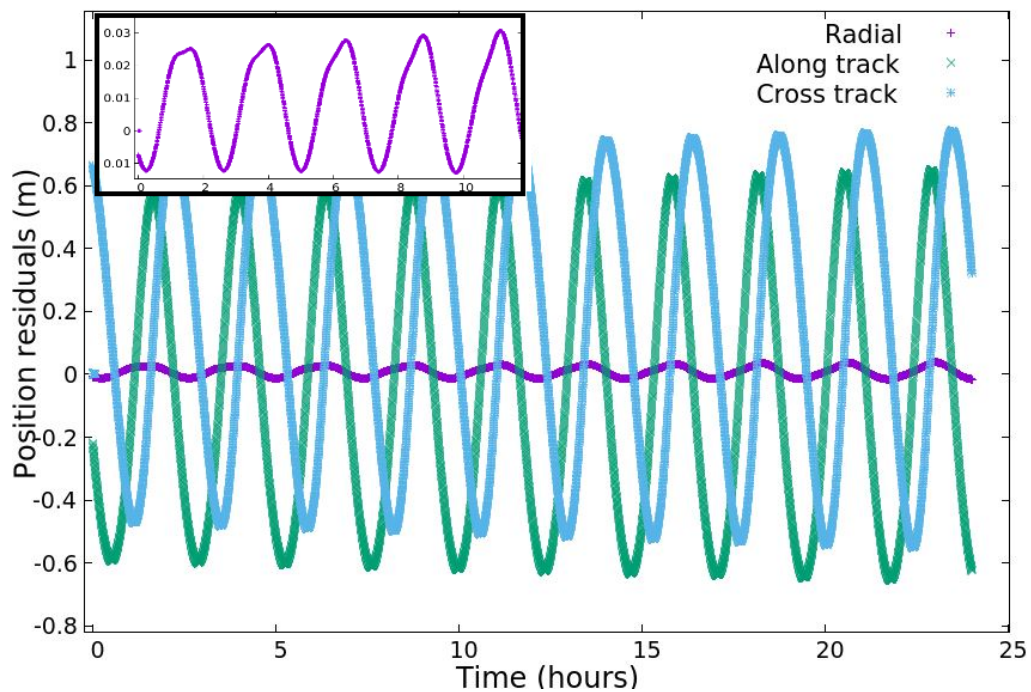


Fig. 6.9: Position residuals in radial, along-track and cross-track directions in the last iteration of orbit reconstruction zero test

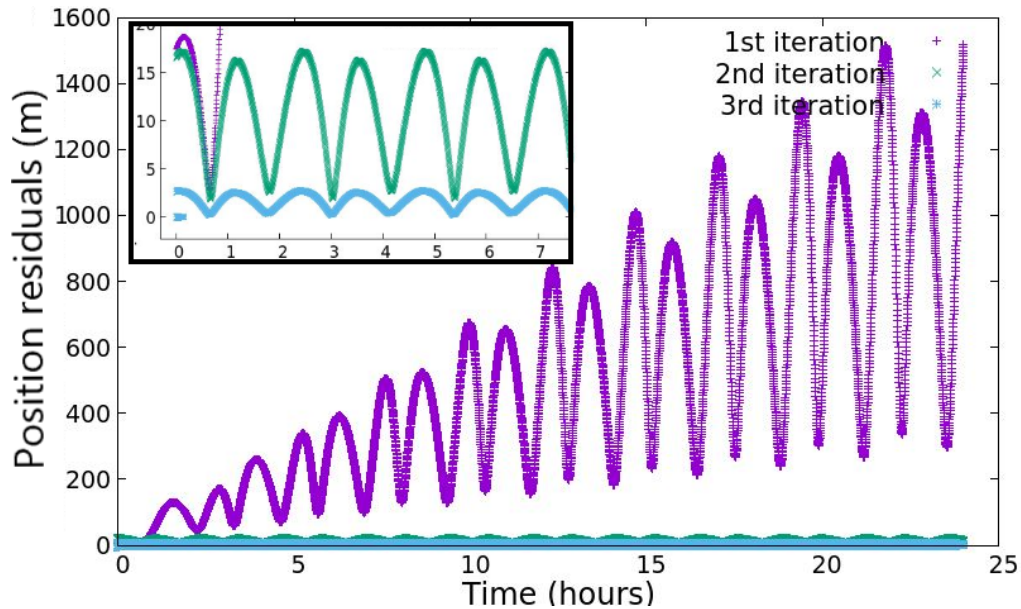


Fig. 6.10: Norm of position residuals in different iterations resulted from a zero test when there are gaps in the Doppler data because of MPO's occultation behind Mercury for one daily arc

values.

6.3.3 Orbit recovery tests for 100 days

The results of the full orbit reconstruction for 100 days of the mission using a complete model (including the desaturation maneuvers and the accelerometer) with different assumptions are presented in table 6.1. Figure 6.12 shows the norm of the position residuals in 5 days of mission using a constant Doppler noise and 2 ground stations available. It can be seen that with three ground station we reach the best accuracy of about 4.5 m in the norm of position residuals. with two ground stations the accuracy will degrade to around 6.1 m and with one ground stations the norm of position residuals will reach to around 9.5 m. These values are comparable with the values that are archived by the MORE team [Cicalò et al., 2016].

We need to mention that using a single ground station causes a divergence in the orbit recovery of some daily arcs. This problem usually happens during the daily arcs when the spacecraft goes to occultation in each orbital period. We conclude that the imperfect knowledge on non-gravitational forces (especially the desaturation maneuvers) combined with the lack of Doppler observations for more than two third of the daily arcs causes this problem. In this situation the accelerometer is not able to estimate the non-gravitational forces with a sufficient accuracy and it causes a failure in the recovery of the orbit. This problem needs to

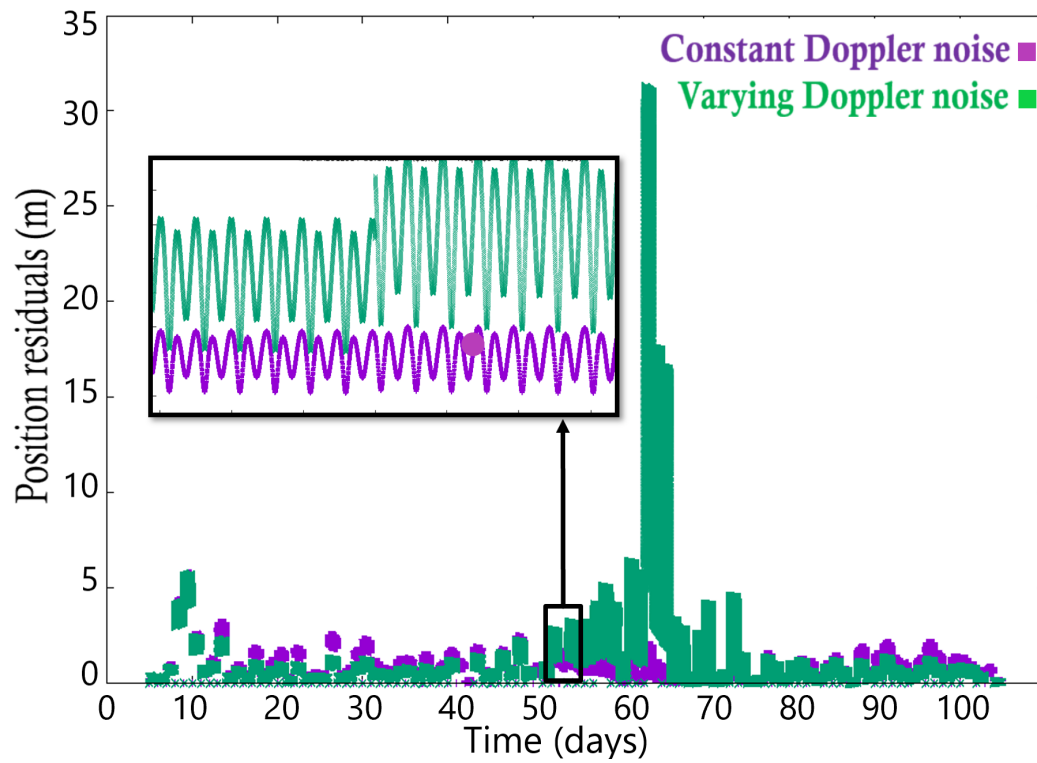


Fig. 6.11: Orbit residuals in 100 days of the mission. Purple: assuming a constant Doppler noise; Green: Assuming the impact of solar plasma on Doppler noise

Tab. 6.1: Position errors in orbit recovery tests with different assumptions. X, Y and Z are components of inertial frame

| Condition | RMS errors (m) | | | |
|-------------------|----------------|------|------|------|
| | Norm | X | Y | Z |
| 3 ground stations | 4.54 | 4.06 | 1.52 | 1.48 |
| 2 ground stations | 6.15 | 5.13 | 2.40 | 2.38 |
| 1 ground station | 9.51 | 7.55 | 4.08 | 4.00 |

be investigated by using a better model of the accelerometer noise and by adding empirical accelerations to see whether or not the effect of unmodelled dynamics can be absorbed.

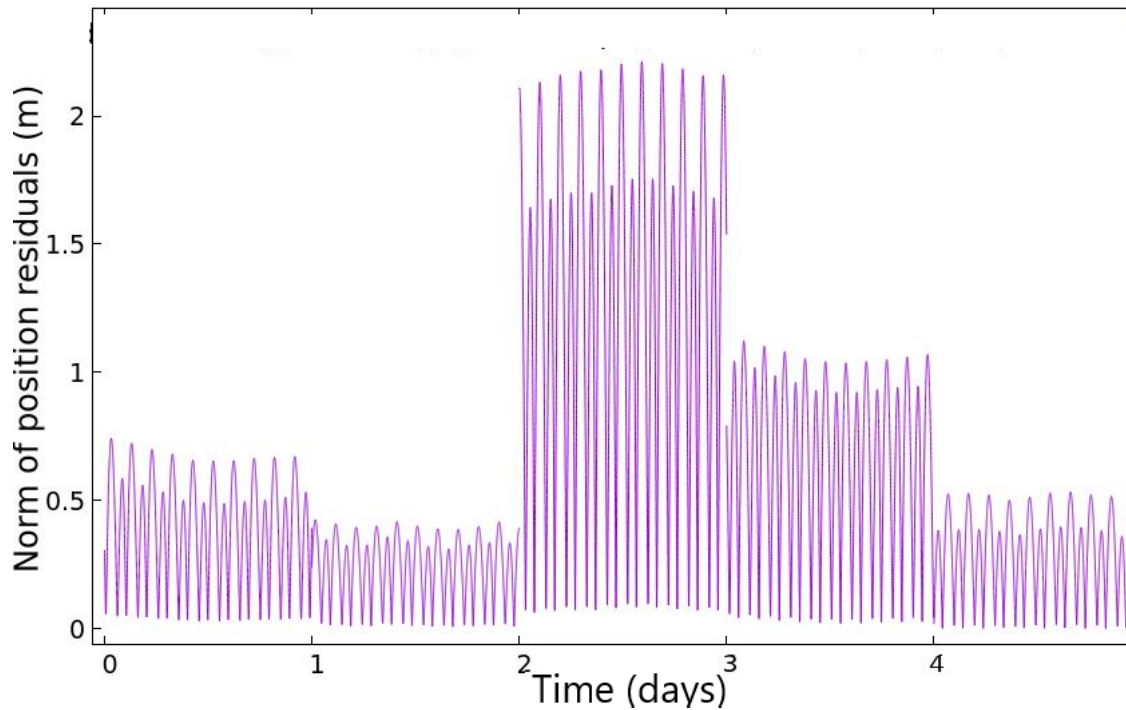


Fig. 6.12: Norm of position residuals in 5 days of mission using 2 ground stations

6.4 *Improvement of orbit and geophysical parameters using laser altimetry data*

6.4.1 *Modelling*

In this section, we use the modelling for the laser altimetry, including the range noise model and planet terrain model presented in chapters 2 and 4, to produce realistic laser altimetry observations for the whole duration of nominal mission. Then we use the PyXover [Bertone et al., 2019], Python software package recently developed by Dr. Stefano Bertone at NASA Goddard Space Flight Center (GSFC) to estimate the impact of BELA measurements at crossover points on the recovery of orbit and geophysical parameters. We present the modelling that is used in this study and the preliminary results.

The simulation results, including appropriate relative weights for the crossovers and an extended parametrization to account for orbital errors in each arc, are applied to our analysis of the full simulated dataset acquired by the BELA instrument. Crossover measurement weights are based on both the observation geometry (see figure 6.13) and the individual errors associated with each BELA measurement (also see section 4).

To find the impact of the laser altimetry observations at crossover points on the orbit recovery, we first simulate a series of laser altimetry observations with realistic frequency (10 observations per second) in one year of mission. This simulation is based on the modelling in chapters 2 and 4 and contains a realistic range error depending on the spacecraft altitude and the planet terrain on the laser spot. Then we detect the locations of the laser altimetry ground track crossover points and we set up orbit and geodesy improvement in a least square minimization of crossover discrepancies.

6.4.2 *Detection of the crossover points*

A crossover measurement is a differential measurement between two distinct observations of the same surface location at two different times. Any difference in the height measurements at a crossover intersection is mainly due to the following effects:

- Errors in the spacecraft orbit and attitude, or BELA boresight orientation
- Interpolation errors of the surface topography between MLA footprints
- Geophysical signal due for instance to mismodeled time-varying planetary rotation or to tidal vertical motions

For the detection of crossover points we separate laser altimetry observations in arcs (roughly one arc per orbit) where the PFD is smaller than 10 %. As a result we have around 10

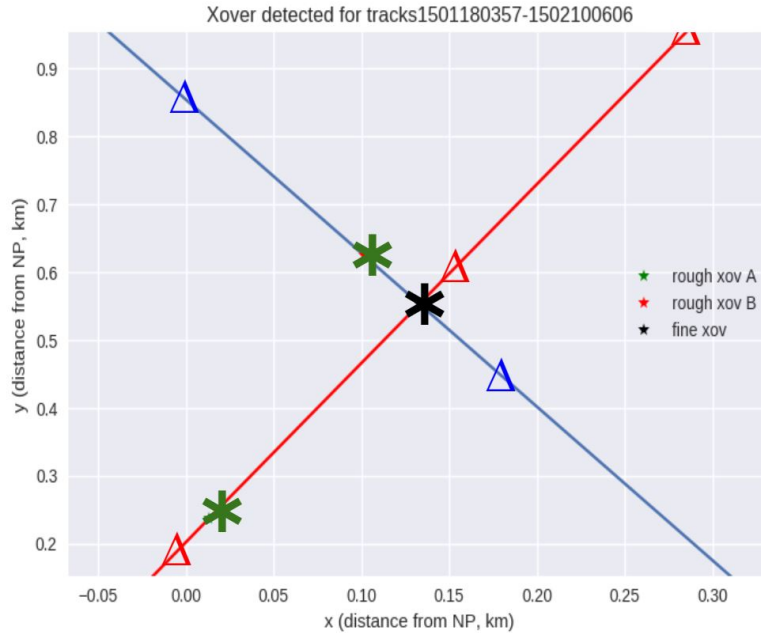


Fig. 6.13: Intersection of two ground-tracks. Δ : altimetry observations, crossover locations: \star rough, \star fine search [Bertone et al., 2019]

arcs of data in each day of the mission. Then we geolocate BELA observations on the ground by using an iterative procedure. Then we look for intersections among all point of arcs. Most crossover points, are distributed around the poles of the planet at high latitudes, because of the geometry of the orbit. Figure 6.14 shows the distribution of crossover points in the first two months of mission.

6.4.3 Results

Figures 6.15 to 6.24 show the value of the crossover discrepancies (Δh) sensitivity to the spacecraft orbit, attitude, rotational parameters and tidal deformations ($d(\Delta h)/d(\text{parameter})$). Figures 6.15 to 6.17 show the sensitivity of the crossover discrepancies to the orbit. Among them, figure 6.15 shows a much higher sensitivity to orbit in radial direction in the latitudes between 0 to 85 degrees, while 6.16 shows the same sensitivity to along-track direction over the surface of the planet. The sensitivity to cross-track direction 6.17 seems similar in northern and southern hemisphere but the sensitivity seems to be higher at lower latitudes and close to the planet equator.

Figures 6.18 and 6.19 show the sensitivity to the attitude of spacecraft. They all show a higher sensitivity at lower latitudes. Figures 6.20 and 6.23 show the sensitivity to the orien-

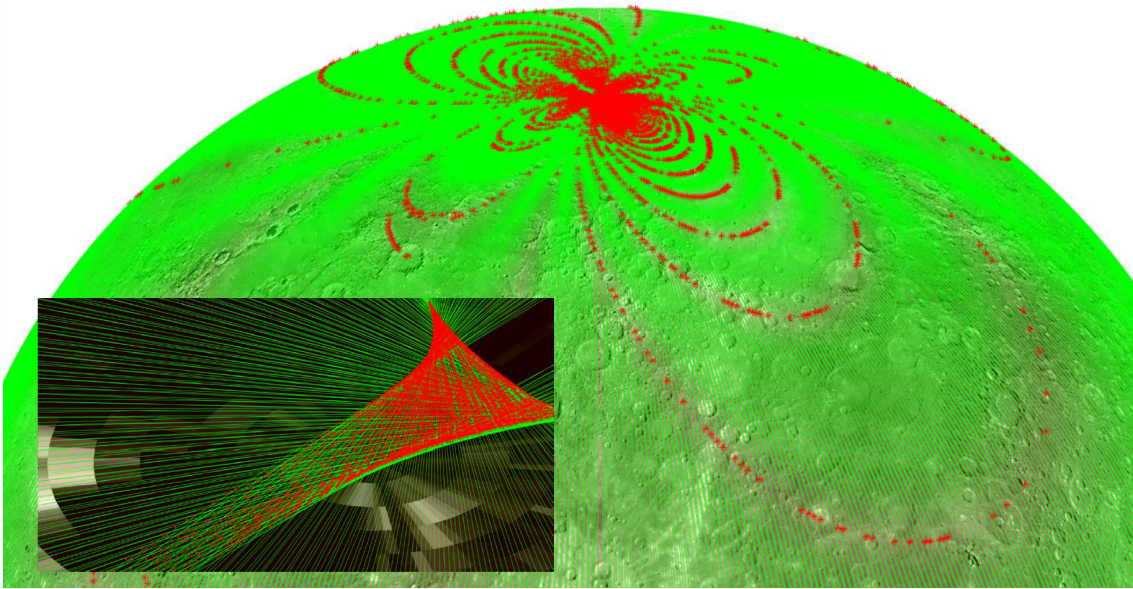


Fig. 6.14: Distribution of crossover points (red dots) around the North Pole of the planet in two months of mission (green lines are altimetry ground tracks and red points are crossover points)

tation and rotational parameters of the planet. They also show a higher sensitivity at lower latitudes and close to the equator. Figure 6.24 presents the sensitivity to the Love number h_2 . It also shows the same pattern: higher sensitivity around the equator.

The inverse of these sensitivities is then closely related to the formal errors expected from the recovery of the orbital and geodetic parameters. Together with the residuals $d(\Delta h)$, the partial derivatives constitute the basis for a least square improvement of the spacecraft orbit and planetary geodesy. The presented results of this work is still preliminary and it will be investigated further.

At the moment the weights of the individual BELA observations is not used, but a full analysis should make use of the sigma of error of each observation which is available in the BELA simulated data. Direct altimetry data (by comparing them with a MLA based DTM) the improvement of orbit and planet geophysical parameters using the direct altimetry data.

Figures 6.15 to 6.24 show the importance of crossovers at latitudes close to the planet equator. Unfortunately, the orbit of MPO doesn't allow for a high number of crossovers at lower latitudes. Therefore, we suggest to design several off-nadir maneuvers during the period that the spacecraft is passing over the equator. These maneuvers can be performed in a few

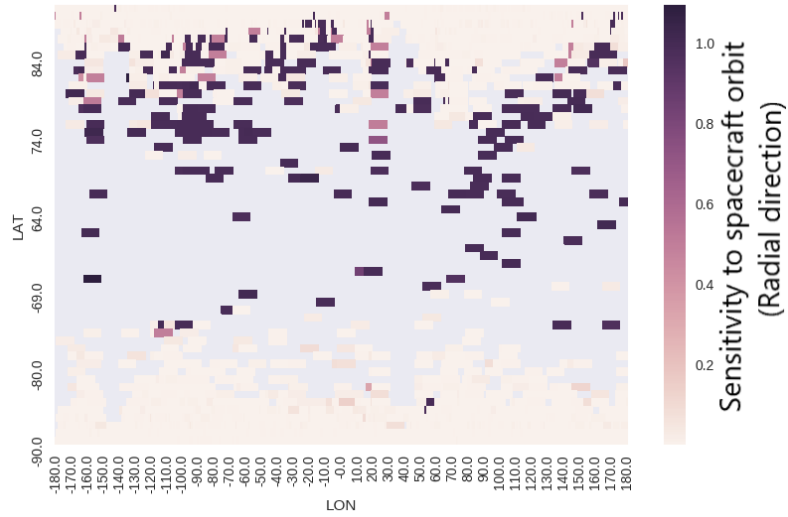


Fig. 6.15: Crossover measurement (Δh) sensitivity to the spacecraft orbit correction in radial direction (unitless)

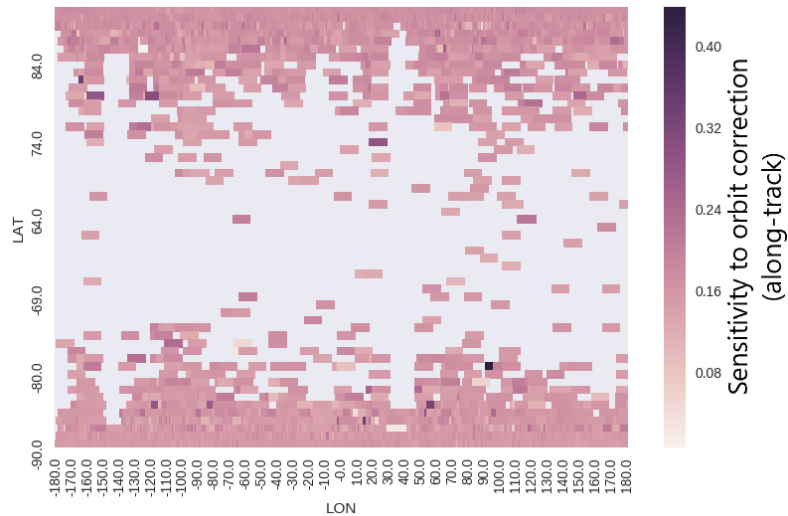


Fig. 6.16: Crossover measurement (Δh) sensitivity to the spacecraft orbit correction in along-track direction (unitless)

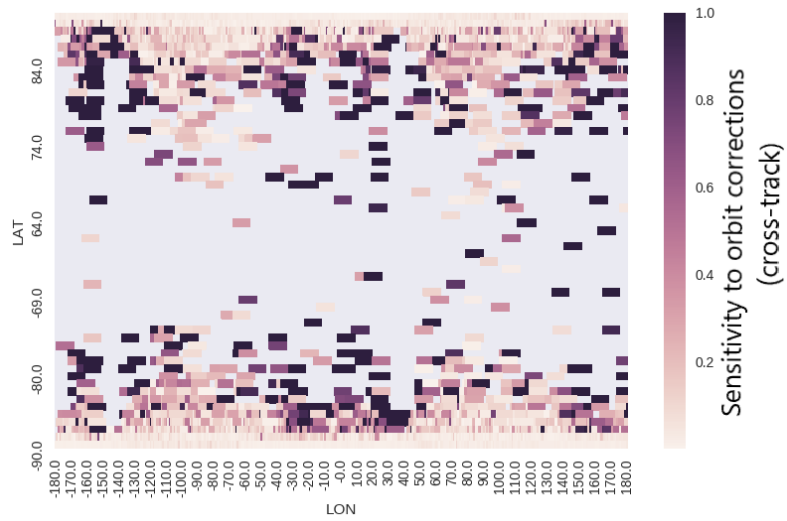


Fig. 6.17: Crossover measurement (Δh) sensitivity to the spacecraft orbit correction in cross-track direction (unitless)

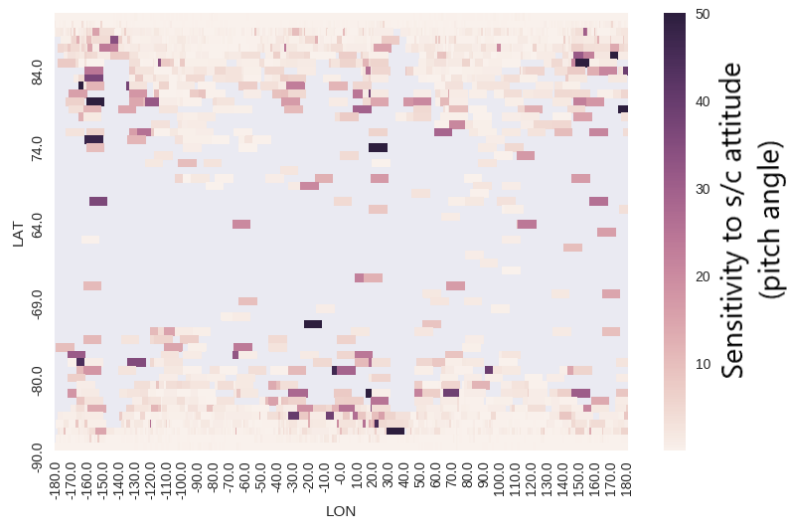


Fig. 6.18: Crossover measurement (Δh) sensitivity to the spacecraft attitude corrections in pitch direction ($m/arcsec$)

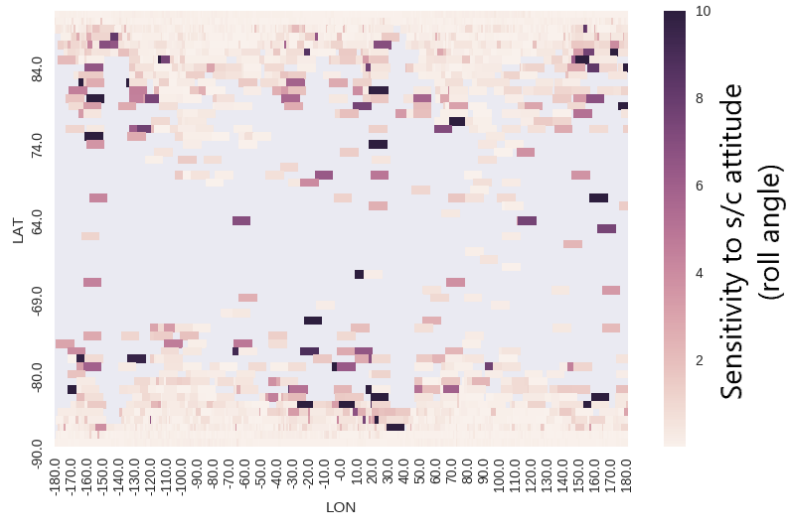


Fig. 6.19: Crossover measurement (Δh) sensitivity to the spacecraft attitude corrections in roll direction ($m/arcsec$)

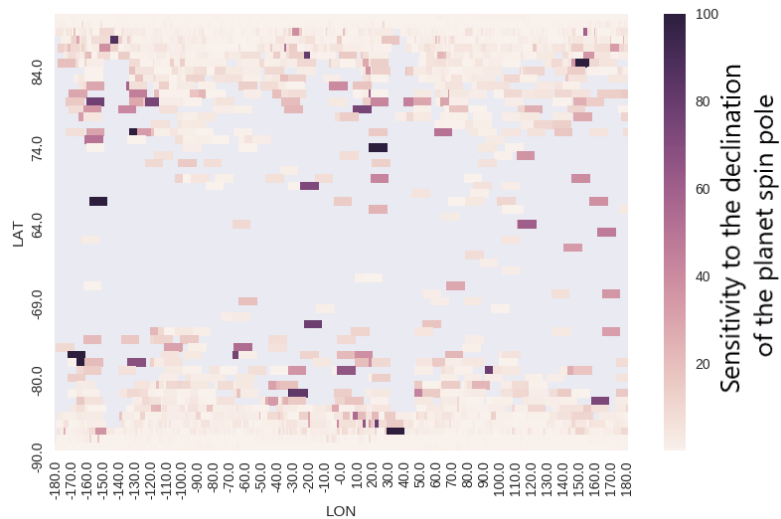


Fig. 6.20: Crossover measurement (Δh) sensitivity to the declination of the planet spin pole at J2000 ($m/arcsec$)

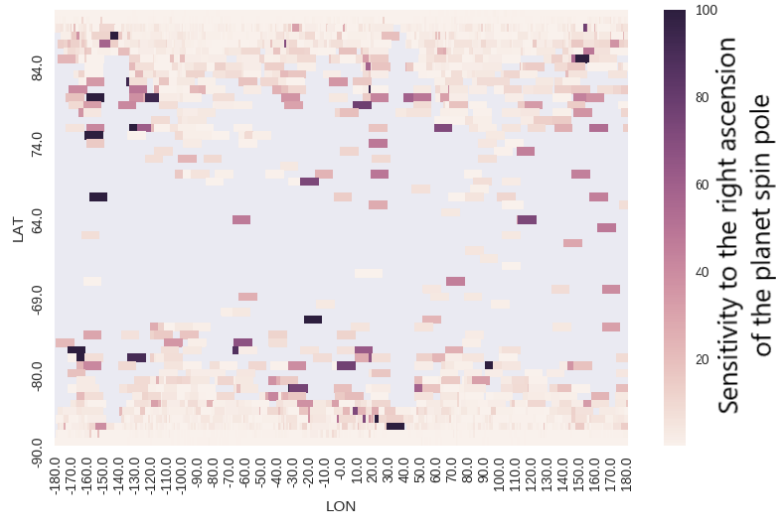


Fig. 6.21: Crossover measurement (Δh) sensitivity to the right ascension of the planet spin pole at J2000 ($m/arcsec$)

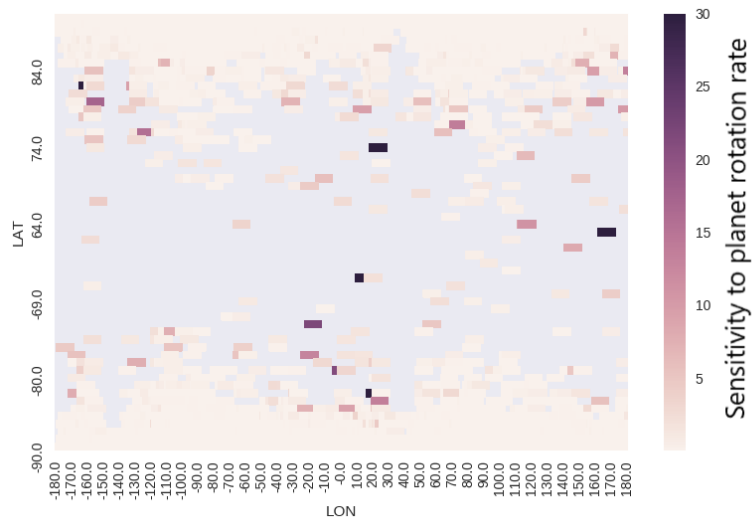


Fig. 6.22: Crossover measurement (Δh) sensitivity to the planet rotation rate ($m. Julian year/arcsec$)

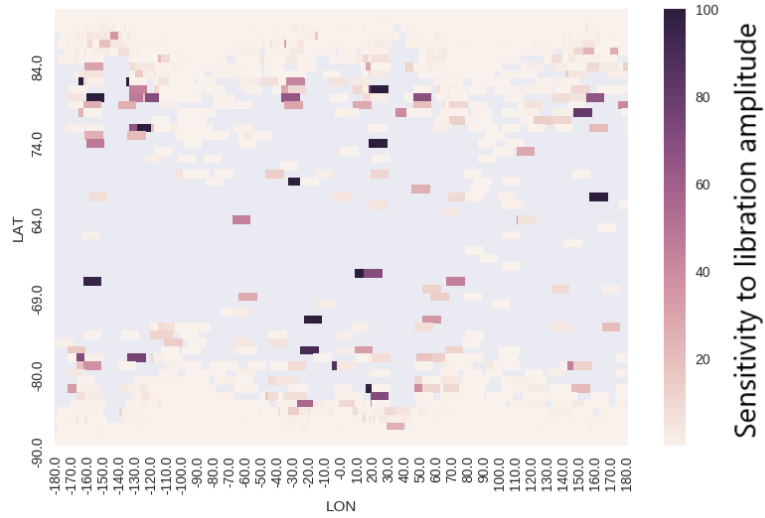


Fig. 6.23: Crossover measurement (Δh) sensitivity to the planet amplitude of libration ($m/arcsec$)

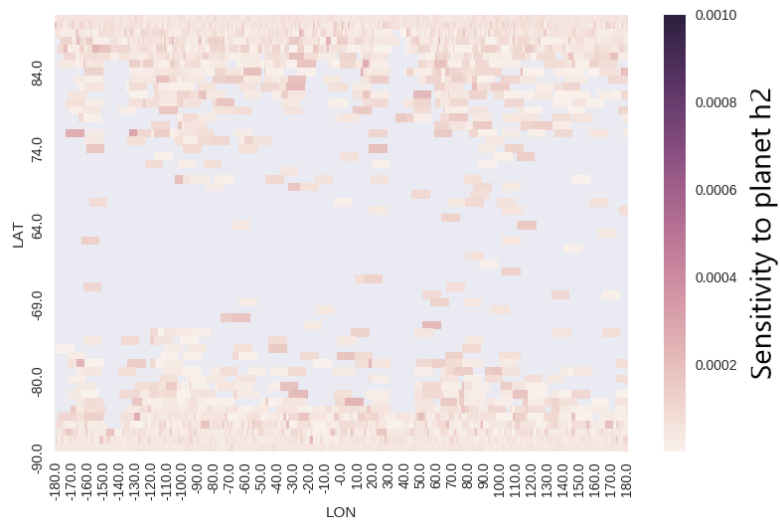


Fig. 6.24: Crossover measurement (Δh) sensitivity to the Love number h_2 (m)

minutes each day to avoid a noticeable negative impact on the measurements of other instruments. As a result, the number of crossover points at lower latitudes can have a huge impact on improving the spacecraft orbit and the planet geophysical parameters. These maneuvers can also be designed to be performed over smooth plains, so that the BELA does not miss an important information about the planet terrain.

7. CONCLUSION AND PERSPECTIVE

7.1 Objectives and approach

The main objectives of BELA are to measure the figure parameters of Mercury, the topographic variations relative to the reference figures and other properties of the surface e.g. local slopes, surface roughness and albedo. However, it is also possible to use the laser altimetry data in the form of crossovers to significantly improve the spacecraft orbit and infer geophysical properties. The main goal of this PhD thesis is to analyse the performance of the instrument in a comprehensive in-orbit performance model and to recommend technical settings, potential calibrations and approaches to enhance the scientific outcome of BELA.

We use the laser altimetry performance model described in [Gardner \[1992\]](#) as our basis and we implement the test results on BELA in the laser altimetry test laboratory of the University of Bern to our modeling of the instrumental noise. We then model the probability of false detection for each observation and based on that, we produce a coverage map over different surface terrains. This results in a performance map over the surface of Mercury and we study the quality of observations and the expected accuracy of the recovery of surface features, e.g. local slopes, roughness and albedo, in different conditions and over different terrains.

Together with this, we also perform a Doppler-only orbit determination and we study the potential contribution of using BELA data at crossover points to the recovery of MPO orbit and of Mercury geophysical parameters. Our extensive modelling of Doppler orbit determination includes gravitational and non-gravitational forces for orbit propagation, desaturation maneuvers and accelerometer noise model and the simulation of Doppler tracking measurements include 2-way X-band and K-band Doppler measurements, station and planetary eclipses, solar plasma noise and the relativistic corrections. We perform several Doppler-only orbit reconstruction tests using daily arcs with noise modulated Doppler data. Then, to study the impact of BELA on improving the orbit and geodesy, we simulate a series of laser altimetry observations around crossover points. Then we set up orbit and geodesy improvement in a least square minimisation of crossover discrepancies. The preliminary results are presented in the last chapter of the thesis.

7.2 *Summary of the results*

Several tests have been performed on the RFM standalone of BELA instrument: Gaussian pulses are sent to the RFM and the measured time of flight, pulse width and pulse energies are compared to the expected ones. We use these laboratory-based performance tests to construct an accurate instrument noise model.

We draw a few main conclusions from these tests. First, systematic biases have been observed in all three laser altimetry measurements (TOF, pulse width and pulse energy); Second, the instrument TOF measurement accuracy in laboratory condition is very high with respect to the requirement. For short pulses and with a spacecraft height lower than 1000 km we set around 1.64 ns (equivalent to 25 cm in range measurement). The accuracy decreases with increasing height and the received pulse width but its RMS is still below 3.35 ns (equivalent to 50 cm in range). Finally, the accuracy of pulse width and pulse energy measurements highly depends on the possibility of removing the systematic bias.

We use the results of the above laboratory-based performance tests to develop a comprehensive performance in-orbit performance model for BELA during its primary mission orbits at Mercury. We use this performance model to evaluate the measurement performance in different conditions and over different terrains.

One of the most important performance parameters of the instrument is the PFD. The PFD determines the working limit of the instrument in different conditions. We assume the signal to be detectable when the PFD is below 10%. The PFD is determined at different gain settings and among them the highest performance happens with gain code 7 (gain code 15 also has a similar performance) and with APD-A gain of 1.5 MV/W. With this gain setting and after considering the effects of degradation, the maximum working limit of the instrument ranges between 1040 to 1180 km over the smooth plains and rough terrains. Therefore the instrument meets the ranging requirement. It also means that BELA will be able to have a full coverage (except for some crater walls) of the whole planet in the first year of the mission even with the highest possible degradation.

Using the high gain settings (gain code of 7 or 15 and APD-A gain of 1.5 MV/W) over the crater walls the working limit ranges between 700 km to 1150. Also for local albedos lower than 14%, the working limit of the instrument would be less than 1050 (even for smooth plains). It means that other than steep crater walls at high altitudes and local dark spots, the rest of the planet will be fully covered by BELA. Over the crater walls, the detection of the pulse will depend on the altitude of the spacecraft and the slope angle of the wall. For instance, in the first two

months of the mission all the crater walls between latitudes of around 80 deg North to 40 deg South will be fully covered and only highly steep crater walls outside this latitude range would not be covered by the instrument.

At the end of the extended mission (two years) the latitude of Periherm will go down to around 40 deg South and as a result the orbital height will increase to around 1300 km over the North pole. As a result of this, the BELA will not be able to cover the area around the North Pole in the last few months of the extended mission, even over smooth plains and with the lowest degradation.

To avoid any danger arising from exceeding the APD breakdown voltages, the recommended HV has decreased to 340 V (correspond to APD-A gain of 0.75 MV/W). In this case, the maximum working limit of the instrument over flat surfaces and with low degradation is expected to be 1050 km and over other terrains or higher levels of degradation, the working limit is always below 950 km. This is 100 km lower than the ranging requirement and as a result the instrument will not be able to cover the area around the South Pole in the first two months of mission. However, considering the rotation of the argument of periherm, the instrument will be able to cover both poles with one year of data. We have to stress that even though with APD-A gain of 0.75 MV/W, the instrument will be able to achieve full coverage by the end of the mission but the density of data around the poles will be considerably lower.

For the TOF (or range) measurement, pointing calibration has the highest impact on performance. Therefore a further calibration of BELA using its own scientific data will be the layout of future. For pulse width and pulse energy measurements, systematic bias calibration plays the same role. However, it is not clear yet how far the systematic biases can be removed. The reason for this, is that the systematic biases are detected using the RFM standalone and using synthetic Gaussian pulses as input. More realistic tests based on non-Gaussian pulses has to be performed to determine whether the instrument has the same behaviour and if the calibration can fully remove the systematic offset.

We present two different methods for surface slope measurement: single shot method and double shot method. We show that the accuracy of double shot is considerably higher than the single shot, however they measure the slope angle in different baselines. The accuracy of double shot slope measurement is always better than one degree, while the single shot method leads to average accuracies between 1.2 to 3.8 degrees. Also, single shot slope measurement error decreases with the slope angle, while the other way around is true for double shot slope measurement. Therefore, one might consider using a combination of both approaches to determine the surface slope of the planet.

For single shot slope measurement, we distinguish between negative errors and positive errors on the slope measurement, which are different over smaller slope angles. Since the absolute slope angle cannot be smaller than zero, the negative error on slope measurement cannot be bigger than the slope angle itself. In smaller slope angles, the negative error goes to zero, while the positive side of error reaches higher values with RMS of 7.7 degrees. With the increase of slope angle, the RMS of this error decreases to a minimum value of 1.8 degrees. Slope measurement error is always lower if a priori knowledge of roughness is available.

[Gunderson and Thomas \[2010\]](#) predict the accuracy in range measurement to be between 25 cm up to 2 meters (before the PFD goes higher than 0.1). The lower limit of this is in agreement with the measurement accuracy of the instrument from laboratory tests and the higher limit is in agreement with the measurement accuracy of in-flight performance analysis, while we predict this errors with higher accuracy and in different conditions and over different terrains. The predicted accuracy of the pulse widths error in [Gunderson and Thomas \[2010\]](#) is between 5 to 20 ns and we predict this accuracy to be in the range of 4-15 ns depending on the altitude and the systematic bias.

[Steinbrügge et al. \[2018\]](#) predicte the accuracy in roughness measurement to be around 1.5 meters, while our study shows a value in the range 0.3 to 0.5 m over smooth or rough terrain. However, we perdict the error to go up to 3.5 m over crater walls. Steinbrügge's study also predicts the minimum detectable terrain slope (using single shot method) at lower altitudes to be 10 degrees and our study shows this value to be around 5-6 degrees. Moreover, we predict that at high altitudes the instrument will only be capable of measuring slopes up to around 15 – 20 degrees, while we expect to be able to detect almost all the surface slopes, including the steepest crater walls, from altitudes lower than 670 km when the APD-A gain = 1.5 MV/W .

One of the improvements in our study with respect to previous publications, is the more accurate modeling of BELA measurement noise by using the latest test results on the BELA. The other very important improvement is that by using an in-orbit model of the laser altimetry and by using a ground model for the Mercury surface, we are able to predict the performance over different regions and terrains with much higher accuracy than before. As a result, it has become clear that the range measurement accuracy cannot be as good as it has been in the laser altimetry laboratory and in the best case scenario (best possible pointing calibration and over a smooth plain) this error will have a value of around 80 cm (whereas the instrument itself is able to detect ranges down to 25 cm in laboratory conditions).

The instrument degradation impact on the measurement accuracies is negligible. However,

it considerably changes the working limits of the instrument. In other words, the instrument will lose more signals with high degradation, but if the return signal is detected, then the measurement accuracies will be almost the same.

By studying the performance over crossover points with temporal proximity, we noticed a good performance in measuring the ΔH (with RMS of around 1.1 m to 1.2 m). This will be valuable for measuring the tidal deformation of the planet and also for the improvement of orbit accuracy using laser altimetry data.

Chapter 6 presents the results of the work that is done on the precise orbit determination of MPO using radio science data and laser altimetry data. The results of the full Doppler orbit reconstruction for 100 days of the mission shows that with three ground stations we reach the best accuracy of about 4.5 m in the norm of position residuals. With two ground stations the accuracy will degrade to around 6.1 m and with one ground station the norm of position residuals will be around 9.5 m. We need to mention that using a single ground station causes a divergence in the orbit recovery of some daily arcs. This problem usually happens during the daily arcs when the spacecraft goes to occultation in each orbital period. We conclude that the imperfect knowledge on non-gravitational forces (especially the desaturation maneuvers) combined with the lack of Doppler observations for more than two thirds of the daily arcs causes this problem. In this situation the accelerometer is not able to estimate the non-gravitational forces with a sufficient accuracy and it causes a failure in the recovery of the orbit. This problem needs to be investigated by using a better model of the accelerometer noise and by adding empirical accelerations to see whether or not the effect of unmodelled dynamics can be absorbed.

In the last part of the thesis, we calculate the sensitivity of crossover discrepancies to the spacecraft orbit, attitude, rotational parameters and tidal deformations. The results show the importance of crossovers at latitudes close to the planet equator. The inverse of these sensitivities is then closely related to the formal errors expected from the recovery of the orbital and geodetic parameters. The presented results of this work is still preliminary and it will be investigated further.

7.3 Recommendations for the improvement of BELA performance

One of the advantages of using a comprehensive in-orbit simulation, is the ability to use this environment to simulate the instrument condition in flight and compare different observations under different conditions and over different terrains. Using this simulation environment, we are able to see what kind of data might be problematic or have bad resolution, what kind of change could improve it, what are the settings that should be used for the instrument to have

the maximum performance and what techniques/weightings can be used to combine different observations.

We highlight two main aspects which would improve the performance of the instrument:

7.3.1 *Gain settings*

The BELA team should consider the possibility of using a APD-A gain higher than 0.75 MV/W to improve the performance of the instrument, but lower than 1.5 MV/W to avoid any danger to it. Also, switching between the gain setting at low and high altitudes can be considered. In this approach, at lower altitudes, the instrument will use the safe low APD-A gain without losing any data and in high altitudes (higher than 850 km), the instrument will switch to high APD-A gain to reach the requirement and detect as much data as possible. We need to point out that changing the gain settings will not impact the quality of the measurements and only changes the working limit of the instrument.

7.3.2 *DTM recovery*

For generating the DTM from the altimetry observations, one can only use the range measurement data. The sigma of range error has different values depending on the slope angle and spacecraft altitude. Unless there is a very good pointing calibration for BELA line of sight, at high spacecraft altitude and over crater walls, the error can get values higher than 10 meters. Because of this, one might consider using other altimetry observation, such as the broadening of the return pulse, to determine the local slopes and integrate them along the ground track to recover the DTM.

Due to the low accuracy of range measurement and high accuracy of the single pulse slope measurement over highly steep surfaces like the crater walls, this approach can be very useful for DTM recovery. In contrary, over the smooth plains, the single shot slope measurement has a bad accuracy, so one can use the double shot slope measurements to recover the local slopes.

The other recommended approach is to use both observations for DTM recovery, but give them different weightings depending on the expected surface slope. This can be done in a closed loop, so that in the beginning we use the current knowledge of the surface features to determine the first weightings and then, after the recovery of the surface features, the updated surface model can be used to update the observation weightings.

7.4 Future studies and possible experiments

We recommend eight pieces of study to further improve the performance of the instrument in the future:

7.4.1 Investigating the potential sources for the systematic biases

The source of the systematic bias that has been observed on the measurements (chapter 2) is not yet known, though the BELA team observed that they might be a product of the pulse detection algorithm that is used in RFM. More tests are needed to confirm or reject this idea. Also, we have to consider that they might be the result of the experimental setup used in the laboratory.

7.4.2 Calibration of systematic biases for all types of return signal

Theoretically, the systematic biases on the instrument measurements can be removed from the observations using the suggested equation in tables 2.2 and 2.3 to improve the quality of the observations. Still, these tests have been performed by using a Gaussian signal sent to RFM, while the real pulses from the ground will not be Gaussian.

To adapt our tests to non-Gaussian signals, we first need to determine the shape of the return pulses based on different terrains that we see on Mercury. Then, another set of similar laboratory performance tests with non-Gaussian pulses should be performed on the BELA flight spare model to confirm whether or not we see the same behavior with non-Gaussian signals.

7.4.3 Optimisation of the pulse families

BELA uses four predefined pulse families to detect the return signal (See section 3 for more details). If the shape of the return signal matches one of the pulse families, the instrument detects the signal. One of the most important advantages of BELA is the possibility of changing the pulse families that are used to detect the signal. We need to be able to properly use this advantage to improve the performance of the instrument.

We recommend to use an optimization algorithm to improve the families of pulse templates that are currently used to detect the pulses in BELA. The performance improvement has been tested in a few special cases and it is shown that, e.g. using pulse families that are combinations of two gaussian signals might be able to improve the performance of the instrument at low SNR values. This study can be done by using both the pulses that were measured during the tests in laboratory and also by using the predicted shape of the return pulses from the different regions and terrains. Some simple tests with the PFD simulation environment has

been performed with different optimized pulse templates. The results of these have confirmed the possibility of having higher instrument working limit by optimizing the pulse families but this needs more investigation.

7.4.4 Pointing calibration study using crossover points

The dominating part of the range measurement error is the pointing uncertainty. Therefore determining the possible alignment offsets caused by launch and due to changes in the thermal environment could dramatically improve the range measurement performance.

One possible approach is to use BELA's range measurement data at crossover point for alignment calibration of a laser altimeter with respect to the spacecraft reference frame. Crossover points, specially in off-nadir situations, are extremely sensitive to the accurate knowledge of the laser altimeter boresight and consequently on the alignment of the laser altimeter instrument. This study needs to be done in a realistic simulation of BELA in-flight around Mercury, such as the one described in section 4.

7.4.5 Improving the orbit and planet geophysical parameters using laser altimetry crossovers

The preliminary results of geodesy improvement using PyXover is presented in section 6.4. This preliminary results includes the sensitivity analysis of crossover discrepancies to the different parameters of orbit and planet geophysics. We will continue this study by finding the final impact of one year laser altimetry crossover data on the improvement of geodesy. Also, we will study the impact of using the observation weighting based on the error model presented in chapter 4 to see if a better weighting of the laser altimetry data will improve the results.

7.4.6 Studying the impact of off-nadir maneuvers for orbit and geodesy improvement

The results of 6.4 show the importance of crossovers at latitudes close to the planet equator. Unfortunately, the orbit of MPO doesn't allow for a high number of crossovers at lower latitudes. Therefore, we suggest to design several off-nadir maneuvers during the period that the spacecraft is passing over the equator. These maneuvers can be performed in a few minutes each day to avoid a noticeable negative impact on the measurements of other instruments. As a result, the number of crossover points at lower latitudes can have a huge impact on improving the spacecraft orbit and the planet geophysical parameters. These maneuvers can also be designed to be performed over smooth plains, so that the BELA does not miss important information about the planet terrain.

7.4.7 Further developing the simulation environment

As shown in chapter 6, the impact of BELA on the orbit determination is studied using a the simulation environment in Bernese software (for the observation model) and the PyXover code to determine the impact of laser altimetry on the orbit and planet geophysical parameters.

The in-orbit simulation environment of BELA in the Bernese software can be further developed to include the impact of BELA on precise orbit determination and gravimetry inside the same environment. For this, the crossover discrepancies can be used as constraint in radial direction. Bernese can also be further developed to solve for other geophysical parameters e.g. tidal deformation, amplitude of libration in parallel with the orbit and gravity field. Possible application of such a code would be to perform any in-orbit simulation test including the off-nadir looking tests for determining some specific geometrical and geophysical parameters of the planet.

7.4.8 In-orbit performance evaluation of Ganymede Laser Altimeter (GALA) for the JUICE Mission

Ganymede Laser Altimeter (GALA) is the laser altimeter of ESA's JUICE mission to Jupiter icy moons. It is designed based on BELA, so that there is a lot of similarities in both laser altimeters. The in-orbit performance model developed during my PhD could be applied to predict the performance of GALA in orbit around Ganymede. For this, the instrument properties in the instrument model have to be adopted to GALA's properties. Then the orbit of the spacecraft and the planet surface model have to be updated accordingly. Finally the same study can be done for GALA and the performance of the instrument including the working limits, TOF, pulse width, pulse energy can be evaluated. Also the accuracy of the measurement of surface properties, e.g. surface slope, roughness and albedo variations can be studied in the same environment.

Appendices

Appendix A

MPO RELATIVE ORBIT ERROR MODELLING USING THE BERNESE GNSS SOFTWARE: A TECHNICAL REPORT ON BELA

A.1 Scope of the report

This report provides a measure of the sensitivity of the MPO orbit propagation to measurement errors in the initial conditions. This is needed to describe the accuracy of the in-flight calibration of the BELA instrument relatively to the SIMBIO-SYS instrument onboard MPO. We define the relative orbit error as the error that would get on MPO position after propagating its orbit for 1 minute from the initial condition, also affected by experimental errors.

A.2 Introduction

The BELA to SIMBIO-SYS calibration approach consists in using these instruments to observe the same area on the surface of Mercury. Thus, the link between the instruments is established through the ground observations. The problem, which arises with this approach is that coordinates of ground observations are subject to different errors. The relative orbit error is one of the sources of error in this process. In order to model the MPO orbits and calculate the relative orbit error, we used the Bernese GNSS Software (BSW, Dach, 2015), which has been developed at the astronomical institute of the University of Bern and has been used for satellite orbit determination since 1988. We added some routines to the software to use it for orbit modelling of interplanetary trajectories.

A.3 Assumptions

The nominal initial position of the probe depends on the orbit determination method. Here we assume the current ESA initial navigation accuracy and we assume that we cannot use other techniques like VLBI. With these assumptions, the orbit determination accuracy at the beginning of mission would be around 10 meters in the line of sight of Mercury from Earth and 100 meters in other orthogonal directions (we assume this is a 1-sigma error). The initial epoch for our modelling is assumed to be the current estimated arrival date of MPO to Mercury, i.e., 27/03/2025 - 22:14:32.14

A.4 Modelling the orbit

In our orbit propagation, we use the d/o 50 gravity field Hgm005 (derived from NASA Messenger data). Moreover, we model the gravitational effect of the Sun and of other planets on the orbit of MPO. We also assume a cannonball model for the spacecraft (With the area to mass ratio of 0.01 kg/m²) to take into account the effect of solar radiation pressure. In our model the effect of IR radiation and albedo from the surface of Mercury on the orbit of the spacecraft are ignored because their effect is at least one order of magnitude smaller than the effect of solar radiation pressure (Stanbridge et al, 2011) so that their effect on the orbit after 1 min would be negligible. With these assumptions, the MPO orbit has been propagated over one day and verified against DLR provided orbit. (Figures 1, 2 and 3)

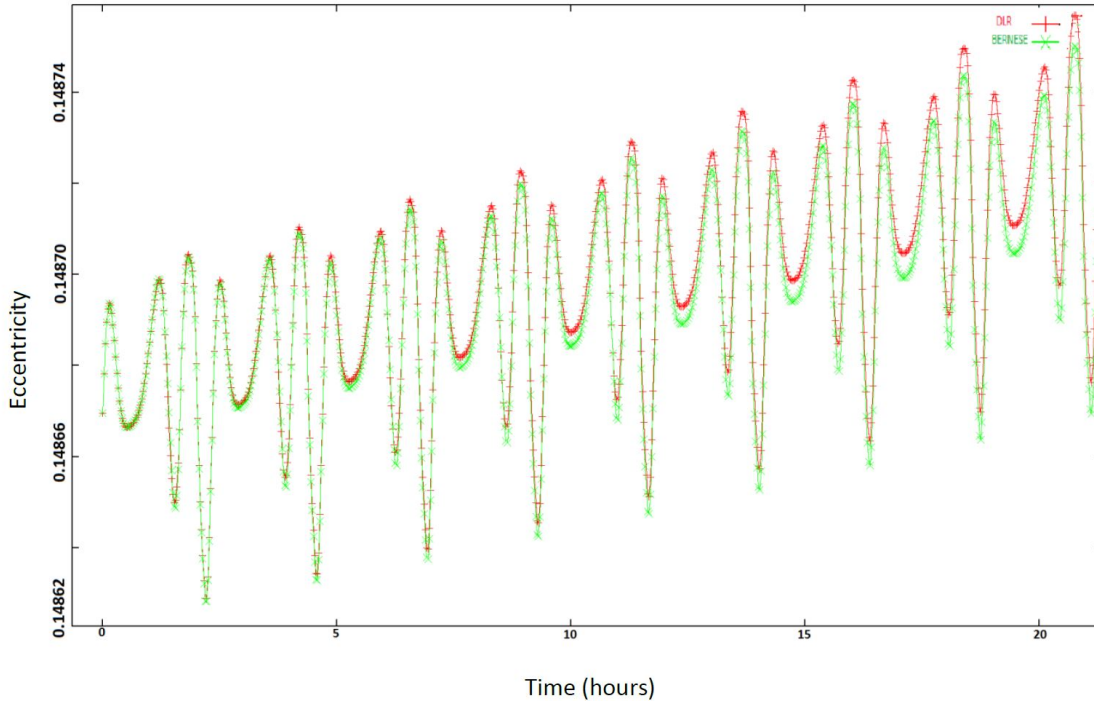


Fig. A.1: Bernese propagated orbital eccentricity against DLR's propagated orbit

A.5 Approach

We assume the modelling error for MPO position at time t_0 to be :

$$dr(t_0) = r_{model}(t_0) - r_{true}(t_0) \tag{A.1}$$

At time $t_1 = t_0 + 1 \text{ min.}$, we then have a position error as below:

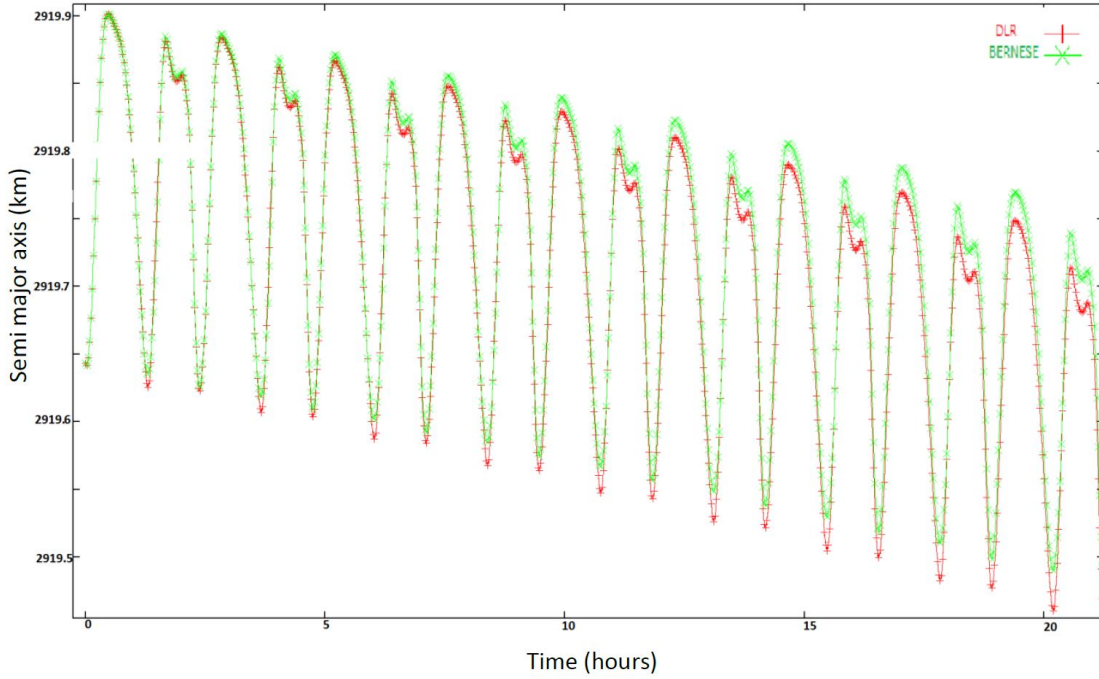


Fig. A.2: Bernese propagated orbital semi major axis against DLR's propagated orbit

$$dr(t_1) = r_{model}(t_1) - r_{true}(t_1) \quad (\text{A.2})$$

What we are interested in is $|dr(t_1) \backslash dr(t_0)|$, i.e. the relative orbit error. The question now is how to construct $r_{model}(t)$ and $r_{true}(t)$. For $r_{true}(t)$ we can assume a true initial state vector, a true gravity field and then propagate the trajectory from t_0 to t_1 . The state vector at the initial epoch 27/03/2025 – 22 : 14 : 32.14 is

$$[144.01056, -2127.59657, 2545.080057, -0.578022, -2.193193, -1.304730]$$

The coordinate system for the state vector is the Mercury centric J2000 frame. the positions are given in km and the velocities are in km/s. To compute r_{model} we can consider three different types of modelling errors: The error due to determination accuracy of the initial position, of the initial velocity and the error due to uncertainties in the gravity field coefficients. Here we neglect the effect of initial velocity and focus on the other two. To test the impact of uncertainties in the gravity field we used four existing gravity field models of Mercury to propagate the trajectory with the same initial state vector and compare the final positions after 1 minute. In this study, changing the gravity field model resulted in 2.2 cm $1 - \sigma$ error after 1

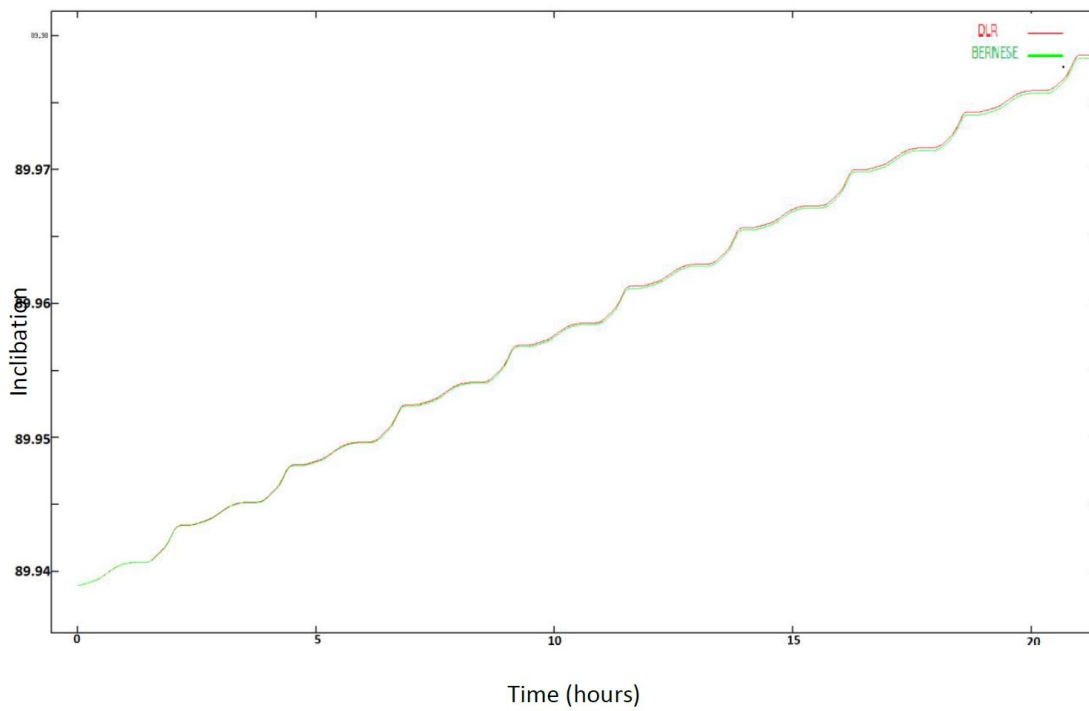


Fig. A.3: Bernese propagated orbital inclination against DLR's propagated orbit

minute, which is negligible. Now we want to model a certain position error for $r_{model}att_0$ using the same velocity and gravity field as for r_{true} . We can rewrite the relative orbit error as:

$$\begin{aligned} \text{Relative orbit error} &= | dr(t_1) - dr(t_0) | \\ &= | r_{model}(t_1) - r_{true}(t_1) - r_{model}(t_0) + r_{true}(t_0) | \\ &= | r_{model}(t_1) - r_{model}(t_0) - r_{true}(t_1) + r_{true}(t_0) | \quad (\text{A.3}) \end{aligned}$$

By setting $dr_{model} \equiv r_{model}(t_1) - r_{model}(t_0)$ and $dr_{true} \equiv r_{true}(t_1) - r_{true}(t_0)$, we have:

$$\text{Relative orbit error} = | dr_{model} - dr_{true} | \quad (\text{A.4})$$

For calculating the relative orbit error, we run the BSW with 200 different initial positions randomly distributed around the true initial position. $\sigma_1(t_0) = [10, 100, 100]m$. We use 5 sec integration step size and in each case, we determine the final position after 1 min. The final positions then used to calculate the standard deviation of the relative orbit error are in the same coordinate frame we had for the initial errors (x- line of sight of Mercury from Earth, y-orthogonal direction to x in ecliptic plan and z- orthogonal to x and y). In a second step, we assume that the accuracy of the initial state is improved by one order of magnitude using VLBI or after orbit reconstruction. Therefore, the 1-sigma error would be 1 meter in line of sight direction and 10 meters in other directions $\sigma_2(t_0) = [10, 100, 100]m$. Then we propagate the orbit 200 times.

A.6 Results

As a result we get that when the initial position error standard deviation is 10 meters in the line of sight and 100 meters in other directions, the relative orbit error ($(t_1) - dr(t_0)$) after 1 min is 1.1 cm in line of sight and about 11 cm in other directions. $\sigma_{1(\text{relativeerror})}(t_1) = [1.1, 10.7, 11.9]$ cm. On the other hand, when we assume that the initial position error is one order of magnitude smaller, we get a relative orbit error after 1 min of 0.1 cm in line of sight and 1 cm in other directions. $\sigma_{2(\text{relativeerror})}(t_1) = [0.1, 1.1, 1.1]$ cm. Therefore, we can conclude that the relative orbit error after 1 min. is negligible caused by uncertainties in the initial position determination and the gravity field.

Appendix B

SUBMITTED PAPER ON PLANETARY AND SPACE SCIENCE JOURNAL

Comprehensive in-orbit performance evaluation of BepiColombo laser altimeter (BELA)

Alireza Hosseiniarani^{a,*}, Stefano Bertone^{c,d}, Daniel Arnold^b, Thomas Beck^a, Alexander Stark^e, Hauke Hussmann^e, Clemence Herny^a, Antoine Pommerol^a, Adrian Jäggi^b, Nicolas Thomas^a

^aPhysics Institute, University of Bern, Switzerland

^bAstronomical Institute, University of Bern, Switzerland

^cNASA Goddard Space Flight Center (GSFC), Code 698, 8800 Greenbelt Road, Greenbelt, MD 20771, USA

^dCenter for Research and Exploration in Space Science and Technology, University of Maryland Baltimore County, 1000 Hilltop Circle, Baltimore MD, USA

^eGerman Aerospace Center (DLR), Berlin, Germany

Abstract

The BepiColombo Laser Altimeter (BELA, [Thomas et al., 2007](#)) is on its way to Mercury on board the Mercury Planetary Orbiter (MPO), one of the two spacecrafts of the European Space Agency’s BepiColombo mission ([Benkhoff et al., 2010](#)). It will arrive at Mercury by 2025 and start its measurements of Mercury’s surface. The goal of this study is to analysis the performance of BELA by determining the in-orbit measurement quality and recovery of surface features by using a comprehensive performance model for BepiColombo laser altimeter.

To determine the performance in-flight, we first model the probability of false detection for each observation and based on that, we produce a coverage map over different surface terrains. Then we use the laser altimetry performance model described in [Gardner \(1992\)](#) as our basis and we implement the end-to-end test results on BELA in the Starsim laboratory of the University of Bern to our modeling of the instrumental noise.

Finally, we produce a performance map over the surface of Mercury and we study the attainable topography and the expected accuracy of the measurements of surface properties e.g. local slopes, surface roughness and albedo in different conditions and over different terrains. We also suggest potential calibrations which could result in improved performance.

Keywords: BELA; laser altimetry; Performance; Mercury; Topography

1. Introduction

1.1. Laser altimetry

Laser altimetry is a powerful remote sensing technique used in both Earth and planetary science. The basic concept is rather simple: we measure the time-of-flight (TOF) of a pulse of light from an orbiter to the surface and back. The range z from the laser to the illuminated spot on the surface is related to the laser pulse time-of-flight ΔT by

$$z = c \frac{\Delta T}{2}, \quad (1)$$

with c the speed of light. This means that a 1 ns delay corresponds to around 15 cm in range. As the laser operates several times per second, e.g. at 10 Hz, the repeated laser footprints provide a terrain profile and finally measurements obtained at different orbits allow the construction of a global terrain model of the planet.

1.2. BELA

BELA is the laser altimeter of the ESA BepiColombo mission to Mercury and has successfully launched on 20 th October 2018 ([Benkhoff, 2018](#)). The main objectives of BELA are to measure the figure parameters of Mercury, to establish accurate reference surfaces, topographic variations relative to the reference figures, surface roughness, local slopes and albedo variations, also in permanently shaded craters near the poles.

The instrument was built in collaboration of several institutions and industries in different countries. The main contributors were the Physikalisches Institut in Bern, the DLR Institute of Planetary Research in Berlin and the Instituto de Astrofísica de Andalucía in Spain as well as the Max-Planck-Institute for Solar System Research in Germany.

BELA uses the "direct-detection" approach to laser altimetry. Pulses with high energy (~ 50 mJ) at 1064 nm are emitted from a Q-switched laser at 10 Hz. The emission time of each pulse is measured by a photodiode. The laser beam is reflected from the surface and received around 5 ms later at a 20 cm diameter telescope. The image is refocused onto a silicon avalanche photodiode (APD) through a narrow bandpass interference filter. The signal is then sampled and fed to a digital pulse discrimination electronics. This system determines the time of flight (and therefore range), the integrated pulse intensity, and its width. The data are passed to a digital processing

*Alireza Hosseiniarani
Email address: seyedalireza.hosseiniarani@space.unibe.ch
(Alireza Hosseiniarani)

unit which controls the operation and services the spacecraft interface (Thomas et al., 2007).

BELA will provide 2 ns time resolution which is commensurate with the expected knowledge of the spacecraft position. The experiment will provide return pulse intensity and width information allowing for an assessment of surface albedo and roughness at 20 m scales including in unilluminated polar craters. The instrument properties (Steinbrügge et al., 2018) are summarized in Table 1 in order to get a complete overview about the assumptions made for the modeling.

We define two kinds of gain for BELA: The *Avalanche Photodiode Assembly (APD-A)* gain, which is a function of APD high voltage (HV) and determines the AEU input voltage amplification and the *instrument gain code*, defining the voltage gain factor of the *Analogue Electronics Unit (AEU)*. The instrument gain code has an integer value between 0 to 15, corresponding to the lowest and highest amplification, while the APD-A gain is between 0.75 MV/W (Mega-Volts / Watt) to 1.5 MV/W depending on the HV set point.

An APD-A gain of 0.75 MV/W corresponds to high voltage (HV) set point of 370 V, while an APD-A gain of 1.5 MV/W corresponds to the HV set point of 340 V. The recommended HV set point was reduced from 370 V to 340 V to avoid any danger arising from possibly exceeding the APD breakdown voltage. We need to stress that 340 V produces a responsivity (gain) that is considerably lower than can be achieved in optimum condition.

1.3. Previous studies and goals

Gunderson et al. (2006) presents an analytical model of the BELA system performance. The model draws on a diverse set of instrument and environmental parameters to predict signal-to-noise ratios, false detection probabilities and range measurement uncertainties. The model shows that the baseline instrument is capable of meeting the performance requirements of PFD < 0.1 and range error < 10 m out to altitudes of 1050 km. Gunderson and Thomas (2010) extended the above model to contain the time-varying orbital conditions and instrument degradation over the mission life time. Also measurement accuracy predictions has been broadened to include albedo and return pulse width in addition to range accuracy.

Steinbrügge et al. (2018) presents a semi-analytical instrument performance model, in which signal-to-noise ratio, single shot probability of false detection, range errors and the accuracy of pulse width reconstruction are estimated. It also performs numerical simulations of the instrument performance expected in orbit about Mercury and studies the measurement accuracy of topography, surface slopes and roughness, and tidal amplitude.

In this study, we focus on a comprehensive performance analysis for BELA by including all of the above factors synthesised in one single numerical model. Moreover, we base our analysis on a more accurate instrument noise model based

on the noise information gathered from the laboratory tests on BELA. Our modelling contains an instrument degradation model, a planet surface model and an in-flight model of the laser altimetry. We use these models to have an extensive and accurate performance evaluation of BELA on its orbit around the planet Mercury.

In section 2, we present our extensive modeling of BELA in orbit around Mercury. Section 3 presents our results about the different measurements noises and the working limits of the instrument. Finally, we summarize our conclusions in section 4.

2. Modeling

2.1. In-flight model of the laser altimeter

Our modeling consists of several different components, as detailed in figure 1. In particular, we model the error budget for the three main measurements by BELA: Time of flight (TOF), pulse width and pulse energy measurements, including the noise directly from the instrument, the noise caused by uncertainties in the dynamics of the system and the noise affecting measurements due to the properties of the surface. Therefore, our setup consists of a model for the planet surface properties (e.g. local height, slope, roughness), in a dynamical model for the rotation of the planet and one for the orbit and attitude of the spacecraft carrying the instrument.

We use this model to predict the accuracy of the instrument in measuring the surface properties. We also study the working limit of the instrument by modeling the PFD for each observation.

We determine a set of observation epochs for BELA, based on a repetition rate of 10 Hz for the whole nominal mission. At these epochs, we use the dynamical model to determine the position of MPO around Mercury and the rotational state of the planet itself. Then using the spacecraft attitude and knowing the position of the instrument inside the spacecraft frame, we calculate the onward laser leg, the incidence time and position on the planet surface. Then from the planet terrain model, we determine the surface properties at the laser spot (see section 2.4) and we calculate the properties of the return signal. Then, we calculate the laser return leg and finally, using the instrument model and considering the noise from different sources, we determine the TOF, pulse width and pulse energy measurement errors (Hosseiniarani et al., 2018).

2.2. Laser altimetry noise model

2.2.1. TOF measurement noise model

The time of flight (TOF) measurement, like any other observation is not ideal. The TOF measurement error is a combination of the following error sources (Gardner, 1992):

- Error due to surface slope:

$$\sigma(\Delta T)_{slope} = \frac{2\sqrt{2}}{C} \left[\frac{F}{N} + \frac{1}{K_s} \right]^{\frac{1}{2}} z \tan \theta_t \tan S \quad (2)$$

Table 1: Instrument parameters in the beginning of life used for the modelling

| Parameter | Symbol | Value | Unit |
|--|-------------|---------------|-----------------|
| Laser pulse energy | E_t | 50 | mJ |
| Laser pulse width (1- σ , Gaussian) | σ_0 | 2.2 | ns |
| Shot frequency | f | 10 | Hz |
| Wavelength | λ_T | 1064 | nm |
| 1/e ² beam divergence (half cone) | Θ_T | 25 | μrad |
| Telescope radius | r_R | 0.1 | m |
| Field of view of the receiver telescope | Θ_R | 450 | rad |
| Transmission of receiver optics | T_r | 76.7 % | |
| Gain | M | 122.4 – 242.6 | |
| Analog (TIA) bandwidth | B_0 | 25 | MHz |
| Sample resolution | adc | 12.5 | ns |

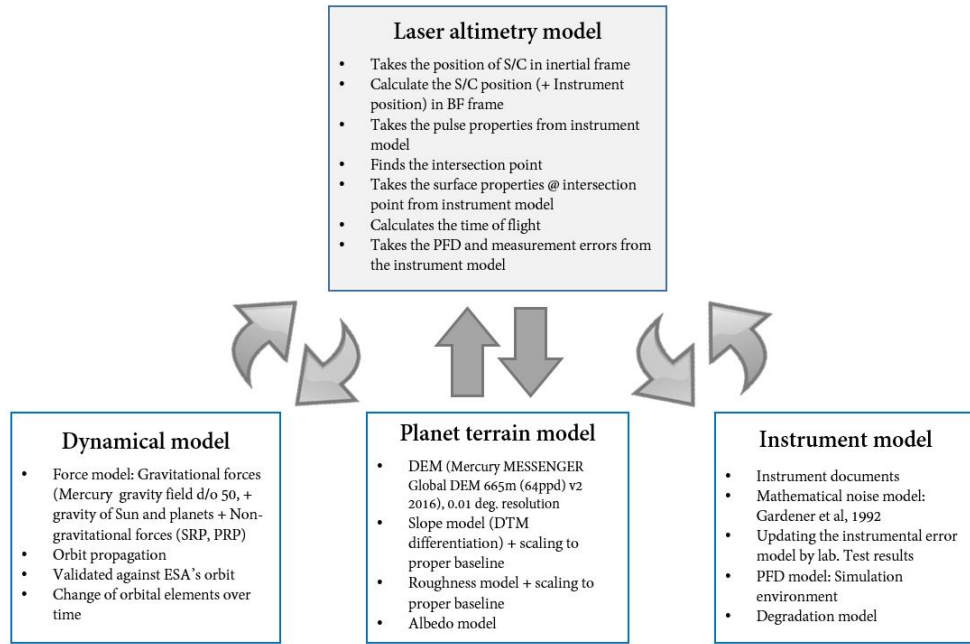


Figure 1: Modelling of an in-flight laser altimeter

- Error due to surface roughness:

$$\sigma(\Delta T)_{Roughness} = \frac{2}{C} \left[\frac{F}{N} + \frac{1}{K_s} \right]^{\frac{1}{2}} Std(\Delta \zeta) \quad (3)$$

- Error due to pointing uncertainties:

$$\sigma(\Delta T)_{PointingError} = \frac{2\sqrt{2}}{C} z \tan S Std(\Delta \Phi) \quad (4)$$

- Instrumental error

where

- F: Excess noise factor of the detector
- N: Mean number of total detected photons
- K_s : Ratio of receiver area to speckle correction area
- θ_t : Laser beam divergence HW @ $e^{-1/2}$ (rad)
- C: Speed of light (m/s)
- z: Altimeter altitude (m)
- S: Surface slope (rad)
- $\Delta \Phi$ pointing uncertainty

The total TOF measurement error can be formulated as the quadratic sum of the above values. The last component of the TOF measurement is the instrumental error which just depends on the instrument properties and pulse detection algorithm. This error is called "system error" in the work of Gardner, but here,

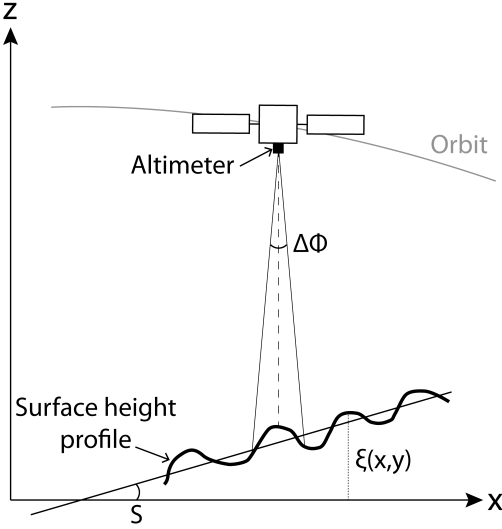


Figure 2: geometry of a beautiful laser altimeter and ground target

for avoiding a confusion between this and the systematic bias in different measurements, we call this component "instrumental error".

BELA uses a digital pulse sampling and performs a pulse fitting on the signal using a specific pulse detection algorithm. This technique is different from older laser altimetry techniques which try to detect the analog signal among the noise and is more advantageous since it leads to a better TOF resolution. As a result of using this algorithm, the nature of BELA instrumental errors are different from the instrumental errors in [Gardner et al, 1992]. Therefore, we do not use the proposed equation in [Gardner et al, 1992] for instrumental errors and instead we measure this error by analysing the test results on BELA at the laser altimetry test laboratory of the University of Bern. The summary of the results are provided in section 2.5 and the detail of this study is presented in section ??.

2.2.2. Pulse width measurement noise model

According to Gardner (1992), the return pulse from the planet surface, experiences a broadening because of the surface slope, the surface roughness and the beam curvature, resulting in a total error σ_t , so that

$$\sigma_t = \sqrt{\sigma_0^2 + \sigma_{bc}^2 + \sigma_r^2 + \sigma_s^2} \quad (5)$$

with

$$\sigma_{bc} = \frac{2z}{c} \tan^2 \theta_t \quad : \text{beam curvature} \quad (6)$$

$$\sigma_r = \frac{2}{c} Std(\Delta\zeta) \quad : \text{roughness effect} \quad (7)$$

$$\sigma_s = \frac{\sqrt{2}z}{c} \tan \theta_t \tan S \quad : \text{slope effect} \quad (8)$$

Where $Std(\Delta\zeta)$ is the definition of roughness in our work. Due to the limited bandwidth of the receiver system, the analog signal experiences an additional broadening (Gundersen and Thomas, 2010), which can be expressed by

$$\sigma_p = (2\sqrt{2\pi}B_0)^{-1} \quad (9)$$

leading to a total temporal width of the return pulse after the receiver electronics

$$\sigma = \sqrt{\sigma_t^2 + \sigma_p^2} \quad (10)$$

The full width half maximum (FWHM) of the pulse can be calculated as

$$FWHM = 2\sqrt{2 \ln 2} \sigma \quad (11)$$

Fig. 6 provides the FWHM of the return pulse width in different altitudes and over different terrain types. According to the model described in Gardner (1992), the error on pulse width measurement has the same component as the TOF error with the difference that the pointing error has no impact on the results. The components of pulse width error can be calculated using

$$Std(\sigma)_{roughness} = \frac{2}{c} \left[\frac{F}{2N} \right]^{\frac{1}{2}} Std(\Delta\zeta) \quad (12)$$

and

$$Std(\sigma)_{slope} = \frac{2}{c} \left[\frac{F}{N} \right]^{\frac{1}{2}} z \tan \theta_t \tan S \quad (13)$$

The third component of the pulse width measurement is the instrumental error in the pulse width measurements. For the same reason as TOF error, we do not use the proposed equation in [Gardner et al, 1992] for instrumental errors and instead calculate this error by analysing the tests results on BELA at the laser altimetry test laboratory of the University of Bern that is explained in section 2.5.

2.2.3. Pulse energy measurement noise model

The pulse energy measurement is not sensitive to the local slope and roughness and it is independent of the pointing uncertainties. Thus, for determining the performance in pulse energy measurement, we only consider the instrumental errors from the laboratory based tests.

In order to compute the value of Eqs. (2) to (4) and also (12) to (13) for realistic operative configurations of BELA, we developed a detailed modeling for both ESA BepiColombo orbit and attitude and for Mercury surface properties.

2.3. Dynamical model of Bepicolombo spacecraft

2.3.1. Spacecraft orbit

For modelling the orbit of MPO around Mercury, we use an extensive force model, including Mercury gravity field GGMES_100V07 (up to degree and order 50), solid tides, solar and planetary -including albedo and IR- radiation pressure, third body

perturbations and relativistic effects including the Schwarzschild, Lense-Thirring and de Sitter terms. To consider the effect of non-gravitational forces on the spacecraft, we use a 33-plates macromodel of MPO, including both visible and IR optical properties.

With these assumptions, the MPO orbit has been propagated and verified against orbits provided by ESA (Jehn, 2015). This modelling is done using the planetary extension of the Bernese GNSS Software (Dach et al., 2015) that has been developed at the Astronomical Institute of the University of Bern (AIUB).

The Mercury Planetary Orbiter (MPO) is a three-axis stabilised spacecraft with a perihelion altitude of 480 km and an aphelion altitude of 1508 km. The orbit is polar with its perihelion over the equator to ensure a global coverage of the planet and has a period of 2.3 h. At the start of mission the argument of the perihelion is around 16 degree, the altitude of spacecraft over the North Pole is around 800 km and over the south pole is around 1050 km. But the orbital elements drift over time and the argument of perihelion goes to around -40 degree at the end of extended 2-year mission (Jehn, 2015; Luedicke, 2014).

Also the orbit becomes more elliptical, so that after two years of mission (one year of nominal and one year of extended mission), the perihelion is expected to lower to 260 km and the aphelion is also expected to increase to around 1720 km. It has to be mentioned that considering the uncertainties of the gravity field determined by the analysis of the NASA MESSENGER radio science data (e.g., Genova et al. (2019)), the orbit of the spacecraft after two year might be different from the predicted orbit and in the worst case scenario, the orbit can get even below 100 km after two years in Mercury orbit (Luedicke, 2014).

2.3.2. Pointing uncertainty

The Attitude and Orbit Control Subsystem (AOCS) contribution to attitude estimation varies between 1.06 to 2.09 arc seconds, depending on the AOCS configuration (e.g. number of Gyro and star trackers involved)(Casasco, 2017). Nevertheless, the biggest contribution to BELA's attitude estimation is caused by thermo-elastic effects which correspond to deformations of the spacecraft optical bench and distortions between the star trackers' lines-of-sight and the BELA line-of-sight.

BELA's pointing performance can be compatible with the 20 arc seconds scientific requirements only if the static and slowly-varying thermo-elastic distortions can be cross-calibrated against camera data and the orbital position of the spacecraft is known with high accuracy by means of the radio science experiment (Marabucci, 2012).

Several approaches for in-flight calibration of BELA's line of sight are suggested. Among them, in-flight cross-calibration with high spatial resolution images taken by BepiColombo on-board camera provides the best cross-calibration accuracy and allows compliance with the requirement. According to Casasco

(2017), such an in-flight calibration can reduce the pointing uncertainty to an average value of 15 arc seconds (2σ).

Hence, we assume this value as our first estimate of the pointing error. Moreover, we take into account the possibility of further calibrations of BELA based on, e.g., data analysis at crossover points. For this reason, we compare the measurement errors resulting from three possible pointing error values: the nominal 15 arc second error; 7.5 arc seconds (calibration of 50% of pointing error); 3 arc seconds (a best case scenario with an 80% decrease in pointing error).

2.4. Mercury terrain model

For determining the in-flight performance of BELA, we need to have a realistic model of the surface of Mercury. We use the MESSENGER MLA and camera derived digital elevation model (DEM) (Becker et al., 2016), local slopes and roughness and a reflectance model.

2.4.1. Surface elevation model

We linearly interpolate the DEM from Becker et al. (2016) which has a resolution of 665.24 meters/pixel.

2.4.2. Terrain types

We consider two types of terrains in our simulation of the Mercury's surface, according to Figure 1 of Denevi et al. (2013): a) smooth plains and b) rough (cratered) terrains. On the surface of Mercury, topographic depressions turn out to be rather smooth, whereas most of the highlands are heavily cratered (Yang et al., 2016).

2.4.3. Local slope model

Slope and roughness have different definitions in different studies. According to the model presented in Gardner (1992), we differentiate the vertical linear variation of surface height, which we assume as slope, from the quasi-random height variation, i.e. the RMS, of which is assumed as roughness in our model (Figure 2).

The distribution of slopes is only known for baselines larger than the average laser altimetry footprint (the size of footprint increases with the altitude). To model the expected average slopes within the laser altimetry footprint, we fit the distribution of average slope angles given in Pommerol et al. (2012) using an exponential law $y = Ax^b$. We get $A = 1.182$ and $b = -0.416$ for the smooth plains and $A = 2.533$ and $b = -0.311$ for the rough terrains (see Fig. 3). Based on this fit, we extrapolate the expected slopes down to the laser altimetry footprint sizes.

We model the local slopes by differentiating the DEM, then rescale it so that the average slope at each baseline is consistent with the extrapolated values from Pommerol et al. (2012). This

extrapolation predicts an average slope of around 7 degrees over a 20 meter baseline. We need to stress that the slope angles over meter sized baselines is not known for Mercury and our derived average slope is coming from the best model to our knowledge. In reality there might be one or multiple break points within the power law for slope extrapolation. As consequence the fit at smaller baselines might be significantly different and the average slope might be smaller than this prediction. Since there is no information available on this we continue with our extrapolation results, but later we perform a sensitivity study to find the impact of smaller slopes on instrument measurement errors.

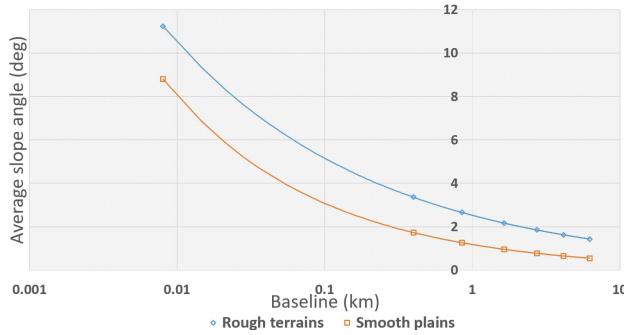


Figure 3: Extrapolation of average slope to smaller baselines

2.4.4. Surface roughness model

Similar to the slope angles, the mean roughness of mercury's surface is only known in kilometer-scale baselines. Therefore, we fit a power law such as

$$y = Ax^b \quad (14)$$

to values from [Susorney et al. \(2017\)](#) to extrapolate the average roughness at the laser altimetry footprint size for different terrain types (Figure 4). We get $A = 57.91$ and $b = 0.8769$ for smooth plains and $A = 69.49$ and $b = 0.8769$ for rough terrains.

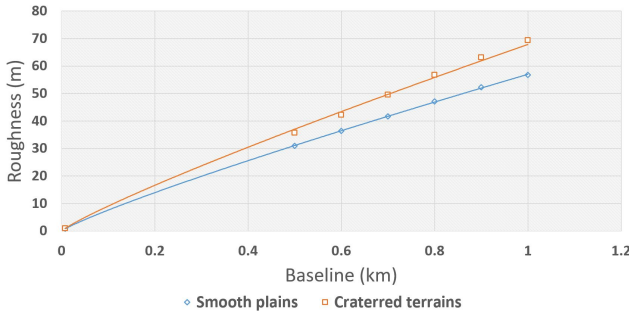


Figure 4: Extrapolation of roughness to smaller baselines

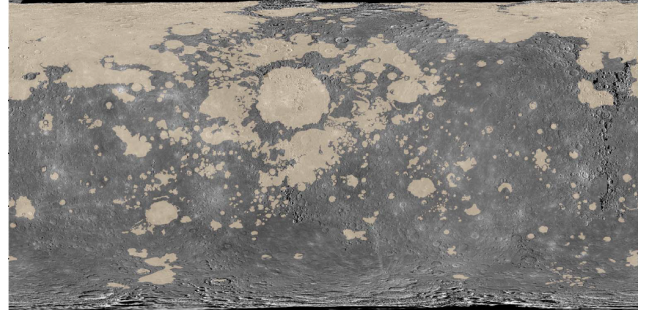


Figure 5: Mercury surface terrains. khaki: Smooth plains; gray: rough terrains ([Denevi et al., 2013](#))

2.4.5. Surface reflectance model

Maps are available from MLA data or from MESSENGER MDIS camera data (?), but due to the insufficient accuracy at the laser altimeter wavelength of $1 \mu\text{m}$, we rather base our analysis on the distribution of reflectance provided in [J. \(2015\)](#), which is an asymmetrical Gaussian with average value 0.19.

2.5. BELA instrument noise model

The modelling of the BELA instrument in our simulation is based on the experimental results obtained in the Starsim laboratory of the University of Bern. We send several thousand Gaussian pulses to the Range finder module (RFM) standalone and test the instrumental performance on determining the range, pulse width and pulse energy.

The detailed investigation is presented in [HosseiniArani \(2019\)](#). To summarise, a systematic offset in TOF, pulse width and pulse energy measurement noises seems to be present depending on the altitude and gain settings. Further assessment of these issues shall be investigated in future work. The pulse width error contains both random errors and biases terms due to laser divergence and receiver impulse response. These terms can be subtracted from the pulse width measurement. Knowing the specifications of the instrument, it is possible to calibrate the systematic part of this error ([Gardner, 1992](#)).

We also see a scale error when we measure the pulse energy, *i.e.* a systematic bias in the measured pulse energy that is proportional to the amount of expected pulse energy. To improve the instrumental accuracy, such an offset should be removed from the measurements. In our analysis, we assume only the random noise after removing the systematic biases on the measurements.

2.5.1. Instrument degradation model

According to different studies by [Gunderson and Thomas \(2010\)](#), [Kallenbach et al. \(2013\)](#), [Heesel \(2014\)](#) and [Metz \(2014\)](#), there will be three major instrument degradation affecting the

Table 2: Instrument laboratory-based performance before and after calibration for systematic offset

| Measurement | Altitude | Error STD |
|----------------|-----------|-----------|
| Time of flight | < 1000 km | 1.00 ns |
| | ≥ 1000 km | 1.28 ns |
| | total | 1.13 ns |
| Pulse width | <1000 km | 4.2 ns |
| | ≥ 1000 km | 6.2 ns |
| | total | 5.3 ns |
| Pulse energy | < 1000 km | 18 % |
| | ≥ 1000 km | 26 % |
| | total | 20 % |

instrument: The degradation of the laser power, the degradation of the physical transmission of receiver optical subsystem (ROSS) and the degradation of the APD bulk dark current.

BELA delivers at least 300 million laser pulses with 50 mJ. In the study by [Kallenbach et al. \(2013\)](#), a BELA laser life model, containing flight representative optics, passed the required 300 Mshots of operation at 10 Hz repetition rate. This life model shows a initial power degradation of around 10% after about four million shots that is presumed to be caused by a phenomenon known as "infant mortality" (See figure 7 of [Kallenbach et al. \(2013\)](#) and is probably the influence of early mortality of the diode laser bars. When present, this typically occurs during the first 10 to 20 MShots of operation. This reduction in laser power could be compensated for by increasing the pump time.

A degradation of 8.3% has been measured after 200 kRad of gamma irradiation and a total degradation of 11.3% has been measured following an additional 200 kRad of proton irradiation (See Fig. 9 of [Kallenbach et al. \(2013\)](#)). This degradation too could be compensated by increasing the pump time from (typically) 125 μ sec to 200 μ sec. However, the BELA laser should only experiences up to 20 krad of irradiation during the full mission duration of BepiColombo at its well-shielded location ([Kallenbach et al., 2013](#)).

Considering all these laser degradation effects effects together, we study three possible scenarios for laser power degradation: no degradation of the pulse energy during the nominal life time (through compensation); a 10% degradation (either from the "infant mortality" phenomenon or from the bad shielding against radiation); a 20% degradation due to uncompensated effects of both infant mortality and radiation in space (worst case scenario).

The degradation also effects the performance of BELA receiver. The ROSS transmission was measured to be 76.7 % during the tests at the University of Bern. But according to the BELA reports by [Heesel \(2014\)](#) and [Metz \(2014\)](#), this value at

the end of the nominal life is expected to be 67.3%. Since the degradation of ROSS transmission is due to the radiations and it starts from the launch date, we use the value for EOL for the whole simulation of two years of mission.

The last parameter that we expect to degrade is the APD bulk dark current. The value of this parameter at the BOL is 50 pA, but according to [Gunderson and Thomas \(2010\)](#), we expect an increase up to 100 pA.

Four degradation scenarios will be considered in the simulations. First, the beginning of life condition with no degradation at all. Second, a low degradation where we only assume the degradation of ROSS transmission. In this scenario, it is assumed that the laser power can be compensated and there will be no decrease in the power. Considering that there is a redundant laser, this will be the most likely scenario for the time the spacecraft arrives Mercury.

Third, we assume a medium level of degradation, where we also assume a 10 % depreddation of laser power and a 25% increase in APD bulk dark current (I_{db}) in additional to the ROSS transmission degradation. Finally the final scenario contains a high level of degradation where all the impacts has considered at it's maximum level (20 % depreddation of laser power and a 50% increase in APD bulk dark current, I_{db}). This will be the least likely scenario.

2.5.2. The impact of solar noise on the instrument measurements

[Gunderson et al. \(2006\)](#) and [Gunderson and Thomas \(2010\)](#) have studied the impact of solar noise on the range error and they find that range errors arising from SNR effects in the receiver chain will be dominated by other range error components. The latest study shows that both the range error and pulse width error at low altitudes in the presence of the solar background are insensitive to the solar background, even at aphe- lion, where the solar backscatter is strong. Therefore we ignore this impact in our study.

3. Results

3.1. BELA in-orbit measurement error

3.1.1. Time of flight measurement errors

Table 4 shows the main components of the simulated TOF measurement errors computed as described in section 2.3 for several assumptions about the pointing uncertainty and calibration. It can be clearly seen that the error caused by pointing uncertainty is the dominating part of range measurement error.

The results of TOF measurements in different condition are summarized in table 5. A major improvement can be done on TOF measurement by the calibration of pointing uncertainties.

Table 3: Degraded values of instrument parameters over its mission lifetime (Begin Of Life: BOL; End Of Life: EOL; Receiver Optical Sub-System: ROSS).

| Time degradation level | BOL | EOL | | |
|------------------------|----------------|-------|--------|--------|
| | No degradation | Low | Medium | High |
| ROSS transmission | 76.7% | 67.3% | 67.3% | 67.3% |
| Laser pulse energy | 50 mJ | 50 mJ | 45 mJ | 40 mJ |
| APD bulk dark current | 50 pA | 50 pA | 75 pA | 100 pA |

Table 4: Components of TOF (range) measurement error

| Component of error caused by | Pointing uncertainty | RMS error |
|------------------------------|----------------------|------------------|
| the surface slope | | 1.33 ns (0.20 m) |
| the roughness | | 1.6 ns (0.24 m) |
| pointing uncertainty | 15 arc sec. | 27.9 ns (4.19 m) |
| | 7.5 arc sec. | 17.4 ns (2.61 m) |
| | 3 arc sec. | 9.3 ns (1.4 m) |
| Instrumental errors | | 1 ns (0.15 m) |

Table 5: BELA TOF measurement total error

| Measurement | Pointing uncertainty | RMS error |
|--------------------|----------------------|-----------|
| TOF error | 15 arc sec | 30.7 ns |
| | 7.5 arc sec | 19.8ns |
| | 3 arc sec | 10.0 ns |
| Pulse width (FWHM) | - | 4.9 ns |
| Pulse energy | - | 19 % |

But there is no huge improvement done on by removing the systematic bias of the instrumental noise.

3.1.2. Pulse width and pulse energy measurement errors

Table 6 and 5 show the pulse width and pulse energy measurement errors due to different error sources. If no systematic bias removal is preformed, the dominating part is the instrumental error. So the key parameter in determining the pulse width is the systematic bias on instrumental error and whether it can be removed or not. Table 5 show the total accuracy with and without the systematic biases.

Table 6: Components of pulse width (FWHM) measurement error

| Component of error | RMS error |
|-----------------------------|-----------|
| Caused by the surface slope | 2.45 ns |
| Caused by roughness | 3.0 ns |
| Instrumental error | 3.0 ns |

3.2. Expected instrument coverage

3.2.1. Average PFD over the surface of planet

We determine the coverage of the instrument by checking the PFD of for each measurement. We simulate the pulse detection algorithm and the process performed by BELA to detect the pulse. This simulation environment can predict the PFD of a specific return pulse in a specific noise environment (See appendix)

On top of the calculated PFD, We add the impact of degradation on ROSS transmission and laser power, which finally leads to a decrease in return pulse amplitude and signal to noise ratio.

Surface slope and roughness both cause a broadening on the return pulse width. In smooth plains the broadening of the return pulse has the smallest value and crater walls cause the largest broadening because of the highest slope angles.

Figure 6 shows the return pulse width against spacecraft altitudes for different types of terrains, while figure 7 shows the detectable pulses (PFD lower than 10 %) at different altitudes and return pulse widths. These plots are generated assuming the instrument gain code to be 7 and APD-A gain to be 1.5 MV/W (see section 1.2) and also assuming a low instrument degradation.

One can conclude with high APD-A gain, the smooth plains can be covered up to 1180 km, rough terrains can be covered up to 1145 km. Some shallow crater walls can be covered up to 1000 km but the steep crater walls can only be covered if the spacecraft altitude is less than 670 km. In this situation the instrument can meet the requirement for smooth plains and rough terrains even with the highest degradation.

On the other hand, with lower APD-A gain of 0.75 MV/W and with low degradation, the smooth plains can be covered up to 1050 km and the requirement can be met, but over the other terrains or with higher degradation the maximum working limit of the instrument would be below the requirement. Figures 8 to ?? show the average PFD over the entire surface of the planet for beginning of the mission and end of the extended mission for both APD-A gains of 1.5 MV/W and 0.75 MV/W.

Table 7: Predicted instrument working limit with high APD-A gain based on different degradation levels (BOL: Beginning of life, EOL: end Of Life); Green: Meet/better than the requirement; yellow: Sometimes not meet the requirement; Red: Not meet the requirement

| Region | BOL | EOL | | |
|---------------------|----------------|-----------------|--------------------|------------------|
| | No degradation | Low degradation | Medium degradation | High degradation |
| Over smooth plains | 1260 km | 1180 km | 1125 km | 1060 km |
| Over rough terrains | 1200 km | 1145 km | 1090 km | 1040 km |
| Over crater walls | 700-1050 km | 670-1000 km | 640-950 km | 615-890 km |

Table 8: Predicted instrument working limit with low APD-A gain based on different degradation levels (BOL: Begin Of Life; EOL: End of life)

| Region | BOL | EOL | | |
|---------------------|----------------|-----------------|--------------------|------------------|
| | No degradation | Low degradation | Medium degradation | High degradation |
| Over smooth plains | 1100 km | 1050 km | 985 km | 925 km |
| Over rough terrains | 980 km | 940 km | 900 km | 850 km |
| Over crater walls | 575-900 km | 550-850 km | 530-810 km | 500-760 km |

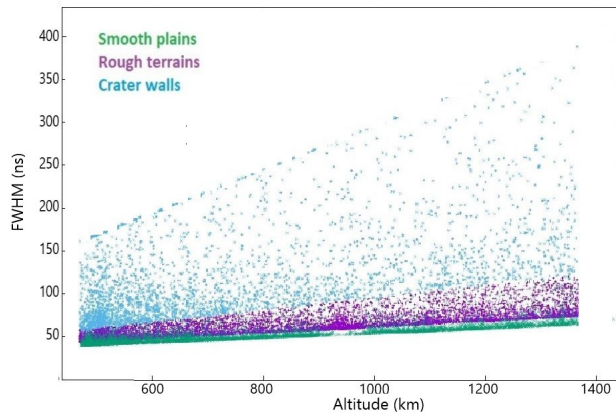


Figure 6: The FWHM of the return pulse as a function of altitude for different terrain types; Green: over a smooth plain; Purple: over a rough terrain; Blue: over a crater wall

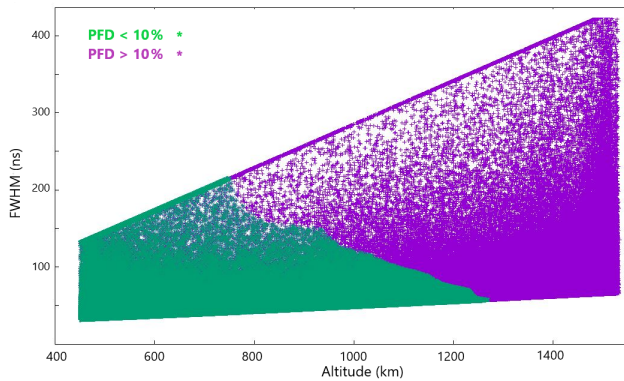


Figure 7: The range of altitude and return pulse width that make the pulse detectable ($PFD < 0.1$)

3.2.2. The impact of degradation on the coverage

Tables 7 and 8 provide the working limit of the instrument over different terrain types and in different degradation levels for high and low APD-A gains. Because of the wide range of slope angles on the crater walls, the working limit of the instrument over this type of terrain is shown in a range. The first value on this range corresponds to the steep and the second value corresponds to the shallow crater walls. One can notice that the impact of degradation decreases the working limit of the instrument by 50 km (for low degradation) to 150 km (for high degradation).

3.2.3. The impact of local albedo on the coverage

The above PFD and coverage is assuming a constant value of 0.19 for the surface albedo all over the planet's surface. Moreover, the local reflectance can vary between 4% to around 50% (J., 2015). This means that when the PFD is zero, there is still a chance of having a false detection caused by the low reflectivity of the surface at the laser spot. The return pulse energy as a function of spacecraft altitude and local reflectance is given by

$$E_R = E_T \cdot \rho \cdot T_r \cdot r_R^2 / z^2 \quad (15)$$

Where E_T , T_r and r_R are instrumental parameters and we assume them as fixed values. As the minimum detectable pulse energy E_{Rmin} is a constant value, one can write that ρ / z_{wl}^2 is constant for the minimum detectable pulse energies. z_{wl} is the maximum working limit of the instrument. This altitude corresponds to the critical (minimum detectable) pulse energy, where the PFD of the return signal reaches 10%.

We take into account that the local albedo, ρ , can differ from $\rho_0 = 19\%$. The real working limit of the instrument can be written as

$$z_{wl_{real}} = z_{wl_0} \cdot \sqrt{\rho / \rho_0} = z_{wl_0} \cdot \sqrt{\rho / 0.19} \quad (16)$$

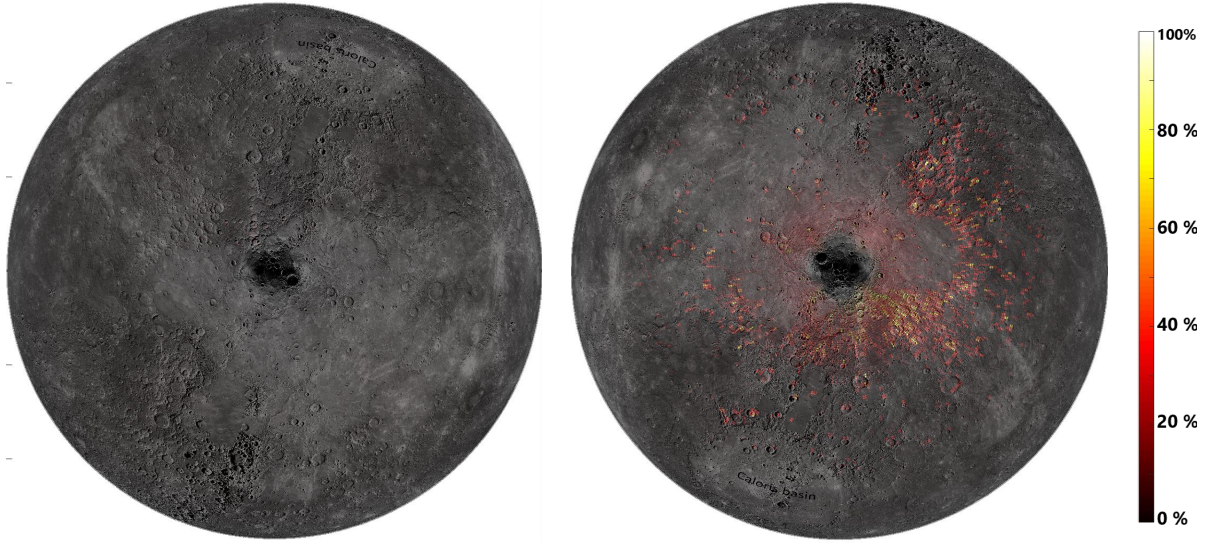


Figure 8: Average PFD at the beginning (left) and end (right) of mission over Mercury's northern hemisphere (APD-A gain = 1.5 MV/W, Low degradation)

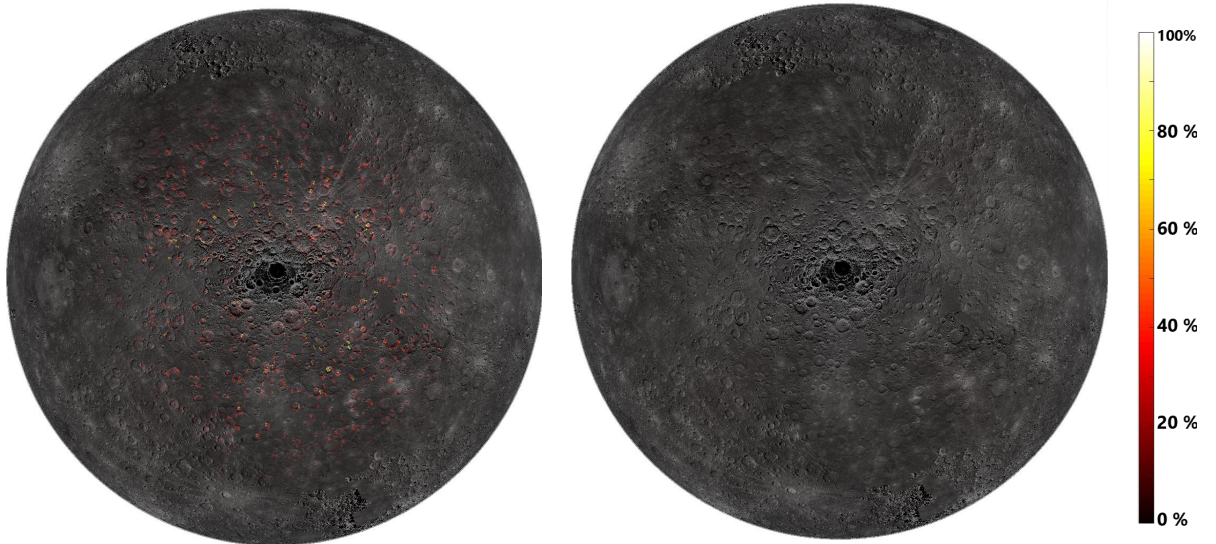


Figure 9: Average PFD at the beginning (left) and end (right) of mission over Mercury's southern hemisphere (APD-A gain = 1.5 MV/W, Low degradation)

Where z_{wl_0} is the working limit of spacecraft when the albedo is assumed to be 19 % and ρ is the real local albedo. In figure 12 the real working limit of the spacecraft is plotted against the local albedo for different terrains. Over an area with the lowest reflectivity, the instrument would not be able to work higher than 550 km even over a smooth plain. On the other hand, with highest local reflectivity, the real working limit of the instrument could reach 2000 km for smooth plains and a return pulse from the steepest crater wall could be detected up to an altitude of 1200 km. These considerations should be applied to the expected coverage, as soon as there is an accurate reflectance map available for the planet.

3.3. Expected performance in measuring surface features

3.3.1. Topography measurement accuracy

The horizontal resolution of the topography measurement depends on the proximity of laser spots on the planet surface at the end of mission. The laser spot size changes with the spacecraft altitude. It has a size of 24 m to 66 m depending on the spacecraft altitude. The consecutive spot to spot distance is 245 m at 480 km and it decreases to 174 m at the altitude of 1050 km. The laser spots in two adjacent orbits are separated by 25 km at the equator, crossing at the poles. But the distance between tracks decrease at the end of the mission lifetime. At the EOL, the accumulated measurements are expected to be 6 km apart at the equator as a results of multiple passes and orbital

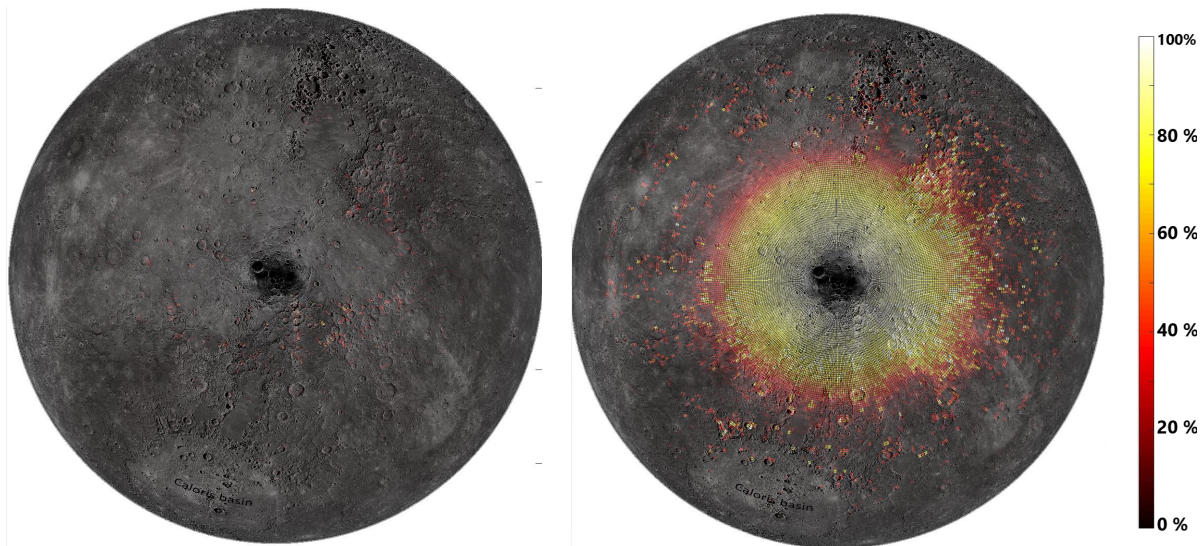


Figure 10: Average PFD at the beginning (left) and end (right) of mission over Mercury's northern hemisphere (APD-A gain = 0.75 MV/W, Low degradation)

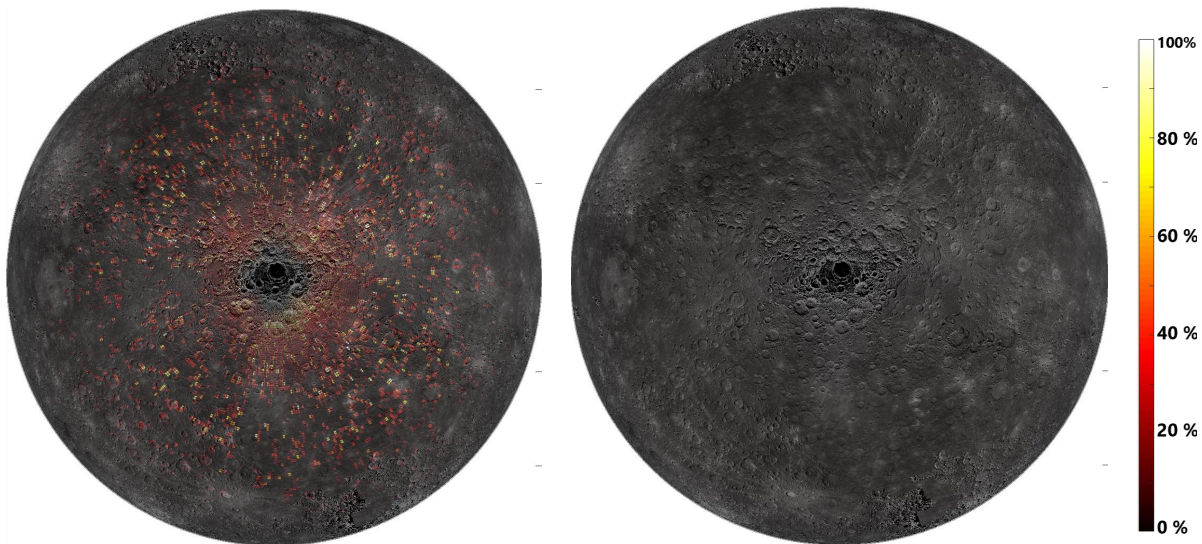


Figure 11: Average PFD at the beginning (left) and end (right) of mission over Mercury's southern hemisphere (APD-A gain = 0.75 MV/W, Low degradation)

phasing.

The accuracy of the elevation recovery at the laser spot is equal to the total range error (Table 9). As described in section 3.1, the key parameter here is the pointing uncertainty. The vertical accuracy with 15 arc sec pointing uncertainty is expected to be around 4.4 meters ($1 - \sigma$). If we assume the pointing uncertainties to be half this value (7.5 arc sec) the vertical accuracy will improve to 2.8 meters and if we assume the pointing error to be 3 arc sec, the total local height accuracy of DTM will be around 1.5 meters.

The accuracy of the elevation recovery will be different at

different latitudes and also over different terrain types (Table 10). The most accurate range measurements would be collected over smooth plains, with a RMS of 0.65 to 1.50 meters (depending on the pointing uncertainty). Over the rough terrains, we expect an accuracy of 0.80 to 2.15 meters, while over crater walls we expect larger RMS of 2.70 to 8.70 meters, depending on the pointing uncertainty.

The accuracy of the orbit using radio science data is predicted by Marabucci (2012) and is shown in table 11. According to this study the radial component is negligible with respect to the radial error on altimetry given in Table 9.

Figures 13 and 14 show the instrument performance map in

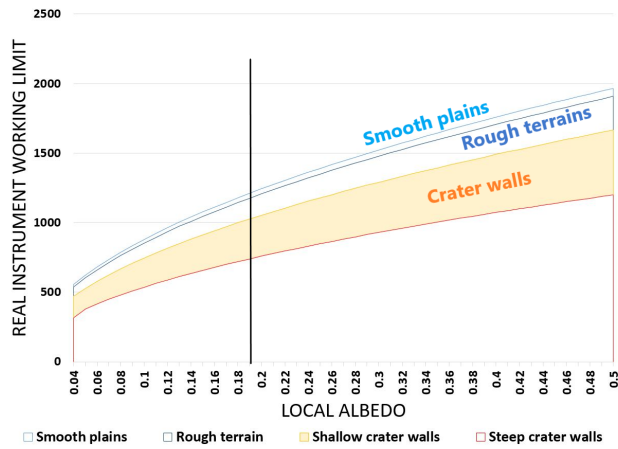


Figure 12: Real instrument working limit as a function of local reflectance of the surface for different terrains, the vertical bar shows the average albedo (0.19)

Table 9: Instrument performance in local height measurement

| Measurement | Pointing uncertainty | RMS error |
|-------------|----------------------|-----------|
| Height | 15 arc seconds | 4.4 m |
| | 7.5 arc seconds | 2.8 m |
| | 3 arc seconds | 1.5 m |
| | 3 arc seconds | 1.4 m |

Table 10: Elevation recovery error over different terrains

| Condition | RMS error | | |
|-----------------|---------------|----------------|--------------|
| | smooth plains | rough terrains | crater walls |
| 15 arc seconds | 1.55 m | 2.15 m | 8.70 m |
| 7.5 arc seconds | 1.05 m | 1.40 m | 5.40 m |
| 3 arc seconds | 0.65 m | 0.8 m | 2.70 m |

Table 11: Position formal uncertainties after Doppler orbit reconstruction using multi-arc approach [Marabucci, 2012]

| Formal uncertainties | R (m) | T (m) | H (m) |
|----------------------|--------|--------|--------|
| | 0.0476 | 13.377 | 16.772 |

local height measurements over the entire surface of the planet and figure 15 shows the same performance over a smaller area around the North Pole. It can be seen that over the smooth plains, the instrument has the best accuracy. The accuracy gets worse over cratered areas and the worst accuracy happens over crater walls.

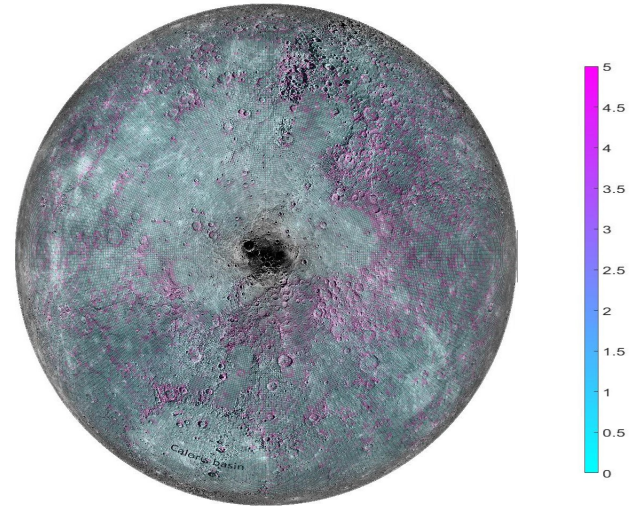


Figure 13: Local height measurement error over Mercury's northern hemisphere (m)

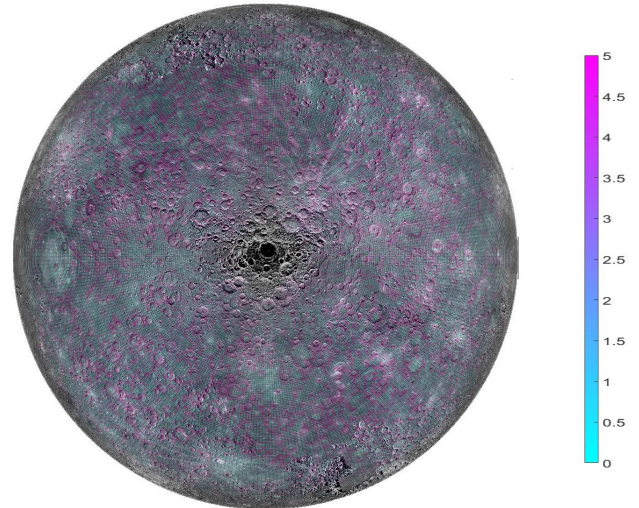


Figure 14: Local height measurement error over Mercury's southern hemisphere (m)

3.3.2. Performance in measuring the surface slope

There are two ways for determining the surface slope from laser altimetry data. The first method is to calculate the slope by dividing the height difference of two consecutive shot by distance between the spots (double shot slope measurement). The

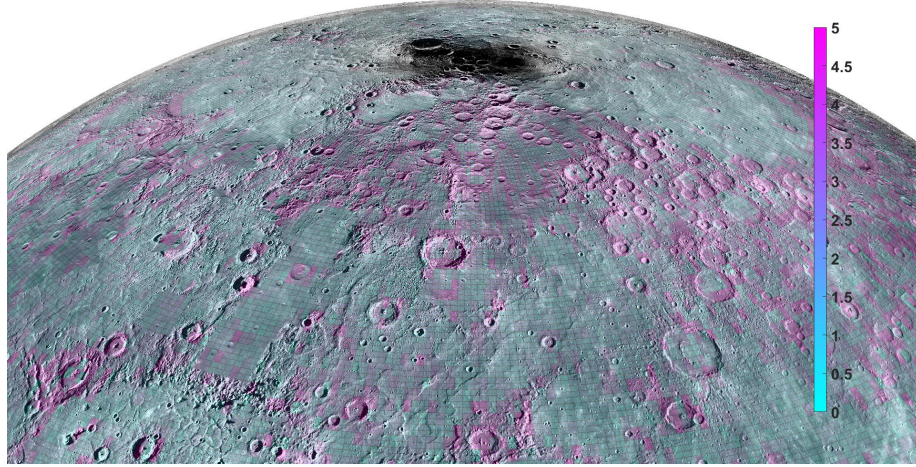


Figure 15: Local height measurement error over the North Pole (m)

second method is to determine the slope inside the laser slope by using the width of the return pulse (single shot slope measurement). According to Gardner (1992) the accuracy of double shot slope measurements can be calculated from the following equations.

$$Var(\tan S) = \frac{2F}{N(\Delta x)^2} [Var(\Delta\xi) + z^2(\tan S)^2(\tan \theta_i)^2 + Var(\Delta\phi)] \quad (17)$$

And the accuracy of single shot slope measurement can be calculated from:

$$Var(\tan S) = \frac{F}{2N} [(\tan S)^2 + (\tan \theta_i)^2 + \frac{Var(\Delta\xi)}{z^2(\tan \theta_i)^2}] \quad (18)$$

To predict the error with the "single shot" method, one can use the suggested equation in Gardner (1992). But instead we calculate directly the slope error from the broadening of the return pulse using the equations 6 to 11. Using this approach has two advantageous: First, the impact of low-pass filtering, which causes larger errors on slope measurement on smaller slopes, is not taken into account in Gardner's equation. Second, we can distinguish between negative errors and positive errors on the slope measurement, which are different over smaller slope angles. Since the absolute slope angle cannot be smaller than zero, the negative error on slope measurement cannot be bigger than the slope angle itself.

Table 12 provides the accuracy of these measurements with different methods and with different assumptions. Figure 16 shows the single shot measurement errors (positive and negative) in different surface slopes. These errors are calculated from the direct measurement of pulse broadening. In smaller

slope angles, the negative error goes to zero, while the positive side of error reaches higher values with RMS of 7.7 degrees. With the increase of slope angle, the RMS of this error decreases to a minimum value of 1.8 degrees.

Figure 17 provides the same errors with an assumption that a priori knowledge of roughness is available. By comparison to figure 16, it can be seen that the slope measurement error is always lower if a priori knowledge of roughness is available. As can be seen in figure 17, the positive measurement error in small slope angles has a RMS of 3 degrees, while the negative error is close to zero. In larger slope angles the negative error goes up but it cannot be larger than the slope angles itself.

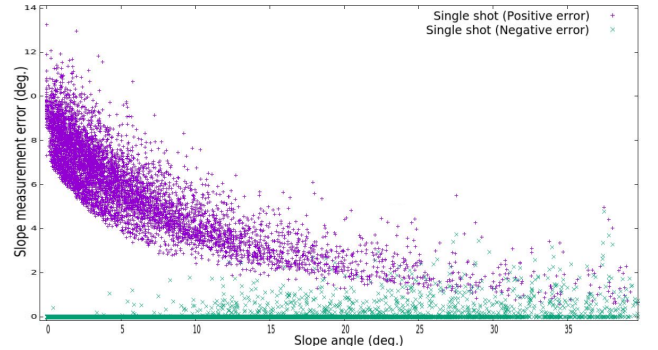


Figure 16: Single shot slope measurement error in different slope angles (Assumption: no knowledge of local roughness is available)

Figure 18 compares the average value of positive and negative errors calculated from the broadening of the return pulse in figure 17 with the same error calculated using the suggested equation in Gardner (1992). In the small slope angles, the Gardner's equation predicts smaller errors, but over the higher slope angles, both approaches predict the same error RMS. The accuracy of double shot slope measurement does not have a high

Table 12: Instrument performance in measurement of surface slope and roughness

| Measurement | Condition | STD error |
|-----------------------------------|---------------------------------|-----------|
| Slope (single shot) | No knowledge of roughness | 3.1 deg |
| | a priori knowledge of roughness | 2.0 deg |
| Slope (double shot) | 15 arc seconds pointing error | 0.16 deg |
| | 3 arc seconds pointing error | 0.11 deg |
| Roughness | No priori knowledge of slope | 1.7 m |
| | Local slope as a priori | 0.45 m |
| Surface albedo ($\delta\alpha$) | - | 4 % |

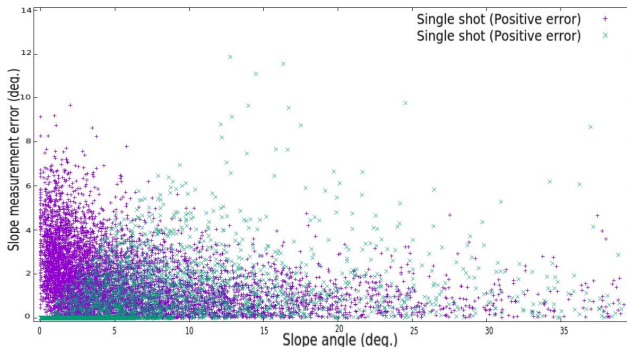


Figure 17: Single shot slope measurement error in different slope angles (Assumption: a priori knowledge on local roughness is available)

dependency on slope angle and is always better than one degree, while the single shot method leads to average accuracies between 1.2 to 3.8 degrees.

Figures 16 and 17 are plotted for the altimetry observations with low PFD. Considering all the observations, including the ones with high PFD, we see another increase in RMS error at larger slope angles (see the red dots in figure 18).

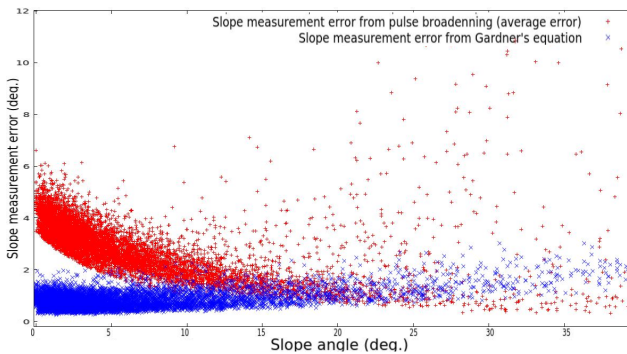


Figure 18: Slope measurement average error compared to the measurement error from suggested equation in Gardner (1992)

The other conclusion that can be drawn is that with single

shot method and no a priori knowledge of roughness, the slopes smaller than 5-6 degrees are hard to detect. The reason is that the amplitude of error at slope angles smaller than 5-6 degrees are as big as the slope itself.

3.3.3. Performance in measuring the surface roughness

The surface slope and roughness both cause a broadening in the return signal and there is no straight forward way to differentiate between them. One approach is to use the double shot method for measuring the surface slope and then use the pulse broadening to determine the roughness assuming that the slope inside the laser spot is constant. The other possible approach would be to have a priori knowledge on either slope or roughness and use the pulse broadening to calculate the other variable.

Table 12 provides the accuracy of the roughness measurements for both the conditions that a priori information on slope is available or that it is not. This means that depends on how accurate we can predict the slope angles, the roughness measurement will have a RMS error of 0.45 up to 1.7 m. Figure 23 also shows the same accuracy over surfaces with different slope angles.

Figures 19 to 22 and tables 13 and 14 provide more information on the distribution of slope and roughness measurement errors over different regions and terrains of the planet. For instance one can clearly see that the single shot slope measurement accuracy is better over crater walls and worse over smooth plains, while the double shot slope measurement has better accuracy over plains and flat surfaces. Knowing this, we recommend to use a combination of both approaches to determine the slope angles over the surface of the planet.

Also, all the different slope measurement approaches have better accuracy in the equatorial regions when compared to north and South poles. For example, the double shot slope measurement has a very good accuracy of 0.08 deg over the equatorial region. At the beginning of life the accuracy of slope measurement is better over the North Pole due to lower altitude of the spacecraft, while at the end of life, the accuracy over the South pole is better.

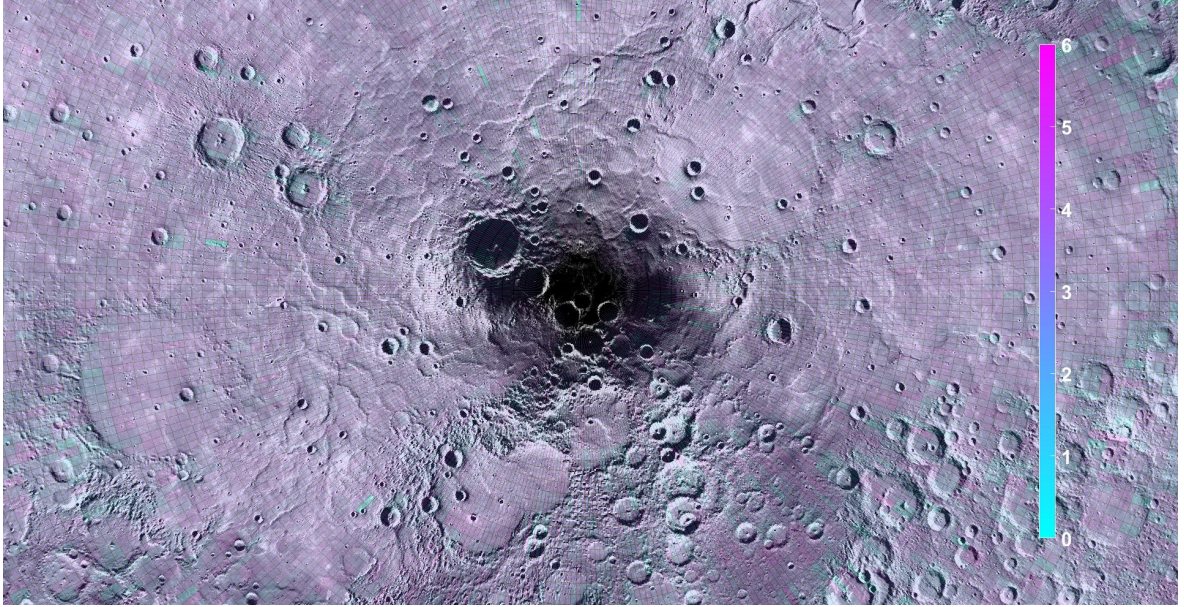


Figure 19: Single shot slope measurement error over the North Pole of the planet (deg)

3.3.4. Albedo measurement performance

The local albedo can be directly calculated from the received pulse energy. A bias observed on the measured pulse energy (details in section ??), can cause a systematic error on the albedo measurement. Table 12 provides the errors of the albedo measurement ($\alpha_{real} = \alpha_{measured} \pm \delta\alpha$) after removal of the systematic bias.

3.3.5. The impact of instrument degradation

The effect of degradation on the instrument working limit is presented in section 2.5. Here we want to investigate the impact of degradation on the instrument measurement accuracy. Table 15 provides this effect in four situations: BOL situation with no degradation and EOL situation with three different levels of degradation. As it can be seen from this table, there is a very small impact (3% inferior in worst case scenario) on the measurement accuracy due to the degradation effects. Considering table 15 and table 7, one can conclude that the degradation effects will cause an earlier rise in the probability of false detection of the pulse and a lower working limit for the instrument, but if the pulse is detected, there is no major impact on the measurement accuracy as a result of the degradation.

3.3.6. Performance sensitivity to Mercury average slope angle

In section 2.4 we mentioned that because of the absence of knowledge about the slopes at meter size baselines, we extrapolated the average slope angles at longer baselines to shorter baselines using a power function and we scale our slope model based on the predicted average slopes.

In reality, the power function might change in smaller slopes and as a result the average slope angles might be smaller than the predicted values. This will impact the results of the elevation recovery, slope and roughness measurement. Since we do not have any information on this, we continued to use one power function for the performance model. But, here we want to do a sensitivity study to find the impact of smaller slope values on our measurement accuracies.

Let us assume a break point at 100 meters for the slope extrapolation and then assume that average slope angle stays constant for baselines lower than this. This assumption is qualitatively similar to the slope-baseline function over the surface of Moon (Pommerol et al., 2012). Using this assumption, the average slope angles will be around 3 degrees, instead of around 7 degrees in the main model. We repeat the performance analysis using this slope model to find the sensitivity of instrument to average slope angles. The results of this study can be found in table 16.

As expected, all the modelled measurement expected accuracies have smaller values with respect to the previous slope model, but the single shot slope measurement has a slightly higher error. The reason is that this measurement is less accurate at smaller slope angles. The biggest change here is in the elevation recovery, where we get around 33% smaller errors.

3.4. Height difference performance on crossover points

Crossovers points are locations where two altimetry ground tracks intersect. It can be imagined as a differential measurement between two observations at the same location but at dif-

Table 13: Regional performance in slope and roughness measurement

| Measurement | RMS error | | |
|--|---------------|----------------|--------------|
| | smooth plains | rough terrains | crater walls |
| Slope (single shot-No roughness knowledge) | 3.2 deg | 3.6 deg | 1.6 deg |
| Slope (double shot-15" pointing error) | 0.12 deg | 0.14 deg | 0.24 deg |
| Slope (double shot- 3" pointing error) | 0.10 deg | 0.11 deg | 0.12 deg |
| Roughness (No knowledge of slope) | 0.42 m | 0.52 m | 3.5 m |
| Roughness (Slope as a priori info) | 0.32 m | 0.32 m | 0.8 m |

Table 14: Regional performance in slope and roughness measurement (BOL condition)

| Measurement | RMS error | | |
|--|-------------------|------------|------------|
| | Equatorial region | North pole | South pole |
| Slope (single shot-No roughness knowledge) | 3.1 deg | 3.2 deg | 3.9 deg |
| Slope (single shot-Roughness as a priori) | 2.3 deg | 1.8 deg | 1.9 deg |
| Slope (double shot-15" pointing error) | 0.08 deg | 0.18 deg | 0.22 deg |
| Slope (double shot- 3" pointing error) | 0.04 deg | 0.14 deg | 0.15 deg |
| Roughness (No knowledge of slope) | 1.8 m | 0.85 m | 1.45 m |
| Roughness (Slope as a priori info) | 0.45 m | 0.4 m | 0.5 m |

Table 15: Predicted performance degradation of BELA instrument over its mission lifetime used for simulations (Begin Of Life: BOL; End Of Life: EOL)

| Measurement | Accuracy degradation | | |
|-------------------|----------------------|--------------------|------------------|
| | Low degradation | Medium degradation | High degradation |
| Local elevation | 0.8 % | 1.6 % | 2.4 % |
| Surface slope | 0.6 % | 1.2 % | 1.8 % |
| Surface roughness | 1 % | 2 % | 3 % |
| Local albedo | 0.1 % | 0.1 % | 0.2 % |

Table 16: Instrument performance when assuming a break point for surface slope extrapolation

| Measurement | Condition | STD error |
|---------------------|---------------------------------|-----------|
| Elevation recovery | Pointing error = 15" | 3.1 m |
| | Pointing error = 3" | 0.9 m |
| Slope (single shot) | No knowledge of roughness | 3.5 deg |
| | a priori knowledge of roughness | 2.2 deg |
| Slope (double shot) | 15 arc seconds pointing error | 0.14 deg |
| | 3 arc seconds pointing error | 0.11 deg |
| Roughness | No priori knowledge of slope | 1.05 m |
| | Local slope as a priori | 0.35 m |

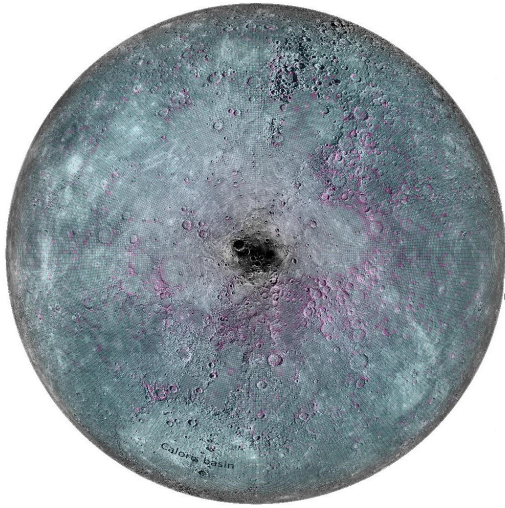


Figure 20: Double shot slope measurement error over Mercury's northern hemisphere (deg)

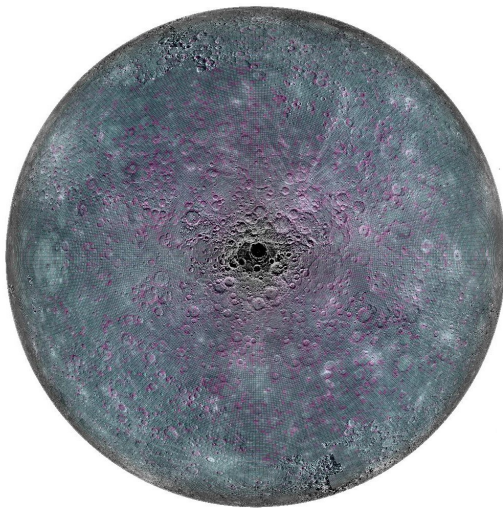


Figure 21: Double shot slope measurement error over Mercury's southern hemisphere (deg)

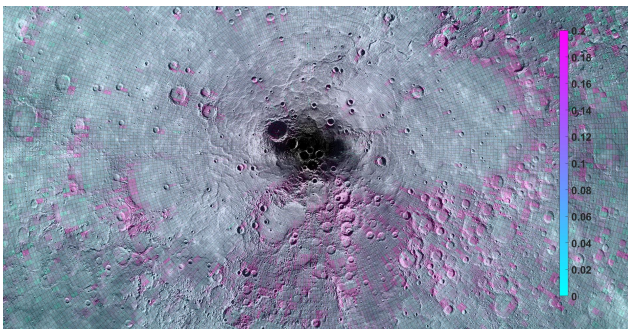


Figure 22: Double shot slope measurement error over the North Pole (deg)

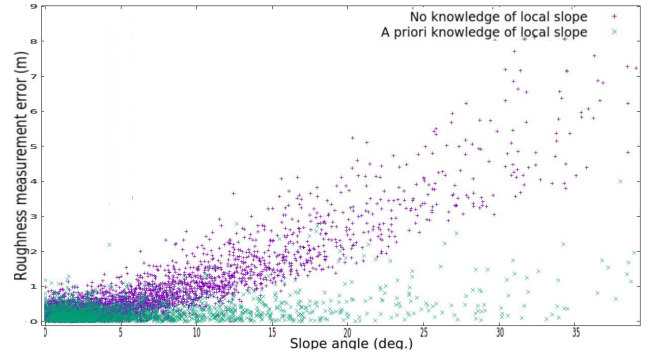


Figure 23: Roughness measurement error in different slope angles

Table 17: Instrument performance in ΔH measurement over crossover points

| Condition | Pointing uncertainty | RMS error |
|-----------------------|----------------------|-----------|
| Temporal proximity | 1.5" (Only jitter) | 1.22 m |
| | 1.5" (Only jitter) | 1.07 m |
| No temporal proximity | 15" | 6.2 m |
| | 7.5" | 4.0 m |
| | 3" | 2.1 m |
| | 3" | 2.0 m |

ferent times. Any difference in the height measurements δh at a crossover intersection is either caused by errors in the orbit or pointing reconstruction, interpolation errors of the surface topography between BELA footprints and/or any residual geophysical signal (*e.g.*, due to mismodelings of the planetary rotation).

According to Steinbrügge et al. (2018), the pointing error is one of the main sources of uncertainty in the crossover analysis. However, when the two intersecting tracks are close in time, only the error caused by the spacecraft pointing jitter (Casasco, 2017) should be accounted for.

Most of the pointing error is caused by deformation of the spacecraft optical bench, which is a very slow process. Since crossovers are a differential measurement, we assume this "quasi-constant" component to be negligible over short timescales.

These considerations lead to an improved error budget for BELA crossover analysis (see Table 17), likely increasing its impact on both orbit determination and on the expected accuracy of its recovery of geophysical parameters (*e.g.*, tidal deformations) with respect to previous estimates (Marabucci, 2012; Steinbrügge et al., 2018).

4. Conclusion and perspective

4.1. Summary of the results

We use the results of the laboratory-based performance tests (HosseiniArani, 2019) to develop a comprehensive performance in-orbit performance model for BELA during its primary mission orbits at Mercury. We use this simulation environment to evaluate the measurement performance and the working limit of the instrument in different conditions and over different terrains.

One of the most important performance parameters of the instrument is the PFD. The PFD determines the working limit of the instrument in different conditions. We assume the signal to be detectable when the PFD is below 10%. The PFD is determined at different gain settings and among them the highest performance happens with gain code 7 (gain code 15 also has similar performance) and with APD-A gain of 1.5 MV/W. With this gain setting and after considering the effects of degradation, the maximum working limit of the instrument ranges between 1040 to 1180 km over the smooth plains and rough terrains. Therefore the instrument meets the ranging requirement. It also means that BELA will be able to have a full coverage (except for some crater walls) of the whole planet in the first year of the mission (nominal mission) even with the highest possible degradation.

Using the high gain settings (gain code of 7 or 15 and APD-A gain of 1.5 MV/W) over the crater walls the working limit ranges between 700 km to 1150. Also for local albedos lower than 14%, the working limit of the instrument would be less than 1050 (even for smooth plains). It means that other than steep crater walls at high altitudes and local dark spots, the rest of the planet will be fully covered. Over the crater walls, the detection of the pulse will depend on the altitude of the spacecraft and the slope angle of the wall. For instance, in the beginning of the mission all the crater walls between the latitude of around 80 deg to -40 deg will be fully covered and only highly steep crater walls outside this latitude range would not be covered by the instrument.

At the end of the extended mission (two years) the argument of Perihelion will go down to around -40 deg and as a result the orbital height will reach to high altitudes (around 1300 km) over the North pole. As a result of this, the coverage will not be complete over the North Pole at the end of extended mission, even over smooth plains and with the lowest degradation.

To avoid any danger arising from possibly exceeding the APD breakdown voltages, the recommended HV has decreased to 340 V (correspond to APD-A gain of 0.75 MV/W). In this case, the maximum working limit of the instrument over flat surfaces and with low degradation is expected to be in the 1050 km and over other terrains or higher levels of degradation, the working limit is always below 950 km which is 100 km lower than the ranging requirement and as a result the instrument will not have a full coverage of South Pole at the beginning of mission. However, considering the rotation of the argument of per-

ihelion, the instrument will be able to cover both poles with one year of data. We have to stress that even though with APD-A gain of 0.75 MV/W, the instrument will be able to have a full coverage in the whole mission but the density of the data around the poles would be considerably less than the time we use higher APD-A gains.

For the range measurement, pointing calibration has the highest impact on performance. Therefore a further calibration of BELA using its own scientific data will be studied later. For pulse width and pulse energy measurements, systematic bias calibration plays the same role. However, currently, it is not clear how far the systematic biases can be removed. The reason for this, is that the systematic biases are detected using the RFM standalone and using synthetic Gaussian pulses as input. Therefore, a more realistic tests has to be done later with non-Gaussian pulses to determine whether the instrument has the same behaviour or not or whether the calibration can fully remove the systematic offset.

In the beginning of mission, the performance in all the measurements in the northern hemisphere is better than the southern hemisphere due to the lowest altitude of spacecraft. For the same reason, at the end of extended mission, the performance in southern hemisphere is better. In total, the best performance in all the topographical measurements happens in the equatorial region where the altitude of spacecraft is always around its lowest values. We also have to take into account that in some points over the North Pole and in a lot of points over the South pole, we will not have a correct measurement due to the high PFD. Losing the signal usually happens when we are passing over a crater wall with high slope angle or when the local albedo has lower values.

Gunderson and Thomas (2010) predicts the accuracy in range measurement to be between 25 cm up to 2 meters (before the PFD goes higher than 0.1). The lower limit of this is in agreement with what is measured as measurement accuracy of the instrument in the laboratory and the higher limit is also in agreement with the results of our study. The difference is that that we predict this errors with higher accuracy and in different conditions and over different terrains.

The predicted accuracy of the pulse widths error in Gunderson and Thomas (2010) is between 5 to 20 ns and we predict this accuracy to be in the range of 4-15 ns depending on the altitude and the systematic bias.

Steinbrügge et al. (2018) predicted the accuracy in roughness measurement to be around 1.5 meters, while our study shows a value in the range 0.3 to 0.5 m over smooth or rough terrain, however we predict the error to go up to 3.5 m over crater walls. Steinbrügge's study also predicts the minimum detectable slope (using single shot method) at lower altitudes to be 10 degrees and our study shows this value to be around 5-6 degrees. Moreover, we predict that at high altitudes the instrument will only be capable of measuring slopes up to around 15 – 20 degrees, while we expect to be able to detect almost all

the surface slopes, including the steepest crater walls, from altitudes lower than 670 km when the APD-A gain = 1.5 MV/W (and lower than 550 km when APD-A gain is 0.75 MV/W.)

One of the improvements in our study with respect to above publications, is the more accurate modeling of BELA measurement noise by using the latest test results on the BELA. The other very important improvement is that by using an in-orbit model of the laser altimetry and by using a ground model for the Mercury surface, we are able to predict the performance over different regions and terrains with much higher accuracy than before. As a result, it has become clear that the range measurement accuracy cannot be as good as it has been in the laser altimetry laboratory and in the best case scenario (best possible pointing calibration and over a smooth plain) this error will have a value of around 80 cm (whereas the instrument itself is able to detect ranges down to 25 cm in the laboratory condition).

Instrument degradation impact on the the measurement accuracies is negligible. But it considerably changes the working limits of the instrument. In other words, the instrument will loose more signals with high degradation, but if the return signal is detected, then the measurement accuracies will be almost the same.

Finally, by studying the performance over crossover points with temporal proximity, we noticed a good performance in measuring the δH (with RMS of around 1.1 m to 1.2 m). This will be valuable for measuring the tidal deformation of the planet and also for the improvement of orbit accuracy using laser altimetry data.

4.2. BELA performance improvement

One of the most advantages of using a comprehensive in-orbit simulation, is the ability to use this environment to simulate the real condition in flight and compare different observations under different conditions and over different terrains. Using this simulation environment, we are able to see what kind of data might be problematic or have bad resolution and what kind of change could improve it. What are the settings that should be used for the instrument to have the maximum performance. What techniques/weightings can be used to combine different observations. To improve the performance of the instrument a couple of points has to be mentioned:

4.2.1. Gain settings

The BELA team should consider the possibility of using a APD-A gain higher than 0.75 MV/W to improve the performance of the instrument, but lower than 1.5 MV/W To avoid any danger. Also, switching between the gain setting in low and high altitudes can be considered to increase the amount of time the instrument works with high APD-A gain and decrease the chance of any damage. In this approach, in lower altitudes, the instrument will use the safe low APD-A gain without losing

any data and in high altitudes (higher than 850 km), the instrument will switch to high APD-A gain to reach the requirement and detect as much data as possible. We need to point out that changing the gain settings will not impact the quality of the measurements and only changes the working limit of the instrument.

4.2.2. DTM recovery

For generating the DTM from the altimetry observations, one can only use the range measurement data. The sigma of range error has different values depending on the slope angle and spacecraft altitude and unless there is a very good pointing calibration for BELA line of sight, at high spacecraft altitude and over crater walls, the sigma of error can get values higher than 10 meters. Because of this, one might consider using other altimetry observation, the broadening of the return pulse to determine the local slopes and integrate them along the ground track to recover the DTM.

Due to the low accuracy of range measurement and high accuracy of the single pulse slope measurement over highly steep surfaces like the crater walls, this approach can be very useful for DTM recovery. In contrary, over the smooth plains, the single shot slope measurement has a bad accuracy, so one can use the double shot slope measurements to recover the local slopes.

The other recommended approach is to use both observations for DTM recovery, but give them different weightings depending on the expected surface slope. This can be done in a closed loop. Such that in the beginning, we use the current knowledge of the surface features to determine the first weightings and then after the recovery of the surface features, the updated surface model can be used to update the observation weightings and so on.

4.3. Future studies

The in-orbit simulation environment of BELA in Bernese software can be further developed to include the impact of BELA on precise orbit determination and Gravimetry. It can also be further developed to include the accuracies of the measurement of geophysical parameters e.g. tidal deformation, libration amplitude. This code. then can be used to perform any in-orbit simulation test including the off-nadir looking tests for determining some specific geometrical and geophysical parameters of the planet.

5. Acknowledgements

This study has been funded with the support of the Swiss National Foundation (SNF) and NCCR PlanetS. Stefano Bertone acknowledges support by the Swiss National Science Foundation within the Advanced Postdoc Mobility program and by NASA's Planetary Science Division Research Program.

Appendix A. Single shot probability of false detection

Appendix A.1. Introduction

One of the most important parameters in determining a laser altimeter performance is the PFD. This value shows if the detected signal is reliable or not. We assume a detected pulse as reliable if the PFD at that condition is below 10%. The PFD of the instrument depends on the altitude of the spacecraft, return pulse width and instrument gain settings.

Like the other classic laser altimeters, BELA sends a laser pulse to the surface. The beam produces a spot of 20-50 m on the surface. The laser beam is reflected from the surface and around 5 ms later it is received with the telescope. The received signal may have a much higher amplitude by the noise floor (e.g. when the altitude is low and the surface is smooth) or it may be close to or even below the noise level (e.g. when the altitude is high and the surface is rough or steep). In both cases the instrument tries to find the returned signal in the noise using a specific (proprietary) algorithm. According to the requirement, the instrument should be able to detect the pulses up to the altitude of 1050 km.

Appendix A.2. PFD determination in a simulation environment

We determine the single shot PFD in a simulation environment software developed at the University of Bern. We use the simulation environment to simulate the RFM algorithm and to see if the pulse can be detected or not. To have a value for the PFD, we repeat the process several times for different pulse width and pulse energies. then we check the number of times the algorithm has been able to find the pulse inside the noise environment and from this we calculate the PFD.

To provide the most realistic PFD calculation, we use the noise samples that were measured onboard MPO during the final tests of the instrument before flight. Tables A.18 and A.19 show the PFD in different altitudes and pulse widths. It can be seen that the PFD increases with the pulse width. In other words, the maximum working altitude decreases when we have more broaden pulses arriving at the telescope.

Appendix A.3. The impact of Instrument gain settings

Table A.20 provides the results of the PFD tests that were conducted on BELA at the University of Bern using the same noise samples as in section ??, but in different gain settings. Therefore one can use it to compare the impact of different gains on the PFD results. BELA can have 16 different gain codes (from 0 to 15). The gain code and the gain of the APD can change the PFD (Thomas et al., 2019). We tested the PFD in six different gain settings for the instrument: three gain codes (0, 7 and 15) and two APD-A gains (0.75 and 1.5 MV/W).

As shown in tables A.20 to ??, using instrument gain code 7 BELA will have a better performance with respect to gain code

0, but the difference between gain codes 7 and 15 is negligible in most of the cases. It is important to mention that all the tables in this section are provided assuming a constant surface reflectance of 19% and no degradation on instrument characteristics.

Appendix A.4. The impact of solar noise on PFD

In general the noise consists of four components. Solar noise, shot noise, dark current and the electronic noise floor (see Steinbrügge et al. (2018) for further details). The first contribution, the solar noise, is the sunlight reflected from the surface of the planet within the field of view of the receiver. The second contribution is the shot noise. This is the additional noise caused by the statistical nature of the multiplication process that the APD experiences when it is illuminated. This contribution is called shot noise and depends on the incident optical power.

To add the impact of solar noise on top of the calculated PFD, we use the relation between PFD to Signal-to-Noise. This relation has been found empirically by testing the actually implemented algorithm for a statistical set of laser pulses under different SNR conditions by Steinbrügge et al. (2018).

$$\text{PFD} = \frac{\text{erfc}(0.69 \cdot \text{SNR} - 1.64)}{1.98} \quad (\text{A.1})$$

Signal-to noise ration can also be calculated by the following equation:

$$\text{SNR} = \frac{R_0^2 M^2 P_{\text{peak}}^2 R_i^2}{(2q * (I_{ds} + (I_s + I_{db} + I_{sn}) M^{(2+x)}) + n_f^2) * B_0 R^2} \quad (\text{A.2})$$

Where I_s is the solar noise, I_{SN} is the shot noise, I_{ds} is APD dark current (surface), I_{db} is APD dark current (bulk), M is the nominal gain, x the excess noise factor and n_f the noise floor. The assumed values are given in table 1. The solar noise can be calculated using the following equation:

$$I_s = q \epsilon_i \epsilon_o \epsilon_{qe} \rho_0 \cos(i) A_{FOV} \Omega_R \frac{F \lambda}{hc} \sigma_{rf} \quad [\text{A}] \quad (\text{A.3})$$

Where:

$$A_{FOV} = \pi H^2 \tan^2(\theta_{FOV}) \quad [\text{m}^2] \quad (\text{A.4})$$

To find the impact of solar noise on PFD we first find the SNR based on the PFD that is predicted without solar noise. Then we find the change in SNR after adding the solar noise and finally, we go back from SNR to PFD and find the corrected PFD using the new value for SNR.

Assuming the noise floor to be $3.2 \text{ pA} / \sqrt{\text{Hz}}$, adding the impact of solar noise on PFD, brings the PFD from zero up to around 5% (in worst case) when sun is shining directly from behind (figure A.25). The average value of PFD at zero incidence

Table A.18: Probability of false detection in different altitudes and return pulse widths. provided for gain code 7 and APD-A gain = 0.75 MV/W

| Return Pulse Energy (Joules) | Altitude (km) | FWHM of the return signal | | | | | | | | | | |
|------------------------------|---------------|---------------------------|-------|-------|-------|-------|-------|-------|-------|-------|-------|--------|
| | | 10 ns | 25 ns | 30 ns | 35 ns | 40 ns | 50 ns | 60 ns | 70 ns | 80 ns | 90 ns | 100 ns |
| 7.93E-16 | 300 | 0 % | 0 % | 0 % | 0 % | 0 % | 0 % | 0 % | 0 % | 0 % | 0 % | 0 % |
| 4.46E-16 | 400 | 0 % | 0 % | 0 % | 0 % | 0 % | 0 % | 0 % | 0 % | 0 % | 0 % | 0 % |
| 2.86E-16 | 500 | 0 % | 0 % | 0 % | 0 % | 0 % | 0 % | 0 % | 0 % | 0 % | 0 % | 0 % |
| 1.98E-16 | 600 | 0 % | 0 % | 0 % | 0 % | 0 % | 0 % | 0 % | 0 % | 0 % | 0 % | 0 % |
| 1.46E-16 | 700 | 0 % | 0 % | 0 % | 0 % | 0 % | 0 % | 0 % | 0 % | 0 % | 0 % | 0 % |
| 1.12E-16 | 800 | 0 % | 0 % | 0 % | 0 % | 0 % | 0 % | 0 % | 0 % | 0 % | 2 % | 4 % |
| 8.81E-17 | 900 | 0 % | 0 % | 0 % | 0 % | 0 % | 0 % | 4 % | 10 % | 10 % | 32 % | 34 % |
| 7.14E-17 | 1000 | 0 % | 0 % | 0 % | 2 % | 2 % | 8 % | 34 % | 34 % | 44 % | 66 % | 66 % |
| 5.90E-17 | 1100 | 6 % | 2 % | 8 % | 14 % | 34 % | 64 % | 52 % | 64 % | 82 % | 90 % | 92 % |
| 4.96E-17 | 1200 | 22 % | 12 % | 28 % | 30 % | 60 % | 76 % | 84 % | 84 % | 92 % | 90 % | 96 % |
| 4.22E-17 | 1300 | 56 % | 36 % | 46 % | 70 % | 70 % | 88 % | 90 % | 100 % | 96 % | 96 % | 98 % |
| 3.64E-17 | 1400 | 62 % | 58 % | 78 % | 82 % | 84 % | 92 % | 92 % | 100 % | 100 % | 98 % | 98 % |
| 3.17E-17 | 1500 | 80 % | 76 % | 86 % | 96 % | 92 % | 96 % | 96 % | 100 % | 100 % | 100 % | 100 % |
| 2.79E-17 | 1600 | 92 % | 94 % | 84 % | 96 % | 96 % | 96 % | 100 % | 100 % | 100 % | 100 % | 100 % |
| 2.47E-17 | 1700 | 98 % | 94 % | 96 % | 98 % | 98 % | 96 % | 100 % | 100 % | 100 % | 100 % | 100 % |

Table A.19: : Probability of false detection in different altitudes and return pulse widths. provided for gain code 7 and APD-A gain = 1.5 MV/W

| Return Pulse Energy (Joules) | Altitude (km) | FWHM of the return signal | | | | | | | | | | |
|------------------------------|---------------|---------------------------|-------|-------|-------|-------|-------|-------|-------|-------|-------|--------|
| | | 10 ns | 25 ns | 30 ns | 35 ns | 40 ns | 50 ns | 60 ns | 70 ns | 80 ns | 90 ns | 100 ns |
| 7.93E-16 | 300 | 0 % | 0 % | 0 % | 0 % | 0 % | 0 % | 0 % | 0 % | 0 % | 0 % | 0 % |
| 4.46E-16 | 400 | 0 % | 0 % | 0 % | 0 % | 0 % | 0 % | 0 % | 0 % | 0 % | 0 % | 0 % |
| 2.86E-16 | 500 | 0 % | 0 % | 0 % | 0 % | 0 % | 0 % | 0 % | 0 % | 0 % | 0 % | 0 % |
| 1.98E-16 | 600 | 0 % | 0 % | 0 % | 0 % | 0 % | 0 % | 0 % | 0 % | 0 % | 0 % | 0 % |
| 1.46E-16 | 700 | 0 % | 0 % | 0 % | 0 % | 0 % | 0 % | 0 % | 0 % | 0 % | 0 % | 0 % |
| 1.12E-16 | 800 | 0 % | 0 % | 0 % | 0 % | 0 % | 0 % | 0 % | 0 % | 0 % | 0 % | 0 % |
| 8.81E-17 | 900 | 0 % | 0 % | 0 % | 0 % | 0 % | 0 % | 0 % | 0 % | 0 % | 0 % | 0 % |
| 7.14E-17 | 1000 | 0 % | 0 % | 0 % | 0 % | 0 % | 0 % | 0 % | 0 % | 0 % | 0 % | 0 % |
| 5.90E-17 | 1100 | 0 % | 0 % | 0 % | 0 % | 0 % | 0 % | 0 % | 0 % | 0 % | 0 % | 0 % |
| 4.96E-17 | 1200 | 0 % | 0 % | 0 % | 0 % | 0 % | 0 % | 0 % | 0 % | 2 % | 6 % | 16 % |
| 4.22E-17 | 1300 | 0 % | 0 % | 0 % | 0 % | 0 % | 0 % | 6 % | 8 % | 18 % | 24 % | 52 % |
| 3.64E-17 | 1400 | 0 % | 0 % | 0 % | 2 % | 4 % | 2 % | 20 % | 24 % | 66 % | 72 % | 76 % |
| 3.17E-17 | 1500 | 4 % | 2 % | 2 % | 6 % | 10 % | 20 % | 46 % | 56 % | 66 % | 78 % | 86 % |
| 2.79E-17 | 1600 | 6 % | 8 % | 10 % | 24 % | 38 % | 56 % | 72 % | 74 % | 88 % | 86 % | 94 % |
| 2.47E-17 | 1700 | 30 % | 22 % | 26 % | 40 % | 54 % | 66 % | 74 % | 36 % | 92 % | 96 % | 98 % |

Table A.20: PFD in different S/C altitudes and in different gain settings for a return pulse width of 10 ns

| | | FWHM = 35 ns | | | | | |
|---------------|------------------|------------------|-------------------|------------------|-------------------|------------------|-------------------|
| Distance (km) | Pulse Energy (J) | PFD | | | | | |
| | | Gain code 0 | | Gain code 7 | | Gain code 15 | |
| | | APD-A gain = 1.5 | APD-A gain = 0.75 | APD-A gain = 1.5 | APD-A gain = 0.75 | APD-A gain = 1.5 | APD-A gain = 0.75 |
| 300 | 7.93333E-16 | 0 % | 0 % | 0 % | 0 % | 0 % | 0 % |
| 400 | 4.4625E-16 | 0 % | 0 % | 0 % | 0 % | 0 % | 0 % |
| 500 | 2.856E-16 | 0 % | 0 % | 0 % | 0 % | 0 % | 0 % |
| 600 | 1.98333E-16 | 0 % | 0 % | 0 % | 0 % | 0 % | 0 % |
| 700 | 1.45714E-16 | 0 % | 0 % | 0 % | 0 % | 0 % | 0 % |
| 800 | 1.11563E-16 | 0 % | 0 % | 0 % | 0 % | 0 % | 0 % |
| 900 | 8.81481E-17 | 0 % | 0 % | 0 % | 0 % | 0 % | 0 % |
| 1000 | 7.14E-17 | 0 % | 20 % | 0 % | 2 % | 0 % | 2 % |
| 1100 | 5.90083E-17 | 0 % | 44 % | 0 % | 14 % | 0 % | 16 % |
| 1200 | 4.95833E-17 | 0 % | 70 % | 0 % | 28 % | 0 % | 48 % |
| 1300 | 4.22485E-17 | 2 % | 80 % | 0 % | 70 % | 0 % | 66 % |
| 1400 | 3.64286E-17 | 4 % | 86 % | 2 % | 82 % | 0 % | 86 % |
| 1500 | 3.17333E-17 | 32 % | 94 % | 10 % | 96 % | 0 % | 96 % |
| 1600 | 2.78906E-17 | 40 % | 94 % | 24 % | 96 % | 20 % | 96 % |
| 1700 | 2.47059E-17 | 82 % | 100 % | 40 % | 98 % | 42 % | 100 % |

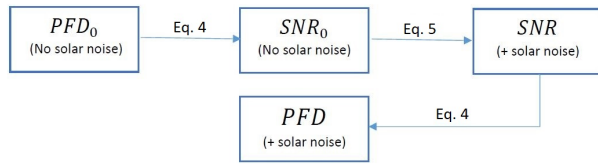


Figure A.24: Process of calculating the impact of solar noise on PFD using SNR to PFD relation

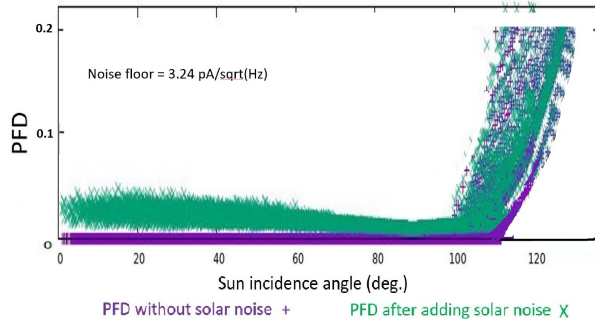


Figure A.25: PFD as a function of Sun incidence angle

angle would be 2.5 %. Considering that the effect of solar noise can increase the PFD from zero to a maximum percentage of 5 % and considering that we assume the signal to be detectable when the PFD is below 10%, we conclude that the solar noise has a negligible impact on the coverage of BELA and therefore it will not be considered in in-orbit simulations of BELA in sections 3 and 4.

PFD tables in figures A.18, A.19 and ?? are provided assuming that the surface reflectance is 19%, where the reflectance of Mercury surface vary between 5% to 45% in different regions. At the moment there is no reliable global map at 1064 nm but after BepiColombo's arrival at Mercury, updates on the global reluctance map will be provided.

Finally it has to be mentioned that all the errors that are given in this study are derived from the analysis of the test results in the laboratory and therefore, they don't include the error component due to orbital error or pointing uncertainties. The in-flight performance of the instrument that includes all the errors will be presented in another study.

Several hundred tests have been performed on RFM standalone of BELA instrument. On these tests Gaussian pulses are sent to the RFM and the measured time of flight, pulse width and pulse energies are compared to the expected ones. There are a few main conclusions to be drawn from this test. First, the TOF measurement accuracy with respect to height accuracy is very high. This accuracy for short pulses with a spacecraft height of lower than 1000 km is around 1.64 ns (equivalent to

25 cm in range measurement). The accuracy decreases with increasing height and the received pulse width but it's RMS is still below 3.35 ns (equivalent to 50 cm in range).

The energy measurement shows an overall accuracy of about 5% to 100%. But a linear offset also exists here. By analysing the test results, it is shown that after calibration for this systematic offset, the error on energy measurement reduces to 20%.

The probability of false detection determines the working limit of the instrument in different condition. The PFD of the instrument is determined at different gain settings and among them the highest performance happens with gain code 7 (gain code 15 also has similar performance) and with APD_A gain of 1.5 MV/W. The maximum working limit of the instrument in this case ranges between 1000 to 1600 km depends on the return pulse width. This is far better than the requirement of 1050 km, but it has to be mentioned that in flight around Mercury this limit is expected to be less due to the degradation effects.

References

- Becker, K.J., Robinson, M.S., Becker, T.L., Weller, L.A., Edmundson, K.L., Neumann, G.A., Perry, M.E., Solomon, S.C., 2016. First digital elevation model of mercury. 47th Lunar and Planetary Science Conference, held March 21-25, 2016 at The Woodlands, Texas. LPI Contribution .
- Benkhoff, J., 2018. Bepicolombo en route to mercury. American Geophysical Union, Fall Meeting 2018, abstract P23F-3501 .
- Benkhoff, J., van Casteren, J., Hayakawa, H., Fujimoto, M., Laakso, H., Novara, M., Ferri, P., Middleton, H.R., Ziethe, R., 2010. Bepicolombo—comprehensive exploration of mercury: Mission overview and science goals. Planetary and Space Science 58, 2 – 20. doi:<https://doi.org/10.1016/j.pss.2009.09.020>. comprehensive Science Investigations of Mercury: The scientific goals of the joint ESA/JAXA mission BepiColombo.
- Casasco, M., 2017. BepiColombo pointing and micro-vibration performance. Report BC-EST-TN-26268, Issue:3. ESA.
- Dach, R., Lutz, S., Walser, P., Fridez, P., 2015. Bernese GNSS Software Version 5.2.
- Denevi, B.W., Ernst, C.M., Meyer, H.M., Robinson, M.S., Murchie, S.L., Whitten, J.L., Head, J.W., Watters, T.R., Solomon, S.C., Ostrach, L.R., Chapman, C.R., Byrne, P.K., Klimczak, C., Peplowski, P.N., 2013. The distribution and origin of smooth plains on mercury .
- Gardner, C.S., 1992. Ranging performance of satellite laser altimeters. IEEE Transactions on Geoscience and Remote Sensing 30, 1061–1072. doi:[10.1109/36.175341](https://doi.org/10.1109/36.175341).
- Genova, A., Goossens, S., Mazarico, E., Lemoine, F.G., Neumann, G.A., Kuang, W., Sabaka, T.J., Hauck, S.A., Smith, D.E., Solomon, S.C., Zuber, M.T., 2019. Geodetic Evidence That Mercury Has A Solid Inner Core. Geophys. Res. Lett. 46, 3625–3633. doi:[10.1029/2018GL081135](https://doi.org/10.1029/2018GL081135).
- Gunderson, K., Thomas, N., 2010. Bela receiver performance modeling over the bepicolombo mission lifetime. Planetary and Space Science 58, 309 – 318. URL: <http://www.sciencedirect.com/science/article/pii/S0032063309002451>, doi:<https://doi.org/10.1016/j.pss.2009.08.006>. comprehensive Science Investigations of Mercury: The scientific goals of the joint ESA/JAXA mission BepiColombo.
- Gunderson, K., Thomas, N., Rohner, M., 2006. A laser altimeter performance model and its application to bela. IEEE Transactions on Geoscience and Remote Sensing 44, 3308–3319. doi:[10.1109/TGRS.2006.880623](https://doi.org/10.1109/TGRS.2006.880623).
- Heesel, E., 2014. Optical design and analyses report. Report BC-BEL-RP-92014-I2-RO-RxBP. ESA.
- HosseiniArani, A., 2019. BepiColombo laser altimeter (BELA) performance evaluation: from laboratory tests to simulations of flight observations (Unpublished doctoral thesis). Ph.D. thesis.

- Hosseinianari, A., Bertone, S., Jaeggi, A., Thomas, N., 2018. Improved modelling of bela altimetry observation for mpo orbit reconstruction. 20th EGU General Assembly, 8-13 April, 2018, Vienna, Austria, p.10178 .
- J., G., 2015. Performance analyses of a laser altimeter system: BepiColombo Laser Altimeter. Ph.D. thesis.
- Jehn, R., 2015. BepiColombo Mercury Cornerstone Consolidated Report on Mission Analysis. Report 525, BC-ESC-RP-05500, Issue 5.2. EUROPEAN SPACE AGENCY, EUROPEAN SPACE OPERATIONS CENTRE GROUND SYSTEMS ENGINEERING DEPARTMENT Mission Analysis Section.
- Kallenbach, R., Murphy, E., Gramkow, B., Rech, M., Weidlich, K., Leikert, T., Henkelmann, R., Trefzger, B., Metz, B., Michaelis, H., Lingenauber, K., DelTogno, S., Behnke, T., Thomas, N., Piazza, D., Seiferlin, K., 2013. Space-qualified laser system for the bepicolombo laser altimeter. *Appl. Opt.* 52, 8732–8746. URL: <http://ao.osa.org/abstract.cfm?URI=ao-52-36-8732>, doi:10.1364/AO.52.008732.
- Luedicke, F., 2014. Orbit simulations for bepicolombo using messenger-based high-order mercury gravity field data. European Planetary Science Congress 2014, EPSC Abstracts, Vol. 9, id. EPSC2014-548 .
- Marabucci, M., 2012. The determination of Hermian gravity and topography from radioscience and laser altimetry data of the BepiColombo mission. Ph.D. thesis. Sapienza University of Rome.
- Metz, B., 2014. Extended lifetime test diodes degradation. Report BC-BEL-NC-60048-1-2. ESA.
- Pommerol, A., Chakraborty, S., Thomas, N., 2012. Comparative study of the surface roughness of the moon, mars and mercury. *Planetary and Space Science* 73, 287 – 293. URL: <http://www.sciencedirect.com/science/article/pii/S0032063312002577>, doi:<https://doi.org/10.1016/j.pss.2012.08.020>. solar System science before and after Gaia.
- Steinbrügge, G., Stark, A., Hussmann, H., Wickhusen, K., Oberst, J., 2018. The performance of the bepicolombo laser altimeter (bela) prior launch and prospects for mercury orbit operations. *Planetary and Space Science* 159, 84 – 92. doi:<https://doi.org/10.1016/j.pss.2018.04.017>.
- Susorney, H.C.M., Barnouin, O.S., Ernst, C.M., Byrne, P.K., 2017. The surface roughness of mercury from the mercury laser altimeter: Investigating the effects of volcanism, tectonism, and impact cratering. *Journal of Geophysical Research: Planets* 122, 1372–1390. URL: <https://agupubs.onlinelibrary.wiley.com/doi/abs/10.1002/2016JE005228>, doi:10.1002/2016JE005228, arXiv:<https://agupubs.onlinelibrary.wiley.com/doi/pdf/10.1002/2016JE005228>.
- Thomas, N., Hussmann, H., Lara, L.M., 2019. The bepicolombo laser altimeter (bela): a post-launch summary. *CEAS Space Journal* URL: <https://doi.org/10.1007/s12567-019-00270-y>, doi:10.1007/s12567-019-00270-y.
- Thomas, N., Spohn, T., Barriot, J.P., Benz, W., Beutler, G., Christensen, U., Dehant, V., Fallnich, C., Giardini, D., Groussin, O., Gunderson, K., Hauber, E., Hilchenbach, M., Iess, L., Lamy, P., Lara, L.M., Lognonné, P., Lopez-Moreno, J., Michaelis, H., Oberst, J., Resendes, D., Reynaud, J.L., Rodrigo, R., Sasaki, S., Seiferlin, K., Wiczorek, M., Whitby, J., 2007. The bepicolombo laser altimeter (bela): Concept and baseline design. *Planetary and Space Science* 55, 1398 – 1413. doi:<https://doi.org/10.1016/j.pss.2007.03.003>.
- Yang, D., Zuber, M.T., Head, J.W., Solomon, S.C., 2016. Distribution of topographic slope and roughness in mercury’s northern hemisphere. 44th Lunar and Planetary Science Conference, held March 18-22, 2013 in The Woodlands, Texas. LPI Contribution .

BIBLIOGRAPHY

S. W. Asmar, J. W. Armstrong, L. Less, and P. Tortora. Spacecraft doppler tracking: Noise budget and accuracy achievable in precision radio science observations. *Radio Science*, 40(2), 2005.

Thomas Beck. *Modeling and verification of BELAs thermal behavior and range finder performance*. PhD thesis, University of Bern, 2011.

K. J. Becker, M. S. Robinson, T. L. Becker, L. A. Weller, K. L. Edmundson, G. A. Neumann, M. E. Perry, and S. C. Solomon. First digital elevation model of mercury. *47th Lunar and Planetary Science Conference, held March 21-25, 2016 at The Woodlands, Texas. LPI Contribution*, 2016.

Johannes Benkhoff, Jan van Casteren, Hajime Hayakawa, Masaki Fujimoto, Harri Laakso, Mauro Novara, Paolo Ferri, Helen R. Middleton, and Ruth Ziethé. Bepicolombo—comprehensive exploration of mercury: Mission overview and science goals. *Planetary and Space Science*, 58 (1):2 – 20, 2010. ISSN 0032-0633. doi: <https://doi.org/10.1016/j.pss.2009.09.020>. Comprehensive Science Investigations of Mercury: The scientific goals of the joint ESA/JAXA mission BepiColombo.

W.I. Bertiger, E.S. Davis J.R. Guinn B.J. Haines R.W. Ibanez-Meier J.R. Jee S.M. Lichten W.G. Melbourne R.J. Muellerschoen T.N. Munson Y. Vigue S.C. Wu T.P. Yunck B.E. Schutz P.A.M. Abusali H.J. Rim M.M. Watkins Y.E. Bar-Sever, E.J. Christensen, and P. Willis. Gps precise tracking of topex/poseidon: results and implication. *Journal of Geophysical Research*, 99, 1994.

S. Bertone, . Jaeggi, A. Beutler G. Arnold, D., and L. Mervart. Doppler orbit determination of deep space probes by the bernese gnss software: First results of the combined orbit determination with inter-satellite ka-band data from the grail mission. *25th International Symposium on Space Flight Dynamics ISSFD*, 18, 2015.

Stefano Bertone, Erwan Mazarico, Michael Barker, Sander J Goossens, Antonio Genova, Terence J Sabaka, Gregory A Neumann, and David E. Smith. New analysis of mercury laser altimeter crossovers to improve geodetic constraints by messenger. *American geophysical union (AGU) fall meeting 2019, AGU Abstracts*, 2019.

G. Beutler. *Methods of Celestial Mechanics*. 2005.

- Massimo Casasco. Bepicolombo pointing and micro-vibration performance. Report BC-EST-TN-26268, Issue:3, ESA, 2017.
- S. Cicalò, G. Schettino, S. Di Ruzza, E. M. Alessi, G. Tommei, and A. Milani. The BepiColombo MORE gravimetry and rotation experiments with the orbit14 software. *Monthly Notices of the Royal Astronomical Society*, 457(2):1507–1521, 02 2016. ISSN 0035-8711. doi: 10.1093/mnras/stw052. URL <https://doi.org/10.1093/mnras/stw052>.
- Rolf Dach, Simon Lutz, Peter Walser, and Pierre Fridez. *Bernese GNSS Software Version 5.2*. 2015.
- Brett W. Denevi, Carolyn M. Ernst, Heather M. Meyer, Mark S. Robinson, Scott L. Murchie, Jennifer L. Whitten, James W. Head, Thomas R. Watters, Sean C. Solomon, Lillian R. Ostrach, Clark R. Chapman, Paul K. Byrne, Christian Klimczak, and Patrick N. Peplowski. The distribution and origin of smooth plains on mercury. 2013.
- B.W Denevi. Mercury messenger mdis basemap md3 color global mosaic 665m (64ppd). 2016.
- David A. Fassett, Caleb I. and Minton. Impact bombardment of the terrestrial planets and the early history of the solar system. *Nature Geosci*, 6(1):520–524, June 2013.
- Chester S. Gardner. Ranging performance of satellite laser altimeters. *IEEE Transactions on Geoscience and Remote Sensing*, 30(5):1061–1072, Sep 1992. doi: 10.1109/36.175341.
- Antonio Genova, Sander Goossens, Erwan Mazarico, Frank G. Lemoine, Gregory A. Neumann, Weijia Kuang, Terence J. Sabaka, Steven A. Hauck, David E. Smith, Sean C. Solomon, and Maria T. Zuber. Geodetic Evidence That Mercury Has A Solid Inner Core. , 46(7):3625–3633, Apr 2019. doi: 10.1029/2018GL081135.
- V. E. J Girardin. Impact of non-gravitational forces on gps-based precise orbit determination of low earth orbiters. implemented in the bernese gnss software, master thesis, 2016.
- J. Gouman. *Performance analyses of a laser altimeter system: BepiColombo Laser Altimeter*. PhD thesis, 2015.
- K. Gunderson, N. Thomas, and M. Rohner. A laser altimeter performance model and its application to bela. *IEEE Transactions on Geoscience and Remote Sensing*, 44(11):3308–3319, Nov 2006. doi: 10.1109/TGRS.2006.880623.
- Kurt Gunderson and Nicolas Thomas. Bela receiver performance modeling over the bepi-colombo mission lifetime. *Planetary and Space Science*, 58(1):309 – 318, 2010. ISSN 0032-0633. doi: <https://doi.org/10.1016/j.pss.2009.08.006>. URL <http://www.sciencedirect.com/science/article/pii/S0032063309002451>. Comprehensive Science Investigations of Mercury: The scientific goals of the joint ESA/JAXA mission BepiColombo.

- E. Heesel. Optical design and analyses report. Report BC-BEL-RP-92014-I2-RO-RxBP, ESA, 2014.
- Alireza Hosseiniarani, Stefano Bertone, Adrian Jaeggi, and Nicolas Thomas. Improved modelling of laser altimetry observation for mpo orbit reconstruction. *20th EGU General Assembly, 8-13 April, 2018, Vienna, Austria, p.10178*, 2018.
- V. Iafolla, D.-M. Lucchesi, S. Nozzoli, and F. Santoli. The bepicolombo mission to mercury: Reaction wheels desaturation manoeuvres and the isa accelerometer δv measurements. *Planetary and Space Science*, 59:51–62, 2011. doi: <https://doi.org/10.1016/j.pss.2010.11.001>.
- L. Less and G. Boscagli. Advanced radio science instrumentation for the mission bepicolombo to mercury. *Planetary and Space Science*, 19(14-15):1597–1608, 2001. doi: [https://doi.org/10.1016/S0032-0633\(01\)00096-4](https://doi.org/10.1016/S0032-0633(01)00096-4).
- L. IMPERI. *AN ANALYSIS OF THE GEODESY AND RELATIVITY EXPERIMENTS OF BEPICOLOMBO*. PhD thesis, 2015-2016.
- Adrian Jäggi. *Pseudo-Stochastic Orbit Modeling of Low Earth Satellites Using the Global Positioning System*. PhD thesis, 2007.
- R. Jehn. Bepicolombo mercury cornerstone consolidated report on mission analysis. Report 525, BC-ESC-RP-05500, Issue 5.2, EUROPEAN SPACE AGENCY, EUROPEAN SPACE OPERATIONS CENTRE GROUND SYSTEMS ENGINEERING DEPARTMENT Mission Analysis Section, 2015.
- K. Kabin, T.I. Gombosi, D.L. DeZeeuw, and G. Powell. Interaction of mercury with the solar wind. *Icarus*, Feb 2000.
- Reinold Kallenbach, Eamonn Murphy, Bodo Gramkow, Markus Rech, Kai Weidlich, Thomas Leikert, Reiner Henkelmann, Boris Trefzger, Bodo Metz, Harald Michaelis, Kay Lingenauber, Simone DelTogno, Thomas Behnke, Nicolas Thomas, Daniele Piazza, and Karsten Seiferlin. Space-qualified laser system for the bepicolombo laser altimeter. *Appl. Opt.*, 52(36):8732–8746, Dec 2013. doi: 10.1364/AO.52.008732. URL <http://ao.osa.org/abstract.cfm?URI=ao-52-36-8732>.
- F. Luedicke. Orbit simulations for bepicolombo using messenger-based high-order mercury gravity field data. *European Planetary Science Congress 2014, EPSC Abstracts, Vol. 9, id. EPSC2014-548*, 2014.
- Manuela Marabucci. *The determination of Hermian gravity and topography from radioscience and laser altimetry data of the BepiColombo mission*. PhD thesis, Sapienza University of Rome, 2012.
- B. Metz. Extended lifetime test diodes degradation. Report BC-BEL-NC-60048-1-2, ESA, 2014.

- A. Pommerol, S. Chakraborty, and N. Thomas. Comparative study of the surface roughness of the moon, mars and mercury. *Planetary and Space Science*, 73(1):287 – 293, 2012. ISSN 0032-0633. doi: <https://doi.org/10.1016/j.pss.2012.08.020>. URL <http://www.sciencedirect.com/science/article/pii/S0032063312002577>. Solar System science before and after Gaia.
- F. Santoli, V. Iafolla, E. Fiorenza, C. Lefevre, D. M. Lucchesi, M. Lucente, C. Magnafico, and R. Peron. The isa accelerometer for bepicolombo: Data processing and operations. *2018 5th IEEE International Workshop on Metrology for AeroSpace (MetroAeroSpace)*, pages 216–221, June 2018. ISSN 2575-7490. doi: 10.1109/MetroAeroSpace.2018.8453599.
- S. Schulze-Walewski. Range finder module interface control document. Technical report, Ruag Aerospace AG, 2011.
- Sean C. Solomon, Ralph L. McNutt, Robert E. Gold, and Deborah L. Domingue. Messenger mission overview. *Space Science Reviews*, 131(1):3–39, Aug 2007. ISSN 1572-9672. doi: 10.1007/s11214-007-9247-6. URL <https://doi.org/10.1007/s11214-007-9247-6>.
- Paul D. Spudis. 2001.
- G. Steinbrügge, A. Stark, H. Hussmann, K. Wickhusen, and J. Oberst. The performance of the bepicolombo laser altimeter (bela) prior launch and prospects for mercury orbit operations. *Planetary and Space Science*, 159:84 – 92, 2018. ISSN 0032-0633. doi: <https://doi.org/10.1016/j.pss.2018.04.017>.
- H. C. M. Susorney, O. S. Barnouin, C. M. Ernst, and P. K. Byrne. The surface roughness of mercury from the mercury laser altimeter: Investigating the effects of volcanism, tectonism, and impact cratering. *Journal of Geophysical Research: Planets*, 122(6):1372–1390, 2017. doi: 10.1002/2016JE005228. URL <https://agupubs.onlinelibrary.wiley.com/doi/abs/10.1002/2016JE005228>.
- B.D. Tapley, B.E. Schutz, and G.H. Born. *Statistical Orbit Determination*. 2004.
- N. Thomas, T. Spohn, J.-P. Barriot, W. Benz, G. Beutler, U. Christensen, V. Dehant, C. Fallnich, D. Giardini, O. Groussin, K. Gunderson, E. Hauber, M. Hilchenbach, L. Iess, P. Lamy, L.-M. Lara, P. Lognonné, J.J. Lopez-Moreno, H. Michaelis, J. Oberst, D. Resendes, J.-L. Reynaud, R. Rodrigo, S. Sasaki, K. Seiferlin, M. Wieczorek, and J. Whitby. The bepicolombo laser altimeter (bela): Concept and baseline design. *Planetary and Space Science*, 55(10):1398 – 1413, 2007. ISSN 0032-0633. doi: <https://doi.org/10.1016/j.pss.2007.03.003>.
- Nicolas Thomas, Hauke Hussmann, and Luisa M. Lara. The bepicolombo laser altimeter (bela): a post-launch summary. *CEAS Space Journal*, Aug 2019. ISSN 1868-2510. doi: 10.1007/s12567-019-00270-y. URL <https://doi.org/10.1007/s12567-019-00270-y>.

-
- D. Yang, M. T. Zuber, J. W. Head, and S. C. Solomon. Distribution of topographic slope and roughness in mercury's northern hemisphere. *44th Lunar and Planetary Science Conference, held March 18-22, 2013 in The Woodlands, Texas. LPI Contribution, 2016.*

Acknowledgements

I would like to express my special appreciation and thanks to my advisor Prof. Dr. Nicolas Thomas, you have been a tremendous mentor for me. I would like to thank you for for giving me this opportunity for being a PhD student and for allowing me to grow as a research scientist. Your advice on both research as well as on my life and career have been priceless. I would like to express my deepest appreciation to my co-advisors, Dr. Stefano Bertone and Dr. Daniel Arnold, for their great help, guidance and support during my PhD. A very special gratitude goes out to Prof. Dr. Adrian Jäggi for his valuable advice and for providing me the opportunity to use the great capabilities of Bernese software during my PhD. I also want to thank Dr. Alexander Stark for his invaluable insight into my work. I would like to thank all the people of the BELA team, specially Urs Geissbühler, for providing me with the information and data I needed for my PhD. I would like to thank Gisela Herren and all the other administrative staff of the University of Bern. All of you have been there to support me whenever I needed you.

A very special thanks to my parents. Words cannot express how grateful I am to my mother and father, for all of the uncountable sacrifices that you've made on my behalf. I would like to express my deepest gratitude to my beloved wife, Shima, who spent sleepless nights to help me and was always my support in the moments when there was no one to answer my queries. The completion of my thesis would not have been possible without the support of you all. I would also like to thank my sweet little daughter, Baran, for the happiness she brought me.

I am grateful to my brother and sister, Amirhossein and Reyhaneh, who have provided me through moral and emotional support in my life. I am also grateful to my mother, father and brother-in-law who have supported me along the way. I would like to thank all of my friends at the University of Bern for letting my PhD be an enjoyable period of my life.

And finally, last but by no means least, to my great teachers and university professors, Mr. Didehban, Mr. Hamed, Mr. Soudi, Dr. Mirshams, Dr. Novinzadeh, Dr. Pourtakdoust and also to all the other mentors I have had in my life, without their help, support and advise, I wouldn't be able to reach this point.

Thanks for all your encouragement!

I'd like to acknowledge that this PhD has been funded with the support of the Swiss National Foundation (SNF) and NCCR PlanetS. Stefano Bertone acknowledges support by the Swiss National Science Foundation within the Advanced Postdoc Mobility program and by NASA's Planetary Science Division Research Program.

Declaration of consent

on the basis of Article 28 of the RSL Phil.-nat. 05

Name/First Name: HosseiniArani, Seyed Alireza

Registration Number: 15-138-589

Study program: Physics

Bachelor

Master

Dissertation

Title of the thesis: BepiColombo laser altimeter (BELA) performance evaluation: from laboratory tests to simulations of flight observations

Supervisor: Prof. Dr. Nicolas Thomas

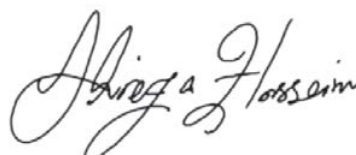
I declare herewith that this thesis is my own work and that I have not used any sources other than those stated. I have indicated the adoption of quotations as well as thoughts taken from other authors as such in the thesis. I am aware that the Senate pursuant to Article 36 paragraph 1 litera r of the University Act of 5 September, 1996 is authorized to revoke the title awarded on the basis of this thesis.

For the purposes of evaluation and verification of compliance with the declaration of originality and the regulations governing plagiarism, I hereby grant the University of Bern the right to process my personal data and to perform the acts of use this requires, in particular, to reproduce the written thesis and to store it permanently in a database, and to use said database, or to make said database available, to enable comparison with future theses submitted by others.

Bern 18.12.2019

Place/Date

Signature



Alireza Hosseiniarani



Profile

PhD candidate at the University of Bern working on BepiColombo laser altimeter (BELA) performance evaluation and its contribution to MPO orbit improvement

Skills

- Strong skills in classical Astrodynamics (+GR to a lesser extent)
- Precise orbit determination and planetary gravimetry for space missions
- Planetary science (surface geology and planetary dynamics)
- Laser altimetry instrument
- Spacecraft trajectory design and optimization
- Spacecraft attitude dynamics and control
- Spacecraft system engineering
- Optimization algorithms (GA and PSO)
- Strong programming and modeling skills in MATLAB and Fortran
- Machine learning and deep learning
- Laboratory experience with space borne laser altimetry systems + measurement data analysis
- Languages: English (fluent), German (A2 level), Persian (mother language)
- Teamwork

Education and Trainings

| | | |
|---------------------------------------|---|-------------------------------------|
| <i>Jan. 2016 to Now</i> | University of Bern PhD student in Physics Thesis: “BepiColombo Laser Altimeter (BELA) performance evaluation: from laboratory tests to simulations of flight observations” | <i>Bern, Switzerland</i> |
| <i>Feb. 2019</i> | Workshop on Machine learning Supervised and unsupervised machine learning techniques on astronomical data | <i>Geneva, Switzerland</i> |
| <i>Sep. 2017</i> | SDSM 2017 Satellite dynamics and space missions: Theory and applications of Celestial Mechanics | <i>San Martino al Cimino, Italy</i> |
| <i>Sep. 2016</i> | SPICE training workshop SPICE-based applications supporting space science research Presented by Naif, NASA, Hosted by ESA Madrid | <i>Madrid, Spain</i> |
| <i>July 2016</i> | Bernese GNSS Software workshop Bernese: Precise orbit determination software for Earth and planetary missions. Presented by the Astronomy institute of the University of Bern | <i>Bern, Switzerland</i> |
| <i>Jan. 2015 to Feb. 2015</i> | Internship in Max Planck Institute for Solar System Research Studying the possibility of measuring the density variations in comet 67p using Philae landing orbit- Dr. Pedro Lacerda | <i>Göttingen, Germany</i> |

| | | |
|------------------------------|---|---------------------|
| Oct. 2007 to Sep. 2010 | K. N. Toosi University of technology Master of Science in space engineering Master thesis: Trajectory design and optimization to | <i>Tehran, Iran</i> |
| Oct. 2003 to Sep. 2007 | IAU University, Science and Researches branch Bachelor of Science: Aerospace engineering Graduate thesis: Modeling the trajectory of spacecraft in 3 body problem | <i>Tehran, Iran</i> |

Working experience

Space research laboratory, K.N. Toosi University

- Simulation of Satellite constellations
- Modeling the perturbing forces and moments due to Earth gravitational potential, 3rd body gravitational effects, solar radiation pressure, Earth magnetic field, Earth gravity gradient
- Conceptual and preliminary design of attitude determination and control subsystem of Zohreh Satellite (a Geo-synchronous communication satellite)
- Developing the orbit propagator code for Zohreh

Publications

- Hosseiniarani, A., Bertone, S., Arnold, D., Jäggi, A., Thomas, N., **“MPO precise orbit determination and Mercury gravimetry experiment using Doppler observations”**. Manuscript in preparation
- Hosseiniarani, A., Beck, T., Bertone, S., Thomas, N., **“Laboratory-based performance evaluation of BepiColombo laser altimeter (BELA)”**, Manuscript will soon be submitted
- Hosseiniarani, A., Bertone, S., Arnold, D., Beck, T., Herny, C., Pommerol, A., Jäggi, A., Thomas, N., **“Comprehensive in-orbit performance evaluation of BepiColombo laser altimeter (BELA)”**, Submitted to Planetary and Space Science journal, Jan. 2020
- Hosseiniarani, A., Bertone, S., Arnold, D., Beck, T., Herny, C., Pommerol, A., Jäggi, A., Thomas, N., **“Comprehensive in-orbit performance evaluation of BepiColombo laser altimeter (BELA)”**, EPSC-DPS Meeting Abstracts Sep. 2019
- Hosseiniarani, A., Bertone, S., Arnold, D., Jäggi, A., Thomas, N., **“Simulation of MPO orbit reconstruction using Doppler observations and comparison with laser altimetry observations”**, EPSC Meeting Abstracts Sep. 2018
- Hosseiniarani, A., Bertone, S., Arnold, D., Jäggi, A., Thomas, N., **“Simulation of MPO orbit reconstruction using Doppler observations and comparison with laser altimetry observations”**, EPSC Meeting Abstracts Sep. 2018
- Hosseiniarani, A., Bertone, S., Jäggi, A., Thomas, N., **“Improved modelling of BELA altimetry observation for MPO orbit reconstruction”**, EGU Meeting Abstracts Apr. 2018
- Hosseiniarani, A., Bertone, S., Jäggi, A., Thomas, N., **“BepiColombo Laser Altimeter (BELA) contributions to MPO orbit improvement towards a better determination of Mercury geophysical parameters”**, EPSC Meeting Abstracts Sep. 2017
- Hosseiniarani, A., Bertone, S., **“MPO relative orbit error modelling using the Bernese GNSS software”** a technical report for DLR Berlin, 2017
- Bertone, S.; Jäggi, A., Arnold, D., Girardin, V., Hosseiniarani, A.; Desprats, W., Inamdar, J. (2017) **“An overview on Bernese projects in planetary geodesy and deep-space orbit determination”**, AGU Fall Meeting Abstracts Dec 2017
- Bertone, S. and Arnold, D. and Jäggi, A. and Hosseiniarani, A. (2016) **“Bernese developments in planetary geodesy: a GRAIL Moon gravity field and tidal solution and an outlook on current projects”**, AGU Fall Meeting Abstracts Dec 2016